UNIVERSITY OF SOUTHAMPTON
FACULTY OF ENGINEERING, SCIENCE AND MATHEMATICS
SCHOOL OF ENGINEERING SCIENCES

The Aerodynamics of an Inverted Wing and a Rotating Wheel in Ground Effect

by

Jacques Heyder-Bruckner

A thesis submitted in partial fulfillment for the
degree of Doctor of Philosophy

Supervisor: Professor Xin Zhang

May 2011

UNIVERSITY OF SOUTHAMPTON

ABSTRACT

FACULTY OF ENGINEERING, SCIENCE AND MATHEMATICS
SCHOOL OF ENGINEERING SCIENCES

Doctor of Philosophy

THE AERODYNAMICS OF AN INVERTED WING AND A ROTATING WHEEL IN GROUND EFFECT

by Jacques Heyder-Bruckner

This study investigates the aerodynamics of an inverted wing in ground effect, a racecar wheel and the interaction between the two components, using numerical and experimental methods. The wheels were located behind the wing at an overlap and gap of $20mm$, and the wing ride height in the vertical direction was the primary variable. Models of 50% scale were used, giving a Reynolds number of 5.8×10^5 based on the wing chord.

The Detached-Eddy Simulation model was validated against wind tunnel measurements including PIV, surface pressures and forces, where it was found to outperform a Reynolds averaged Navier-Stokes approach which used the Spalart-Allmaras turbulence model. It accurately predicted the wing vortex breakdown at low ride heights, which is of the bubble type with a spiralling tail, and the wake of the wheel. A mesh sensitivity study revealed that a finer mesh increased the amount of structures captured with the DES model, improving its accuracy.

The time-averaged wake of a rotating wheel was found to be composed of an upper arch shaped vortex and a wider lower recirculation region. The instantaneous wake structures were found to be different, with vortices shed from the separation around the top and the lower front of the wheel. A stationary wheel was found to have a strong downwash behind it as the flow stays attached around the top, forming two counter rotating vortices originating from the upper tyre shoulders and resulting in a higher drag and lift.

When combined with the wheel, the wing was found to produce less downforce at high ride heights but more at low ride heights compared to the isolated wing. The position of the stagnation point on the wheel relative to the wing contributes to this. The wing vortex breakdown occurs at higher ride heights than in the isolated case. It contributes to a change in the wheel wake, which resembles the wake structure around a stationary isolated wheel at high wing ride heights or a rotating isolated wheel at low ride heights.

Declaration of Authorship

I, Jacques Heyder-Bruckner, declare that the thesis entitled, 'The Aerodynamics of an Inverted Wing and a Rotating Wheel in Ground Effect' and the work presented in the thesis are both my own, and have been generated by me as the result of my own original research. I confirm that:

- this work was done wholly or mainly while in candidature for a research degree at this University;
- where any part of this thesis has previously been submitted for a degree or any other qualification at this University or any other institution, this has been clearly stated;
- where I have consulted the published work of others, this is always clearly attributed;
- where I have quoted from the work of others, the source is always given. With the exception of such quotations, this thesis is entirely my own work;
- I have acknowledged all main sources of help;
- where the thesis is based on work done by myself jointly with others, I have made clear exactly what was done by others and what I have contributed myself;
- parts of this work have been published as:

  Heyder-Bruckner, J. and Zhang, X. Detached Eddy Simulation of a Double Element Wing in Ground Effect. 48th AIAA Aerospace Sciences Meeting including the New Horizons Forum and Aerospace Exposition, 2010, 49pp.

Signed: ____

Date: ____

Acknowledgements

I would like to thank first and foremost my supervisor Professor Xin Zhang for his support throughout my PhD. His input often made me look at things from a different perspective and, while he allowed me to find my own path, his guidance was always helpful.

My thanks extend to the wind tunnel technicians Mike Tudor Pole and Mike Thomas. They always provided support for my experiments and assisted me greatly when required.

Many thanks to Mercedes GP, former Honda Racing F1, for the industrial support and advice. In particular David Jeffrey, Johnathan Zerihan and Jonathan Eccles need to be mentioned.

The supporting staff at the University of Southampton proved indispensable and helped make the various transitions and milestones smoother. I want to especially thank Alessia Plutino for all her assistance.

Finally, I thank my family who believed in me throughout, providing love and support. My colleagues with whom I shared many ideas and theories. Nina whose comforting words rendered stressful times easier to bear. And Amy for providing the Creme Egg Incentive.

Contents

List of Figures

List of Tables

Abbreviations

CFD	Computational Fluid Dynamics
CWW	Combined Wing-Wheel
DES	Detached Eddy Simulation
DNS	Direct Numerical Simulation
FANS	Finite Analytic Navier-Stokes
FIA	Federation Internationale de l'Automobile
LDA	Laser Doppler Anemometry
LES	Large Eddy Simulation
PIV	Particle Image Velocimetry
PSD	Power Spectral Density
RANS	Reynolds Averaged Navier-Stokes
S-A	Spalart-Allmaras
SRANS	Steady Reynolds Averaged Navier-Stokes
RNG	Renormalisation Group theory ($k - \epsilon$ turbulence model)
UDF	User Defined Function
URANS	Unsteady Reynolds Averaged Navier-Stokes

Physical Constants

Density of air (ISA) $\rho = 1.225\ kgm^{-3}$

Viscosity of air (ISA) $\mu = 1.789 \times 10^{-5}\ kgm^{-1}s^{-1}$

Symbols

AR	Wheel Aspect ratio, $AR = W/D = 0.55$	
c	Wing chord	m
C_D	Drag coefficient	
C_L	Downforce coefficient	
C_P	Pressure coefficient, $1 - V^2/V_\infty^2$	
D_{wheel}	Wheel diameter	m
h	Wing ride height	m
P	Pressure	Nm^{-2}
q	Dynamic pressure, $0.5\rho U_\infty^2$	Nm^{-2}
Q	Q criterion, second invariant of ΔU	s^{-2}
Re	Reynolds number, $\rho U_\infty c/\mu$	
t	Timestep	s
U_∞	Freestream velocity	ms^{-1}
U, V, W	Mean velocity components in x, y, z directions	ms^{-1}
W_{wheel}	Wheel width	m
x, y, z	Cartesian right handed coordinates	m
y^+	Non-dimensional normal wall distance, yU_τ/υ	
Δt	Non-dimensional timestep, tU_∞/c	
μ	Molecular viscosity	$kgm^{-1}s^{-1}$
ν	Kinematic viscosity, μ/ρ	m^2s^{-1}
Ω_x	Non-dimensional x-vorticity, $\omega_x c/U_\infty$	
ρ	Density	kgm^{-3}

Chapter 1

Introduction and Literature Survey

This chapter gives an introduction on the subject of aerodynamics in racing cars, with a short historical background of its development in Formula One. This is followed by a review of past studies on the front wing and wheels of open wheel racecars. The motivation and objectives of this research based on the literature review are then outlined.

1.1 Introduction

The study of aerodynamics is normally associated with aircraft development, as it forms an integral part of the design process. On the other hand, it is not usually a major part of the development of road vehicles, where other factors such as styling can be considered more important. Racing cars are an exception and make use of the airflow around them to optimise cooling and performance. Cooling is used to keep the temperature of the engine and brakes to a level where they operate at their highest efficiency, but it is a compromise between the amount of cooling applied and the loss in aerodynamic performance this results in. The aerodynamic performance of the car can be improved in two ways: by reducing the drag, which will result in higher straight line speed, or by increasing the downforce[1], which enhances the grip of the car on the road allowing for faster cornering speeds. Improving the downforce will often adversely affect the drag and vice versa, therefore a compromise between the two is required to optimise performance for a given track layout. Another aspect of the aerodynamics of the car which must be optimised is the aerodynamic balance, which is comprised of the distribution of downforce between the front and rear tires, affecting the handling of the car.

---

[1] Downforce is a term commonly used in racing car aerodynamics which corresponds to negative lift.

Formula One is a motorsport which has existed for more than 50 years, but up until 1967 [1] little use of aerodynamics was made to increase the cornering speed of the car. The bodies were streamlined to reduce the drag but most of the work was concentrated on the engine and on power performance. The first inverted wings were introduced in 1968 and were placed around the front and rear axles, improving the downforce greatly. These devices quickly evolved, becoming larger and more effective, sometimes even with driver control where the wings could act as spoilers to enhance breaking. To avoid compromising the suspension, they were mounted directly onto the unsprung wheel, transferring the aerodynamic load directly into an increase in grip. Unfortunately, structural failure of these devices resulted in fatal accidents and the regulations were consequently changed, restricting their size and limiting them to being connected to the entirely sprung part of the car.

Although the aerodynamic efficiency of these Formula One inverted wings were improved, there was no large advance in aerodynamic performance until 1977, when full ground effect was incorporated. The car's underbody was shaped as an aerofoil thereby producing downforce, while side skirts sealed the air under the car further improving this effect. Over the years, this technique was refined and the cornering speeds increased. In 1989, the regulations changed to ban this by introducing a flat-bottom and the focus of the aerodynamic development shifted to improving small details of the car.

Aerodynamics is now an integral part and one of the most important areas of design of a Formula One car. A high level of downforce is achieved through three main components: the front wing (≈25% of total downforce), the underbody diffuser (≈40% of total downforce) and the rear wing (≈35% of total downforce) [2]. The design of the front wing affects the flow of the underbody diffuser and of the rear wing, so it is important to have a good understanding of the wake it produces. In addition, the wheels of a Formula One car cannot be shrouded, making the flow around them more complex and more important as it interacts with the other components of the car. They account for approximately 40% of the total drag of the car [2], but as their profile is fixed by the supplier, they cannot be modified extensively to improve their aerodynamic performance. Thus, as the front wing affects the airflow around the front wheels, it is used to direct the flow around the wheels to increase their performance.

Aerodynamic development in Formula One is aided by two techniques: wind tunnel testing and Computational Fluid Dynamics (CFD). With wind tunnel testing, many model variations can be tested quickly and measurements of forces and pressures can be made. In addition, visualisation techniques such as oil flow and Particle Image Velocimetry (PIV) can give additional insight into the flow behaviour. But these techniques have their limitations and wind tunnel testing in Formula One is expensive. As computer power has increased over the years, CFD has become an alternative to wind tunnel testing, allowing for the study of the flow in ways not possible experimentally, although its use is still limited by resources and accuracy.

The interaction of the many elements present in a Formula One car is very complex and to increase our understanding of their behaviour, these elements have been studied in isolation. Simplified studies of racing car wings and wheels using both wind tunnel testing and CFD are reviewed in the following section.

1.2 Literature Survey

1.2.1 Wing in Ground Effect

The front wing of a Formula One car affects the aerodynamic elements which are situated behind it (wheels, underbody, rear wing) and small changes to it can have large effects on the overall performance. It is therefore important to understand what happens to the flow around it and looking at the front wing in isolation is the first step to achieving this.

1.2.1.1 One-element wing

Experimental studies The front wing is composed of an inverted aerofoil which creates downforce. It acts in ground effect and has been investigated in a series of studies [3–7]. In 1994, Knowles et al. [3] presented an experimental study of the sensitivity to ground proximity of a single element wing representative of a racing car front wing. A rolling road facility was used and it was found that the downforce increases as the wing approaches the ground because of the increased suction on the lower surface, due to the venturi effect between the wing and ground surface. Only a limited range of heights was investigated which failed to capture the force reduction phenomenon, though stalled flow over the rear portion of the wing was observed.

Ranzenbach and Barlow conducted similar studies using two dimensional experiments on symmetric [4] and cambered [5, 6] NACA aerofoil sections. Both the force-enhancement and the force-reduction phenomena were captured, and it was concluded that the latter occurred due to the merging of the aerofoil and ground boundary layers. It must be noted that a fixed ground was used in the experimental setup.

In 2000, Zerihan and Zhang investigated the effect of changing the ride height of a highly cambered inverted single element wing with endplates using a moving ground facility [8].

Force measurements were obtained as well as pressure distributions around the wing, and a similar trend to Ranzenbach and Barlow was observed, although they came to a different conclusion. No evidence of the force-reduction phenomenon being caused by the two boundary layers merging was found, but instead it was associated to the trailing-edge separation of the boundary layer. The effect of ride height on C_L is shown on Figure 1.1 where maximum downforce occurs at a height of approximately 0.1 chord. It is noted that a fixed ground does not correctly model the flow behaviour, especially at low ride heights. A Laser Doppler Anemometry (LDA) survey of the wake at the centrespan of the wing was also conducted by Zhang and Zerihan [9]. As stated previously, the wake of the front wing is fundamental as it greatly affects the overall performance of the car. This survey showed that the wake grows as the ground is approached and it confirmed that the force-reduction phenomenon is caused by boundary layer separation (i.e. the wing stalling). Vortex shedding in the instantaneous wake was observed and at the lower ride heights the wake exhibits an additional transverse flapping motion .

The front wing will also have three-dimensional effects such as edge vortices. This is quite an important feature, especially for this study, as it interacts heavily with the wheel flow field (this is discussed in more details in Section 1.2.3). Zhang and Zerihan [10] used a range of experimental methods including Particle Image Velocimetry (PIV), LDA and surface flow visualisation to investigate the edge vortices generated by a cambered wing at different ride heights. An edge vortex on the suction surface at the endplate edge, which initiates at the peak suction position, was observed. This vortex causes vortex-induced suction and delays trailing edge separation by effectively reducing the incidence near the endplate. The vortex has got a low streamwise speed core, which means that it can breakdown quickly further downstream. In the force-enhancement zone, the vortex strength increases whereas its size remains relatively unchanged. At heights lower than where the maximum rate of force-enhancement occurs, the vortex starts to breakdown and its size increases. The presence of the edge vortex thus contributes to the force-enhancement process, even though it plays a secondary role.

Numerical studies Ranzenbach and Barlow also conducted a computational analysis of their two-dimensional aerofoils [4, 6]. A multiblock structured grid was used with a Reynolds-Averaged Navier-Stokes (RANS) solver and the ground was modelled both as being fixed and moving. The fixed ground simulation compared well with their experiment whereas the moving ground simulation gave a similar trend to the fixed ground, but showed a much higher value of downforce at low ride heights, confirming that a fixed ground experiment is not accurate.

To complete the study on a single element wing, Zerihan and Zhang performed two-dimensional computations of their wing's centrespan [11], where experiments showed the flow to be quasi two-dimensional. Two numerical models were analysed, namely the Spalart-Allmaras (S-A) model and the $k-\omega$ SST model, using a fully structured grid containing approximately 30,000 grid cells. Everything was modelled to reproduce the experimental conditions used in [8], in order to compare the numerical results to the experiments. Both numerical models overpredicted the wake thickness, but the S-A model gave good qualitative results, predicting the correct trends in pressure distributions at all ride heights. It must be noted that the grid used was coarse. A similar study was done by Mahon and Zhang [12], where the ability of six different turbulence models (i.e. S-A, Standard $k-\epsilon$, $k-\epsilon$ RNG, Realizable $k-\epsilon$, Standard $k-\omega$ and $k-\omega$ SST) in capturing major flow features was investigated. A hybrid grid containing structured and unstructured blocks was used, with approximately 350,000 grid cells. It was concluded that the two-dimensional flow field of an inverted wing in ground effect can be accurately predicted using a RANS model, though two different models gave the most accurate predictions of the surface pressures ($k-\omega$ SST) and of the wake flow field (Realizable $k-\epsilon$).

1.2.1.2 Double-element wing

Experimental studies To improve the performance of a wing, its profile can be optimised to delay separation and achieve high lift to drag ratios. An additional way of improving the performance is to have additional wing elements and Formula One cars now have multiple element front and rear wings. The investigation of an inverted front wing in ground effect thus naturally extended to include a second element. Ranzenbach and Barlow [13] began to address the topic using a two-dimensional NACA 63_2-215 Mod B airfoil, with a 30% slotted flap. A higher downforce than a single element wing was observed, with the force-reduction phenomenon occurring at higher heights, but a fixed ground was used in the experiments which, as mentioned above, gives a bad representation of the real flow.

Jasinski and Selig [14] presented an experimental study of a three-dimensional double element front wing, but again a fixed ground was used. The effect of different endplates and flaps was investigated, but only at a ride height of 0.3 chord. Using a seven hole probe, two trailing vortices were observed rolling up from the endplate, and these increased in size for a larger flap deflection.

Zhang and Zerihan also conducted a study of a double element race car wing in ground effect [15]. For the main element the wing from their previous study [11] was used and for the second element a flap of constant chord was added. Two flap angles were used, a high flap angle and a low flap angle. The pressure distribution around both the main element and the flap was measured, while the downforce and drag of the wing at different ride heights was recorded. Zhang and Zerihan also conducted LDA, PIV and oil flow visualisation. It was found that most of the downforce is produced by the main element as the flap induces a greater circulation around it and that the trend of change of downforce with ride height was similar to that of a single element wing, with an added discontinuity. There was a point in the force-enhancement region where a plateau (for low flap angle) or even a drop in downforce (for the high flap angle) was now present. This was associated to the breakdown of the lower edge vortex.

Mahon investigated in detail the aerodynamics of an isolated two element wing[2] in ground effect [16]. He conducted experiments to analyse the influence of flap location, flap incidence, ride height and the addition of endplate feet. Force and pressure measurements, PIV, oil-flow visualisation and wake studies using Pitot tubes were all performed to obtain qualitative and quantitative results. Mahon discovered that the downforce of the wing in the force-reduction region depends on the starting position. If the wing's initial position, before the wind tunnel is turned on, is at minimum ride height, then the downforce of the wing will be less than if the wing is lowered to that height from a higher point (see Figure 1.2). This was associated to Re-effects during the starting of the tunnel, resulting in a bi-modal behaviour of the flow separation. From the wake studies it was concluded that, in addition to boundary layer separation and edge vortex breakdown, there exists another lift limiting mechanism with flow reversal in the main element wake beneath the flap. This would occur as the wing wake velocity drops due to the adverse pressure gradient from the flap and is a characteristic of slotted wings [17]. This was not proved as no experimental data that explicitly showed the flow reversal was obtained and it was only deduced from Pitot tube measurements which cannot capture flow reversal.

Using PIV, Mahon observed two edge vortices. There was a strong vortex on the inside of the endplate, underneath the wing's suction surface, originating at the location of peak suction. The second vortex was located at the top of the endplate, on the other side, and was much weaker. With the addition of endplate feet, an additional vortex appeared underneath the foot. It introduced a new downforce enhancement mechanism as well as strengthening the other mechanisms, resulting in higher downforce levels. It was found that below a certain ride height the lower edge vortex breaks down, similar to a single element wing, and he too associated it to the discontinuity in the force enhancement region.

---

[2] This wing will be the one used in the current research

The main element wake was found to thicken with its path deflected downwards as the ride height was decreased and it merged with the flap wake at low ride heights. Between the wake and the ground boundary layer, a region with higher than free stream velocity was discovered, and this wall jet increased in strength for decreasing ride heights. Finally, there was a boundary layer present on the moving ground, created by the wing's pressure gradient, and it increased in thickness as the wing approached the ground.

A final study has been done on an isolated double element wing by Van den Berg [18]. He investigated the same wing as Mahon and his tests were mainly done to confirm and correct some of Mahon's theories. He too associated the discontinuity in the force enhancement region to vortex breakdown and showed the resulting flow reversal bubble using PIV. For the force plateau present at lower ride heights, he disagreed with Mahon's theory that flow reversal in the main element's wake was the cause, and explained this characteristic by edge vortex burst. The edge vortex beneath the wing breaks down creating a large region of flow reversal, and the flap surface in proximity produces less downforce. The same double element wing model used by Mahon and Van den Berg will be used in the current study.

Numerical studies Ranzenbach and Barlow also conducted a two-dimensional numerical study of their multi-element aerofoil with a moving ground [13], using a variant of the Standard $k-\epsilon$ model with a fully structured chimera grid of around 31,000 cells, but they only observed slight changes in the downforce at low ride heights and did not alter their conclusion that the force-reduction phenomenon was caused by the merging of the wing and ground boundary layers. Mahon and Zhang [12] performed a two-dimensional analysis of Zerihan's two element wing [7], investigating six turbulence models. A much higher number of grid cells was used when compared to Ranzenbach and Barlow, with a multiblock hybrid grid of around 200,000 cells giving an initial cell spacing normal to the wall of $y^+ \approx 1$. It was confirmed that most of the downforce, up to a maximum of approximately 84% total downforce, is produced by the main element, and that the majority of the drag is produced by the flap. It was suggested that the simulations incorrectly predicted the wake boundary due to the lack of three-dimensionality.

Mahon also performed a complete numerical study of his two element wing [16], using a three-dimensional approach. He used a multiblock hybrid grid, mpeding solver convergence for all the turbulence models used except for the S-A and $k-\omega$ SST models. The suction surface pressures were underpredicted resulting in lower strength edge vortices (which is directly related to the pressure difference between the lower and upper surface of the wing). The wake flow predictions performed better than for the two-dimensional simulations due to the inclusion of three-dimensional effects. Low ride heights were not simulated due to gridding restrictions and only six different ride heights were tested, all of which were in the force enhancement region.

Van den Berg also conducted numerical work using the wing from Mahon's study [18]. He mainly concentrated on improving the simulation by modifying the grid. The CFD wing model was recreated to better match the experimental model by using scanned wing data, as it was noted that the trailing edge of the elements were too thin. Also, the grid was made fully structured and the computational domains were made larger. In an attempt to model boundary layer transition, laminar zones were specified around the wing using oil flow data. The grid contained 3.8 million cells and seven turbulence models were investigated, with the Spalart-Allmaras model as the preferred choice due to its robustness and good qualitative predictions. Compared to Mahon, considerable improvements in the correlation between the computational and experimental values was obtained. It was also noted that the steady RANS simulations did not converge for a range of ride heights ($0.158 < h/c < 0.317$) and this was linked to the steady solver having problems with the unsteady physics related to the vortex breakdown.

A summary of the various numerical simulations of an inverted wing in ground effect which have been published is presented in Table 1.1. It has been shown that a 3D simulation is required to include the wing tip effects and, although steady RANS can capture the pressure distribution and wake qualitatively, it has some difficulties in modelling the vortex breakdown.

1.2.2 Wheel Aerodynamics

A wheel is a bluff body and as mentioned above, 40% of a Formula One car's drag is produced by its wheels. The flow behind bluff bodies is known to be unsteady and to exhibit strong three-dimensional properties [19]. Racing car wheels have the added complexity of rotation, which makes experimental measurements that much more difficult. Also, the wheels deform considerably under load, their temperature changes and this would affect the flow around it. The experimental and computational studies of the flow around an isolated wheel are reviewed below and it can be noted that there has been an increase in the research of wheel aerodynamics in recent years.

Experimental studies The measurements of main concern are the lift and drag force of the wheel and two methods can be applied to obtain these. The first one, the 'Direct Method', uses load cells and balances; the second one, the 'Indirect Method', uses the pressure distribution around the wheel surface to derive the forces. The former becomes difficult when the wheel is in contact with the ground, as it is required to separate the aerodynamic forces from the reaction forces due to the ground, and special pads underneath the wheel would be required to obtain the lift. The latter is hard to obtain for a rotating wheel and the accuracy will depend on the spatial resolution of the pressure measurements. Also, viscous drag is ignored, but this will be negligible compared to the pressure drag.

The first study which was done on a car wheel was in 1969, by Morelli [20]. A wheel that entered into a cut-out of a fixed plate which simulated the ground was used. The lift and drag forces for the stationary and rotating wheel conditions were measured using a balance, and a strong negative lift was obtained for the rotating case. The problem with this setup is that there was a gap between the wheel and the road, allowing air to travel underneath the wheel. In their study of the influence of ground clearance on the flow around a wheel, Stapleford and Carr [21] showed that to represent correctly the flow around a car wheel, a moving ground facility was required, with the wheel in direct contact with it. Due to limited facilities, they could not have the wheel in contact with the ground, so they used a seal between a fixed ground and a rotating wheel. This combination gave rise to positive lift, which was contrary to Morelli's result. They also investigated the forces generated by a rotating wheel situated close to a moving ground, and a strong negative lift was developed. This is due to the flow underneath the wheel being accelerated by a combination of the venturi effect, the moving ground and the rotating wheel, thus creating a large suction under the wheel. They measured static pressures around their wheel using a single static pressure probe, but this method does not give an accurate measurement of the surface pressure around the whole wheel as it is located outside the boundary layer. Cogotti [22] also investigated the effect of wheel to ground gap. He used a rotating wheel with a fixed ground and came to the same conclusions as Stapleford and Carr.

The first study to have a rotating wheel in contact with a moving ground was done by Fackrell and Harvey [23, 24], and their results are still the most accepted and referenced source in this subject area. Being unable to use the 'Direct Method', they resorted to the 'Indirect Method'. They measured the surface pressure distribution of their wheel using a microphone-based system located in the wheel itself, and transported the data out of the rotating wheel using slip rings. A typical pressure distribution around a wheel can be seen in Figure 1.3, and the integration of these for the rotating case resulted in C_L=0.44 and C_D=0.58. They observed a high pressure peak ($C_P > 1$) just in front of the contact patch, associated to viscous effects due to the moving boundaries of the wheel and ground. This high pressure produces a jetting effect and the flow exits from under the wheel with a high transversal velocity. A similar but opposite effect was predicted behind the wheel, where the moving boundary layers would result in a negative pressure peak, but the rising of the moving belt at this location prevented this feature to occur in their results. They investigated the differences between a rotating and stationary wheel, noting the latter had a shorter but wider wake and produced more lift and drag. These differences were associated to the boundary layer around a rotating wheel, which moves with the wheel's surface carrying turbulent fluid upstream and causing separation to occur prior to any adverse pressure gradient. It was also noted that contrary to the Magnus-effect, the stagnation point moves downwards with wheel rotation.

Fackrell and Harvey's work laid down the foundations of wheel aerodynamics and it is only recently that further investigations have been carried out. In 2002, Mears et al. [25, 26] developed a new system to measure the surface pressures around a rotating wheel, which used telemetry to transmit the data. A deformable Go-Kart tyre model was used, but it was not preloaded essentially making it non-deformable. The pressure distribution around the wheel was obtained, with similar trends to Fackrell, although they succeeded in capturing the low pressure after the contact patch. It must be noted that oscillations in the pressure distribution after the pressure peaks were recorded by this measurement system. The effects of a 5° yaw angle were also investigated and lead to a reduction in lift and an increase in drag.

Cogotti [22] proposed a theoretical wake model for a rotating wheel (see Figure 1.4), which was composed of three longitudinal counter-rotating vortex pairs originating from the top, middle (wheel hub) and bottom of the wheel. The rotational sense of the vortices was amended by Mercker et al. [27], who used wake pressure measurements to derive the wake model. Studies of the flow field around a rotating wheel has been performed using tufts [21, 28, 29], total pressure wake measurements [23, 26], PIV [18, 30–32] and LDA [33–35].

It has been observed by Knowles et al. [36] that real wheel geometry and the presence of the support sting suppress some of the theoretical vortical structures seen in Figure 1.4. They also investigated the influence of camber, noticing that a 4° cambered wheel has higher intensity vortex structures, and correspondingly a higher drag than a parallel wheel. Mears et al. [26] describe that the vortices were stronger in the stationary wheel case, which corresponds to a higher energy absorption, and thus higher drag. But as Wäschle et al. [33] noted, the total pressure measurement behind a bluff body results in an unphysical representation due to the angular dependence of the pressure probe and thus must be interpreted with care. Wäschle et al. [33] compared the wake of stationary and rotating wheels using LDA, confirming that the flow separates earlier for the rotating case resulting in a taller wake. The stationary wheel experiences a larger downwash behind the wheel's centreline, which results in the stronger observed lower vortices.

Saddington et al. [34] proposed a revised wake model for the rotating wheel based on their LDA survey (see Figure 1.5). They described the wake as being composed of two counter-rotating vortex pairs initiating from the top and bottom of the wheel and merging together further downstream. But Axerio and Iaccarino [32] noted from steady RANS simulations that a particle released in the upper vortex will travel upstream, an observation supported by the experimentally captured [34] flow reversal that intersects part of the upper vortices and an indication of a different wake structure than that proposed.

All of the references mentioned above essentially used non-deformable tyres, which would not, for example, model the contact patch correctly (a line instead of an area). To reproduce the correct flow features of a deformable tyre, it would need to be preloaded. This would result in excessive wear of the moving belt and a steal belt would be required. Another problem with deformable tyres would be the measurement of the forces. Both the 'Direct Method' and 'Indirect Method' become increasingly complicated because of the added freedom of deformation. The only published study of a deformable tyre was made by Purvis and Garry [37], where the effect of the contact patch size on the wake development was investigated. The tyre was made of foam, and even though it did not have an accurate side profile and suffered from asymmetric wear, it was concluded that the lower half of the wake was the most affected by the contact patch, as it increased significantly in width with increasing contact patch size.

Van den Berg studied the flow around a non deformable cambered F1 tyre, with the hub cavity covered [18]. He obtained drag force measurements, PIV data and the surface pressure distribution using a high quality pressure measurement system. He too observed the high pressure and low pressure peaks in front and behind the contact patch, but in contrast to Mears et al. [25, 26], there were no oscillations after the negative pressure peak. These are believed to be caused by instrumental error. The flow separation from the top surface was observed and it was clearly seen that it occurred before reaching the uppermost point of the wheel, as had been predicted by Fackrell and Harvey. The same wheel model used by Van den Berg will be used in the current study.

Numerical studies The first numerical study to be conducted on wheel aerodynamics was by Axon et al. [38] in 1998. They investigated the validity of CFD for the flow around a rotating wheel in contact with a moving ground. To do so, a simplified version of the B2 wheel used by Fackrell and Harvey [23] was modelled, using a fully structured grid and the CFD results were compared to Fackrell and Harvey's data. The cell quality underneath a non-deformable wheel is compromised by the tangential contact with the ground, so the wheel was modelled as if it was deformable by adding a vertical plinth[3]. It was concluded that CFD can give good qualitative results, predicting well some main flow features.

Over the years, different wheel simulations were achieved and assessed against Fackrell and Harvey's experiment [38–41] or their own experiment [18, 31–33, 42, 43]. Each simulation used different turbulent models with different types of grids and these are summarised in Table 1.2. They all used similar boundary conditions; a velocity inlet, pressure outlet and symmetry on the sides and top of the domain. All of them modelled the moving ground as a translating wall, except Skea et al. [39] who modelled the ground as a symmetry plane, as it was believed to be a fairer representation of the real conditions. CFD was shown to be capable of qualitatively capturing the pressure distribution around the wheel, with the high and low pressure peaks around the contact patch predicted by a good quality simulation.

Knowles et al. [42] used a steady RANS simulation to assess the impact of the wheel support sting used in their experiment and thus had to use a hybrid grid due to the added complexity. By including the sting, experimental conditions were reproduced and the effect of the sting on the wheel flowfield could also be investigated. Their simulation gave an underprediction in drag of 6% compared to their experimental results and incorrectly predicted the location of areas of reversed flow. They also found out that the sting increased wheel drag by 2%, reduces lift by 16% and alters the separation on the top of the wheel. It is noted that they used a relatively coarse grid (less than 1 million cells).

Another numerical study was done by Wäschle et al. [33], who modelled their own wheel. A hybrid grid was used as they modelled the support sting from their experiment. They investigated 2 different CFD codes: STAR-CD$^{\text{TM}}$ and PowerFLOW$^{\text{TM}}$. The achieved results showed good agreement, as the main experimentally observed feature, a pair of ground vortices, was captured by all computations. Nonetheless, local discrepancies remained in both CFD codes and it was concluded that no one method had a clear advantage.

As mentioned earlier, the flow around a wheel will exhibit unsteady characteristics as it is a bluff body. Although Basara et al. [40] published the first unsteady simulations, their grid was coarse (385,000 cells) and it was not until six years later that a more detailed study was published by McManus and Zhang [41]. They investigated a stationary and rotating wheel (from Fackrell and Harvey [23]) using an unsteady RANS solver, testing two different turbulence models (the Spalart-Allmaras (S-A) and Realizable $k-\epsilon$ (RKE) models). A fully structured grid was created, and a grid sensitivity study (ranging from

---

[3] Other methods to solve this problem include sinking the wheel into the ground or using an unstructured grid underneath the wheel

1 to 3 million cells) showed the S-A model to be more dependent on grid resolution, primarily in the wake. The computed surface pressures showed good agreement to Fackrell and Harvey's data, and the large pressure fluctuation at the contact patch was clearly captured (see Figure 1.6). They suggested that the wider wake for the stationary wheel is due to the flow emerging sideways from under the front of the wheel being deflected less by the streamwise flow because of the boundary layer that develops on the ground. They also observed the flow features around the wheel, and characterised three different regions: the upper near wake, the lower separation region and the lower near wake. They described the separation on the top of the rotating wheel as forming an arch shaped vortex.

Although McManus and Zhang used unsteady RANS, they did not investigate unsteady features and the increase in accuracy compared to a steady RANS simulation was not quantified. Axerio et al. [31] compared various turbulence models (SRANS) and a Large-Eddy Simulation (LES) for a stationary wheel case using PIV results. They created a hybrid grid of up to 40 million cells, reproducing their wind tunnel setup. The various CFD methods predicted different positions for the time-averaged wake vortices, all qualitatively similar to the experiment. But the instantaneous flowfield from the LES and PIV results showed that instead of the ground vortex pair, the wake was composed of randomly distributed small eddies.

The flow around the isolated wheel is complex, especially due to the large areas of recirculation, and an unsteady simulation using Detached-Eddy Simulation (DES) would give a better insight in the various flow phenomena.

1.2.3 Combined Wing and Wheel

The isolated inverted wing and wheels have been well studied and many characteristics of the flow have been described using both experimental and computational techniques, but only a few studies have investigated the interaction between the front wing and wheel. The first attempt was by Kellar et al. [44], who published an experimental and computational study of the right-hand quarter of a generic Formula One car. For their experiment, a fixed ground was used with the wheel rotating above it. As discussed in Section 1.2.2, to represent correctly the flow around a rotating wheel, it is best to have it in contact with a moving ground, and thus their experiment was not accurate. They also created a CFD simulation, modelling a moving ground, but left the wheel stationary. They used an unstructured grid with 340,524 cells and simulated the flow with a Mach number of 0.3. Because of the unphysical modelling and coarse grid, it is questionable whether their results represent a realistic flow situation and they will not be discussed here.

Diasinos and Gatto [35] performed an LDA analysis of the effect the angle of attack and span of a single element wing have on the wake of the wheel. They tested at a low Reynolds number of 5.11×10^4 and observed that the lower wing edge vortex interacted with the wake of the wheel after travelling along its side, creating an asymmetric structure. At low wing spans, the vortex travelled around the inside of the wheel, whereas the opposite occurred for large wing spans. The angle of attack of the wing primarily defined the size, strength and degree of movement of the vortex.

A comprehensive study of the interaction of a double element inverted wing and a wheel was conducted by Van den Berg [18] and Van den Berg and Zhang [45]. The wing studied by Mahon [16] was combined with a non-deformable wheel resembling a F1 tyre featuring four longitudinal grooves and a $2.4°$ camber. Both experimental and computational studies were performed investigating different wheel positions and different wing ride heights.

The experiments consisted of PIV, oil flow, hot wire and static pressure measurements, while the forces of the wing were obtained with a three component load cell and the drag of the wheel with a single component load cell. The baseline configuration saw the wheel placed behind the wing with a gap of $20mm$ and an overlap of $20mm$. It was observed that the wheel drag was dependent on the wing ride height; a lower wheel drag, compared to the isolated case, was recorded for ride heights below $h/c = 0.3$, and a higher drag for heights above this. The wheel downforce and sideforce were also probably affected, but no experimental data was obtained to demonstrate this. It was discussed that the effect of the wing on the wheel can be explained by the delayed separation over the top of the wheel, the extra suction on the inside of the wheel and by the wake interaction effects. The latter is dominated by the trajectory of the upper edge wing vortex, which can be either over the top or around the side of the wheel.

Compared to the isolated wing case, more downforce was produced by the wing at low ride heights and less at higher ride heights, and the wing drag was found to be generally higher. Vortex breakdown and separation from the suction side are still the primary downforce limiting mechanisms and the channeling effect, which is said to be enhanced by the wheel rotation at low ride heights, is the primary downforce enhancing mechanism. They explained that the wing downforce was changed by a combination of the wheel circulation effect due to the wheel rotation, the downstream obstruction from the wheel and the dumping effects[4].

---

[4] The dumping effect is when the boundary layer is discharged at the trailing edge into a region of locally higher velocity, reducing the pressure recovery demands.

A sudden change of both wheel drag and wing downforce was experienced at the same ride height, and the coupling of these was associated to circulation effects. The position of this sudden change was found to be influenced by the wing-wheel gap, as it shifted to lower ride heights for an increasing gap. A change of the overlap lead to a vertical translation of the wheel drag and wing downforce curves, reaching higher values for lower overlap values. Although generally the wing downforce was higher at lower overlap values, vortex breakdown at low ride heights meant that a higher global maximum downforce was reached with positive overlap values.

In his computations [18], Van den Berg used a fully structured grid of more than 4 million cells with non-conformal zones around a half-model of the combined wing and wheel used in his experiments. A steady RANS simulation with the S-A turbulence model was applied to different wheel positions, focusing on the baseline configuration of $20mm$ gap and overlap, for varying wing ride heights. Compared to the simulations of the isolated cases, the results correlated less accurately with the experiments. A qualitative trend of the behaviour was captured, but wheel drag could be underpredicted by more than 25% in some cases. The wing results showed a better correlation and revealed that the interaction phenomena upstream are better simulated than the downstream effects on the wheel.

The use of non-conformal zones around the wing have a negative effect on the predicted flow features, especially downstream of the wing and a fully structured grid could improve the results. Also, an alternative to RANS such as DES or LES would be better able to model the vortex interaction with the wheel flow, as it is complex and unsteady. In this current research, Van den Berg's study will be furthered to investigate the flow behaviour in more detail, with a focus on the unsteady features. DES will be used and as such, a review of its use for similar cases is reviewed below.

1.2.4 Detached-Eddy Simulation

Detached-Eddy Simulation (DES) is a hybrid technique which was first proposed by Spalart et al. in 1997 [46] for the prediction of turbulent flows. It combines Large-Eddy Simulation (LES) with a RANS model[5], and aims to make use of the most favourable aspects of the two techniques. LES does a direct resolution of the dominant unsteady structures, and has shown to give good solutions for separated flow, but it has a high computational cost due to the resolution required in the boundary layers, and issues exist with the wall conditions. RANS methods, on the other hand, are designed on the basis of the mean parameters of thin turbulent shear flows and will not represent

---

[5] The majority of DES applications use the Spalart-Allmaras one-equation model [47]

massively separated flows accurately, but most models have shown to yield acceptable accuracy of attached flows [48]. Ideally in DES, the entire boundary layer is treated by RANS with an LES treatment of the separated regions.

Studies have been conducted assessing how DES compares to steady and unsteady RANS models, especially for separated flows such as that present behind a wing or bluff body. These are summarised in Table 1.3 and some are discussed in more detail in the following sections.

1.2.4.1 DES applied to bluff bodies

In 2003, Constantinescu et al. [49] performed simulations around a sphere using different unsteady RANS models, DES and LES, and compared all of these with experiments conducted on spheres at very high Reynolds numbers [50]. A fully structured O–O grid of 450,000 cells was used for a domain which extended from the sphere surface to 15 sphere diameters in the radial direction, and a non-dimensional timestep of 0.02 was specified. The sphere was in freestream and the simulations were performed at a Reynolds number of 1×10^4. The separation was laminar occurring at approximately 83° around the sphere, and DES predicted a slightly later separation of 85.5°. The measured Strouhal number for the vortex shedding was 0.195, and was captured best by LES and DES. It was observed that DES compares favourably to LES as both techniques resolved eddies down to the grid scale in the wake. It was also noted that DES is better able to capture unsteady phenomena (including Kelvin–Helmholtz instabilities in the detached shear layers) than unsteady RANS.

Nishino [51] conducted a study, both experimentally and numerically, on circular cylinders in ground effect, where the flow around the cylinder was investigated at different heights above a moving ground. He used DES for his numerical simulation, though he also performed unsteady RANS simulations for the purpose of comparison. His domain extended 10d in front of the cylinder, 20d behind, 10d on top and 2d spanwise (where 'd' is the cylinder diameter), and was fully structured containing approximately 1,200,000 cells . The boundary conditions were set to best represent the experiment; the ground was modelled as a moving wall with translation velocity equal to freestream, a symmetry boundary condition was used for the upper-side end of the domain and the spanwise ends were imposed a periodic boundary condition. A uniform flow of very low turbulence level was given at the inlet whereas a no-gradient condition was applied to the outlet, and the non-dimensional timestep was set to 0.021. He observed experimentally that as the ride height was reduced, there was a decrease in drag and a cessation of Karman vortex shedding. This was better captured by DES which predicted correctly the cessation of vortex shedding at the appropriate height whereas unsteady RANS predicted the phenomena at a lower ride height. The time-averaged force coefficients, separation angles and velocity profiles in the near wake predicted by DES were in good agreement with the experiments, and the instantaneous flow features from DES and experiments showed similarities.

The above two studies were achieved on simple shapes and can give a very good insight on the flow physics, but do not directly represent engineering problems. A study more representative of a real engineering problem was done by Maddox et al. [52], who conducted steady RANS and DES simulations on the Ground Transportation System. They used an unstructured grid of approximately 6,000,000 cells, and conducted the simulations at a Reynolds number (based on body width) of 2×10^6. They based their work on the experimental study conducted by Storms et al. [53], and the boundary conditions were set accordingly. The no-slip condition was applied on the tunnel walls, which extended 15w in front of the GTS so as to allow the boundary layer on the lower wall to develop the same thickness as measured by Storms et al. [53]. The effect of yaw was also investigated, looking at a 10° yaw case. For 0° yaw, the simulations correlated well with the experiment, with DES being superior to RANS as it predicted drag values in substantially better agreement with the measured values. For the yawed case however, discrepancies were present in the predicted forces. They noted that the corner radius of the ground transportation system challenged the RANS region and transition prediction, and less-rounded geometries might give an improvement.

In 2002, Hedges et al. [54], performed DES and unsteady RANS (with the S-A turbulence model) simulations over a simplified landing gear. They used a structured grid of about 2,500,000 cells, and set up their simulation so as to reproduce the experiment done by Lazos [55]. The Reynolds number of their simulation was 6×10^5 and a dimensionless timestep based on the wheel diameter of 0.03 was applied. The domains extended 3 wheel diameters upstream and 7 wheel diameters downstream, and slip conditions were applied on the tunnel walls. The predicted pressure over the surface of the wheels correlated reasonably well with the test data of Lazos, and DES performed consistently better than the unsteady RANS calculations. Many flow features were well captured only by DES and were in good agreement with the surface pressures, though the agreement on drag was poor. They concluded that DES is very promising for noise prediction, as it can resolve a wide range of unsteady scales of motion without being too computationally expensive.

1.2.4.2 DES applied to lifting bodies

DES studies of lifting bodies such as wings have also been conducted. Cummings et al. [56] performed a detached-eddy simulation of a multi-element wing to investigate slat and flap aerodynamics. An unstructured grid was used with a total of 5,210,000 cells and a non-dimensional time step of 0.01 based on the chord was found to model the flow well. The Reynolds number, based on the chord, of this setup was around 3.7×10^6. Surface pressure information was obtained experimentally for validation and the simulations predicted this fairly well. There was a point though, where flow separation was computed on the upper surface of the flap, whilst the experiments showed the flow to still be attached. This might have been due to grid density or the use of an unstructured grid. Cummings then analysed the flow using DES, and captured the different trailing vortices which arise from the slat and flap, and the interaction of the slat tip vortex with the main element wing was found to cause highly unsteady separation.

The flow over a delta wing is dominated by vortical structures and RANS turbulence models are inadequate for such flowfields. Morton et al. [57] investigated the ability of DES to accurately predict vortex breakdown at high Reynolds number. They used detailed experiments of a delta wing performed at Onera [58] to assess the validity of RANS and DES methods, and their computational mesh was unstructured with 2,450,000 cell. Although solutions obtained with DES were sensitive to time accuracy in the frequency domain, an asymptotic solution was achieved for small enough time steps. RANS turbulence models failed to correctly capture the physics of vortex breakdown whereas DES captured the spectrum of frequencies correlating well with experiments and was therefore successful in capturing vortical flowfields.

The accuracy of DES with unstructured grids in contrast to structured grids has been assessed in another study by Morton et al. [59]. Spalart's guidelines [60] were used when creating the grid, so as to meet the requirements of DES. Three high-Reynolds number turbulent flows of aerodynamic interest were considered: the massively separated flow over a forebody in crossflow, the flow over a delta wing at 27° angle of attack and the flow around an F-15E at 65° angle of attack. Extensive grid refinement was conducted on the latter two, and it was observed that a wider range of turbulent length scales is captured on finer grids. Comparing structured and unstructured grid results for the forebody in crossflow, similar wake structures and very close pressure distributions were obtained. Also, the fine unstructured grid used for the delta wing predicted accurately the turbulent kinetic energy in the core of the vortex, which was in close agreement with experiments. They concluded that unstructured grids are capable of meeting the requirements for DES, and that a refinement of such grids can be achieved rapidly, reducing numerical errors.

1.3 Objectives

The flow behaviour around a whole racecar is too complex to analyse in detail with the available resources and focusing on isolated components is an initial step in understanding it. A rotating wheel alone results in complex flow behaviour with unsteady effects and this is not captured fully by a steady numerical analysis. In the literature review, it has been shown that considerable research has gone into studying the aerodynamics of a racecar front wing and wheel in isolation, both experimentally and numerically, and a detailed study on the interaction between the two has been conducted by Van den Berg. Transient effects, which are of special importance due to the wheel's unsteady flow properties, is an unexplored area and this PhD research will investigate them. A study of the wing-wheel interaction involving an unsteady approach should give a more profound understanding of the physics, but unsteady flow features can be difficult to analyse experimentally and a numerical approach is more appropriate in this case as it offers the possibility to look at features otherwise difficult or impossible to analyse experimentally.

The aim of this research is to analyse the unsteady behaviour of the flow around a racecar wing and wheel. This is the primary focus of this research, but each component (wing and wheel) in isolation are also studied, as they are simpler cases and are useful as references to see how each component affects the other. The experimental studies done by Mahon [16] and Van den Berg [18] can be used extensively to validate the computational work, although some new additional measurements are done in this research to complement those studies. DES was chosen as the main numerical method as it has proven to be capable of reproducing unsteady flows (such as behind a bluff body) qualitatively while not being too resource intensive and also provides information on the transient behaviour of the flow.

To attain the aim of this project, various objectives have been defined:

1. Validate the DES model for an isolated wing in ground effect, an isolated wheel case, and the combined wing-wheel case.
2. Describe the flow for the three studied cases.
3. Investigate transient effects for all three cases with particular attention to flow features such as vortex breakdown, vortex interaction and flow separation from the wheel.

These objectives can be further expanded for each case. For the isolated wing, the main objective is to investigate how accurately the DES model captures the edge vortices at varying ride heights, ranging from the force enhancement region to the force reduction region, and to assess how it improves over SRANS simulations. The isolated wheel flow studies have focused on a two-dimensional steady analysis, and the aim of this research is to expand this to a three-dimensional unsteady analysis using DES, investigating both a rotating and stationary wheel. Finally, the main objective of the combined wing-wheel study is to investigate the nature of the sudden change in wheel drag which occurs as the wing ride height is changed and to assess any transient features associated with it.

1.4 Report structure

This report is structured so that each case is discussed separately, starting with the isolated elements as they are used as a reference for comparison in the combined wing-wheel analysis. The following chapter starts by detailing the research, explaining the approach taken, and gives a description of the numerical and experimental analysis. It is followed by a discussion on the inverted isolated wing results and then the isolated wheel results are analysed. The next two chapters each focus on an analysis of one of the elements in the combined wing-wheel case. A summary of the results is given in the final chapter and recommendations are made for future research in this area.

AUTHOR	**REF.**	Re-**NUMBER**	**WING**	**GRID**	**NO. CELLS**	**SOLVER**
Ranzenbach & Barlow	[6, 13]	1.5×10^6	Single/Double	2D Struct.	3.0×10^4	FANS
Zerihan & Zhang	[11]	4.6×10^5	Single	2D Struct.	3.0×10^4	SRANS
Mahon & Zhang	[12, 61]	7.9×10^5	Double	2D Hybr.	3.8×10^5	SRANS
Van den Berg	[18]	5.8×10^5	Double	3D Struct.	4.0×10^6	SRANS

Table 1.1: Summary of relevant factors in CFD research for an inverted wing in ground effect.

AUTHOR	**REF.**	Re-**NUMBER**	w/d	**TYPE**	**NO. CELLS**	**SOLVER**
Axon et al.	[38]	5.3×10^5	0.61	Struct.	5.4×10^5	SRANS
Skea et al.	[28, 39]	6.9×10^5	0.5	Struct.	3.6×10^5	SRANS
Kellar et al.	[44]	$2.5 \times 10^4 - 6.5 \times 10^5$	-	Unstr.	3.4×10^5	SRANS
Knowles et al.	[42]	3.69×10^5	≈ 0.44	Hybr.	9.3×10^5	SRANS
Basara et al.	[40]	5.04×10^5	0.79	Struct.	3.9×10^5	URANS
Wäschle et al.	[33]	5.37×10^5	0.37	Hybr.	6.7×10^6	SRANS/URANS
Mears et al.	[43]	2.0×10^5	0.53	Unstr.	3.1×10^6	SRANS
McManus and Zhang	[41]	5.3×10^5	0.46	Struct.	4.0×10^6	URANS
Van den Berg	[18]	6.4×10^5	0.55	Struct.	4.0×10^6	SRANS
Axerio et et al.	[31, 32]	5.0×10^5	-	Hybr.	4.0×10^7	SRANS, LES

Table 1.2: Summary of relevant factors in CFD research for wheel related articles.

AUTHOR	**REF.**	**SIMULATION**	Re-**NUM.**	**TYPE**	Δt	**NO. OF CELLS**	**SOLVER**
Maddox et al.	[52]	Ground Transportation System	2.0×10^6	Unstr.	0.02	6.0×10^6	SRANS, DES
Constantinescu et al.	[62]	Flow over a Sphere	1.0×10^4	Struct.	0.02	4.5×10^5	URANS, DES, LES
Breuer et al.	[63]	Flat plate at high incidence	2.0×10^4	Struct.	–	1.9×10^6	SRANS, DES, LES
Nishino	[51]	Cylinder in ground effect	1.0×10^5	Struct.	0.021	1.2×10^6	URANS, DES
Hedges et al.	[54]	Simplified landing gear	6.0×10^5	Struct.	0.03	2.5×10^6	URANS, DES
Cummings et al.	[56]	High-lift wing	3.7×10^6	Unstr.	0.01	5.2×10^6	DES
Morton et al.	[57]	Delta Wing	1×10^6	Unstr.	0.014	2.7×10^6	SRANS, DES
Forsythe et al.	[64]	Spin for the F-15E	1.4×10^7	Unstr.	0.005	6.5×10^6	SRANS, DES

Table 1.3: Summary of DES studies.

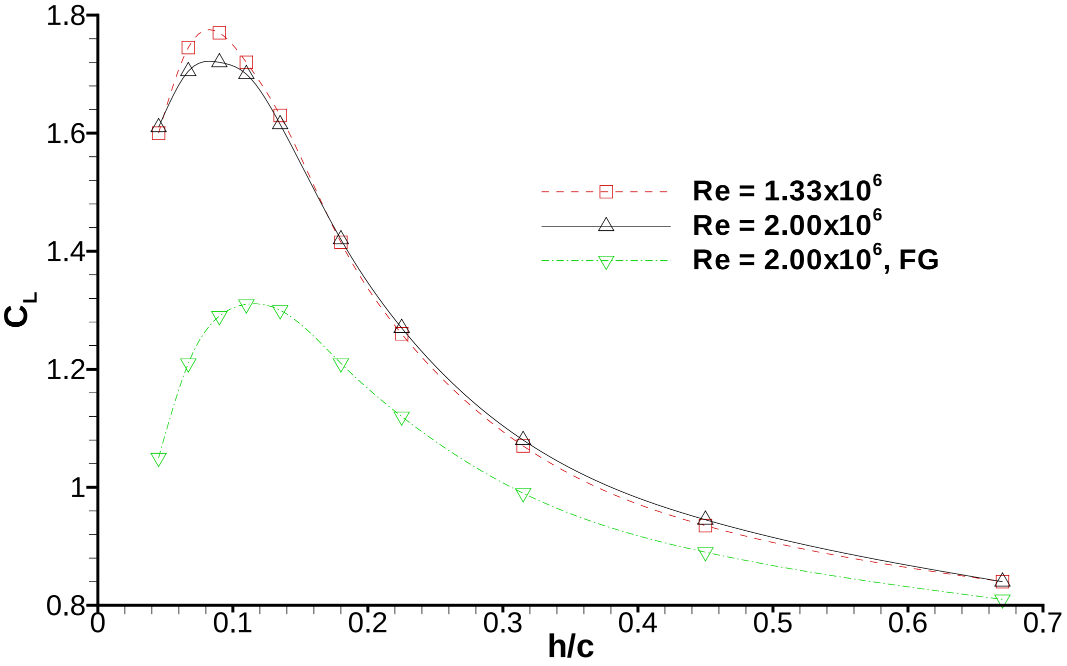

Figure 1.1: Variation of the lift coefficient of a single element inverted wing for different Re values with varying ride height; FG stands for fixed ground, from Zerihan [7].

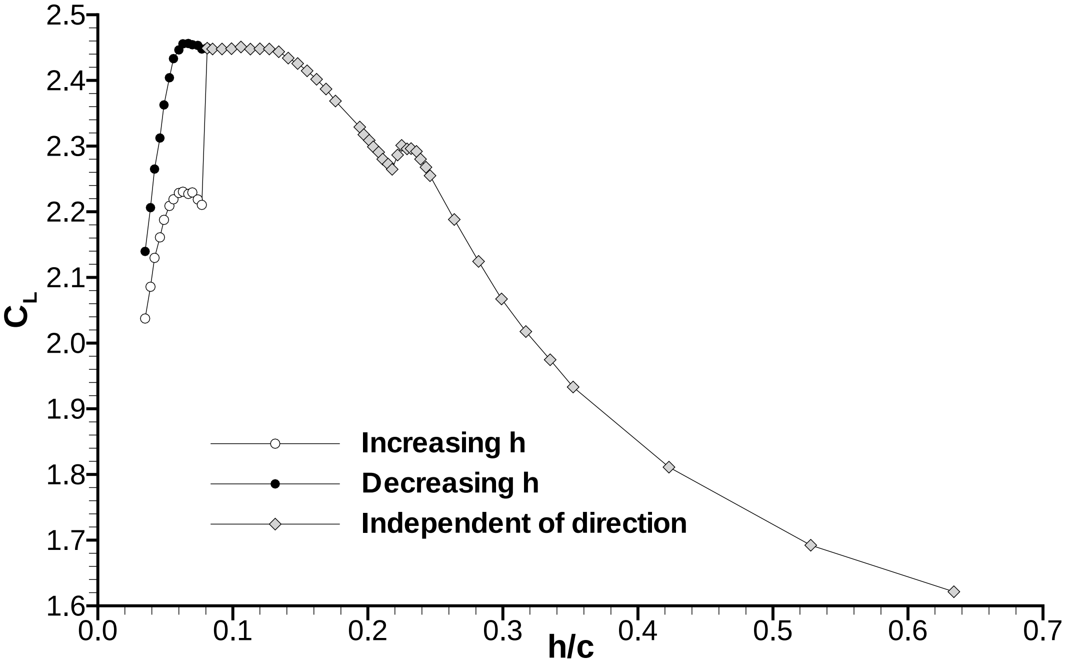

Figure 1.2: Variation of the lift coefficient of a double element inverted wing with varying ride height, from Mahon[16].

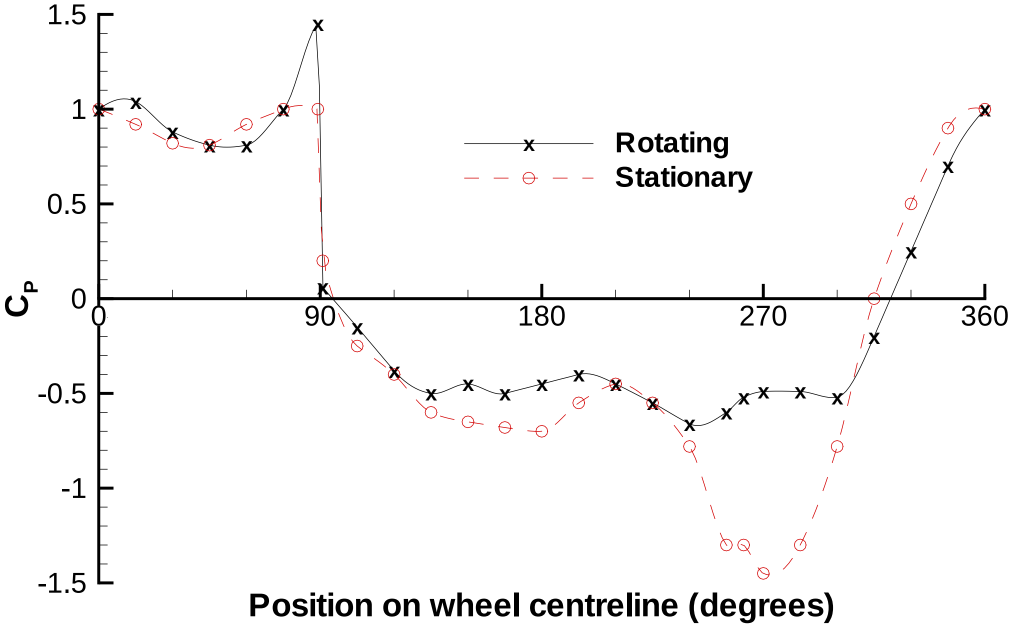

Figure 1.3: Static pressure distribution around Fackrell's Wheel 2, Stationary and Rotating, from Fackrell and Harvey [23].

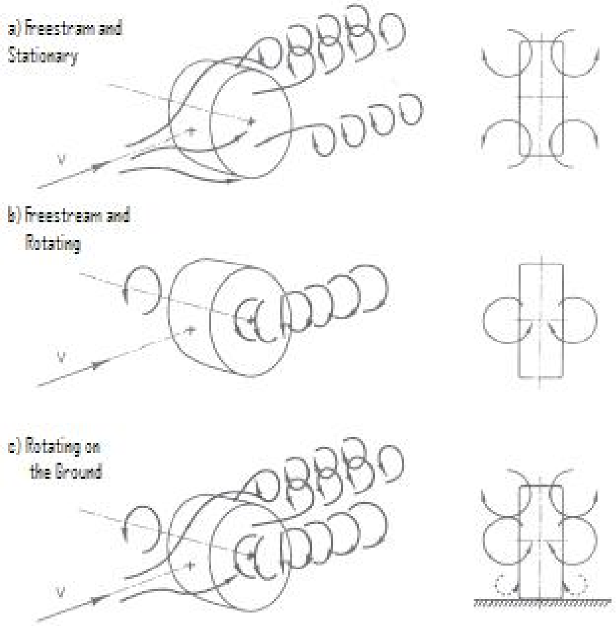

Figure 1.4: Wake pattern due to the wheel shape (a) and to the wheel rotation (b) for a wheel in freestream. The same wake patterns are shown in (c), but superimposed and combined with the ground effect, from Cogotti [22].

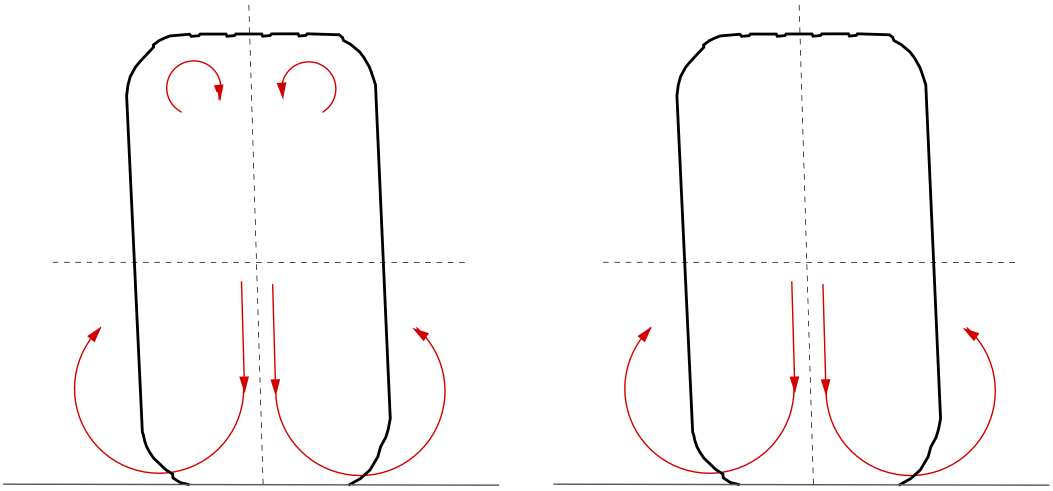

(a) $x/D < 1$ (b) $x/D \geq 1$

Figure 1.5: Proposed model of the trailing vortex system of an isolated rotating wheel by Saddington et al. [34].

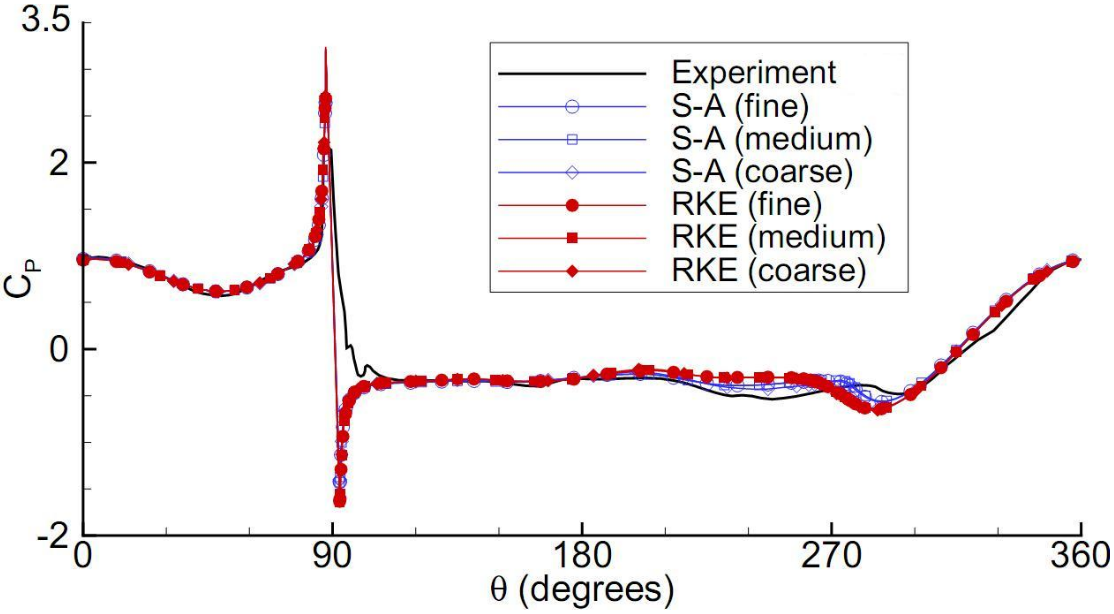

Figure 1.6: Comparison of the pressure distribution around a rotating wheel obtained by McManus and Zhang [41] and Fackrell and Harvey [23].

Chapter 2

Research Description

The first section of this chapter gives a detailed overview of the research with a look at the approach used. Then, Section 2.2 describes the numerical approach, looking at the mesh generation, the solver setup and the post-processing and Section 2.3 details the experimental procedures used.

2.1 Research Outline

This research expands on the work that has been achieved at the University of Southampton in previous years, which is mainly composed of the study by Mahon [16] on wings in ground effect and by Van den Berg [18] on the interaction between the wing and the wheel. The front wing and front wheels are the main focus in this research and some initial simplifications are made. Firstly, components such as the suspension, front nose or underbody are not considered. Secondly, this study does not investigate yaw and assumes the flow to be symmetric about the wing's centrespan. Oil flow results from Mahon have shown this to be a reasonable assumption and it allows only one half of the geometry to be consider by the CFD. Thirdly, a deformed wheel profile is not considered as it is not experimentally feasible and is not consistent with the previous work. This simplification mainly affects the lower wake of the wheel [37] and needs to be kept in mind when analysing the wheel flow.

The wing which is investigated is the same as the one used by Mahon. It is a 50% scale model of a simplified Formula 1 double element[1] front wing fitted with rectangular endplates and is inverted thus producing downforce. It has a span of $580mm$ and a total chord[2] of $284mm$. The main element is set with an angle of attack of $\alpha_{me} = 4^\circ$ and

---

[1] The two elements of the wing will be referred to as the main element and the flap

[2] The total chord is defined as the sum of the main element chord and the flap chord

the flap, which is located above the main element's trailing edge, has an angle of attack of $\alpha_f = 24°$ (see Figure 2.1). The endplates are $275mm$ long, $115mm$ tall and $5mm$ thick, and the lowest point of the main element is located $5mm$ above the lower edge of the endplate. The front, top and rear edges of the endplates have fillets of a radius of $2.5mm$, whereas the bottom edge is flat. A summary of the main features of the wing can be found in Table 2.1. Chosing to analyse a simplified wing reduces the meshing requirements and allows the research to focus on the investigation of the general flow properties of an inverted double element wing in ground effect. It was decided not to alter the flap location or orientation, using the optimal position as defined by Mahon, because most available experimental measurements were conducted with this setup.

Many wheel shapes have been investigated in previous studies, as can be seen in the literature review, making it hard to directly compare the results. In this research, the wheel shape used in Van den Berg's study is chosen for consistency. The wheel is a 50% scale non-deformable model based on an F1 wheel and has 4 longitudinal grooves. It has an average diameter of $313.9mm$, a maximum width of $172.8mm$ and a camber[3] of $2.4°$(see Figure 2.2). The wheel hubs are covered to simplify the geometry and reduce the flow complexity. In addition, this greatly simplifies the simulations removing the need to model the wheel spokes using a moving mesh. The geometry details of the wheel are summarised in Table 2.1. It must be noted here that Van den Berg used two different wheel shapes for his experiments. The wheel shape that is investigated in this research was used by him to obtain forces and PIV data, but he used another wheel to obtain the pressure distribution. The two wheels are relatively similar and Figure 2.3 shows both of them, where it can be seen that the wheel used to collect pressure data is taller and thinner (smaller aspect ratio), but has the same camber and general profile. Their main dimensions are compared in Table 2.2.

When the wheel is studied in isolation, a symmetric setup is reproduced where two wheels are used, separated by a distance equivalent to a specified overlap with the wing as used in the combined wing-wheel case (see Figure 2.4). This ensures consistency so that the results can be used as a reference. In the combined wing-wheel case, the wheels are placed downstream of the wing at a position defined by two parameters: overlap and gap. The overlap is measured from the inside of the endplate to the innermost side of the wheel, $150mm$ from the ground, and is positive when the wheel is located behind the wing (closer to the symmetry plane). The gap is defined as the distance from the trailing edge of the endplate to the foremost point of the wheel, also at a height of $150mm$ from the ground. An overlap of $20mm$ and a gap of $20mm$ was selected as it was the baseline configuration used by Van den Berg, and was the one for which most experimental data

---

[3] The camber is measured as the angle between the ground and the wheel axis when the wheel is standing flat on the ground

is available. As with the flap location, it was decided that the overlap and gap would not be altered as it was not feasible to study this in detail within the timeframe of this research. Figure 2.4 shows the full setup including the dimensions previously mentioned.

The coordinate system used in all cases can be seen in Figure 2.1. The x-axis is positive in the streamwise direction, the z-axis is positive vertically upwards and the y-axis is defined according to the right hand rule. The origin is located on the ground at the symmetry plane, with the x-axis origin defined at the leading edge of the main element. It is noted that as the port side of the wing and wheel is investigated, negative values of y are used.

The cases are studied at a freestream velocity of $30m/s$[4], which is defined by the operating limitations of the experimental facilities (i.e. moving belt and suction system). This corresponds to a Reynolds number of 5.8×10^5 based on the wing chord and ISA (i.e. $\rho = 1.225kg/m^3$ and $\mu = 1.789 \times 10^{-5}kg/ms$), which is about a quarter of the value experienced under real full scale conditions.

The main parameter which is investigated in this research is the wing ride height, which is defined as the vertical distance from the ground to the lowest part of the main element. It is varied within a range of $h/c = 0.070$ to $h/c = 0.458$ and has be chosen based on the heights for which most experimental data is available but also on ride heights in areas of interest. The study focuses on a configuration with rotating wheels, but a stationary case for the isolated wheel was considered to give further insight into the effect the wheel rotation has even though it does not represent real racecar conditions (except in the rare events when the wheels are locked under braking).

2.1.1 Research plan

Once the general outline of the research was determined, the following approach was taken. First, a CFD study, including steady RANS and DES, was conducted on the isolated wing. A few ride heights, which had been selected from the previous studies, were investigated and used to validate the results. The simulations were improved through modifications to the mesh and solver settings, resulting in better result quality and performance. Once the simulations had been validated, a higher number of ride heights were investigated. The performance of DES was compared to that of steady RANS and flow features observed with the simulations were analysed. DES was further used to study the transient features affecting the wing at the various ride heights.

---

[4] The average speed of a Formula 1 car is approximately in the region of $60m/s$

After a study of the isolated wing was completed, the isolated wheel case was considered. A similar approach as described above was used, although it was simpler as there was only one test case (no ride height variation) to analyse. A detailed three-dimensional analysis of the wheel flow, both time-averaged and instantaneous, was done using the DES results and the major flow features were described. The study was further expanded to include a stationary wheel case and an analysis of any differences in transient features. Finally, some additional experimental measurements of the wake (using PIV) were conducted to complement what was available from Van den Berg [18], giving a better insight into the flow but also providing useful data for the CFD validation. The effect of changes in Reynolds number on the wake was also investigated with these experiments.

The next logical step was to combine the wing and the wheel and to analyse their interaction. Again, CFD was conducted using a steady RANS and DES approach, with the experiments from Van den Berg's study (force measurements, pressure distributions, oil flow and PIV results) used for validation. Only a selected few ride heights were investigated, with a focus on the area where a sudden change in wheel drag occurs. As for the isolated wheel case, some flow visualisation of the wake with PIV was conducted to obtain a better understanding of the interaction between the wing vortices and the wheel wake. The results collected were used to inspect the conclusions made by Van den Berg and to describe the transient flow behaviour. The study of the wing wheel interaction was separated, similarly to Van den Berg, into two sections: the effect of the wing on the wheel and vice versa. The results for the isolated components are used for comparison, with any significant changes noted.

2.2 Numerical Approach

The main approach to this study uses CFD and it can be separated into three stages: the pre-processing stage or mesh generation, the solving stage and the post-processing stage. These are each described separately in the following sections.

2.2.1 Mesh generation

The first stage requires the creation of a computational mesh around the models which is used to discretise the domain. The software package Gridgen V15.10 [65] was used for this task. The three-dimensional grids created are multi-block fully structured with hexahedral cells. CAD models of the wing and wheel used in the experiment were imported to ensure the accurate geometry was meshed. The supporting structure was omitted to simplify the overall grid. The symmetry condition and quasi-two-dimensional flow present in the model, at the wing's centrespan, allows for only half the model to be meshed.

The same domain size was used in all the cases, with the wing and wheel always placed in the same streamwise location. The domain extends 5 chord lengths in front of and 15 chord lengths behind the wing. The vertical and spanwise domain size is set as to represent the 7 feet by 5 feet wind tunnel of the University of Southampton, though the corners are simplified and made rectangular. This results in a spanwise domain size of 3.7 chord lengths and a vertical domain of 5.3 chord lengths. The domain can be seen in Figure 2.1.

When creating the grids, a lot of effort was spent ensuring a good cell quality throughout. Spalart's guidelines [60] for a DES grid were followed, thus having y^+ values of the order of 1 in most areas with a growth rate of 1.2, and the same mesh was used for both RANS and DES simulations. Particular attention was paid to having low aspect ratio cells in the wake region and avoiding where possible ambiguous cell sizes where the RANS/LES transition could occur within the boundary layer. It was attempted to keep cell skewness as low as possible and the minimum skewness is 45° in a few complex areas, whereas most cells have a skewness of 60° and above. The grid cells were concentrated around the models and in the wake areas but quickly coarsened in regions further away.

Once the grid is completed, it is exported to Fluent. Each case had specific details concerning the gridding and these are now discussed.

2.2.1.1 Isolated wing

For the isolated wing the ride height needed to be altered and this was done by raising or lowering the ground and roof simultaneously while leaving the wing in the same position, thus keeping a constant size domain and obtaining the desired ride height. Although the size remained the same, the number of cells changed slightly, with an increasing amount for a larger ride height. This method allowed for quick and easy changes in ride height.

The wing and endplate boundary layer grids were wrapped tightly around the geometry (Figure 2.5), thus saving cells, but also introducing singularities and skewness, especially around the bottom of the endplate which contains a 90° corner. This high skewness did not introduce any significant error when compared to a mesh with lower skewness. This grid was also created with the combined case in mind. The approximate number of cells for the isolated wing grid was 4 million.

To investigate the grid sensitivity, two additional grids were created at a ride height of $h/c = 0.246$, where the amount of grid points in the x, y and z direction were all reduced or increased by a factor of 1.3. This resulted in a coarse grid of 2 million cells and a fine grid of 8.7 million cells.

2.2.1.2 Isolated wheel

The isolated wheel was placed in the domain at the position equivalent to an overlap and gap of $20mm$ for the combined wing-wheel case. The wheel grid was complex to create due to the wheel being in contact with the ground. In the experimental conditions, the wheel being non-deformable, the contact patch consisted of a line. This cannot be meshed appropriately as it would result in flat cells. The chosen solution was to add a $0.1mm$ vertical plinth around the contact patch (see Figure 2.7). Cells from the ground and wheel boundary layer end on the plinth, which results in high aspect ratio cells with low skewness, but these are limited to an area close to the contact patch and did not affect the convergence of the solution. An advantage of using a small plinth is that the wheel contact patch is not significantly different from the experimental model, which is an important aspect in correctly predicting the flow in the lower wake of the wheel.

The mesh was wrapped around the wheel, reducing the number of cells. A part of the mesh between the wheel and symmetry plane was not wrapped, but was instead extended from the wheel to the symmetry plane. This was due to considerations for the combined case and simplifies the addition of the wing block. To capture the curvature of the four grooves, a higher cell density is required, but these extra cells are not necessary far away from the wheel surface. Therefore the cells originating from the grooves were wrapped around themselves using a combined C and H grid, worsening the cell quality in a small area but reducing the total cell number by approximately 8%. The wheel hubs are covered with flush discs to match the experimental wheel and also to prevent having to mesh the rim spokes.

To investigate the grid sensitivity, three grids were created, where the amount of grid points in the x, y and z direction were all increased by a factor of 1.3 at each refinement step. The total number of cells was 1.4, 2.9 and 7.0 million for the coarse, medium and fine grids respectively. The fine grid can be seen in Figure 2.6.

2.2.1.3 Combined wing and wheel

The grid of the two combined components uses the same wing block, but the wheel block had to be modified slightly to accommodate the wing. The number of grid points in the z direction on the wheel block was altered to match the wing block. This resulted in some unevenly distributed cells on the front of the wheel, but these were spread out evenly to give a well distributed wake block behind the wheel. The uneven distribution of cells due to the wing presence is not affected much by ride height variations.

The mesh was created by starting from the medium grids of the isolated components and the final grid of the combined wing-wheel contained approximately 6.7 million cells, which varied slightly with ride height. Changing the ride height was not as simple as for the isolated wing grid and it was achieved by moving the wing block while the rest of the grid had to be redistributed accordingly. Five ride heights were chosen, based on the results available from Van den Berg [18]. No grid refinement study was done for the combined wing-wheel case, as it would have been prohibitively expensive and it was decided that the grid refinement study for the isolated components would give sufficient information. The grid for the combined case, at a wing ride height of $h/c = 0.211$, is shown in Figure 2.8.

2.2.2 Solving stage

Once the grid had been created with Gridgen, it was imported in Fluent[5]. Fluent is a commercial CFD software package which can solve many different types of flows. More details are available in the user manual [66]. Single precision[6] was used as it requires less resources while it gives similar results for the cases investigated when compared to double precision. The following sections give a detailed overview of the settings used to simulate the flow with some explanation of the equations used to model the flow.

2.2.2.1 Governing equations and turbulence models

The motion of incompressible fluids can be expressed by the Navier-Stokes equations which are composed of the following continuity and momentum equations[7]:

$$\frac{\partial u_i}{\partial x_i} = 0 \tag{2.1}$$

$$\frac{\partial u_i}{\partial t} + u_j \frac{\partial u_i}{\partial x_j} = -\frac{1}{\rho}\frac{\partial p}{\partial x_i} + \nu \frac{\partial^2 u_i}{\partial x_j \partial x_j} \tag{2.2}$$

where x_i are the Cartesian coordinates ($i = 1, 2, 3$), u_i are the velocities and p is the static pressure. ρ and ν are the density and kinematic viscosity respectively and are constant (ISA values) as the flow is assumed incompressible. These equations are nonlinear and solving them directly (i.e. DNS) quickly becomes too computationally expensive as the

---

[5] Fluent V6.2.16 was used throughout this research

[6] Single precision provides accuracy up to 7 significant figures

[7] The energy equation will not be used in this research and is therefore omitted

flow becomes more complex. Therefore, different approaches which model the turbulence are used in this study and are now discussed.

RANS: Spalart-Allmaras model

Reynolds-averaged Navier-Stokes equations are derived directly from the Navier-Stokes equations by decomposing them into the mean and fluctuating components. The velocity and pressure components are decomposed as follows:

$$u_i = U_i + u_i^{'}, \quad p = P + p^{'} \tag{2.3}$$

where U_i and $u_i^{'}$ are the mean and fluctuating components. Substituting this into Equations 2.1 and 2.2, and taking the ensemble average, the RANS equations are obtained:

$$\frac{\partial U_i}{\partial x_i} = 0 \tag{2.4}$$

$$\frac{\partial U_i}{\partial t} + U_j \frac{\partial U_i}{\partial x_j} = -\frac{1}{\rho}\frac{\partial P}{\partial x_i} + \frac{\partial}{\partial x_j}\left(\nu \frac{\partial U_i}{\partial x_j} - \overline{u_i^{'} u_j^{'}}\right) \tag{2.5}$$

They have a similar form to the instantaneous Navier-Stokes equations, but the variables now represent ensemble averages and there are additional terms, $-\overline{u_i^{'} u_j^{'}}$, which are the Reynolds stresses representing the effects of turbulence. This cannot be solved with the available equations (closure problem) and it needs to be modelled in order to close the equation. Many turbulence models exist, but in this research the one equation Spalart-Allmaras model is used and this is reviewed below.

The S-A turbulence model is an eddy-viscosity based RANS model which employs the Boussinesq hypothesis to relate the Reynolds stresses to the mean velocity gradients:

$$-\overline{u_i^{'} u_j^{'}} = 2\nu_t S_{ij}, \tag{2.6}$$

$$S_{ij} = \frac{1}{2}\left(\frac{\partial U_j}{\partial x_i} + \frac{\partial U_i}{\partial x_j}\right)$$

where ν_t is the turbulent kinematic viscosity and S_{ij} is the mean strain rate tensor. The S-A model solves a single transport equation for the modified turbulent kinematic viscosity, $\tilde{\nu}$:

$$\frac{\partial \tilde{\nu}}{\partial t} + U_i \frac{\partial \tilde{\nu}}{\partial x_i} = \underbrace{C_{b1}\tilde{S}\tilde{\nu}}_{\text{Production}} + \frac{1}{\sigma_{\tilde{\nu}}}\left[\frac{\partial}{\partial x_j}\left\{(\nu + \tilde{\nu})\frac{\partial \tilde{\nu}}{\partial x_j}\right\} + C_{b2}\left(\frac{\partial \tilde{\nu}}{\partial x_j}\right)^2\right] \underbrace{- C_{w1} f_w \left(\frac{\tilde{\nu}}{d}\right)^2}_{\text{Destruction}} \tag{2.7}$$

where

$$\tilde{S} = \sqrt{2\Omega_{ij}\Omega_{ij}} + \frac{\tilde{\nu}}{\kappa^2 d^2}\left(1 - \frac{\chi}{1+\chi f_{v1}}\right), \tag{2.8}$$

$$\Omega_{ij} = \frac{1}{2}\left(\frac{\partial U_i}{\partial x_j} - \frac{\partial U_j}{\partial x_i}\right), \quad f_{v1} = \frac{\chi^3}{\chi^3 + C_{v1}^3}, \quad \chi \equiv \frac{\tilde{\nu}}{\nu}$$

for the turbulent production term and

$$f_w = g\left[\frac{1+C_{w3}^6}{g^6 + C_{w3}^6}\right]^{1/6}, \quad C_{w1} = \frac{C_{b1}}{\kappa^2} + \frac{1+C_{b2}}{\sigma_{\tilde{\nu}}} \tag{2.9}$$

$$g = r + C_{w2}\left(r^6 - r\right), \quad r \equiv \frac{\tilde{\nu}}{\tilde{S}\kappa^2 d^2}$$

for the turbulent destruction term. $C_{b1}, C_{b2}, C_{v1}, C_{w2}, C_{w3}, \sigma_{\tilde{\nu}}$ and κ are constants while d is the distance from the nearest wall boundary. Details on the derivation and meaning of these terms can be found in the original publication by Spalart and Allmaras [47]. The model constants have the following default values:

$$C_{b1} = 0.1355,\ C_{b2} = 0.622,\ \sigma_{\tilde{\nu}} = \frac{1}{2},\ C_{v1} = 7.1,\ C_{w2} = 0.3,\ C_{w3} = 2.0,\ \kappa = 0.4187$$

The turbulent kinematic viscosity is finally obtained using the following relationship:

$$\nu_t = \tilde{\nu} f_{v1} \tag{2.10}$$

It can be noted that f_{v1} acts as a viscous damping function in the near-wall regions and in the rest of the flow $\tilde{\nu}$ is identical to ν_t. The S-A model is effective at modelling attached flows with reasonable accuracy, but it becomes less adequate for separated flow.

Detached Eddy Simulation

Detached Eddy Simulation is a hybrid RANS/LES model [46], combining the efficiency of unsteady RANS modelling in the near-wall region with the accuracy of LES[8] in far-wall regions. The main drawback of LES is its high computational cost due to the need of a fine grid and small timestep to properly resolve the boundary layer. DES on the other hand allows for the grid to be stretched in the directions parallel to the wall surface, as the unsteady RANS is now resolving the boundary layer, and this significantly reduces the computational cost while the large eddy structures in the far-wall regions are still captured.

In the DES model proposed by Shur et al. [67], the Spalart-Allmaras model is used for the unsteady RANS in the near-wall, and it becomes the subgrid-scale model for the LES in far-wall regions. As can be seen from the previous section, the S-A model uses the

---

[8] A description of the LES model can be found in the Fluent user manual [66]

distance to the closest wall to define a length scale d, and this is used to determine the amount of production and destruction of turbulent viscosity (see Equations 2.8 and 2.9). The DES model replaces d with a new length scale, $\tilde{d}$:

$$\tilde{d} = min\left(d, C_{des}\Delta_{max}\right), \quad C_{des} = 0.65, \quad \Delta_{max} = max\left(\Delta x_1, \Delta x_2, \Delta x_3\right) \tag{2.11}$$

where Δx_i is the grid spacing in the i-th direction and C_{des} is an empirical constant. Thus, the DES resolves the ensemble-averaged flow field when $d < C_{des}\Delta_{max}$ (URANS mode) and the filtered flow field when $d > C_{des}\Delta_{max}$ (LES mode). A drawback of this method is the transition region where the model switches from unsteady RANS to LES and the grid must be created following guidelines so as to ensure that the boundary layer is solved using the URANS mode.

2.2.2.2 Boundary conditions

The boundary conditions were set so as to reproduce the experimental conditions while aiming for an optimal configuration. The symmetry plane at centrespan was given a symmetry boundary condition which assumes a zero flux of all quantities across it. The top (tunnel ceiling) and the far side (tunnel wall) of the domain were also defined as symmetry boundary conditions, which is equivalent to a zero-shear slip wall, so as to avoid the high grid density which would be required to resolve the wind tunnel boundary layer.

The upstream boundary was defined as a velocity inlet and a normal velocity of $30m/s$ was specified. A low turbulent viscosity ratio of 1×10^{-7} was used as the wind tunnel is of low turbulence intensity ($\approx 0.3\%$). The downstream boundary was set to a pressure outlet with a gauge pressure of 0 and the same low turbulent viscosity ratio of the inlet was used for the backflow. The air density and viscosity were set to constant values based on ISA.

The bottom of the domain, the ground, was defined as a no-slip moving wall, with a velocity equivalent to the freestream (i.e. $30m/s$). The wing is a no-slip wall, whereas the wheel surface was defined as a rotating wall. It was given an angular velocity of $193.6rad/s$ about its rotational axis. This gives the wheel tread, which is in contact with the ground, a tangential velocity of $30m/s$ based on the average wheel diameter. The plinth is also defined as a moving wall with a velocity of $30m/s$ in the streamwise direction. For the stationary wheel case, the ground, plinth and wheel were defined as stationary no-slip walls. No roughness was applied to the wall surfaces as the boundary layers are fully resolved.

Mahon [16] and Van den Berg [18] used oil flow results to define where transition occured and set the solver to be laminar in the corresponding areas in an attempt to model the transition. The use of this method was investigated (with the SRANS model) but was found to result only in small changes of wing downforce and drag in the range of ride heights tested. It was also found to be the cause for the poor convergence Van den Berg experienced within a range of ride heights in his isolated wing simulations, where the flow at the intersection of the main element and endplate had been incorrectly forced to be laminar, inducing flow separation.

For the computations done in this research, it was decided not to model laminar to turbulent boundary layer transition. Thus, using the S-A turbulence model, the flow is always turbulent resulting in faster boundary layer growth than if an initial laminar layer was present. The experiments were all performed without any boundary layer control on the models.

2.2.2.3 Solution procedure

The implicit segregated solver with a node-based gradient method was used for all simulations. The RANS simulations used a second order upwind scheme to interpolate the variables $(U_i, \tilde{\nu})$ during the discretisation process. For the DES however, a second-order central differencing scheme was used to reduce the effect of numerical dissipation in the LES regions. The interpolation of the pressure used a second-order scheme and the SIMPLEC algorithm was selected for the pressure-velocity coupling. The unsteady simulations need to be further discretised in time and a second-order implicit scheme was chosen. Due to the solver being implicit, the solution is unconditionally stable irrespective of the CFL value, but it needs to converge at each timestep and sub-iterations are required.

For the steady RANS simulations, the flow was initialised using the inlet conditions and the solution was iterated until convergence was achieved. Convergence was considered reached when the residuals and the force coefficients had stabilised at a certain value. This required approximately 8000 iterations.

The unsteady simulations were initialised using a converged steady RANS simulation. A non-dimensional time step of $\Delta t = 0.01$, based on the freestream velocity and a characteristic length (wing chord or wheel diameter), was specified. This resulted in CFL values of the order of 1 in most areas, with a maximum value of 50. For the grid refinement study of the isolated cases, the timestep was changed along with the cell density by a factor of 1.3, resulting in $\Delta t = 0.013$ and $\Delta t = 0.0077$ for the coarse and fine grids respectively. Therefore, the CFL values were kept at similar values.

The amount of sub-iterations was set to 15 after an investigation of the residuals (see Figure 2.9) and was chosen to maximise the efficiency while not compromising the accuracy. The flow was first allowed to develop over 5000 timesteps (50 passages[9]) and statistical data (mean and RMS) was collected for a further 7000 timesteps (70 passages). The time taken to achieve this was on average 15 days using 32 processors on the Iridis2 cluster at the University of Southampton .

2.2.3 Post-processing stage

Once the simulation is completed, the data is exported from Fluent. The post processing is mainly achieved using the commercial software Tecplot, Ensight and Matlab. The first objective in the post processing was to extract and process the data for comparison with the experimental results.

The forces were non-dimensionalised by the dynamic pressure ($512Pa$) and the area of the model concerned. The area of the wing was computed from the total chord multiplied by the span. It must be noted that in the CFD, only half the wing area was used because only half of the model was simulated. For the wheel, its projected frontal area onto a vertical plane was used.

The chordwise pressure taps on the experimental wing were located at centrespan and at 91% span ($25mm$ inboard of the endplate) and were easily extracted from the CFD by intersecting a constant Y plane with the wing surface. For the wheel, five pressure taps were used to obtain the surface pressure distribution and their location can be seen on Figure 2.2. These were extracted in Fluent using the intersection of a tilted plane with the wheel and are plotted against the angular coordinate of the wheel. These coordinates are defined with the origin (0°) at the front of the wheel and increase clockwise. Therefore, 90° represents the contact patch and 270° is the top of the wheel.

The PIV results, obtained from both Van den Berg's study and this study, are of great value for the CFD validation and the location of the planes which were investigated can be seen in Figure 2.11. These planes were extracted from the CFD results, and care was taken to match them exactly with the PIV. The velocities were non-dimensionalised by the freestream velocity. It must be noted here that in Van den Berg's experiments, he maintained a constant dynamic pressure, but due to temperature changes, the freestream velocity was not constant. The actual freestream velocity was recorded during the tests and this was used to non-dimensionalise the flow for his PIV results. The effect of such

---

[9] A passage refers to a flow particle at freestream velocity covering the distance of the characteristic length

a change in Reynolds number ($\approx 1\%$) on the flow physics is believed to be quite small and the non-dimensionalised velocities of the PIV and CFD can be directly compared.

For the unsteady simulations, after the flow has been allowed to develop, the force coefficients are extracted at every timestep. These are then analysed using a Power Spectral Density (PSD) method to investigate any dominant frequency. The integral of the PSD over a frequency range gives the average power in the signal in that frequency range. The PSD of the signal is estimated using Welch's method [68, 69]. The signal was separated into 5 segments, each with 50% overlap, and a Hamming window was applied to each segment. If low frequencies appeared to be unresolved, additional sampling was done where possible.

Probes at specific locations in the domain were also used to analyse local time statistics. A User Defined Function (UDF) was created in Fluent to extract, at each timestep, the pressure and velocity components at a specified grid node. The location of the various probes was chosen to investigate local flow features such as the wing edge vortex and wheel wake. Correlation between the signal of the various probes and force coefficients was also investigated as it provides information about which effect is responsible for the transient behaviour of the bodies.

2.3 Experimental Approach

Additional PIV experiments were performed around the wheel in the wind tunnel to complement what was already available from the previous studies. In addition, the wheel drag measurements from Van den Berg's study were corrected differently for the rolling resistance.

2.3.1 Testing Configuration

Experiments were performed in the University of Southampton $2.1m \times 1.7m$ wind tunnel to obtain flowfield velocities using PIV. The tunnel is of the conventional return circuit design and is equipped with a moving belt measuring $3.5m \times 1.5m$. Suction is applied beneath the belt to prevent it from lifting and the resulting friction requires the belt to be cooled. The boundary layer that grows along the wind tunnel floor is removed upstream of the belt by using a slot and applying suction through a perforated plate. When the suction is applied, the velocity reaches the freestream value less than $2mm$ above the ground.

For the isolated wheel case, two carbon fibre wheels with the geometry described in Section 2.1 were setup in a symmetric arrangement, with the distance between them representative of an overlap of $20mm$ if the wing were present. They were fixed in place with Y-shaped carbon fibre support stings, shown in Figure 2.10(a), which were connected to the wind tunnel structure through vertical mounting pillars. The height of these pillars was altered to ensure the wheel camber was $2.4°$ so that the complete tread of the wheel was in contact with the ground. As the wheel is non-deformable and is cambered, it is conical and will be prone to vibrations. To reduce these, silicon oil was spread on most of the tread, except at its centre. Thus, the wheel's grip was localised and the rest of the tread was allowed to slip, reducing vibrations.

For the combined wing-wheel setup, a wing model with the geometry described in Section 2.1 was placed in front of the wheels at a gap of $20mm$. The wing elements are made of carbon fibre and the endplates of steel. The model was supported by a shrouded vertical pillar, which allowed for changes in ride height using stepper motors controlled by the wind tunnel's Pi system. The ride height could be adjusted to $0.05mm$ and the initial reference height was set using high precision shims between the lowest point of the wing and the ground. No transition fixing was used on the wing.

2.3.2 Testing Conditions

For most experiments, the wind tunnel freestream velocity was set to $30m/s$, and this value was used to non-dimensionalise the PIV results. For the moving ground (i.e rotating wheel) case, the belt velocity was matched to that of the freestream whereas when studying the stationary wheel, the ground was not moved although the belt suction and boundary layer removal were still applied. The turbulence intensity level of the 7×5 wind tunnel at $30m/s$ has been measured using hot-wire equipment and was found to be 0.3%. Throughout the experiment, the temperature was not controlled and a change of a few degrees occured. As a consequence, the Reynolds number based on the wing chord varied between 5.71×10^5 and 5.92×10^5.

2.3.3 Drag Force Correction

The drag force of the wheel was measured by Van den Berg with a one-component strain gauge load cell, which connects the wheel to the support sting. For the rotating wheel case, the load cell will measure, in addition to the aerodynamic drag, the reaction force due to the moving belt. To correct for this, the force was measured with rotation (i.e. moving belt velocity of $30m/s$) but no wind. This creates another problem as the wheel rotation and moving belt will induce aerodynamic forces. A CFD simulation was used to predict the induced aerodynamic force and the wheel drag was corrected accordingly (see Appendix A). As Van den Berg decided to correct for the reaction force by using a slow speed road only run at $2.5m/s$ (assuming there was no induced aerodynamic force), his results predicted a higher wheel drag.

2.3.4 Particle Image Velocimetry (PIV)

Flow velocities around the wheel were investigated with PIV for the isolated and combined wing-wheel cases. PIV is a non-intrusive technique where a pair of images of seeded particles within a plane in the flow are captured in a short time interval and are then compared to calculate the velocity of the particles by analysing their change of position. To capture the particles in each image pair, they are illuminated using two powerful laser pulses which are expanded through a cylindrical lens to form laser sheets. The system used consists of a Gemini PIV 15 laser, containing two Tempest Ng:YAG lasers of $125mJ$/pulse at a wavelength of $532nm$, and a 2048 × 2048 pixels TSI PowerView CCD camera to capture the images. The seeding material was composed of water based smoke particles of approximately 1 micron in diameter which were generated using a smoke generator located downstream of the test section.

The alignment of the two lasers was carefully checked before a test session to ensure an optimal signal to noise ratio and to make the use of a thinner laser sheet possible. The thickness of the laser sheet is a compromise between better illumination and worse signal to noise ratio due to out of plane velocities. Using the guideline that the out of plane distance travelled by the seeded particles in the time interval between the two pulses is no more than 25% of the laser sheet thickness, a $1mm$ thickness was chosen in combination with a time interval of $15\mu s$ for a freestream velocity of $30m/s$. The out of plane velocity also introduces an error in the data due to the perceived in plane velocity caused by the parallax effect. This error decreases with distance between the camera and the laser sheet, which introduces a compromise for the camera position where a large distance would reduce the parallax error but also reduce the clarity of the image. More details concerning the parallax error can be found in Appendix B.

Two planes were investigated in this research ($X = 0.6D$ and $Y = 0D$)[10] and are defined in Figure 2.11. Plane $X = 0.6D$ is located 60% of the wheel diameter downstream of the wheel axis and plane $Y = 0D$ is aligned with the wheel axis centrespan. The PIV configuration for plane $Y = 0D$ can be seen in Figure 2.10(a) and is also illustrated with a sketch in Figure 2.12. It can be seen that both the laser and camera have to be

---

[10] For convenience, the plane locations are non-dimensionalised by the wheel diameter and use a coordinate system based on the wheel's axis ($X = 0$), its centreline ($Y = 0$) and the ground ($Z = 0$)

placed in the test section to acquire the required data, which introduces some blockage, although it is not believed to significantly influence the measurements.

A strict procedure was followed when setting up the PIV experiments to obtain repeatable and accurate results. First, the laser sheet was aligned in the desired plane with an accuracy of $\pm 0.5mm$ and $\pm 0.1°$. It was then focused on the region of interest to obtain the desired thickness of the laser sheet and was securely fixed into this position. Then, the camera was placed perpendicular to the investigated plane up to within $\pm 0.1°$, at a distance defined by the available focal length and the desired image size, as well as ease of installation. The camera was focused on a ruler placed on the plane of interest and a calibration image was acquired. To keep a good resolution quality, the size of the captured image was kept below $200mm \times 200mm$, and planes $X = 0.6D$ and $Y = 0D$ are in fact composed of multiple smaller images stitched together. The camera and laser were linked to a TSI synchroniser, which is controlled through computer software, and the time interval between the laser pulses was set (the chosen time interval was adapted to the freestream velocity). Once everything was ready, the wind and road were turned on and allowed to stabilise at the desired velocity. Then, the smoke generator was activated with a predetermined cycle and the data was acquired, which took approximately ten minutes per setup configuration (e.g. different wing ride heights).

Adequate seeding is important, as too much smoke reduces the clarity of the captured images whereas insufficient seeding material results in a low signal to noise ratio and failure to capture vortex cores as the particles are ejected by the high level of vorticity. As the wind tunnel is not sealed, smoke needs to be added continuously during the data acquisition phase. The amount required was determined by looking at the success in the correlation of particles between two images and adapting the level of smoke generation until correlation was mostly successful, with spurious data only concentrated around areas of laser reflection or laser blockage.

For post-processing, cross-correlation between the image pairs was done using a deformation grid with an initial interrogation window size of 64×64 pixel with a 50% overlap, which was reduced to 32×32 pixels on the second iteration. The overlap improves the signal to noise ratio by reducing the loss of information at the border of the interrogation windows and the deformation grid displaces the 32×32 pixel interrogation windows of the second image (from an image pair) using the results of the first iteration (64×64 pixels), thus reducing the drop of signal which would occur due to large in plane velocities. In addition, a Gaussian peak was used for sub-pixel interpolation, which improves the capture of low velocities.

Once the cross-correlation was completed, a range validation with limits of $\pm 50m/s$ was used to remove erroneous vectors and the resulting blank spots were interpolated from data on a 3×3 grid around them. The processed image generated a 123×123 grid containing the in plane velocities and the results of 250 double images were averaged to obtain a mean flowfield. Although a higher amount of images would further improve the accuracy of the results, especially in unsteady areas such as the wheel wake, the overall mean velocity profile was found to be converged and a sample of 250 images was chosen as a compromise between accuracy and time efficiency.

For Plane $X = 0.6D$, the parallax error was significant in some regions due to high cross-plane velocities, and this was clearly visible when the four smaller images were merged to form the $320mm \times 320mm$ total image (See Appendix B). To correct for this, the cross-plane velocity was required and a CFD simulation was used to obtain it. Although this is not an exact correction, it is believed to produce a more accurate end result, and indeed the velocity discontinuities between the four images were significantly smaller whereas the observed flow features remained qualitatively the same.

Wing			
main element chord c_m	$139mm$	total chord c	$284mm$
flap element chord c_f	$145mm$	spanwidth b	$580mm$
main element thickness t/c_m	0.14	wing planform S	$0.165m^2$
flap element thickness t/c_f	0.09	aspect ratio AR	2.04
main element angle of attack α_m	+4°	flap overlap	$10mm$
flap element angle of attack α_f	+24°	flap gap	$12mm$
endplate size l×b×h	$275 \times 5 \times 115mm$		
endplate edge fillet radius	$2.5mm$		
Wheel			
maximum radius r_{max}	$157mm$	diameter D_{wheel}	$314mm$
minimum radius r_{min}	$153mm$	maximum width W_{wheel}	$173mm$
average radius r_{av}	$155mm$	frontal area A_{wheel}	$0.052m^2$
cover disc diameter D_{CovD}	$185mm$	aspect ratio AR	0.55
wheel camber angle	2.4°		
grooves width×depth	$7.5 \times 1.25mm$		

Table 2.1: Characteristic dimensions and parameters of the wing and wheel model geometries.

	050-W0-065	**020-W6-006**
Maximum Radius	$157mm$	$161.5mm$
Minimum Radius	$153mm$	$157.5mm$
Maximum Width	$173mm$	$165mm$
Aspect Ratio	0.55	0.51
Camber	2.4°	2.4°

Table 2.2: Summary of the main dimensions of the two different experimental wheels used.

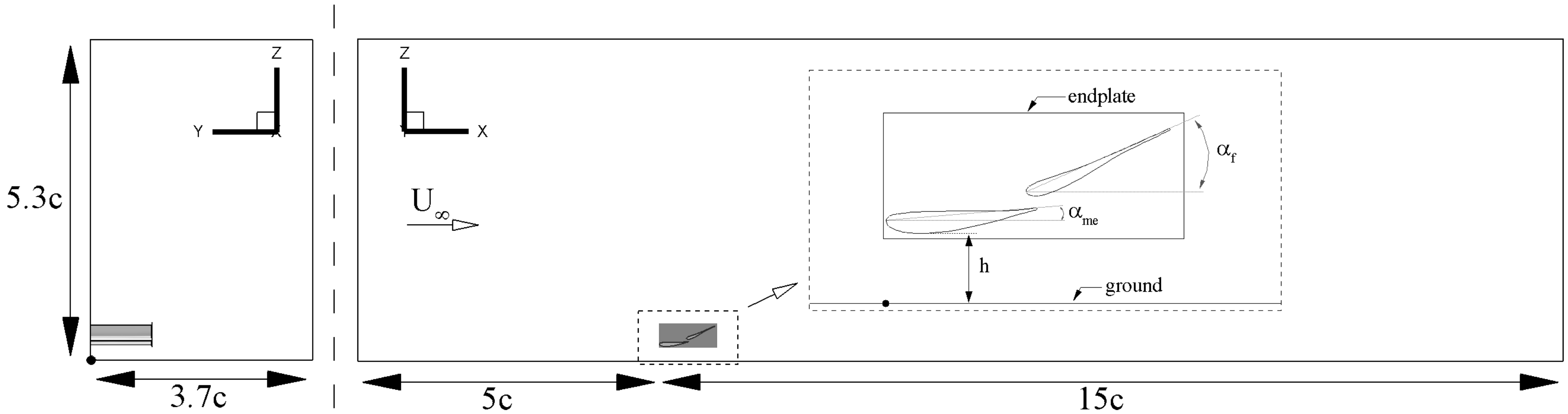

Figure 2.1: Schematic of the computational domain and wing geometry.

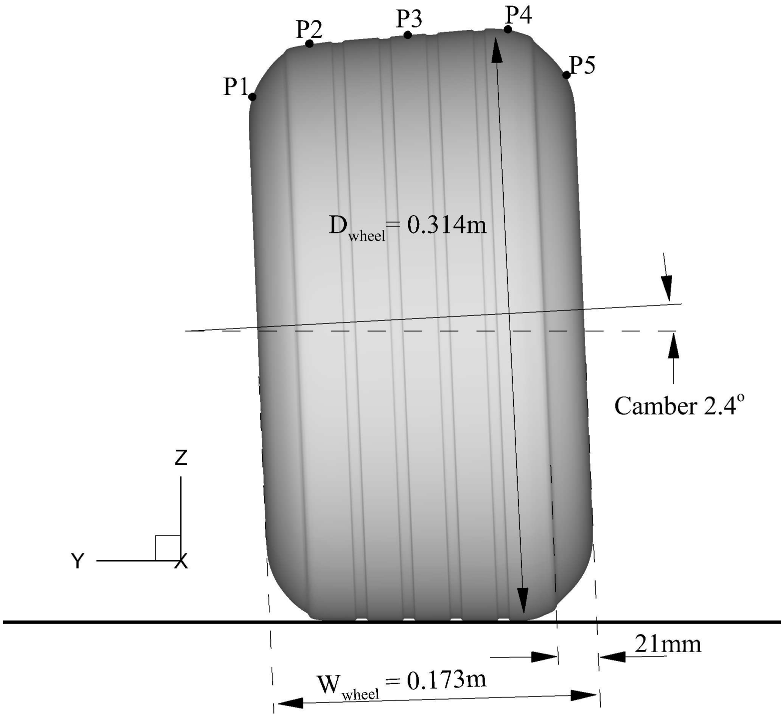

Figure 2.2: Definition of the wheel geometry and location of the pressure tappings (P1-P5).

Figure 2.3: Comparison of the two experimental wheels used. The wheel used for pressure measurements is labelled 020-W6-006 and the wheel used for PIV and forces is labelled 050-W0-065.

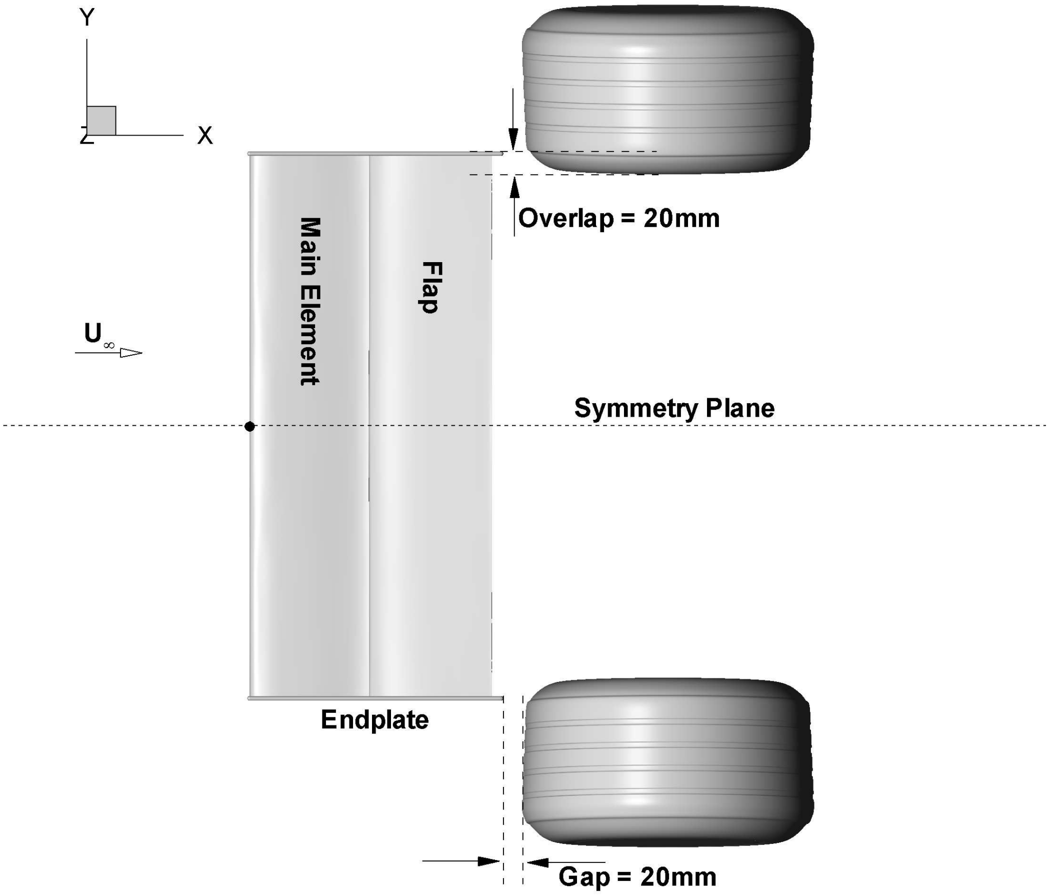

Figure 2.4: Setup description for combined case.

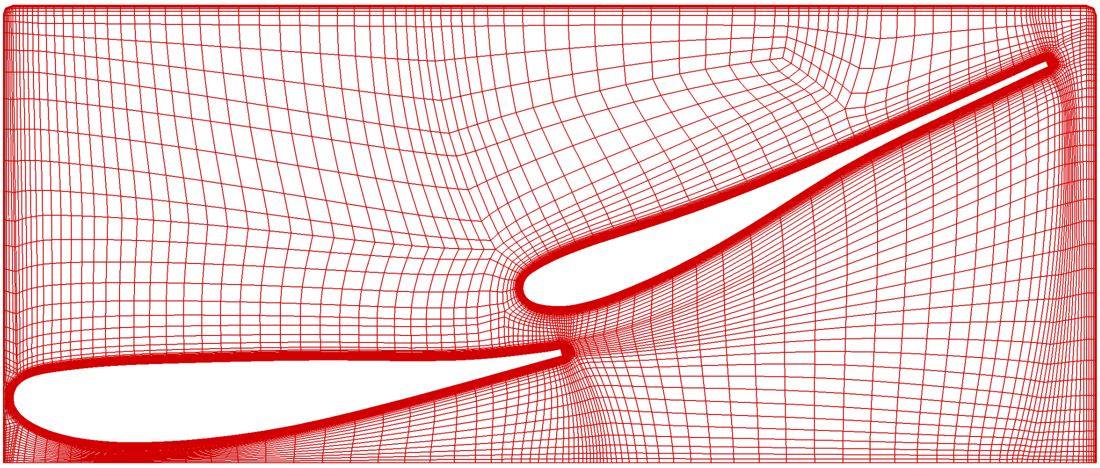

Figure 2.5: Grid topology of the wing. The boundary layers are seen wrapped around the main element and flap, where there is a high density of cells.

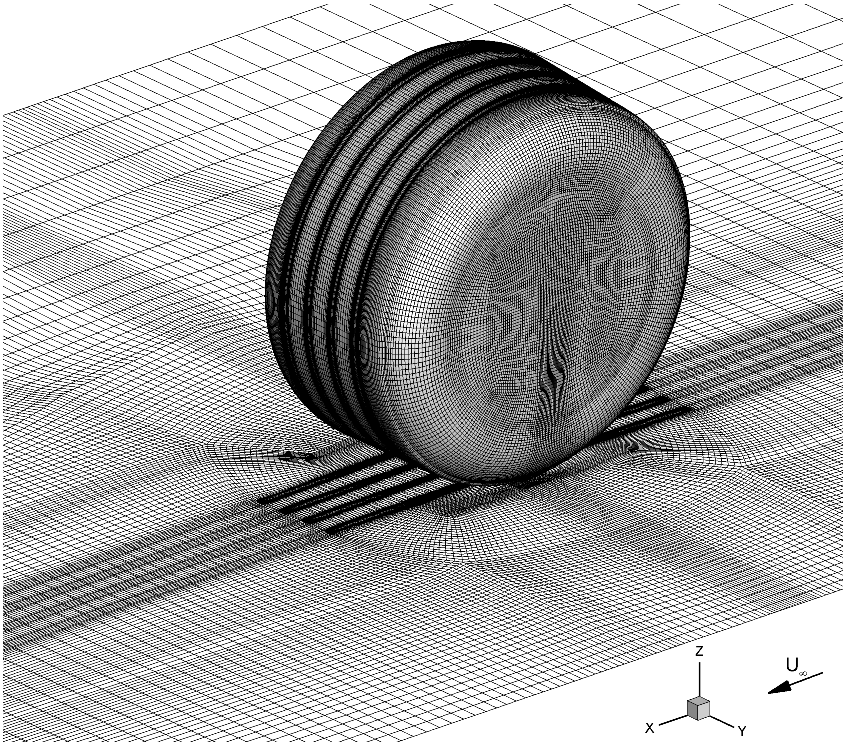

Figure 2.6: Computational grid on the road and wheel surface for the isolated wheel case (fine grid, 7 million cells).

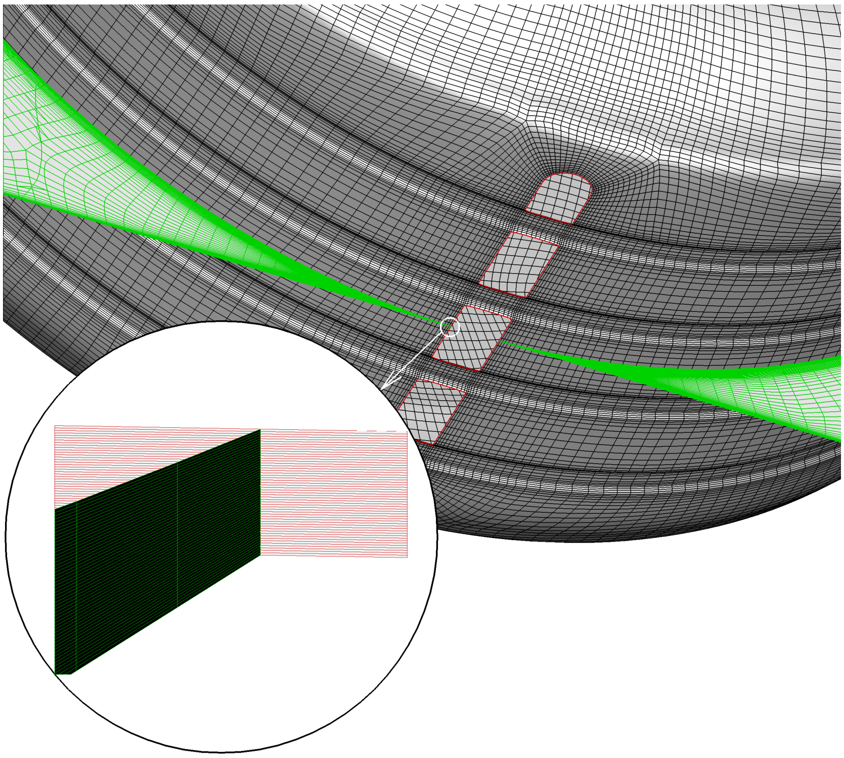

Figure 2.7: Grid of the plinth (red) beneath the wheel (grey), showing the cells that end on the plinth (green).

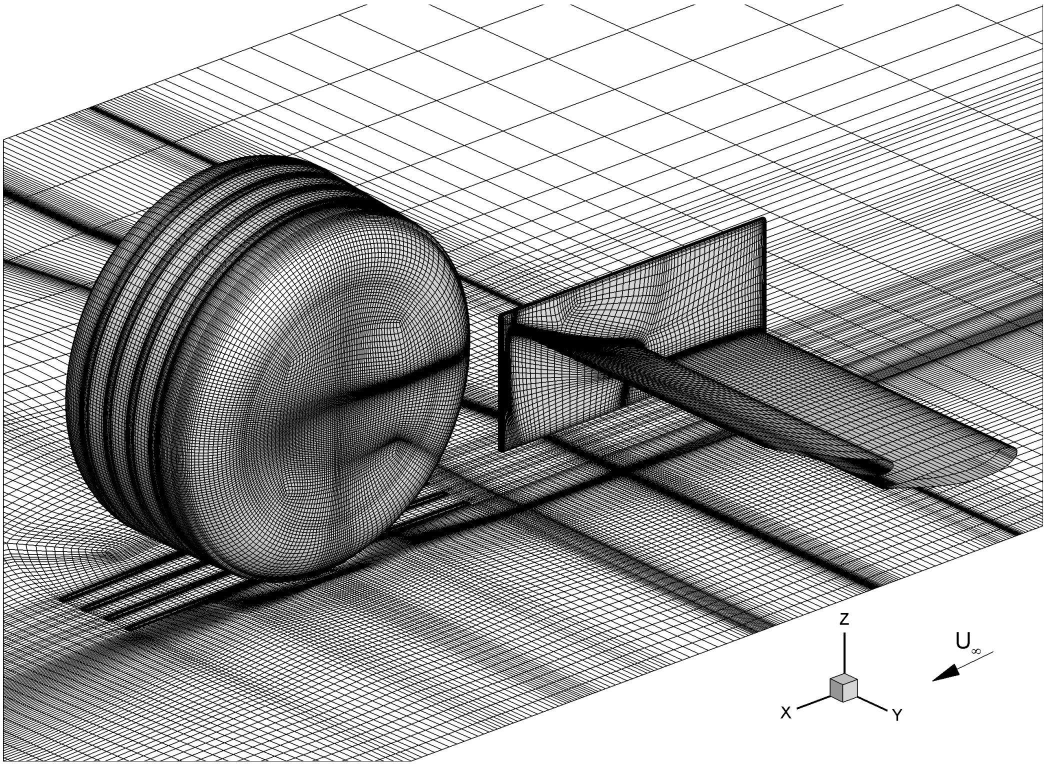

Figure 2.8: Computational grid on the road, wing and wheel surface for the combined wing and wheel case (6.7 million cells).

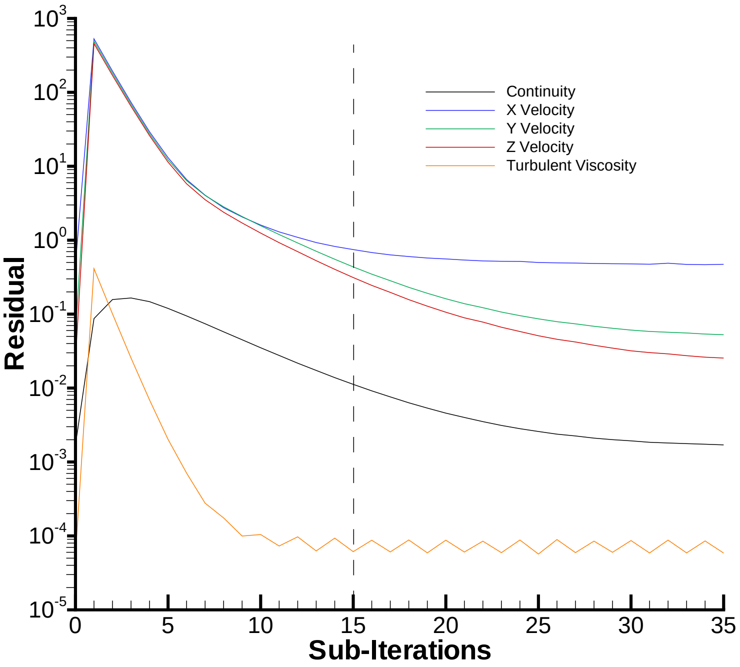

Figure 2.9: DES residuals for sub-iterations during one timestep.

(a) Isolated wheel case.

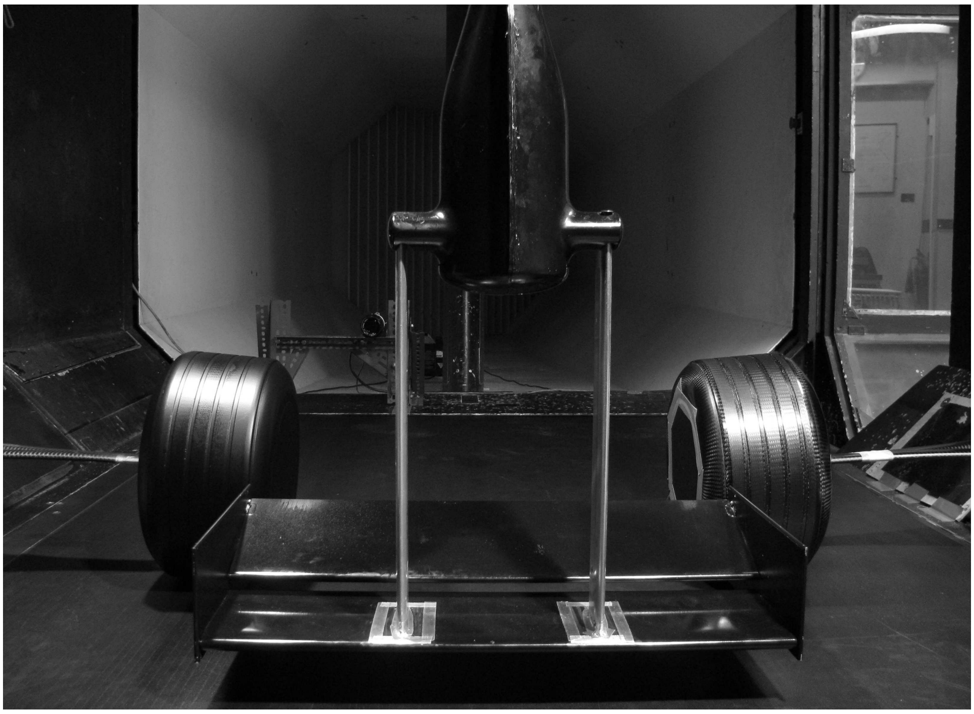

(b) Combined wing and wheel case.

Figure 2.10: Front view of the experimental setups in the Southampton wind tunnel facility with the PIV system installed.

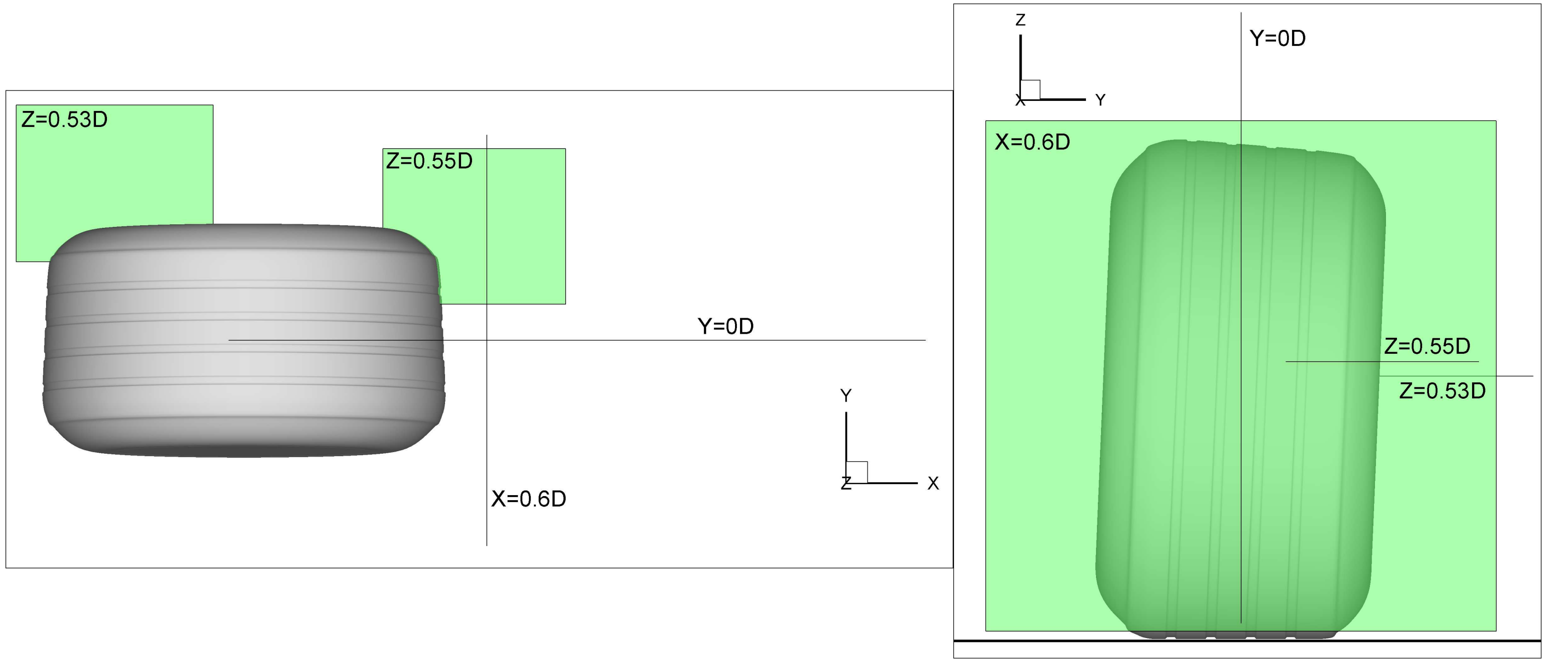

Figure 2.11: Size and location of the various planes investigated around the wheel. PIV results for $Z = 0.53D$ and $Z = 0.55D$ are from Van den Berg [18].

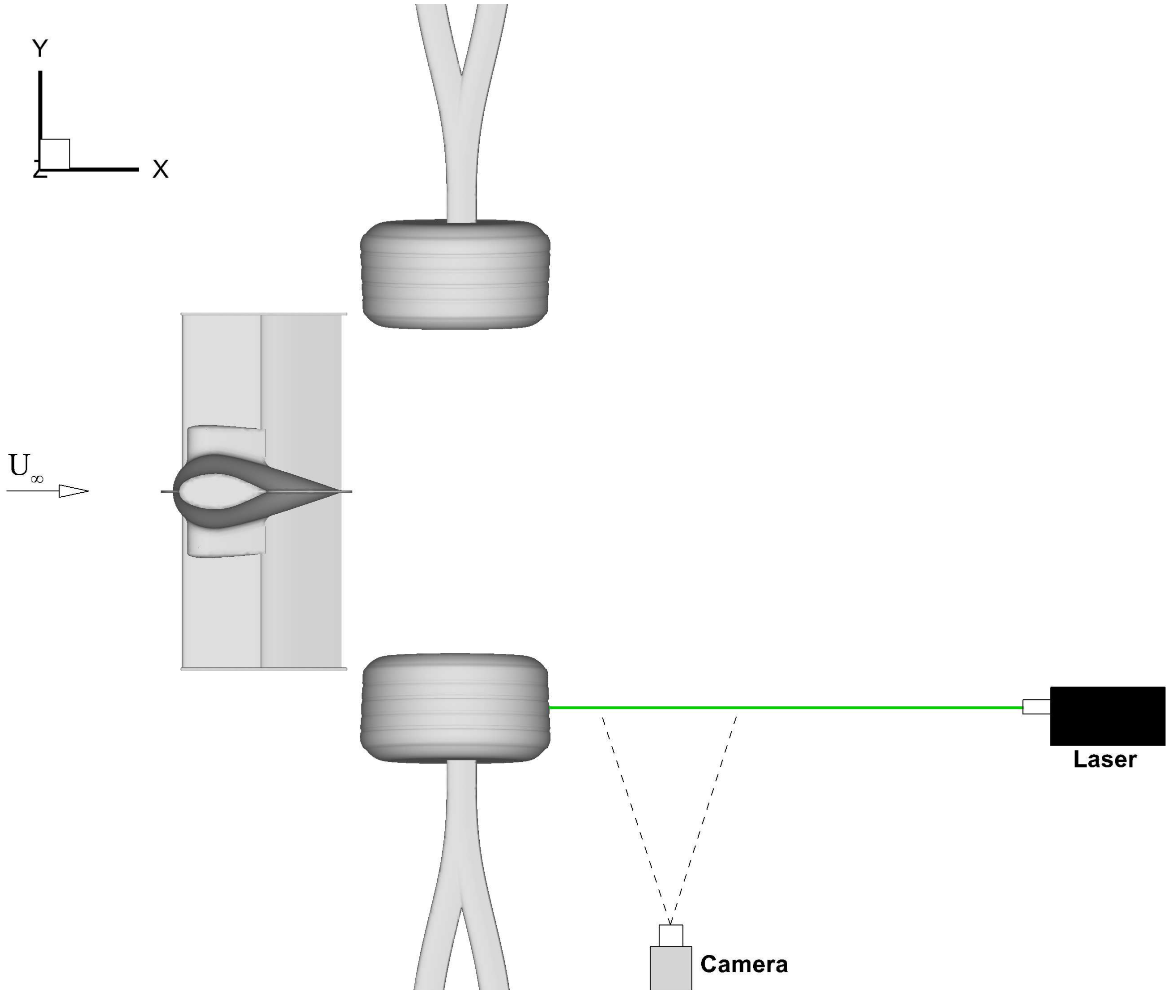

Figure 2.12: Top view sketch of the PIV setup used for plane $Y = 0D$.

Chapter 3

Isolated Wing

A double element front wing of a race car has been extensively studied previously, by Mahon [16] and Van den Berg [18], and therefore it provides useful validation for the CFD, while a greater understanding of the transient flow features can be obtained with the DES. This chapter discusses the results from both SRANS and DES, which are validated using the available experimental data.

3.1 Force Analysis

The integral forces of the wing are a good representation of its efficiency, although they do not give a lot of information on the behaviour of the flow. The force coefficients measured are the downforce (C_L) and the drag (C_D) and their variation with ride height is shown in Figures 3.1 and 3.2 respectively. It is noted that C_L is positive when acting downwards. The force variation with ride height is split into separate regions, as can be seen in Figure 3.1, and are based on experimental results [16].

In force region a, from $h/c = 0.317$ up to 0.236 the downforce increases continuously with decreasing ride height as the channel effect, which is created by the wing and ground acting like a diffuser, becomes more important. In addition, there is a lower edge vortex formed beneath the wing (see Section 3.4) whose strength also increases resulting in larger downforce. This is the first part of the force enhancement region and increases quadratically with a decrease in ride height. Both the SRANS and the DES predict similar trends and values, with a constant underprediction of approximately 7%. In this region, the drag also increases with lowering ride height and the CFD appears to overpredict it, whereas the rate of change is underpredicted.

Further reducing the ride height, there is a discontinuous drop in downforce and drag, defined as region b. It is at this point that the edge vortex beneath the wing begins to break down and results in the small loss of downforce. Although the computation does not predict this loss, the downforce trend from the two numerical methods start to diverge.

After the downforce has reached a local minima at the lower end of region b, it starts increasing with lowering ride height once more, albeit at a slower rate compared to region a. This is the second part of the force enhancement region (region c) and it increases linearly with ride height as the channel effect dominates. The two CFD methods diverge, where the SRANS shows a much steeper gradient than the experiments, and at the lower end of region c, it overpredicts the downforce by 2%. The DES on the other hand follows the general trend and the underprediction of downforce stays approximately constant at 3%. In region b, The drag also starts to rise again, until it reaches its global maximum at the lower boundary of region c. The CFD still overpredicts the drag, with the DES predicting a much steeper gradient, resulting in a similar overprediction as the SRANS (approximately 6%) at the lower ride heights.

In region d, the downforce rises slowly until it levels off and reaches its maximum whereas the drag starts to reduce with lowering ride height as a result of the lower edge vortex breakdown. At the ride height of $h/c = 0.106$ the DES shows a similar drop in C_D compared to the experiment, whereas SRANS predicts a slight increase in drag, which is due to errors in modeling the lower edge vortex.

At the lowest simulated ride height, which is located in region e, a sharp decline in downforce is predicted by the CFD, especially the DES. This drop is due to flow separation over the main element's suction surface and does not occur in the experiments until a lower ride height. In a separate experimental study, where the boundary layer had been tripped, this separation was observed to occur at a higher ride height. It is therefore proposed that the incorrect modelling of the boundary layer laminar to turbulent transition in the CFD is responsible for this discrepancy.

Overall, the DES appears to predict the downforce trend more accurately than SRANS at low ride heights, where vortex breakdown has occurred, but the discontinuity in region b is not captured. The following sections analyse the pressure distribution and edge vortices to understand where the observed discrepancies between the experiments and CFD originate from.

3.2 Surface Pressure Distribution

The pressure distribution around the wing gives a local and detailed insight on the flow behaviour. Figures 3.3 and 3.4 present the pressure distribution around the centrespan and the wing tip respectively, at different ride heights.

Looking at the centrespan at the highest ride height of $h/c = 0.317$ (Figure 3.3(a)), it can be seen that the two CFD methods predict a very similar pressure distribution, with an underprediction of the suction throughout the lower surface of both elements (resulting in the underpredicted downforce), and they qualitatively reproduce the trend obtained from the measurements. The top surface shows a good correlation with the experiment, except for the position of the stagnation point on the flap, which is predicted to be closer to the leading edge and would contribute to the underpredicted suction peak.

As the ride height is reduced (Figure 3.3(b)), there is an increased suction on the lower surface of the main element, whereas the upper surface is unchanged. The pressure distribution of the flap is not sensitive to changes of ride height in this region. Two different ride heights are plotted here; $h/c = 0.246$, which is near the boundary of region a-b and $h/c = 0.211$, which is after the drop in downforce, close to the boundary of region b-c. Both CFD methods predict the same surface pressure, and it should be noted that for the main element, a larger change in suction peak ($\Delta Cp_{peak} = -0.38$) is predicted between the two ride heights compared with the experiment ($\Delta Cp_{peak} = -0.27$). This promotes the rise in downforce predicted by the CFD, which is not in agreement with the experiment.

For the lowest ride height shown, the SRANS predicts a similar suction peak to the experiment, whereas the DES still underpredicts it by approximately 4%. This higher suction predicted by the SRANS contributes to the increase in predicted downforce at lower ride heights and even if the DES appears to be less accurate when comparing absolute values, it follows a more qualitative trend.

At the tip of the wing, most of the main element produces less downforce than at centrespan due to a combination of the lower effective angle of attack resulting from the upwash induced by the lower edge vortex and the pressure losses around the edge of the endplate. On the other hand, the main element trailing edge ($x/c > 0.35$) and the flap show the opposite trend, having lower pressures at the tip than at centrespan. This is associated to the combined effects of the induced velocity from the lower edge vortex and the reduced pressure losses as the bottom edge of the endplate is further away from the wing's lower surface.

At a ride height of $h/c = 0.317$ (Figure 3.4(a)), similarly to the centrespan results, the two CFD methods predict similar pressure distributions. For the main element, the suction is underpredicted on the lower surface, whereas the flap suction is marginally overpredicted, with a steeper adverse pressure gradient.

Figure 3.4(b) compares the pressure distribution at the wing tip for the two ride heights in region b. The experimental data shows that the difference in suction is small between the two ride heights, and for the flap, the peak suction does not change. The CFD on the other hand shows larger suction for the lower ride height, which would result in a larger downforce, and fails to capture the effect which results in the local drop in downforce. It can be noted that the SRANS and DES start to show differences at this point.

For the lower height of $h/c = 0.141$, the DES is seen to predict the pressure distribution at the tip more accurately (see Figure 3.4(c)), without the underprediction experienced at the other discussed ride heights. On the contrary, the SRANS largely overpredicts the suction on the main element, contributing to the overprediction in downforce. For the flap, it overpredicts the peak suction followed by a steep adverse pressure gradient.

Finally, at $h/c = 0.063$ it was observed in Section 3.1 that the DES predicts a sharp fall in downforce. The pressure distribution at centrespan (Figure 3.5(a)) shows that the main element suction on the lower surface is heavily underpredicted, with a slight forward shift of the stagnation point, explaining the underpredicted downforce. The flap is also seen to have an underpredicted suction, which would reduce the circulation effect it has on the main element. Flow separation at 65% of the main element's chord is observed. The SRANS also underpredicts the lower surface suction, but to a lesser extent. The pressure distribution at the wing tip in Figure 3.5(b) shows much less discrepancy between the measurements and the CFD, pointing towards the underprediction in downforce being caused mainly by local separation around centrespan.

In region e, where this ride height is located, the experimental results were dependent on the direction of change of ride height. Although not shown in Figure 3.1, the measured downforce coefficient at $h/c = 0.063$ for the increasing ride height branch is approximately 2.2 (0.2 less than for the decreasing ride height branch) and this loss was linked to large recirculation regions on the flap. The pressure distribution [16] at centrespan and wing tip does not show any difference between the increasing and decreasing ride height cases, which could be because the pressure tappings are not located in the recirculation regions. Although the CFD predicts a sharp fall in downforce, it does not predict the aformentioned recirculation regions. It is believed the cause for the underprediction is incorrect boundary layer transition modelling, which results in early separation.

3.3 Sectional Forces

The pressure distribution at the centrespan and wing tip were integrated to obtain the sectional downforce and drag, in order to investigate each element separately. For the centrespan, it can be seen how the CFD underpredicts the downforce at all ride heights by approximately 7% (Figure 3.6(a)). The flap produces three times less downforce than the main element and is relatively insensitive to changes in ride height. The SRANS and DES are seen to start diverging for the main element at a ride height of $h/c = 0.211$, and this is associated to the DES capturing the lower edge vortex breakdown at the tip more accurately.

At the wing tip, the change of downforce with ride height is quite different (see Figure 3.6(b)). The main element is again seen to produce more downforce than the flap, but to a much lesser extent. The level of downforce it produces increases with lowering ride height, but this stops at $h/c = 0.211$ when the vortex breaks down, and further reductions in ride height result in a drop in downforce. The SRANS does not capture that resulting in a much larger downforce increase, whereas the DES does appears to predict the trend slightly better, although it still fails to capture the overall effect.

The flap produces most of the sectional drag at centrespan (Figure 3.7(a)), whereas at some ride heights the main element produces thrust[1]. The main element is very efficient due to the high suction around its leading edge, which produces thrust and counteracts the pressure drag produced by the rest of the element. It is noted that the CFD underpredicts the drag. This contradicts the results presented in Section 3.1, where the CFD overpredicts the wing drag when compared to load cell measurements. It is believed that the pressure data is more reliable, as the load cell arrangement might contain some errors due to the wing support struts bending.[2]

At the wing tip (Figure 3.7(b), a change in the pressure distribution of the flap is responsible for the drop in drag at the low ride height, which is associated to the lower edge vortex breakdown beneath the flap surface. The main element is responsible for 25% of the drag at the tip even though it produces less downforce than at centrespan. This is because there is no high suction peak at the leading edge, which would reduce the drag of the element. Once again, the CFD mostly underpredicts the sectional drag, with the DES predicting a qualitatively more accurate trend.

---

[1] The sectional force does not include skin friction drag

[2] Although this could not be checked, other possible sources for this discrepancy (viscous drag, tare values) were found not to be responsible.

3.4 Edge Vortex

Due to the difference in pressure between the inside and the outside of the endplates, vortices are created at the edges. The location and general trajectory of the lower and upper edge vortex are shown in Figure 3.8 for reference. These two vortices can be seen on a plane located behind the wing, at $x/c = 0.995$, for three different ride heights in Figure 3.9 and both have a counterclockwise rotation (positive x-vorticity). Also, the maximum value of Ω_x for each vortex for the different cases is summarised in table 3.1.

Comparing the PIV results to the CFD, the DES captures both vortices with more accuracy than the SRANS. Looking at the upper edge vortex, it can be seen that it is not much affected by changes in ride height. The maximum Ω_x for this vortex is underpredicted using the SRANS, with a value of 44, whereas the DES underpredicts Ω_x by a smaller amount. As it is shown in the next section, the prediction of this vortex by the DES would improve with a finer grid.

The lower edge vortex experiences a much bigger dependence on ride height. At the highest ride height, the vortex is strong with a maximum Ω_x of 140, but a big drop in vorticity has occurred at $h/c = 0.211$ as vortex breakdown occurs. The SRANS underpredicts Ω_x of the lower edge vortex at $h/c = 0.317$ and does not predict a sudden change as the ride height is reduced. The DES models a stronger vortex than the SRANS and bigger changes in the lower edge vortex are seen as the ride height is reduced. The underprediction of the lower edge vortex by the computation can be associated to the lower suction observed on the main element, which would result in a lower pressure difference to create the vortex. The prediction of the lower edge vortex at $h/c = 0.211$ by the DES is seen to be different to the experiment and this is explained by the vortex breakdown bubble being predicted just in front of the plane, whereas the experiment shows the breakdown to be slightly further forward (see Figure 3.10(b)).

Figure 3.10 shows the mean streamwise velocity on a vertical plane 25mm inboard of the endplate at different ride heights. This plane cuts through the lower edge vortex, which is indicated by the visible upwash becoming downwash further downstream as the vortex core crosses the plane. Focusing on the highest ride height showed in Figure 3.10(a), it can generally be observed that the CFD underpredicts the velocity beneath the main element trailing edge, which coincides with the lack of suction showed by the pressure distribution. Downstream, where the vortex crosses the plane, the DES predicts the magnitude of the velocity better than the SRANS.

At $h/c = 0.211$ (Figure 3.10(b)), an interesting feature can be seen at $x \approx 250mm$ where there is a small region of flow reversal. This represents a cross section through a vortex breakdown bubble. The SRANS fails to capture this flow phenomena, whereas the DES predicts it with good accuracy slightly further downstream at $x \approx 255mm$. The lowest ride height presented, $h/c = 0.106$ in Figure 3.10(c), shows a large area of flow reversal, as the lower edge vortex breakdown has become more significant. The DES is seen to predict the flow reversal and the velocity beneath the flap very well, whereas the SRANS overpredicts the velocity beneath the main element and flap (resulting in an overpredicted suction), though it still captures some flow reversal.

The vortices can be visualised using the Q-criterion, which is the second invariant of ΔU [70]. Figure 3.11 shows an iso-surface of the instantaneous Q-criterion, coloured by streamwise velocity, for the three ride heights described previously ($h/c = 0.317$, 0.246, 0.106) using the DES results. At $h/c = 0.317$, both upper and lower edge vortices can clearly be seen and are steady. The upper edge vortex is influenced by the stronger lower edge vortex which diverts it inboard and toward the ground. For $h/c = 0.246$, a big change occurs in the lower edge vortex, as its size increases significantly before experiencing a bubble type breakdown, whereas the upper edge vortex is still steady. As the lower edge vortex is stronger and closer to the ground, a secondary vortex which it induces on the ground can now be seen with this value of Q-criterion. This secondary vortex is in line with the research by Harvey and Perry [71], and pushes the lower edge vortex away from the ground. Finally, at $h/c = 0.106$, the lower edge vortex breaks down beneath the main element trailing edge and the flow downstream of that is highly unsteady, with large recirculations beneath the flap causing the loss in downforce at the tip which was observed in Figure 3.6(b). The secondary vortex on the ground is shorter, as it merges and is dissipated by the recirculation, and the upper edge vortex has become unsteady and dissipates quickly as it is influenced by the recirculation region.

3.5 Unsteady Forces

How unsteadiness in the lower edge vortex affects the wing's performance is investigated by observing the transient variations in downforce (using the DES results). At $h/c = 0.317$ the wing downforce coefficient is steady at a value of 2.2, as the lower edge vortex is not predicted to break down and is stationary. Once the vortex breaks down, the wing downforce starts to become unsteady as is seen in Figure 3.12(a). The oscillations are small and using the power spectral density (PSD), which is estimated by Fourier transformation using Welch's method [68], a dominant frequency of approximately $350Hz$ is observed. It was found that this oscillation came primarily from the flap and is directly associated with the breakdown, which is a reasonable distance beneath the flap and therefore does not affect it significantly. The sideforce of the endplate is more susceptible to this transient feature. For the lower ride height of $h/c = 0.106$

shown in Figure 3.12(b), much larger changes in the wing's downforce occur (±4% of the mean value) as a result of the highly turbulent region under the flap tip, where the flow reversal downstream of the vortex breakdown is located (see Figure 3.11(c)). The PSD shows no clear dominant frequency, although there is a slight peak at $350Hz$ caused by the vortex breakdown, and the signal is generally composed of broadband frequencies. A pressure monitor located close to the vortex core measures signals dominated by high frequencies of approximately $350Hz$, showing that the vortex breakdown frequency is still present, and the lower frequencies which are present appear to be linked to a streamwise movement of the breakdown location (close to the main element's trailing edge).

3.6 Wing Wake

The front wing's wake affects the efficiency of the aerodynamic devices downstream (e.g. underbody, diffuser and rear wing) and it is of interest to investigate how it behaves with changes in ride height. The wake at the wing's centrespan differs from the tip wake observed in Section 3.4 as it is further away from the lower edge vortex. Time-averaged and instantaneous contour plots of the wake at centrespan from the DES results are shown in Figure 3.13. Focusing on the time-averaged streamwise velocity (Figure 3.13(a)), the wake of the main element is seen to grow with larger velocity deficits as the wing approaches the ground. On the other hand, the flap wake is much smaller and is not significantly affected by the ground presence except at the lowest ride height shown. The main element wake is seen to expand as it travels beneath the flap, which is caused by the adverse pressure gradient created by the flap, and the velocity deficit is seen to increase.

At $h/c = 0.106$ the streamwise velocity drops to 20% of the freestream velocity and at the lowest ride height, flow reversal occurs in the wake. Mahon [16] measured the wing wake with a pitot rake and although this method does not allow flow reversal to be detected, he predicted that the main element wake would contain negative velocities at the lower ride heights causing a loss of flap downforce. This is a lift limiting mechanism of multi-element wings with high camber which has been documented by Petrov [17], whereby the wake of an upstream element is affected by the adverse pressure gradient of the subsequent elements, causing flow reversal. This off-surface separation, which Petrov called detached separation, results in a loss of aerodynamic loading on the following elements, even though they have a fully attached boundary layer.

The DES results show that when the main element's boundary layer separates at a low ride height, the subsequent wake is adversly affected by the flap leading to flow reversal.

The flap boundary layer is still fully attached and the wake of the two elements merge. Any loses in flap downforce occur close to its leading edge, where the channel flow velocity (between the main element trailing edge and flap) is seen to be lower.

With DES, the instantaneous wake can also be observed (see Figure 3.13(b)). At $h/c = 0.211$ the wake is steady, with only a weak vortex shedding captured using the Q criterion. The shear layers of the main element wake are seen to diverge slightly as a result of the adverse pressure gradient of the flap. At $h/c = 0.106$ an increase in vortex shedding occurs, but the vortices are still relatively weak, and a small flapping motion is observed. It is clear that the flap wake is separate from this and is steady. At the lowest ride height of $h/c = 0.070$, the main element trailing edge separation is seen as the lower shear layer is not diverted upwards anymore. The two wake shear layers thus diverge significantly and strong vortices are shed from each one. The upper shear layer is seen to interact with the flap wake whereas the vortices shed from the lower shear layer interact with the ground boundary layer, inducing vortices as was observed with the lower edge vortex in Section 3.4.

3.7 Grid Sensitivity

SRANS and DES simulations were conducted for the three different size grids created at the ride height $h/c = 0.246$, to investigate the sensitivity of the results to changes in the grid. As Figure 3.14 shows, the effect of the grid changes are very small on the surface pressures. Only the DES results are shown as the SRANS results are very similar.

Figure 3.15 compares the prediction of the two vortices behind the wing, with the maximum vorticity of both vortices summarised in table 3.2. For SRANS, the upper edge vortex is seen to be weaker for the coarse grid, whereas the lower edge vortex gets slightly weaker as the grid is refined. The vortex prediction by the DES is seen to be more affected by the grid changes. The upper edge vortex is predicted to be stronger by 13% for each refinement step, reaching a maximum of 70 for the fine grid, which brings it closer to the experimental value of approximately 110. The lower edge vortex is predicted by DES to have broken down at this ride height (with the breakdown occurring upstream of the plane shown in Figure 3.15), and the size of the breakdown recirculation bubble gets smaller for finer grids.

The medium grid was used for this study as the prediction of surface pressures is not much affected by the grid changes but also because the resources were not available to run the fine grid. For the DES, the fine grid can be seen to predict differences in the vortices as finer structures are captured. It should also be noted that due to the nature of this grid, the region where the wing and endplate meet might cause problems for the DES, especially at the trailing edge of the elements where the boundary layer is thicker and the grid spacing smaller. When the grid is refined, this problem becomes more significant as the DES length scale becomes smaller, and the LES mode would increasingly resolve the boundary layer with a grid too coarse to support it.

3.8 Further Discussion

Various results have been compared and it has been mentioned how DES predicts better trends than the SRANS method, especially at low ride heights. The vortices are predicted more accurately with DES, even capturing the recirculation resulting from the vortex breakdown. The correct prediction of the vortices might not affect the pressure distribution of the wing, but it would become more significant when increasingly complicated simulations of a racecar were performed, as the vortices would interact with other parts of the car located further downstream.

The transition of the boundary layer from laminar to turbulent around the wing elements was not modelled. As the growth of a boundary layer is faster when turbulent, it is expected that the simulations would predict a thicker boundary layer, which would in turn be more susceptible to separation. In addition, the overall blockage is reduced due to the omission of the support structure and wind tunnel wall boundary layer, which can be a contribution to other discrepancies in the simulation results such as the lack of suction on the main element.

Table 3.1: Summary of the maximum Ω_x of the upper and lower edge vortex at the plane $x/c = 0.995$ for various ride heights.

	Top Edge Vortex			Lower Edge Vortex		
h/c	Exp. [18]	SRANS	DES	Exp. [18]	SRANS	DES
0.317	103	45	61	140	32	62
0.211	114	44	62	20	28	52
0.176	109	44	63	12	19	16

Table 3.2: Summary of the maximum Ω_x of the upper and lower edge vortex at the plane $x/c = 0.995$ for different grid sizes at a ride height of $h/c = 0.246$.

	Top Edge Vortex		Lower Edge Vortex	
	SRANS	DES	SRANS	DES
Coarse Grid	39	55	33	32
Medium Grid	45	62	31	32
Fine Grid	43	70	29	44

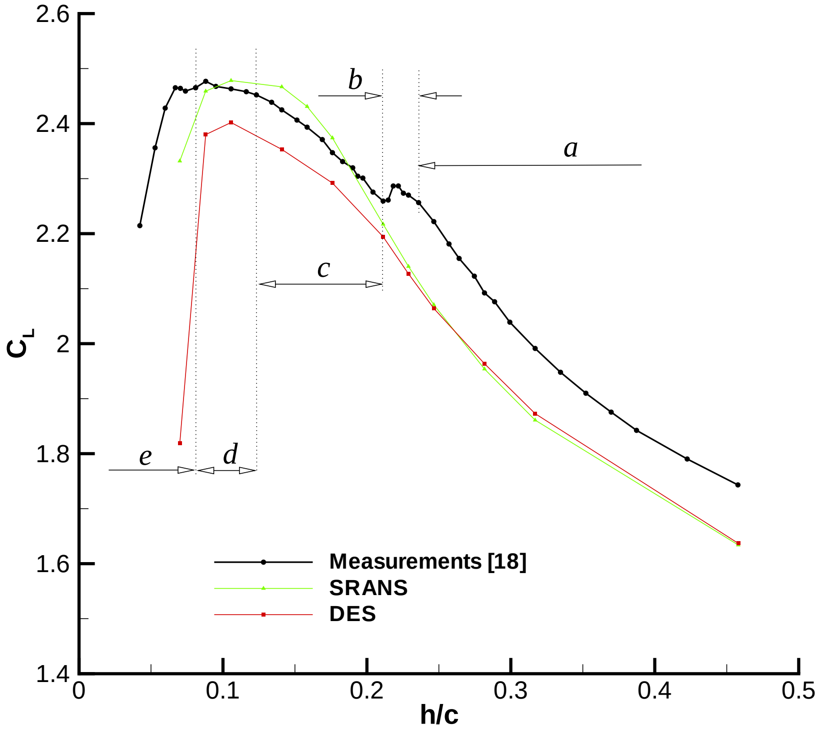

Figure 3.1: Variation of the wing downforce coefficient with ride height.

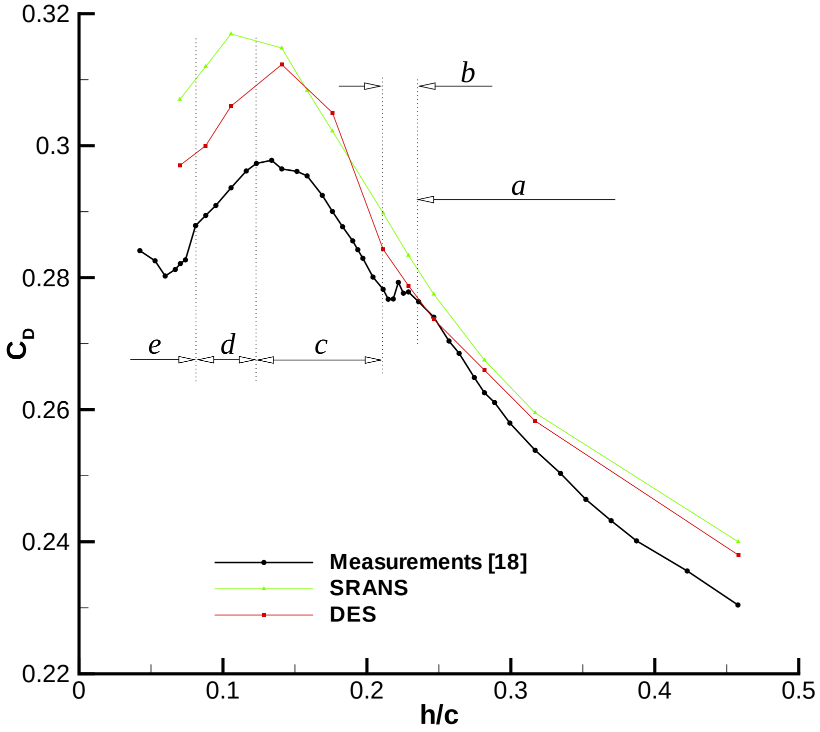

Figure 3.2: Variation of the wing drag coefficient with ride height.

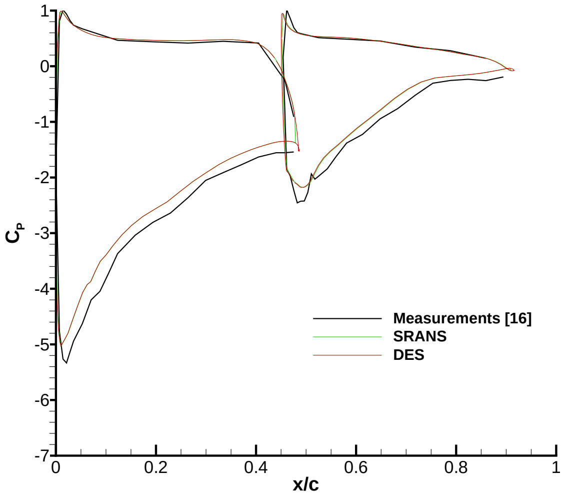

(a) $h/c = 0.317$

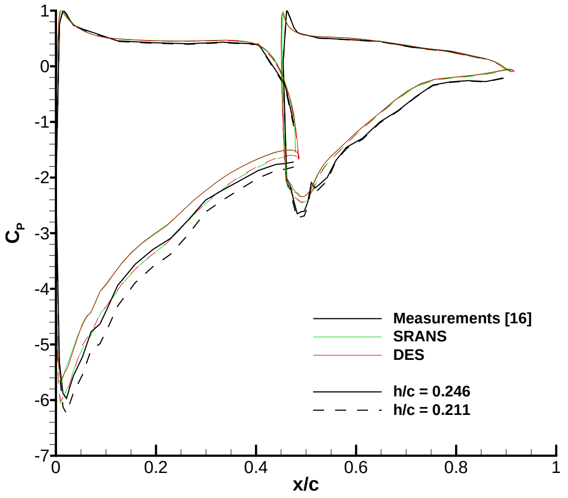

(b) $h/c = 0.211$ & 0.246

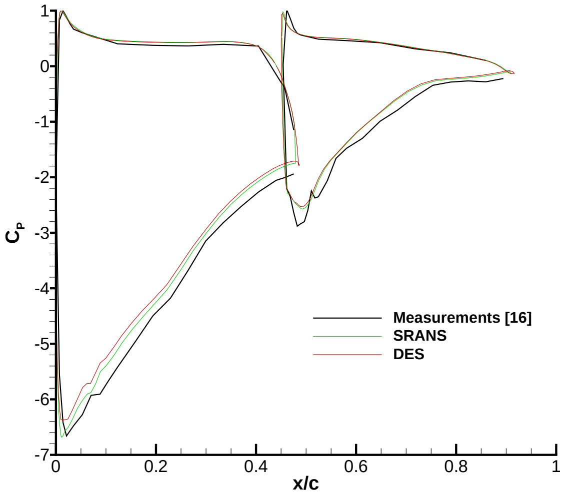

(c) $h/c = 0.141$

Figure 3.3: Pressure distributions at centrespan ($y/c = 0$) for different ride heights.

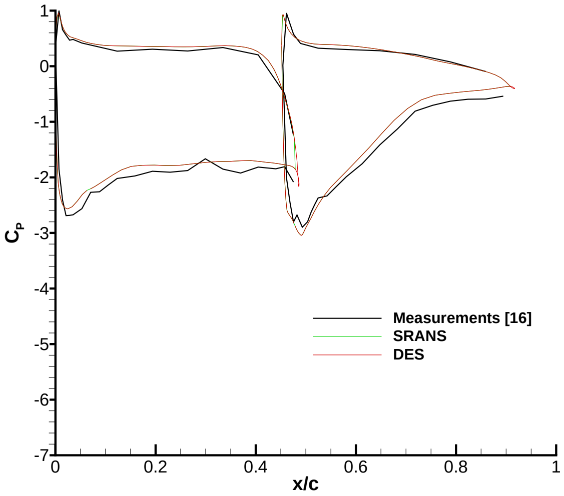

(a) $h/c = 0.317$

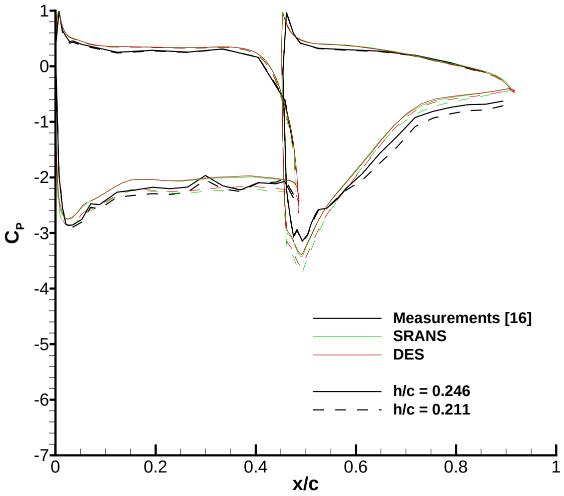

(b) $h/c = 0.211$ & 0.246

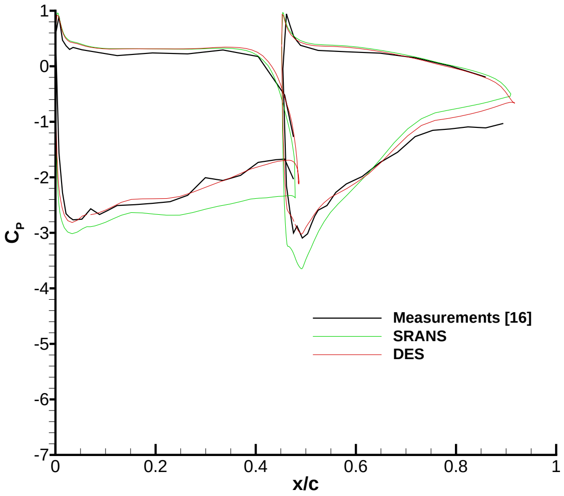

(c) $h/c = 0.141$

Figure 3.4: Pressure distributions at the wing tip ($y/c = -0.93$) for different ride heights.

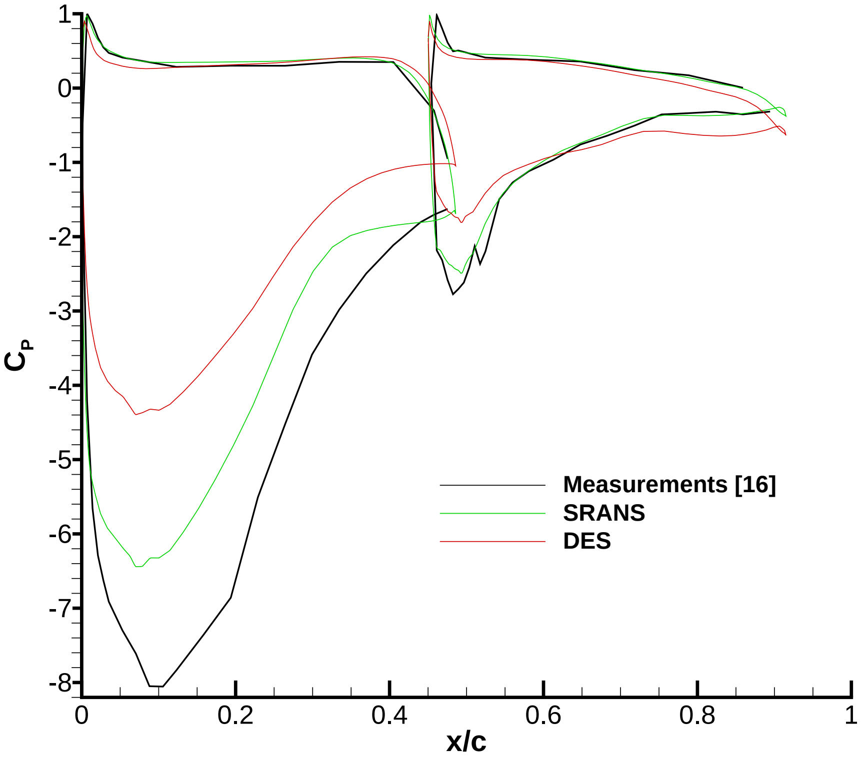

(a) Centrespan ($y/c = 0$).

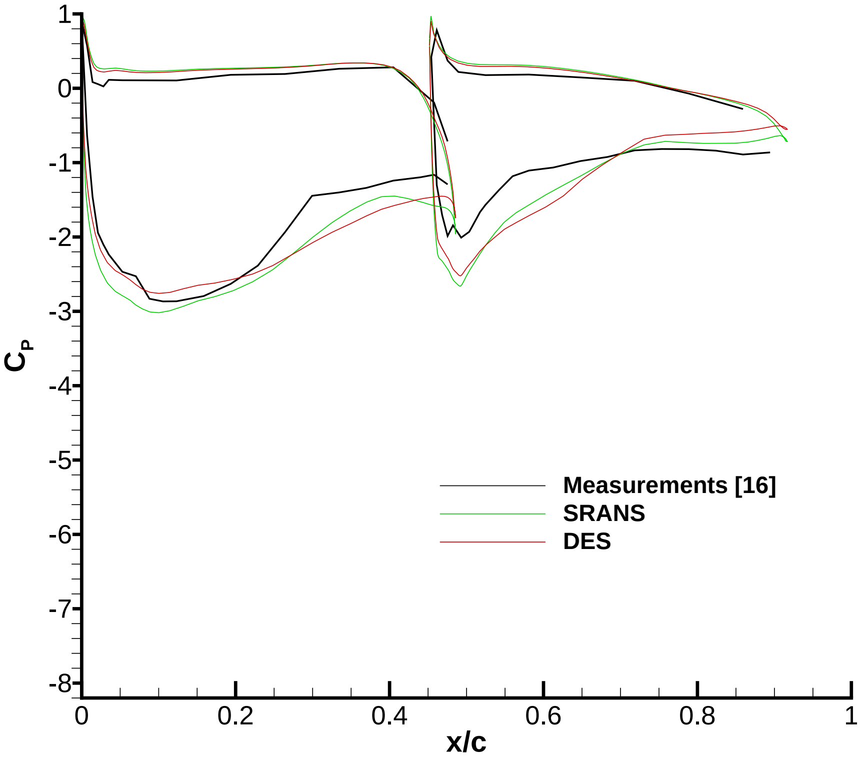

(b) Wing tip ($y/c = -0.93$).

Figure 3.5: Pressure distribution at $h/c = 0.063$.

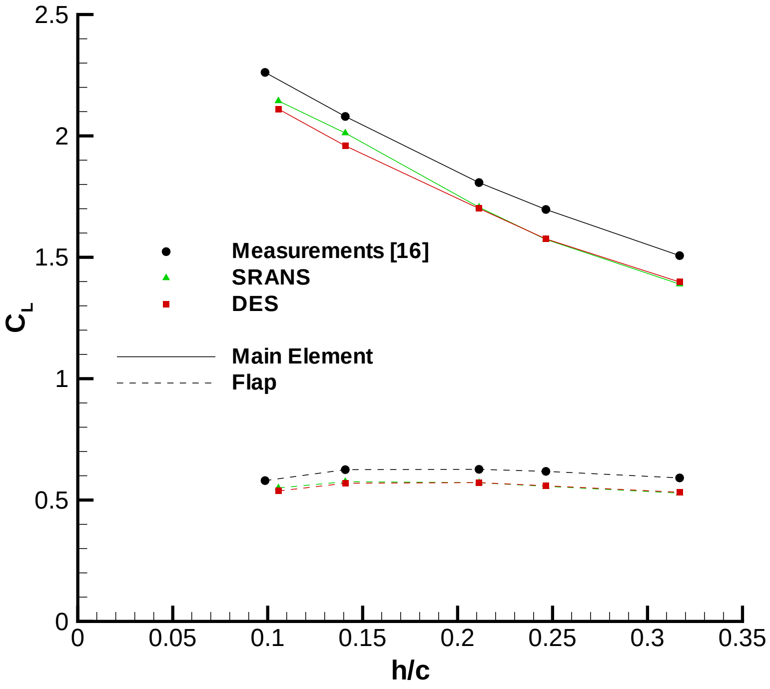

(a) Centrespan ($y/c = 0$).

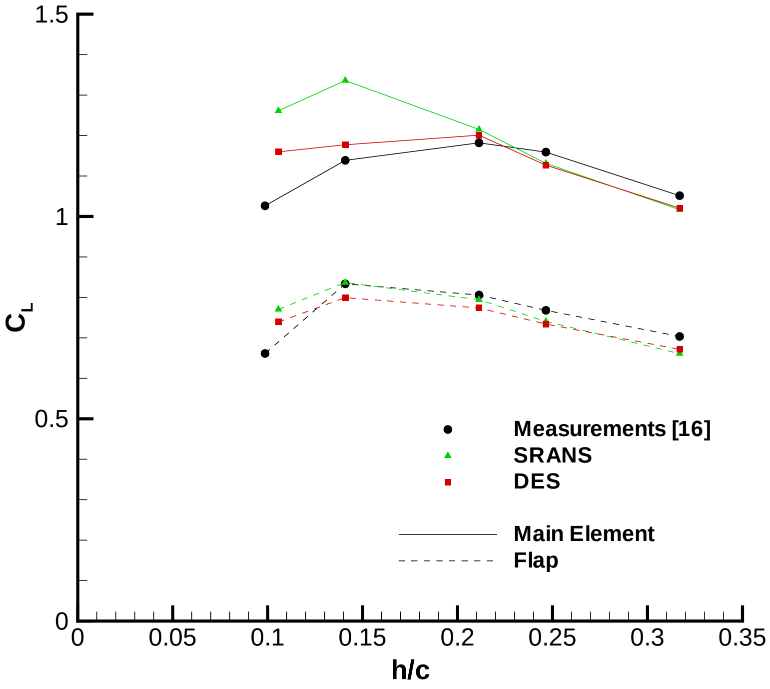

(b) Wing Tip ($y/c = -0.93$).

Figure 3.6: Variation of the sectional downforce coefficient with ride height at the centrespan (a) and wing tip (b).

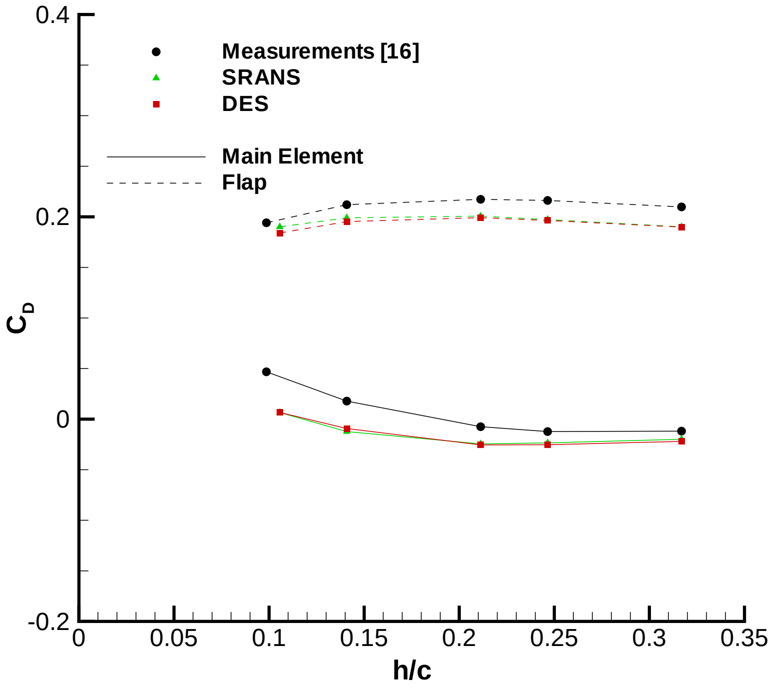

(a) Centrespan ($y/c = 0$).

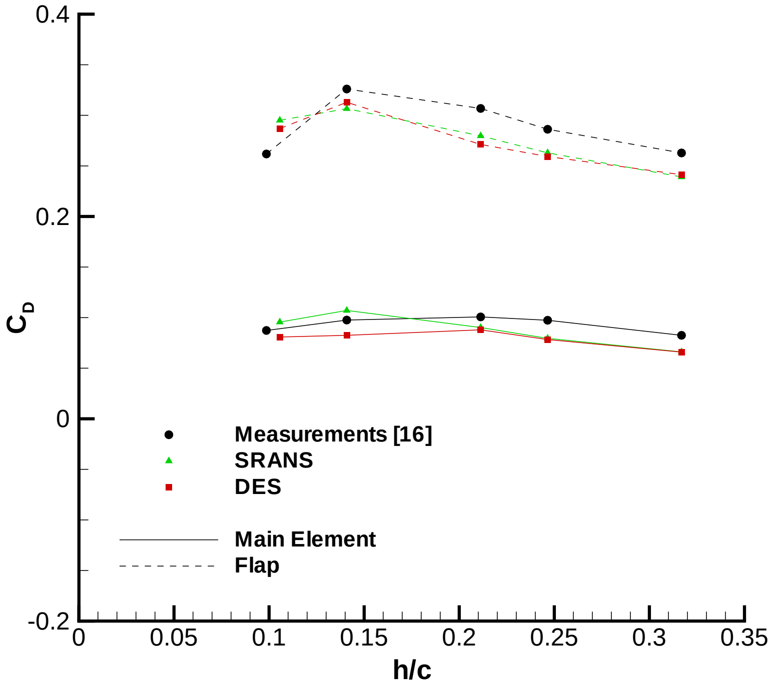

(b) Wing Tip ($y/c = -0.93$).

Figure 3.7: Variation of the sectional drag coefficient with ride height at the centrespan (a) and wing tip (b).

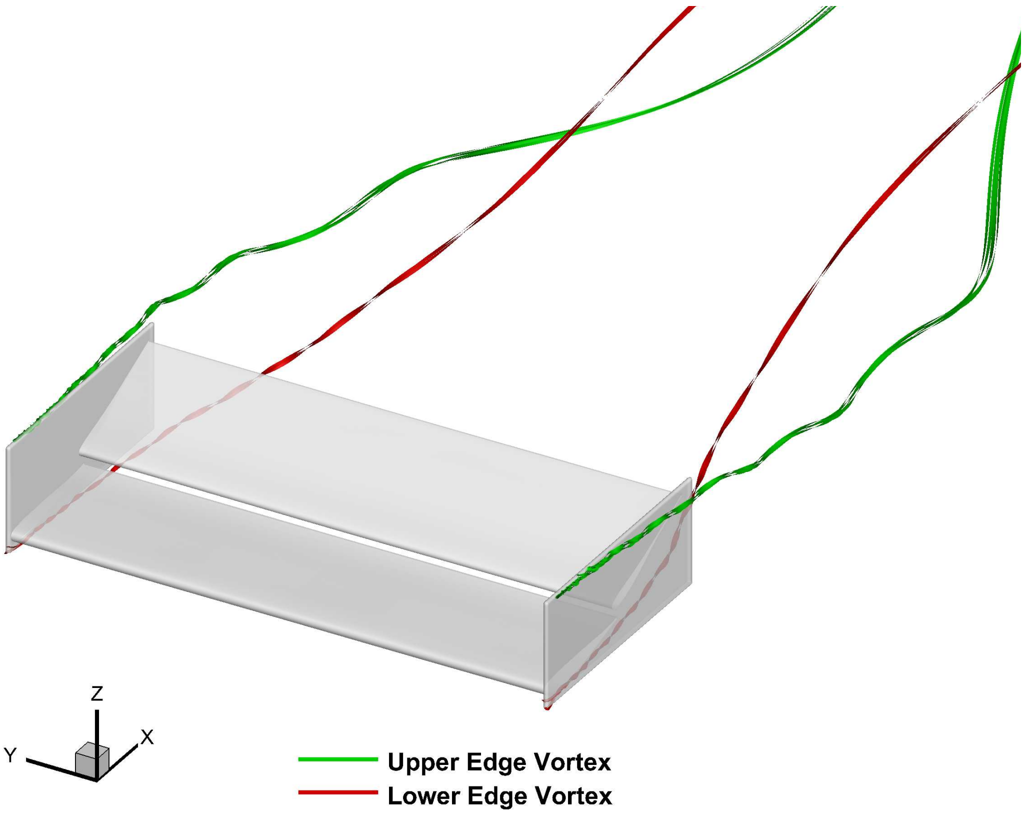

Figure 3.8: Sketch of the wing's upper and lower edge vortices.

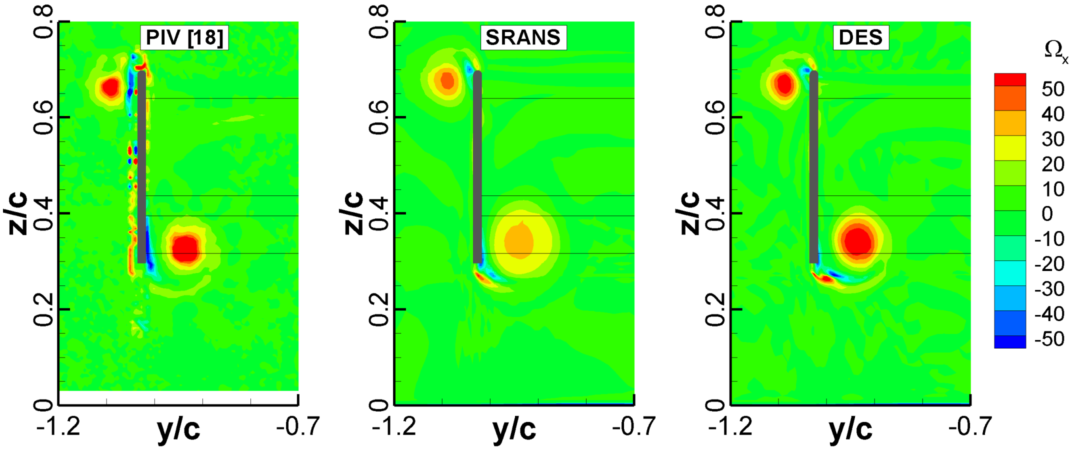

(a) $h/c = 0.317$

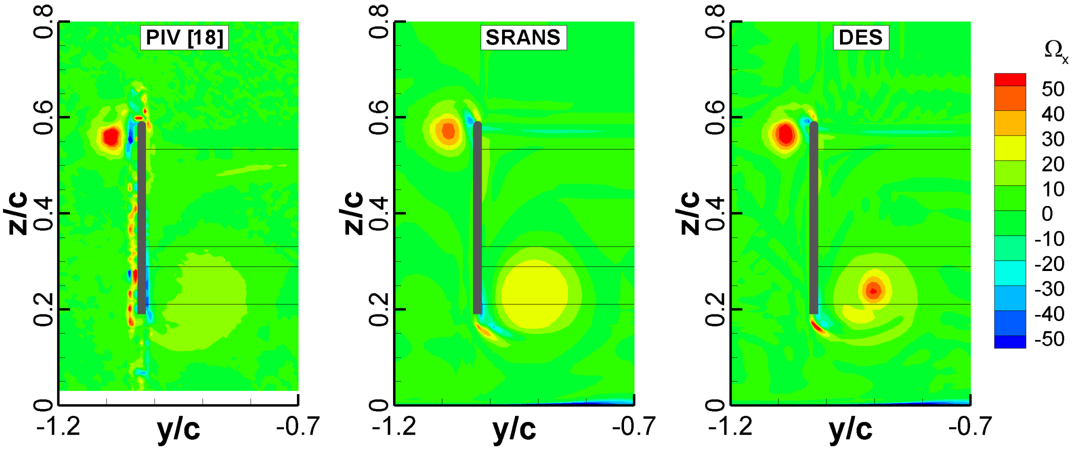

(b) $h/c = 0.211$

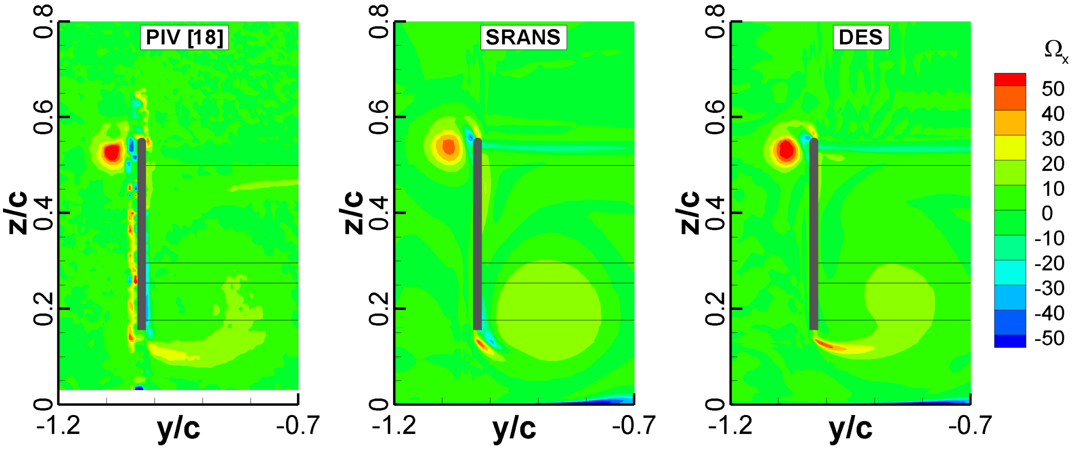

(c) $h/c = 0.176$

Figure 3.9: Comparison of the non-dimensional x-vorticity at the plane $x/c = 0.995$ for different ride heights. The outline of the wing is shown for reference purposes.

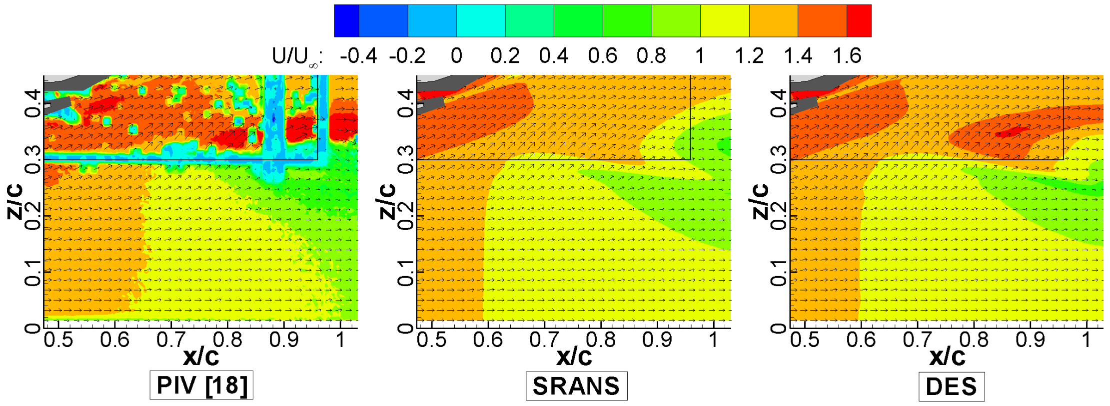

(a) $h/c = 0.317$

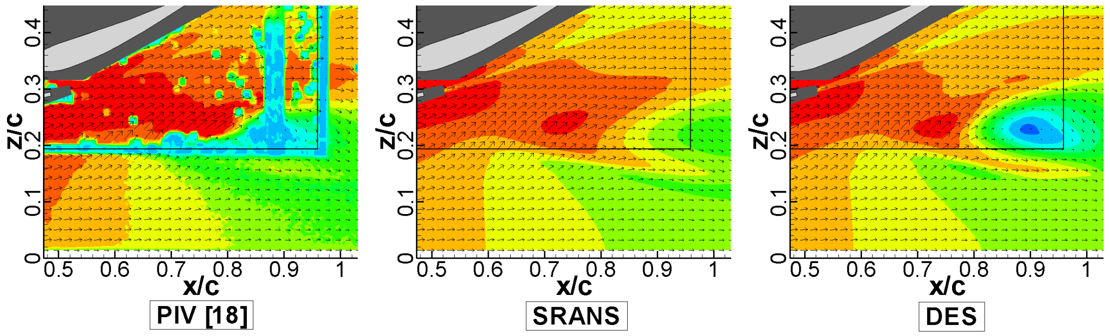

(b) $h/c = 0.211$

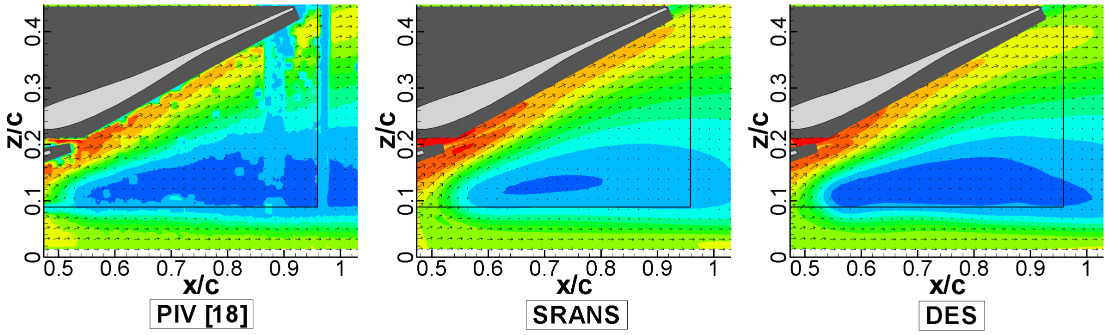

(c) $h/c = 0.106$

Figure 3.10: Comparison of the time-averaged streamwise velocity at plane $y/c = -0.933$ for different ride heights in the isolated wing case. The grey areas hide the zones which the PIV could not capture.

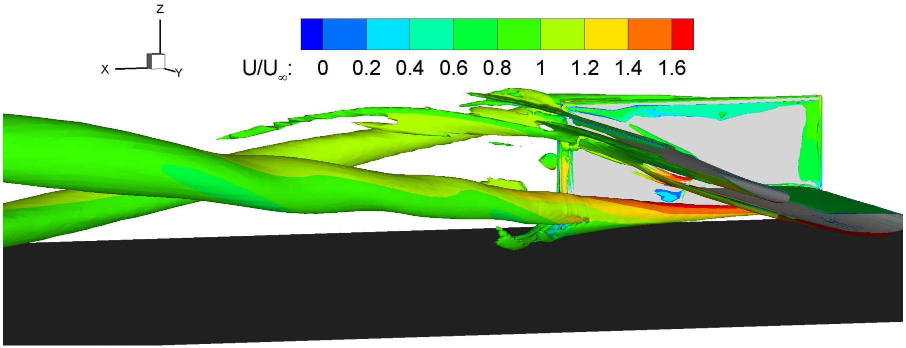

(a) $h/c = 0.317$

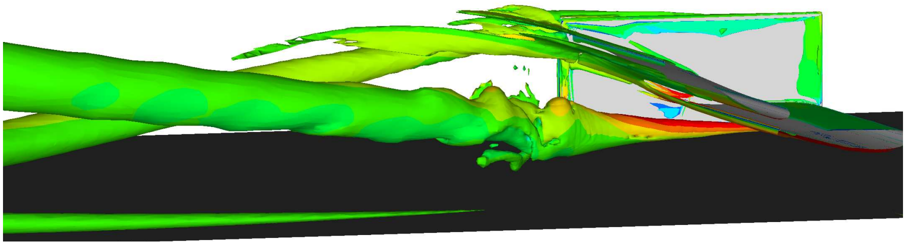

(b) $h/c = 0.246$

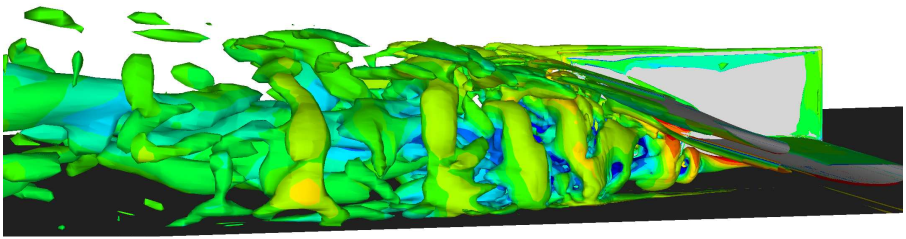

(c) $h/c = 0.106$

Figure 3.11: Iso-surface of the instantaneous Q-Criterion (Q=50000) for the wing at different ride heights. The iso-surface is coloured by streamwise velocity. The results are from the DES model.

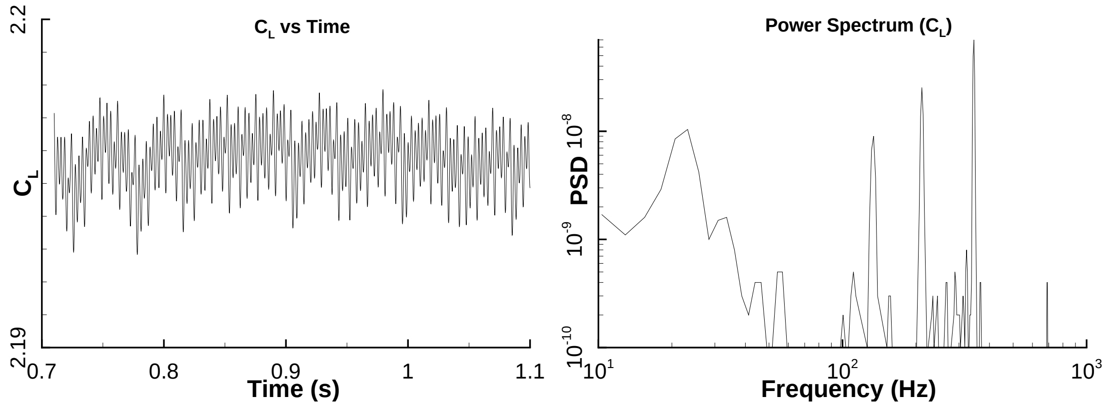

(a) $h/c = 0.211$

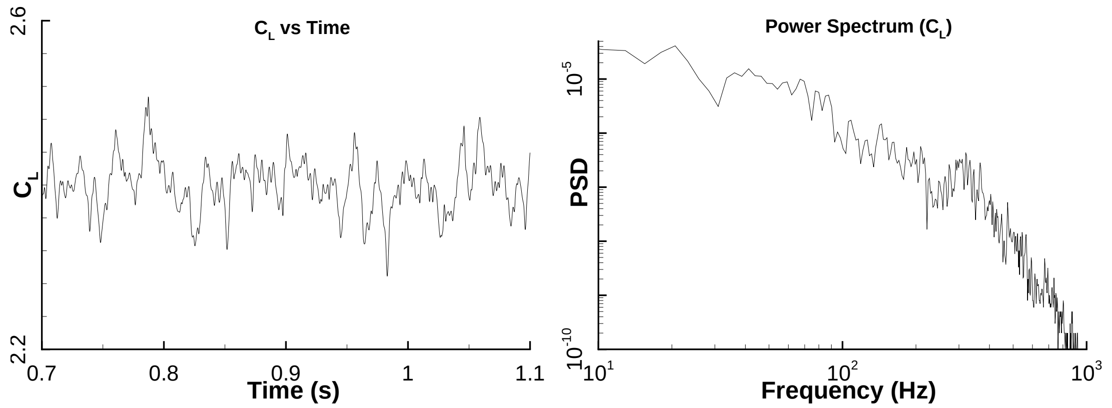

(b) $h/c = 0.106$

Figure 3.12: Time history and power spectral density of the wing downforce coefficient at two ride heights. The results are from the DES model.

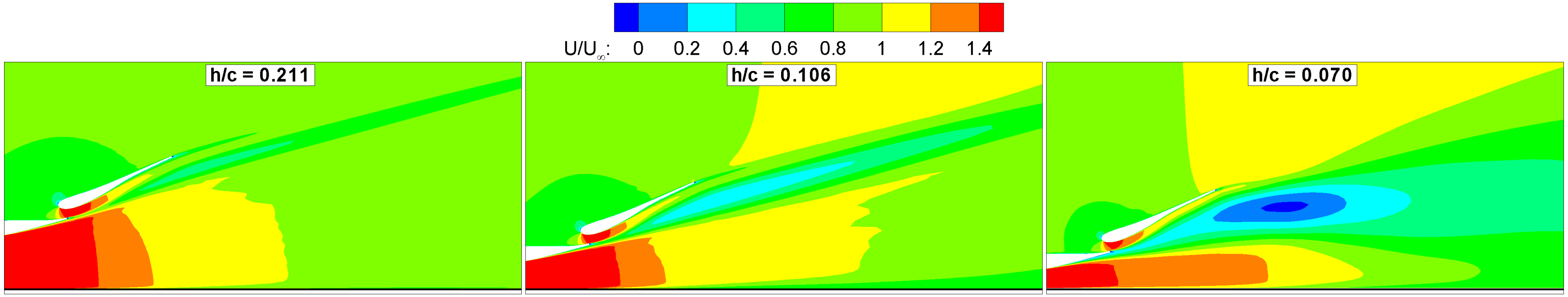

(a) Time-averaged streamwise velocity.

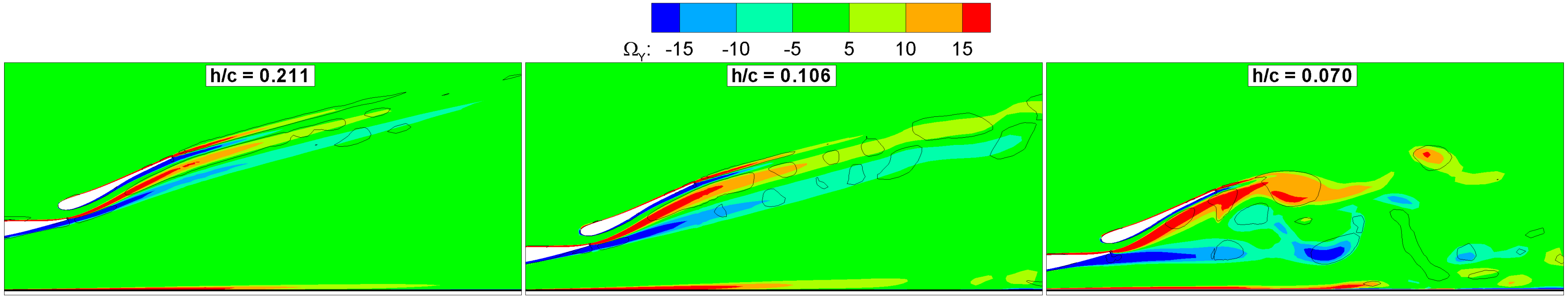

(b) Instantaneous Y vorticity.

Figure 3.13: Contour plot of the centrespan time-averaged streamwise velocity (a) and instantaneous y-vorticity with line contours of the Q-criterion (b) at three different ride heights. Results are from the DES simulation.

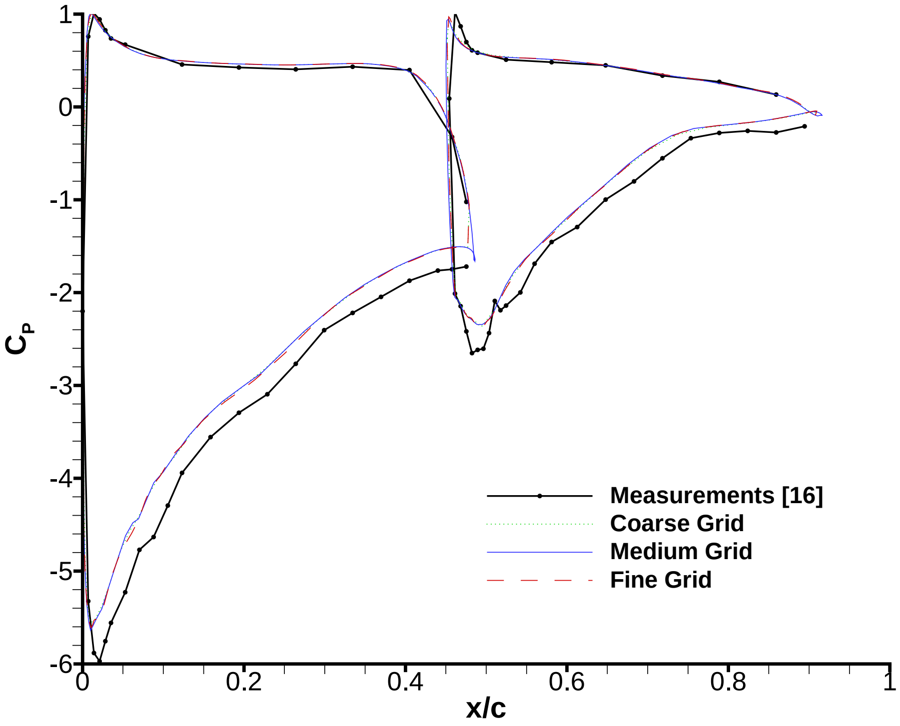

(a) Centrespan ($y/c = 0$).

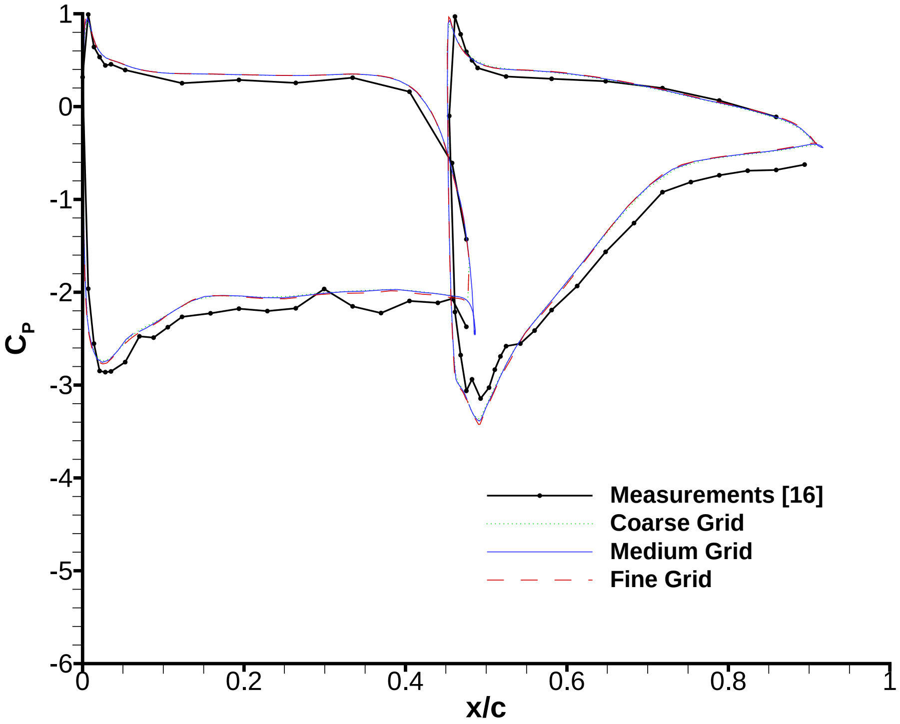

(b) Wing Tip ($y/c = -0.93$).

Figure 3.14: Pressure distribution at centrespan (a) and wing tip (b) for different grid sizes at a ride height of $h/c = 0.246$ predicted by the DES.

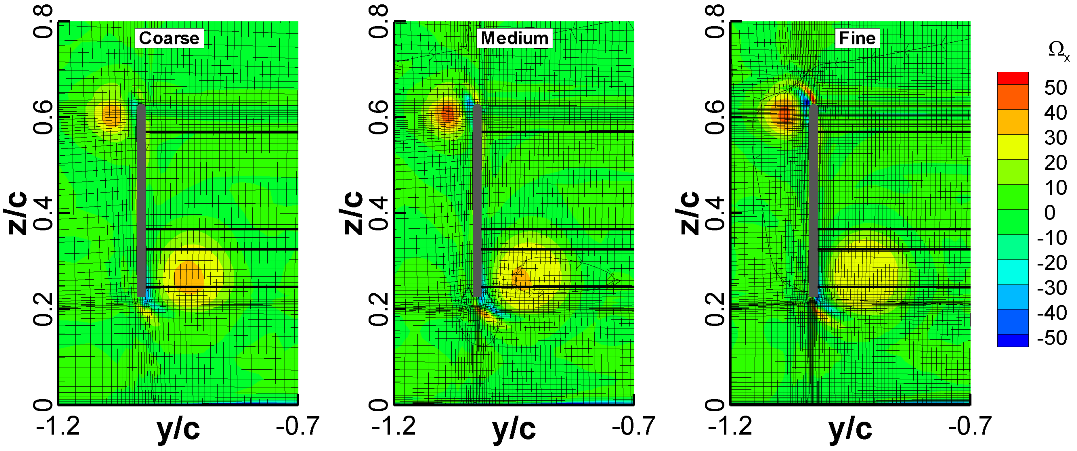

(a) SRANS.

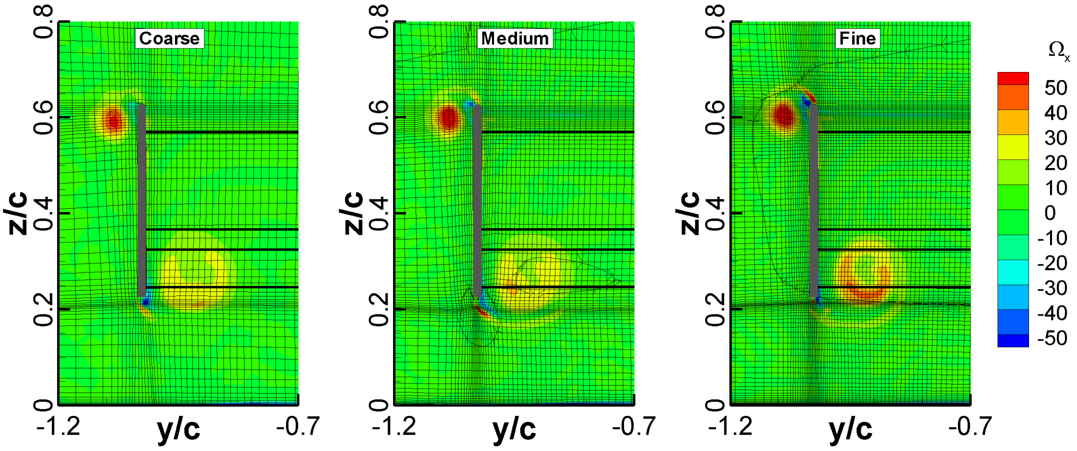

(b) DES.

Figure 3.15: Comparison of the non-dimensional x-vorticity at the plane $x/c = 0.995$ for different grid sizes at a ride height of $h/c = 0.246$. The outline of the wing is shown for reference purposes.

Chapter 4

Isolated Wheel

The flow around a wheel is complex, as it is both three-dimensional and unsteady, but studies have mostly focused on the time-averaged flow. This chapter investigates the aerodynamics of both a rotating and stationary wheel, making use of experimental and computational techniques. The capabilities of DES at resolving the wake is demonstrated and detailed descriptions of the three-dimensional flow for both the time-averaged and instantaneous solutions are given.

4.1 Rotating Case

In this section, the time-averaged and time-dependent characteristic around a rotating wheel are presented. For the time-averaged analysis, both experimental and computational results are used, whereas only DES results are used for the time-dependent analysis. All computational results are from the fine grid.

4.1.1 Time-Averaged Analysis

4.1.1.1 Surface pressure distribution

The surface pressure distribution around the wheel provides an insight into various flow features. Figure 4.1 shows the pressure around the centreline of the wheel tread (location P3), where a similar trend to previous studies [23, 25] is observed. Flow stagnation occurs approximately 5° below the foremost point and the large change in pressure at the contact patch, resulting from the pumping-like action of the moving surfaces, is clearly observed. The pressure oscillations measured by Mears et al. [25] behind the contact patch are not reproduced, neither experimentally nor computationally, and it is believed that these were caused by instrumental error. The flow separates[1] from the top of the wheel at approximately 274° and is followed by a drop in pressure.

The CFD shows qualitative agreement, as both SRANS and DES predict a similar pressure distribution. The pressure peaks around the contact patch are predicted to be larger, and this is associated to a limitation of the experiment which has a lower resolution around the wheel. The main disagreement between the results is around the separation point ($240° < \theta < 290°$), where the CFD underpredicts the suction. Separation is predicted at 275° by both numerical methods and the DES captures a drop in pressure after it. It is surmised that this drop in pressure is due to instantaneous vortical structures from the wake being entrained upstream by the moving surface of the rotating wheel, and the DES is better equipped to capture those structures. On the other hand, the DES shows no benefit compared to SRANS around the front of the wheel where the flow is attached and steady.

Figures 4.2 and 4.3 compare the pressure distributions at the two other locations on the tread, close to the tyre shoulders. There is no stagnation point at these locations (although the maximum local pressure still occurs at approximately 5°) as the flow travels in the spanwise direction due to the wheel's low aspect ratio. Investigating the pressure distribution over the lower front of the wheel ($0° < \theta < 90°$), it can be seen the high pressure peak observed at location P3 is not present at P4, while P2 only shows a slight increase. This is because the wheel surface at these two locations, especially at P4, is not in full contact with the ground, as they are so close to the tyre shoulders. Therefore, the pressure drops to negative values as the flow accelerates around the wheel and through the gap between the ground and wheel surfaces. The discrepancy seen between the experiment results and CFD in this region for P2 is due to the difference in tyre geometry which was discussed in Section 2.1. The wheel used in the CFD has shoulders with smaller radii and therefore the tread is in contact with the ground at P2, resulting in the high pressure peak.

The flow separation appears to be constant along the tread, staying at approximately 275°, and the pressure in the wake stabilises at around $Cp = -0.5$. The CFD once again underpredicts the suction around the top of the wheel, with negligible difference between the SRANS and DES except downstream of flow separation. The separation from the top of the wheel can also be observed from Figure 4.6, although its exact location cannot be found with PIV due to the wheel camber obstructing the camera view. The underprediction in velocity upstream of flow separation by the CFD compared to that of the PIV does not correspond to the large discrepancy in surface pressure observed earlier.

---

[1] The separation location is defined as the point where the pressure gradient becomes zero reaching a local maxima.

This could be a result of the different wheel geometry used to obtained the pressure data or could be due to errors in the pressure measurement system. Nevertheless, the main interest lies in the qualitative pressure distribution and it is believed to be accurately reproduced.

The results of the last two pressure locations are shown in Figures 4.4 and 4.5. These are located on the sides of the wheel and therefore the pressure distribution has little effect on downforce and drag. In the experimental results, the presence of the wheel support strut will affect the pressure distribution at P5, as it causes blockage, creates a wake and deflects the flow if not locally aligned. The lower suction at 0° observed at location P5 and not present at P1 is believed to be associated to the blockage of the support strut. This is further emphasised by the CFD, which does not model the support strut and predicts similar pressure distributions for both locations, with any difference associated to the wheel asymmetry due to its camber. Where the flow is mostly attached and steady, the SRANS and DES simulations predict similar pressure distributions on the tyre shoulder between $270° < \theta < 90°$. The discrepancy between the two models increases around $\theta = 180°$, as the region is affected by changes in the wheel wake prediction.

The computations underpredict the flow acceleration around the tyre, as can be seen in Figure 4.7, resulting in the higher pressure observed at P1. It is noted that the CFD underpredicts the velocity around P1 by $4.8m/s$, which equates to a difference in Cp of 0.5, whereas at 0° in Figure 4.4, the difference in Cp between the experiment and the CFD is 0.7. This discrepancy is believed to be associated with the different wheel geometry used to obtain the pressure data in the experiments, where a different shoulder profile with a more aggressive curvature causes a larger flow acceleration around the tyre resulting in a lower pressure.

A feature experimentally found at P1 but not present at P5 (see Figures 4.4 and 4.5) is the local pressure maxima at $\theta = 180°$, which is caused by local flow separation from the tyre shoulder. The slower flow coming from the wake of the support strut is believed to reduce the separation at location P5, resulting in the different trend. The CFD does not predict this local pressure maxima, instead predicting more suction, which approaches the level seen at $\theta = 0°$. As mentioned above, the experimental wheel used for pressure measurements had a different shoulder profile which is more prone to flow separation due to its different curvature. This is emphasised by comparing the flow velocity measured with PIV (which uses the same wheel geometry as the CFD) around the tyre shoulder at plane $Z = 0.55D$, shown in Figure 4.8, where the pressure probe P1 is at $\theta = 190°$. The PIV and DES results are qualitatively similar, with no significant difference in flow velocity around the location P1 that could explain the Cp discrepancy at $\theta = 190°$ seen in Figure 4.4.

4.1.1.2 Wheel wake

Observing the flow behind the wheel's centreline (see Figure 4.6), the wake can be separated into two regions: an upper wake and a lower wake. The lower wake extends further downstream, as a consequence of the ground presence and jetting effect underneath the front of the wheel. Downstream of the flow separation from the top of the wheel, the shear layer diverts downwards toward the ground. The CFD does not accurately capture this feature, predicting a taller and longer wake, although this is much more evident for the SRANS simulation. The DES captures the lower wake accurately and also shows a good qualitative agreement with the PIV for the upper wake, even though some differences are present.

Plane $Z = 0.55D$ cuts through the upper recirculation region and this can be seen in Figure 4.8. The flow accelerates around the tyre edge, separating when it cannot further sustain the adverse pressure gradient. The recirculation region is concentrated around $Y = 0D$, in agreement with the inverted-T wake observed by Saddington et al. [34]. Both CFD methods correctly predict the attached flow around the wheel edge, but the SRANS fails to capture the wake adequately. It predicts an early separation, a much smaller recirculation region and a thinner wake. On the other hand, the DES predicts the wake profile with good accuracy, showing the capabilities of this method for bluff body studies.

From the qualitatively accurate results of planes $Y = 0D$ and $Z = 0.55D$, using the DES streamwise velocity to correct for the PIV parallax error in plane $X = 0.6D$ (see Appendix B) is believed to be justified. Saddington et al. [34] described two counter-rotating vortex pairs at this position behind the wheel and the same structures are observed in this study, as shown in Figure 4.9. There is downwash behind the centre of the wheel and a vortical structure is present in each wheel quadrant. Once again, it is seen how the SRANS model does not capture the wake adequately, predicting an upwash instead of downwash, with a much stronger crossflow. It is of interest to note that other simulations of a rotating wheel using RANS [32, 41] correctly predicted downwash, but this was not reproduced in this study despite various attempts. The different grid [32] or geometry [41] are believed to be the cause for this inconsistency. The DES results compare qualitatively very well to the PIV and show a near symmetric wake about the wheel centreline. From this, it is deduced that the asymmetry present in the PIV is caused by the support sting (which is not present in the simulations) and the wheel camber only has a small effect on the wake.

It has been shown that DES can accurately capture the flow features around a rotating wheel and further insight into the flow can be obtained from this simulation. Experimental flow visualisation gives a two-dimensional view, which can be difficult to interpret. From LDA results [34], the upper vortex pair in the wheel wake was interpreted as merging with the lower vortex pair further downstream of the wheel. Using Figure 4.10, which displays iso-surfaces of the Q-Criterion to visualise the wake, an alternative description is given. The flow around the upper half of the wheel separates as it reaches the wheel edge and recirculates upstream (label B in Figure 4.10). A plane at $X = 0.6D$ cuts through this recirculation and has lead to its interpretation as a longitudinal vortex. Further downstream, this flow structure is not present, explaining the disappearance of the upper vortex observed in experiments [34]. On the top of the wheel the flow separation and the recirculation region which follows is clearly visible (label A in Figure 4.10). Structures A and B together form the arch-shaped separation vortex as described in Ref. [41].

Looking at the lower part of the wake, another area of recirculation (C in Figure 4.10) is observed. Once again, a plane cutting through this flow structure produces a velocity field which has been interpreted as being a longitudinal vortex. This is seen not to be the case, as the streamlines shown in Figure 4.10 originate from the other side of the wheel, swirl toward the ground and finally move downstream. Another observed feature is the separation of the flow as it moves around the lower front of the wheel (D in Figure 4.10). The jetting effect causes the flow to exit from underneath the wheel with a high transversal velocity, which is rapidly diverted downstream by the oncoming flow, and results in a free shear layer as it cannot stay attached to the wheel surface due to the adverse pressure gradient. Therefore, there is a region of recirculation in this area creating a lower wake larger than the wheel width, as has been observed in previous studies.

Although a three-dimensional description of the wake has been given, it is still hard to interpret the behaviour of the flow due to its unsteady nature, where the time-averaged streamlines do not represent the path the flow necessarily takes. An investigation of the instantaneous flow field is desired to further understand the rotating wheel's wake.

4.1.2 Unsteady Flow Analysis

A plot of the instantaneous Q-Criterion (Figure 4.11) shows a very different wake profile compared to that of the mean flow, with many smaller vortical structures present. The arch-shaped separation vortex which was observed in the time-averaged flow is composed of smaller shed vortices (A and B in Figure 4.11). The power spectral density of the pressure fluctuations measured at monitor 1 (see Figure 4.11) is shown in Figure 4.12(a). There is a broadband peak around $f = 180Hz$ which is associated to the shedding frequency of the aforementioned vortices. There is also a lower frequency peak at $f = 9Hz$ which is caused by a transient motion of the separation point on top of the wheel.

New structures not visible from the time-averaged flow are observed in the lower wake. The flow separation from the lower front of the wheel creates a periodic shedding of vortices transverse to the flow direction (C in Figure 4.11), with one end on the wheel surface and the other end on the ground. These vortices are transported downstream where they are quickly absorbed in the wake (D in Figure 4.11) and dissipate. The PSD from a pressure monitor near the lower side of the wheel (labelled 2 in Figure 4.11) is shown in Figure 4.12(b). The monitor is located within the path of the shed vortices, just downstream of their appearance. The power spectrum is broadband with a high frequency peak at $f = 300Hz$ and the lower wake vortex shedding is associated to this frequency. Using a pressure monitor on the other side of the wheel, the vortex shedding on each side was found to be uncorrelated at the shedding frequency, having different dominant frequencies. This is a result of the wheel camber and its asymmetry, which has a significant influence on the flow around the lower edges of the wheel.

The wake is seen to contain vortical structures of different sizes and orientations, although many have a longitudinal orientation. Particle paths were visualised through time after being emitted around monitor 2. The vortex shedding in that area was clearly visible, followed by the particles dispersing in the wake. When the particles entered the recirculation zone behind the wheel, their path was random, but once they traveled downstream they had a slow longitudinal swirling motion. This could have been induced by the downwash behind the wheel, with the presence of the ground then forcing the flow to divert sideways, starting the swirling motion.

The time history of the wheel downforce and drag coefficients was recorded during the length of the simulation. They experience large changes over time, as is seen in Figures 4.13 and 4.14. The wheel is at all times producing lift, with dominant low frequency fluctuations ($f = 8Hz$ and $15Hz$) as found from the power spectrum. These low frequencies are believed to be associated to two separate effects: the flow separation on top of the wheel, as its location and the subsequent free shear layer are unsteady and oscillate; the lower recirculation bubble which exhibits low frequency changes. It must be noted that the value of this low frequency has not converged and a more accurate result would require further simulation time. The fluctuations in wheel drag are more broadband with no clear dominant frequency, which is a reflection of the range of spatial scales that exist in the wake behind the wheel, as was seen in Figure 4.11. Neither the downforce and drag coefficients are dominated by high frequencies which are associated to the various vortex sheddings identified. This is because the shedding from the top of the wheel is relatively weak whereas the shedding around the lower edge of the wheel mainly affects the side force.

4.1.3 Grid Sensitivity

The effect the grid resolution has on the computed solution was investigated using a coarse, medium and fine grid. It is noted that the timestep in the DES simulations was also modified accordingly in order to keep similar CFL values. The force coefficients for the different grids are presented in Table 4.1. The SRANS simulations predict a lower drag as the grid is refined, with a reduction of around 2% with each step. It is interesting to note that the drag predicted with the coarse grid is closest to the experimental value, emphasising the innacurate representation of simulation validity by aerodynamic forces alone and the requirement of additional data validation. The DES, on the other hand, predicts a higher value of drag as the grid and timestep is refined. The difference between the medium and fine grid is only 0.5%, but caution is required before interpreting this as solution convergence. For example, the downforce coefficient does not appear to converge to a solution, as the fine grid predicts 51% more lift than the medium grid. Unfortunately, no experimental lift value is available for comparison, but analysing the pressure distribution on the tread (Figure 4.1), it can be deduced that the simulations underpredict the lift. A common problem with grid sensitivity studies involving DES is that, conversely to SRANS, a finer grid will not only reduce the discretisation error but will also resolve finer scales of motion as is apparent in Figure 4.15.

Although the correct prediction of the wheel forces is important it might be misleading and the accurate prediction of the wake is also a priority. Figure 4.16 compares the wake profile at the plane $X = 0.6D$ for the three grids. It can clearly be seen that the SRANS simulation incorrectly predicts the wake, with little change between the three grids, even though the wheel drag compared well to the experimental value. The DES experiences more change as the grid is refined, with the solution converging toward the PIV results shown in Figure 4.9. The velocity vectors are shown with a uniform length for the purpose of clarity, but it is of interest to note that the vertical velocity (W) also converges toward the experimental PIV results, with a stronger downwash behind the wheel predicted as the grid is refined.

Overall, the fine grid for the DES was found to predict qualitatively accurate results, and is a good compromise between computational cost and the quality of results. If additional resources were available, a finer grid would be expected to further improve on the accuracy.

4.2 Stationary Case

In this section, the time-averaged and time-dependent characteristic around a stationary wheel are presented and compared to the rotating wheel. Although the flow around a stationary wheel is not representative of a real life scenario, it is still of interest as it gives an insight into the effect of rotation. Less experimental results are available for the stationary case and the CFD results provide the basis for the analysis. All computational results are from the fine grid.

4.2.1 Time-Averaged Analysis

4.2.1.1 Surface pressure distribution

The pressure distribution around the stationary wheel is very different from that of a rotating wheel. Comparing the results[2] obtained on the tread, at location P3 (Figure 4.17), a similar trend as that observed by Fackrell 1.3 is found. The flow around the front of a stationary wheel is similar to a rotating wheel, where a stagnation point is followed by a decrease in pressure as the flow travels above or below the wheel (it is noted that the stagnation point is still located at approximately 5°, contrary to the change observed by Fackrell). The similarity of the flow travelling downwards ends as it approaches $\theta = 90°$, where the high and low pressure peaks around the contact patch no longer exist due to the wheel and ground surfaces now being stationary.

The flow travelling above the wheel differs from that around a rotating wheel at $\theta = 310°$. The pressure does not stop decreasing as the flow stays attached over the top, and this is followed by a region of pressure recovery, until the flow separates at around $\theta = 225°$. The pressure continues to recover aft of this, until it reaches a local maximum of $Cp \approx -0.1$ at $\theta = 200°$, after which the pressure drops rapidly. Figure 4.19(b) gives some insight into what is happening in this region. After the flow separates, it is pushed downwards by the strong downwash present behind the wheel centreline, and consequently reattaches to the surface at $\theta = 205°$. Although this is predicted by the CFD, the PIV does not show this phenomena, instead appearing to stay attached for longer around the wheel.

---

[2] No pressure measurements for the stationary wheel are available. The plots compare the pressure measurements around a rotating wheel to simulations of a stationary wheel.

Further outboard on the tread, the pressure distribution around the front of the wheel once more has similarities with a rotating wheel. Compared to P3, flow separation is clearly distinguishable at $\theta = 228°$ and there is no subsequent reattachment. The base pressure settles at a lower value than for the rotating case, which results in a higher drag (see Table 4.2). In addition, a stationary wheel produces more lift due to the higher suction over the top of the wheel as the flow stays attached.

The two CFD methods predict a similar tread pressure distribution. The separation and reattachment observed at location P3 is close to the tyre wall and is resolved using the S-A RANS model. Therefore, the use of DES does not significantly affect the predicted separation. The main differences between the two models are after separation has occurred behind the wheel, emphasising that the benefits of using DES lie within massively separated flows.

The pressure on the side of the wheel, at location P1 (Figure 4.18), drops as the flow travels around the front ($\theta = 0°$) and the rear ($\theta = 210°$). The location of this minimum pressure at the rear is different compared to a rotating wheel ($\theta = 180°$). Close to the ground the pressure is higher, which is a direct result of the boundary layer which forms on the stationary ground.

4.2.1.2 Wheel wake

The streamwise (Figure 4.19(a)) and vertical (Figure 4.19(b)) velocity behind the wheel at plane Y=0D offer a good description of the wake. The wake of a stationary wheel is fundamentally different from a rotating wheel. Flow reversal is now contained within a small region behind the lower part of the wheel, as the flow stays attached around most of the upper part, which also results in the wake being vertically shorter (less than the wheel height), as had been observed by Fackrell [24]. The wake is also composed of a strong downwash which persists up to 1.5D behind the wheel centreline.

These PIV results also allow the CFD to be analysed. As mentioned earlier, the boundary layer separation is predicted too early by both CFD models, leading to some inaccuracies in the upper near wake. But the DES still predicts the lower wake and far wake with very good precision. Similarly to the rotating wheel, the DES is able to accurately capture the wake profile, therefore allowing further analysis of the wake using the CFD results.

From Figure 4.20, the wake is seen to be composed of a strong downwash directly behind the tyre, and of a vortical structure (labelled A) created by entrained flow from the side of the tyre. The origin of this vortical structure corresponds to the low pressure observed at

$\theta = 210°$ from location P1. The composition of the upper wake is significantly different to what was observed for a rotating wheel, which is a result of the difference in boundary layer separation. As the flow separates earlier for the rotating wheel, there is not such a strong downwash behind the wheel which in turn does not entrain the flow from the wheel sides in the same way.

The lower wake, around the side of the wheel (B in Figure 4.20) is seen to be more comparable to that found with a rotating wheel. One visible difference is the wider expansion the flow experiences. As the pressure at the front of the contact patch does not peak at very high pressures, the transversal velocity of the flow exiting through underneath the wheel is lower (approximately $5m/s$ less) and therefore, the lower wake would be expected to be thinner. But there is less energy in the oncoming flow due to the boundary layer that has developed on the stationary ground, resulting in a slower dissipation of the transversal velocity and in a wider lower wake.

4.2.2 Unsteady Flow Analysis

When considering the instantaneous wake behind the stationary wheel, shown using the Q-Criterion in Figure 4.21, the differences compared to the mean wake are less significant than for the rotating wheel. The vortical structure coming from the tyre shoulder is clearly visible (A in Figure 4.21), although it is seen to quickly dissipate in the lower wake. The region of flow reversal previously observed in Figure 4.19(a) is composed of many vortical structures of various sizes and orientations. Vortex shedding is still apparent in the lower wake (B in Figure 4.21), originating from beneath the front of the wheel in a similar to that described for a rotating wheel. These vortices interact with the vortical structure from the tyre shoulder, and contribute to changes in the wheel lift and drag.

Figures 4.22 and 4.23 show that the fluctuations in the stationary wheel forces have similar amplitudes to that observed for a rotating wheel, even though the wakes differ significantly. For the stationary case, the lower half of the wheel is responsible for the unsteady fluctuations. The lift has a dominant frequency, which is clearly visible in the signal, of approximately $70Hz$ and it is believed to be correlated to the shed vortices from the lower side of the wheel.

4.3 Sensitivity to Freestream Velocity

An aspect which has not been studied before is the effect velocity has on the wheel aerodynamics. Apart from a change in Reynolds number, changing the flow velocity will also result in a different wheel rotation speed. The study of the stationary wheel has shown that the rotation has a large effect on the flow characteristics, promoting earlier separation and modifying the wake. In addition, as the wheel pressure measurements obtained by Van den Berg [18] were at a slower velocity, it is of interest to investigate if those results are valid for comparison to the CFD simulations.

The change in wheel drag force coefficient with varying Reynolds number is shown in Figure 4.24 for both a stationary and rotating wheel. This once again confirms how a stationary wheel produces more drag and it is further noted that for the stationary case, the drag coefficient stays within 1% of the baseline value (at Re$= 6.4 \times 10^5$) throughout the range of Reynolds numbers. This suggests that for this range of velocities, the flow characteristics are not significantly affected. For the rotating case on the other hand, the drag coefficient drops by nearly 5% at the lower Reynolds number, whereas it stays within 1% for Re$> 4.0 \times 10^5$.

Figure 4.25 shows the changes which occur in the wake behind the center line of a rotating wheel for three different testing velocities. There are only very small differences between the two higher velocities, agreeing with the drag coefficient trend which shows a difference of less than 1%. It is of interest to mention that, considering these observations, the wheel pressure data obtained at a slower velocity of $20m/s$ should be qualitatively similar to results at $30m/s$.

For the lowest velocity (Re$= 2.1 \times 10^5$), the wake shows some clear differences. The separation from the top of the wheel occurs later, and as a consequence the wake is shorter (in the Z direction). The two areas of recirculation (upper and lower) are more distinct, and the lower wake is now slightly longer. From these observations it can be concluded that, whereas the stationary wheel results do not change significantly for this range of velocities, the added effect of rotation increases the sensitivity of the separation position and wake profile to the freestream velocity.

Table 4.1: Summary of the wheel aerodynamic force coefficients for the various grid sizes.

	C_D		C_L	
	SRANS	DES	SRANS	DES
Coarse Grid	0.601	0.566	-0.094	-0.106
Medium Grid	0.591	0.572	-0.097	-0.095
Fine Grid	0.579	0.575	-0.107	-0.144
Experiment [18]	0.598		-	

Table 4.2: Summary of the wheel aerodynamic force coefficients for the stationary wheel.

	C_D	C_L
SRANS	0.671	-0.581
DES	0.717	-0.544
Experiment [18]	0.711	-

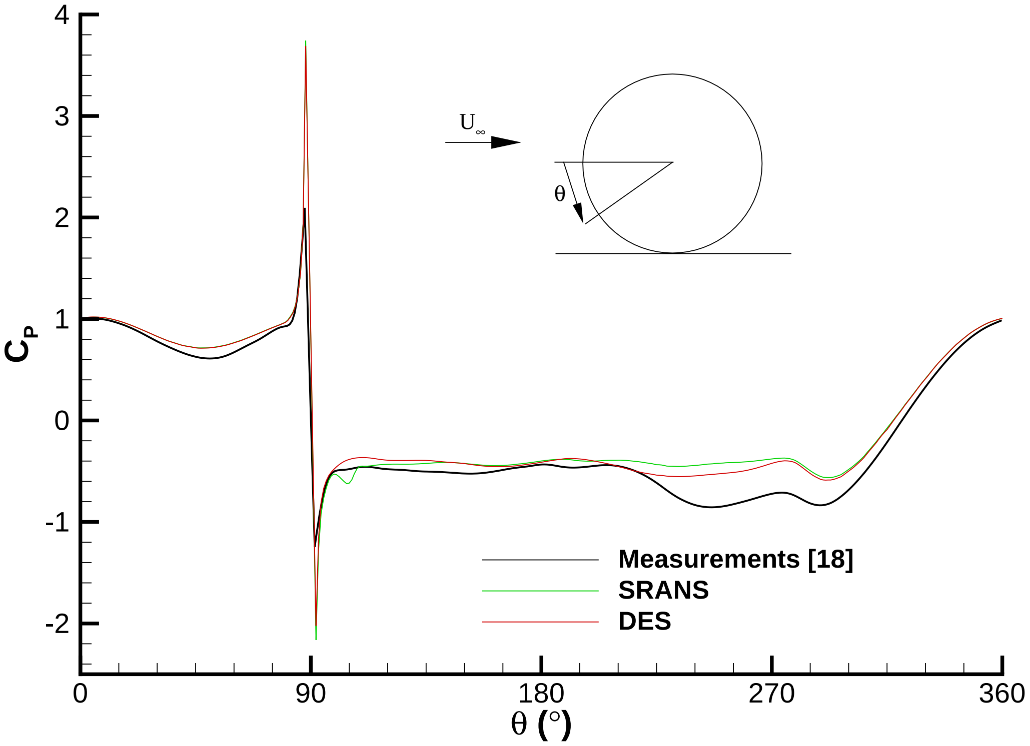

Figure 4.1: Experimental and computational pressure distribution around the rotating wheel centreline P3.

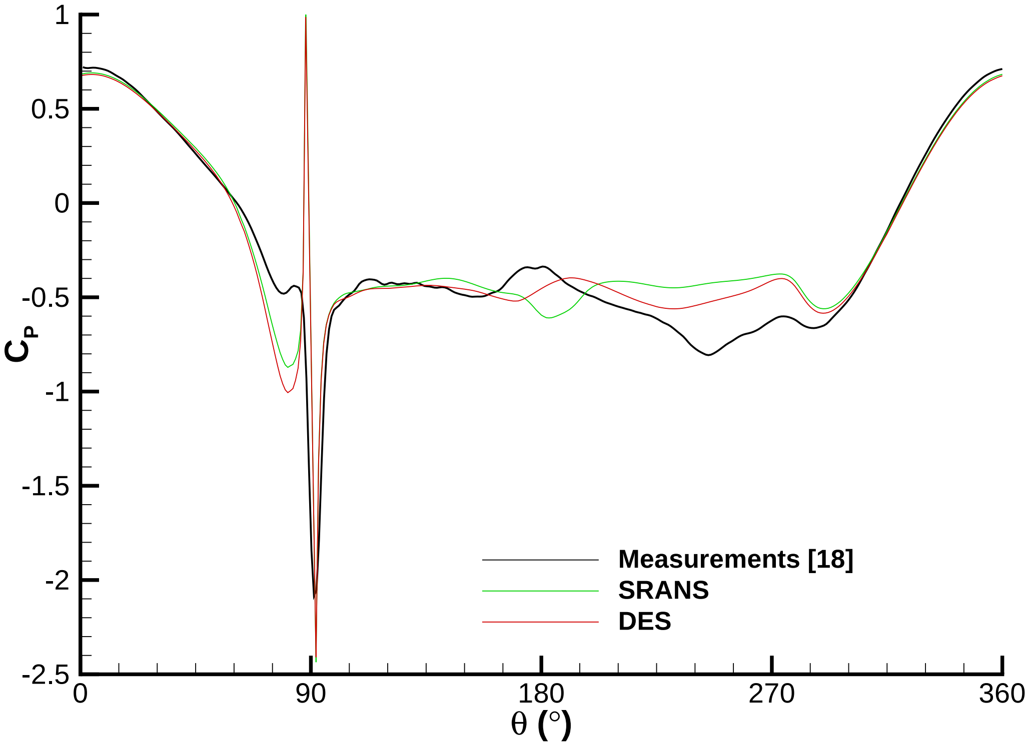

Figure 4.2: Experimental and computational pressure distribution around the rotating wheel at location P2.

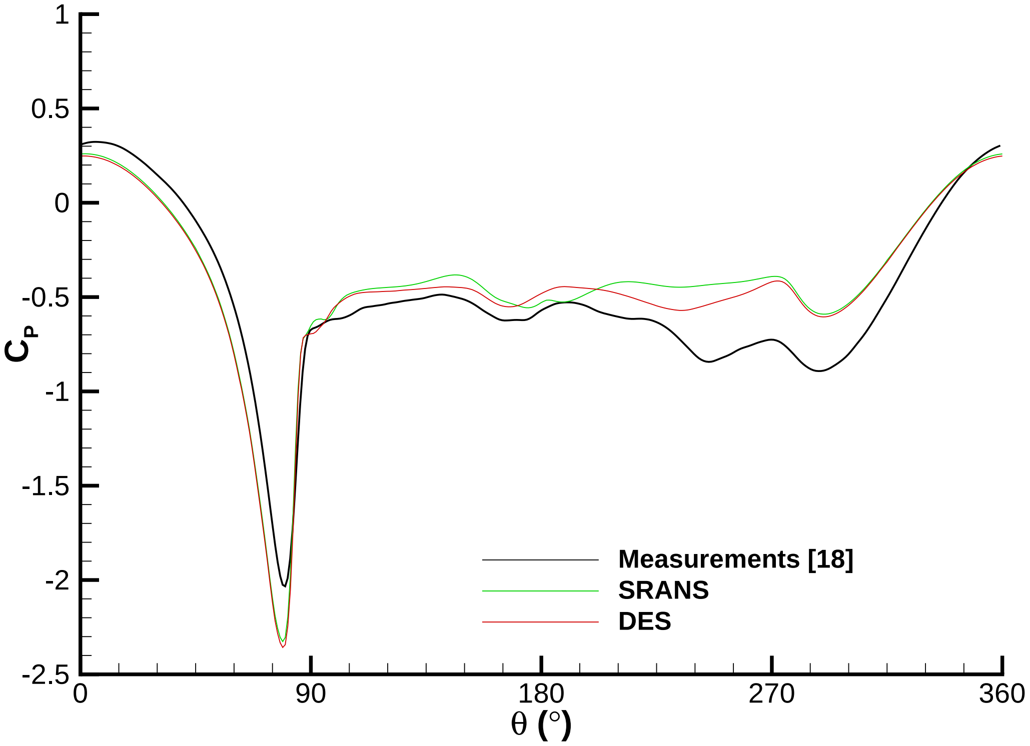

Figure 4.3: Experimental and computational pressure distribution around the rotating wheel at location P4.

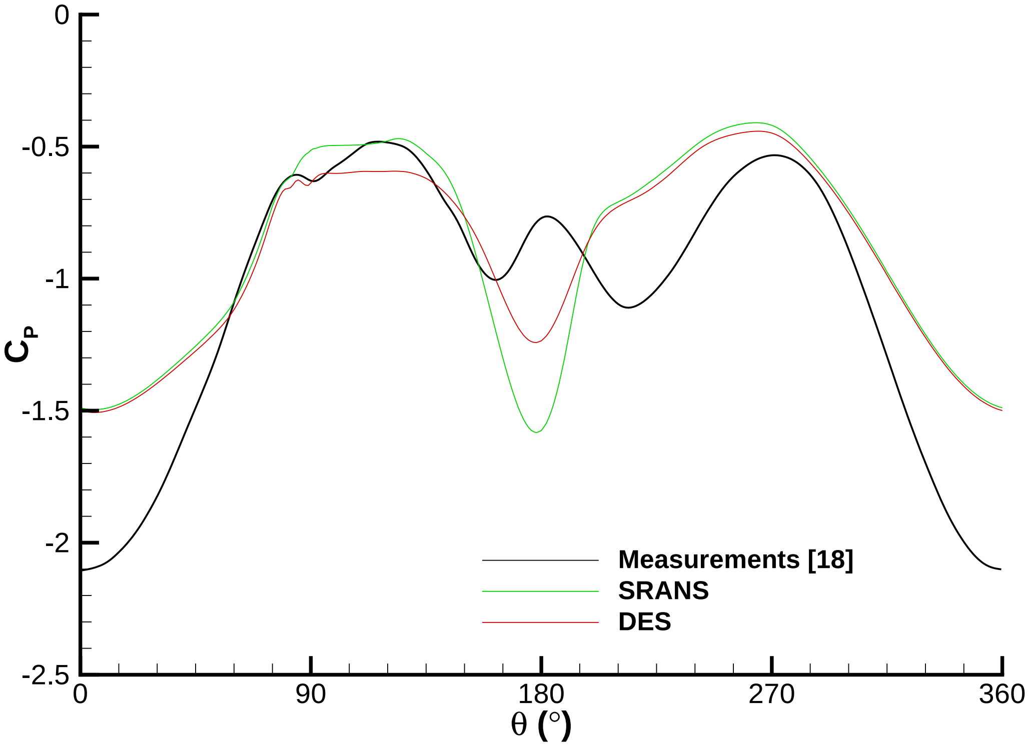

Figure 4.4: Experimental and computational pressure distribution around the rotating wheel at location P1.

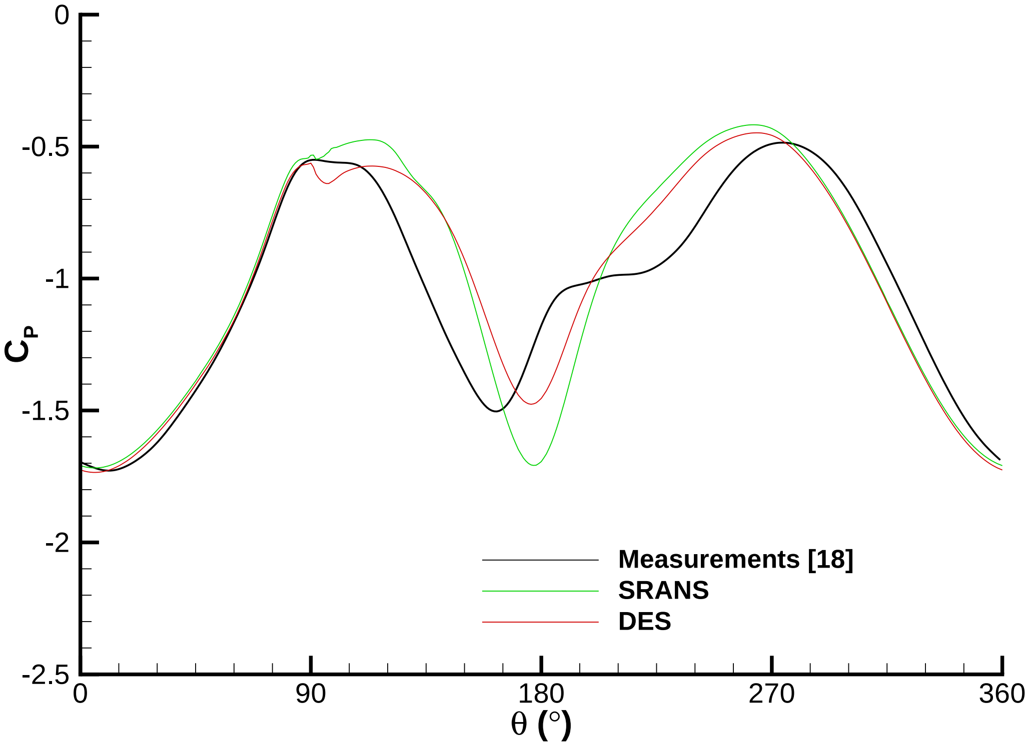

Figure 4.5: Experimental and computational pressure distribution around the rotating wheel at location P5.

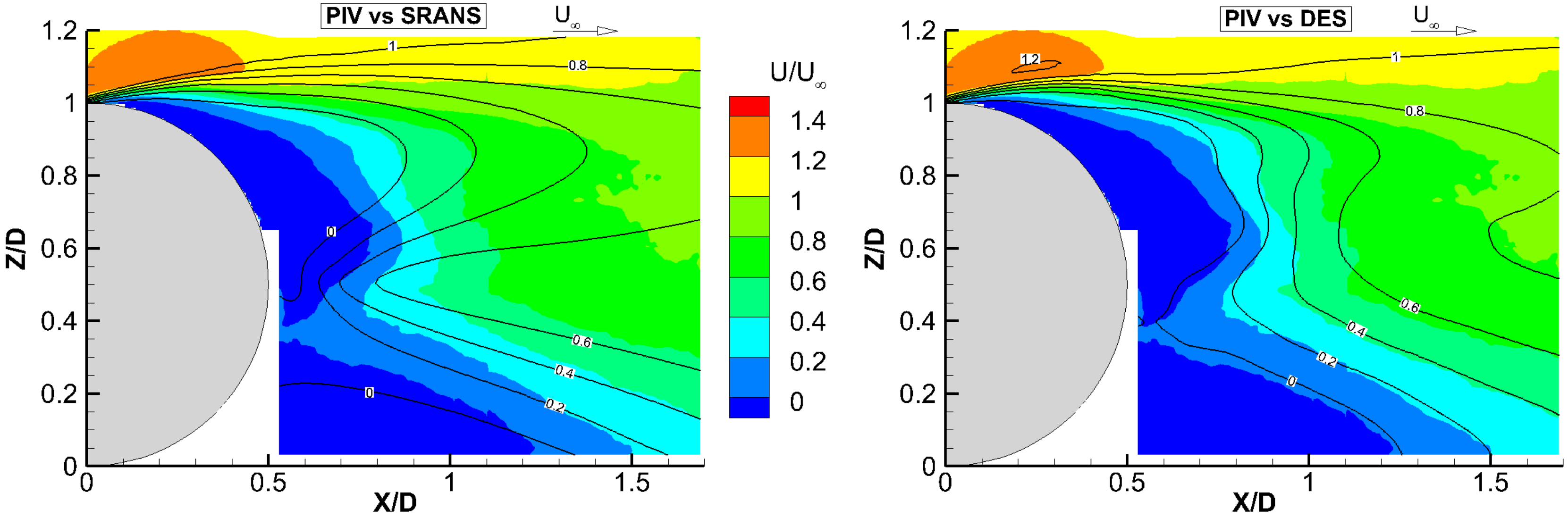

Figure 4.6: Contour plot of streamwise velocity for the rotating wheel at plane $Y = 0D$, including PIV results (flood) and CFD results (lines).

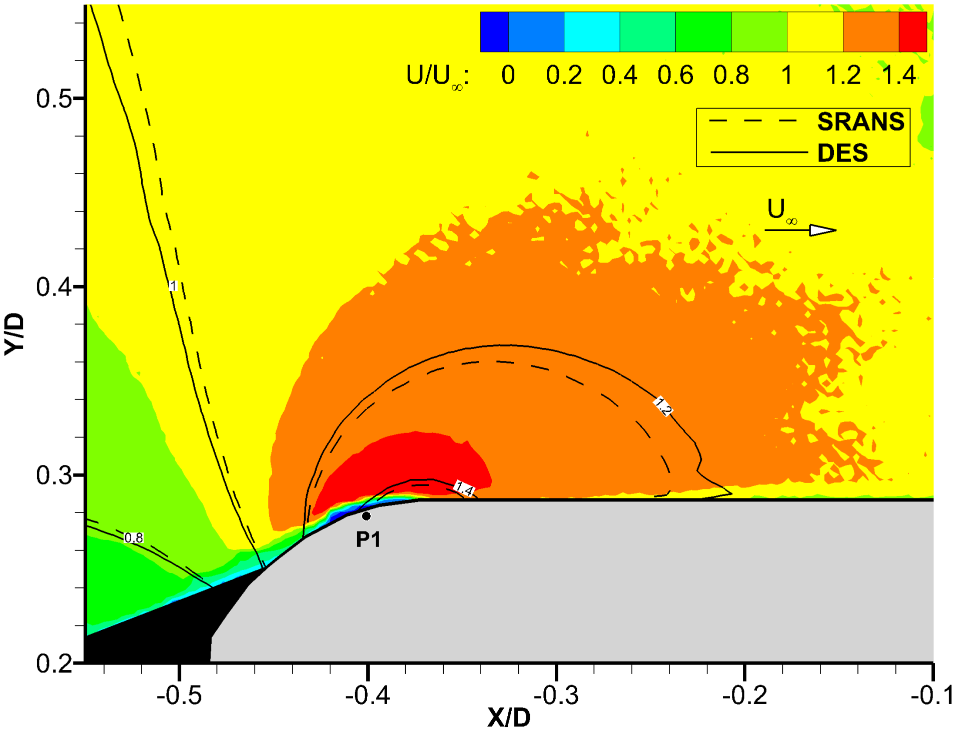

Figure 4.7: Contour plot of streamwise velocity in front of the rotating wheel at plane $Z = 0.53D$, including PIV [18] results (flood) and CFD results (lines).

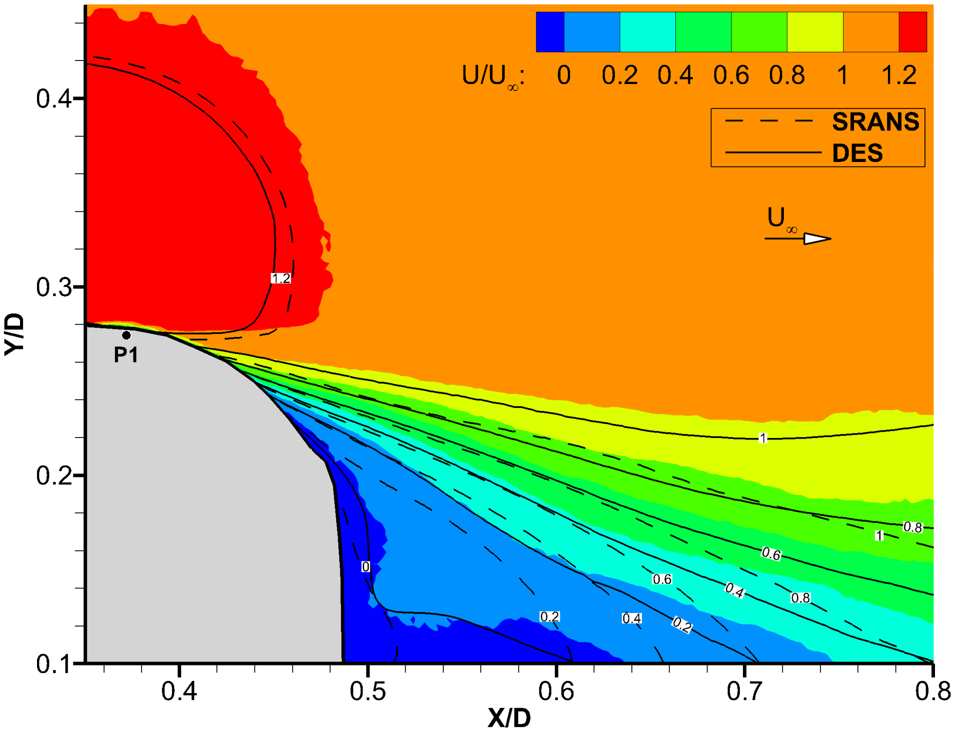

Figure 4.8: Contour plot of streamwise velocity behind the rotating wheel at plane $Z = 0.55D$, including PIV [18] results (flood) and CFD results (lines).

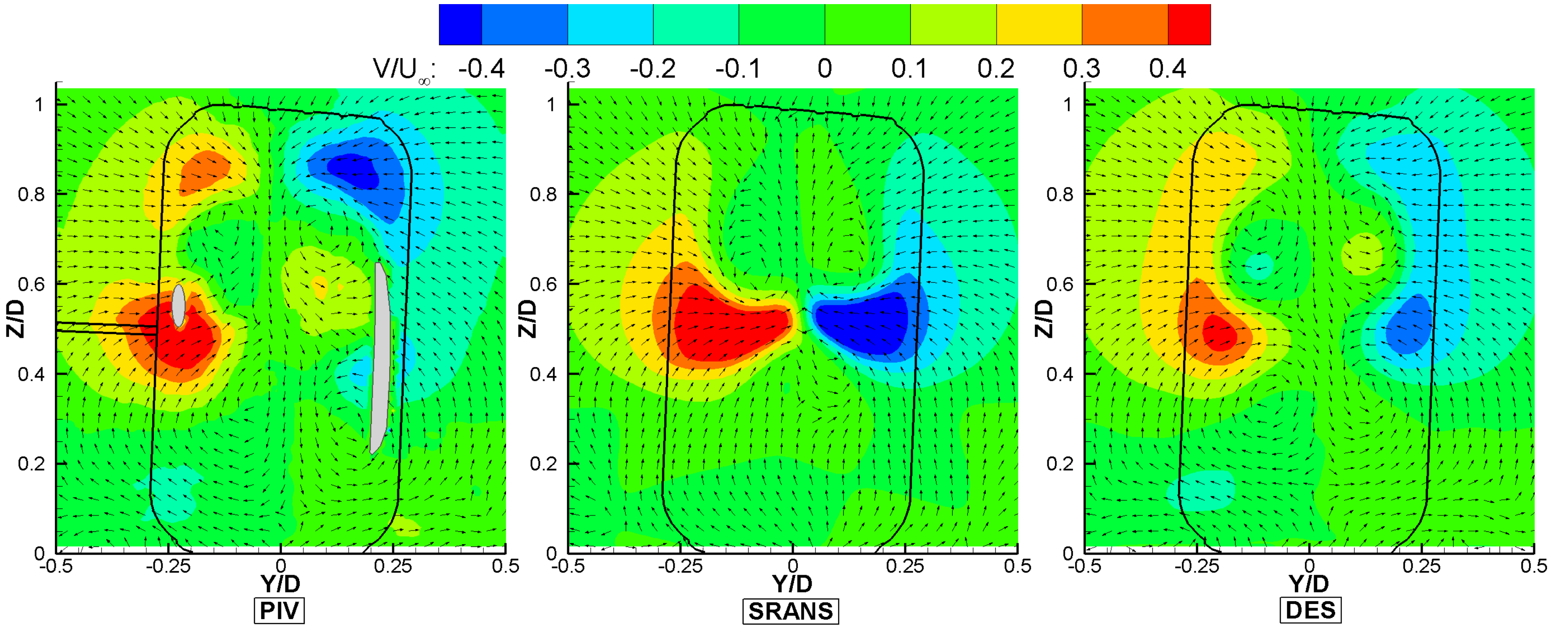

Figure 4.9: Contour plot of horizontal velocity behind the rotating wheel at plane $X = 0.6D$ including a uniform velocity vector plot to show the flow structures. Greyed out zones in the PIV results have no data due to reflections.

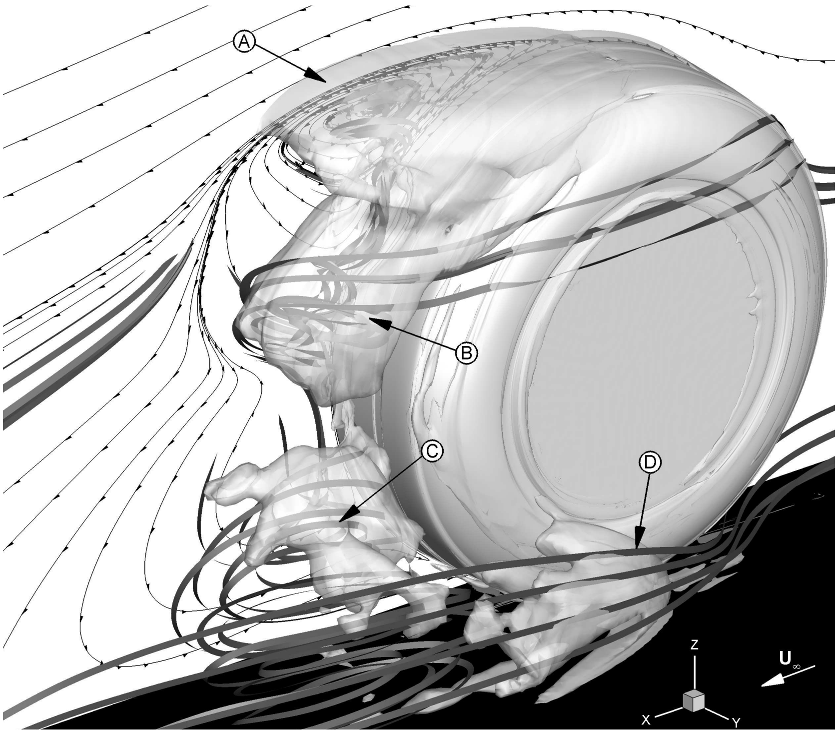

Figure 4.10: Time-averaged plot of the iso-surface of the Q-Criterion ($Q = 100000$) behind the rotating wheel with streamlines on the $Y = 0D$ plane and ribbons showing various flow structures. The results are from the DES model.

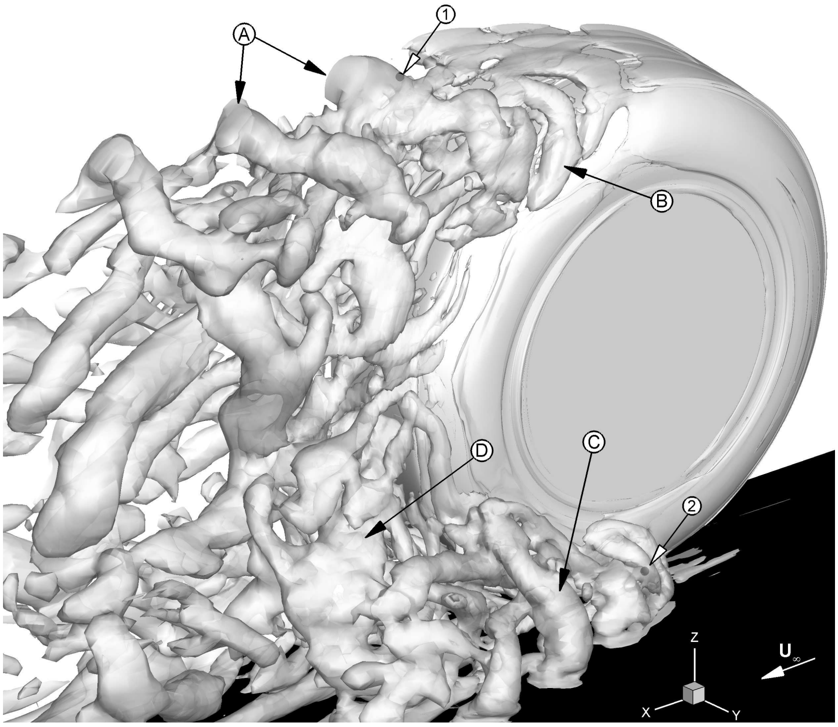

Figure 4.11: Instantaneous plot of the iso-surface of the Q-Criterion ($Q = 100000$) behind the rotating wheel, identifying the various flow structures. The two computational pressure monitors are numerically labelled. For clarity, the image is blanked at the plane $Y = 0D$. The results are from the DES model.

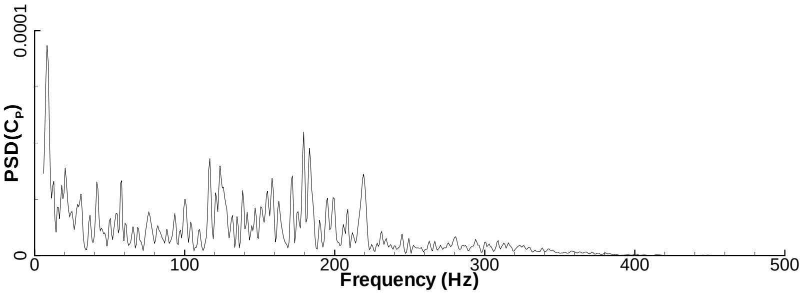

(a)

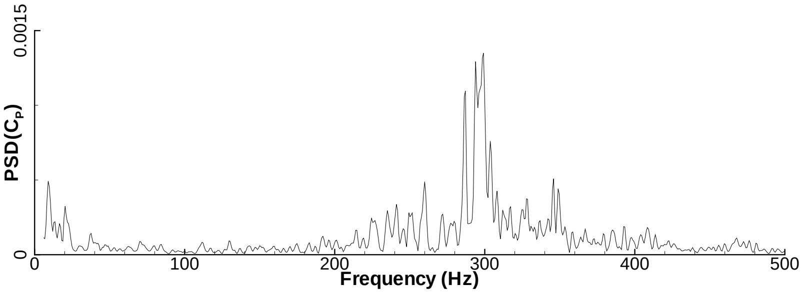

(b)

Figure 4.12: Power spectral density of the pressure measured at (a) monitor 1 and (b) monitor 2 as labelled in Figure 4.11 for the rotating wheel. The results are from the DES model.

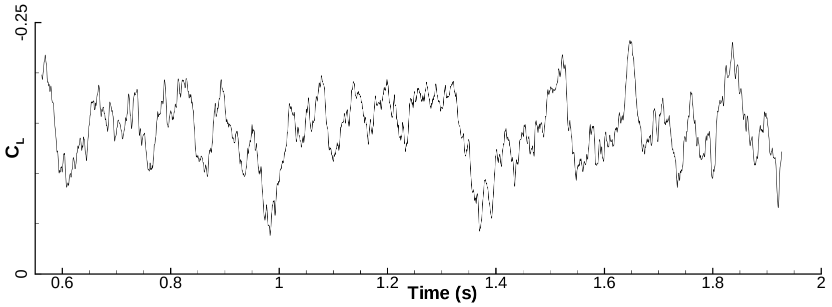

(a) C_L vs Time.

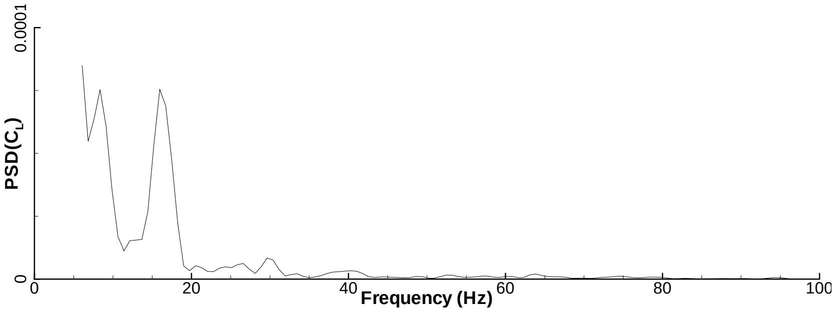

(b) C_L PSD.

Figure 4.13: Time history (a) and power spectral density (b) of the rotating wheel downforce coefficient. The results are from the DES model.

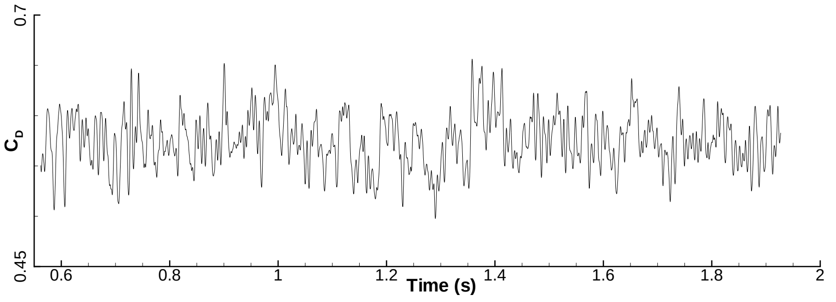

(a) C_D vs Time.

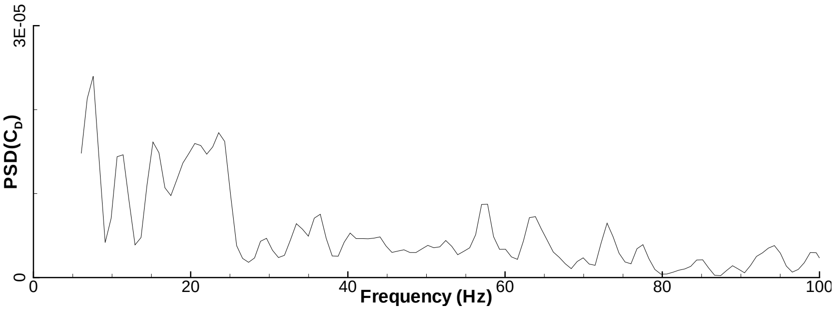

(b) C_D PSD.

Figure 4.14: Time history (a) and power spectral density (b) of the rotating wheel drag coefficient. The results are from the DES model.

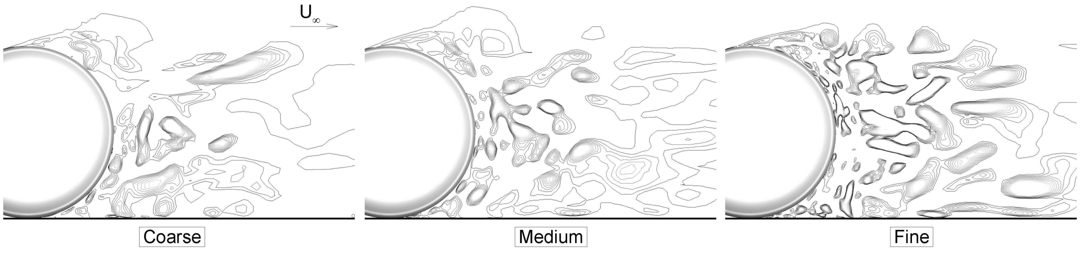

Figure 4.15: Instantaneous contour plot of vorticity for the rotating wheel at the plane $Y = 0D$ from the DES simulations for the three different grid sizes.

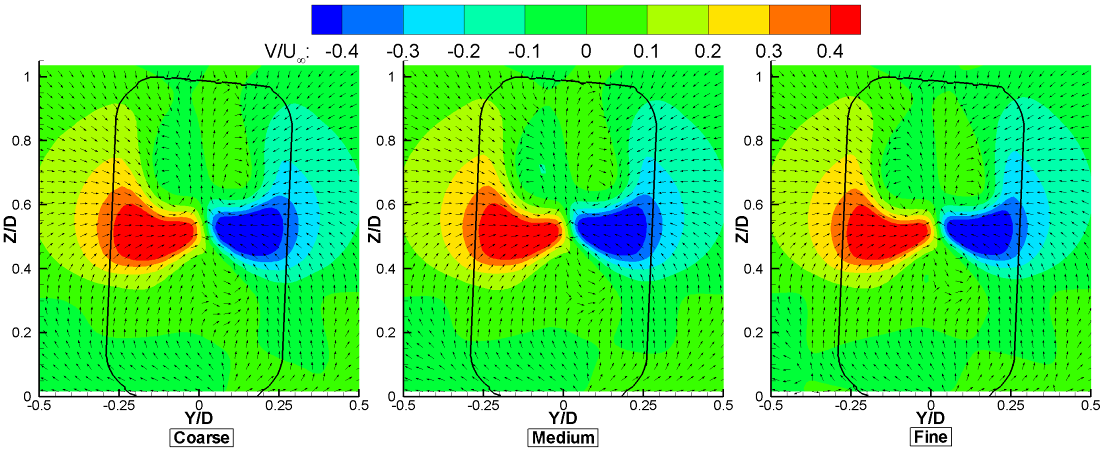

(a) SRANS.

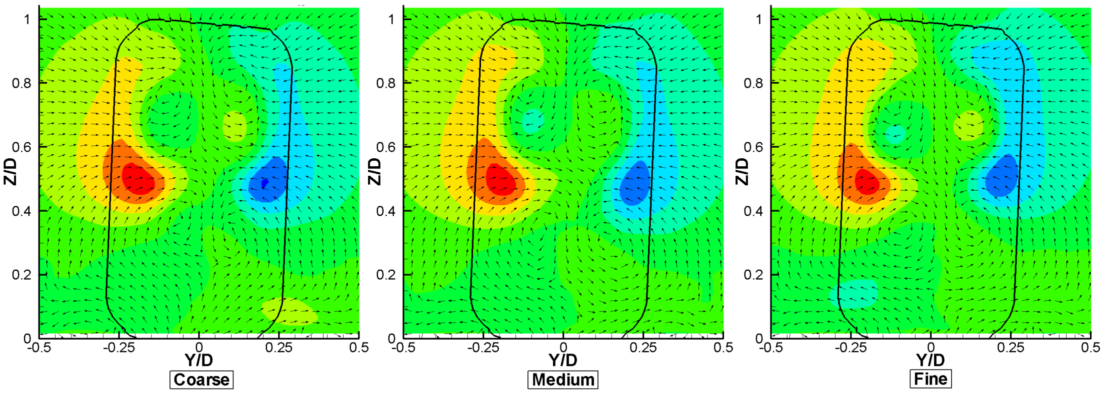

(b) DES.

Figure 4.16: Time-averaged contour plot of the spanwise velocity for the rotating wheel with a uniform velocity vector plot at the plane $X = 0.6D$ for the three different grid sizes.

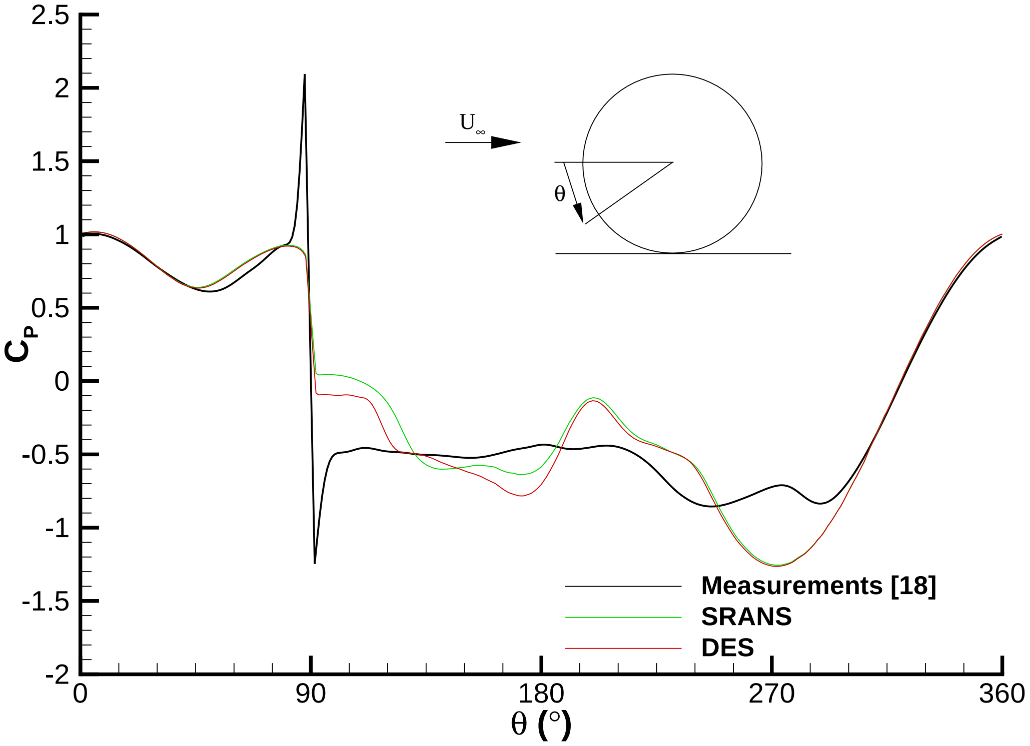

Figure 4.17: Computational pressure distribution around the stationary wheel centreline P3. Experimental results are for the rotating case.

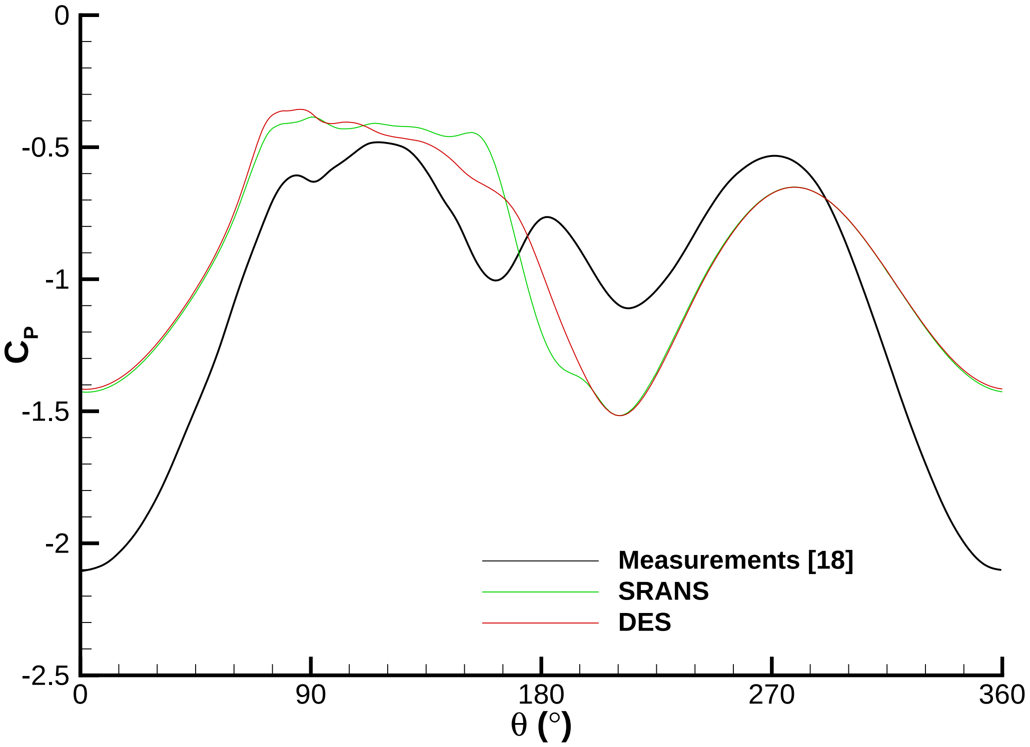

Figure 4.18: Computational pressure distribution around the stationary wheel at location P1. Experimental results are for the rotating case.

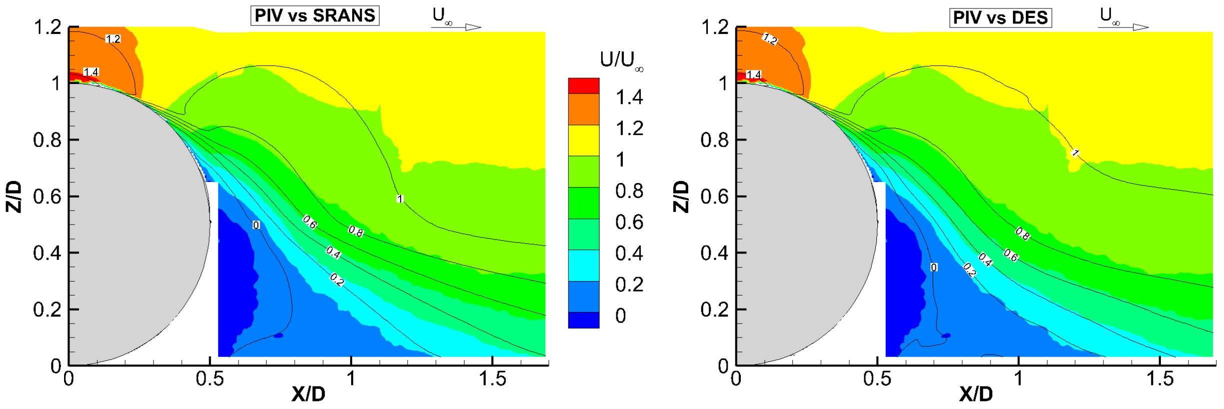

(a) Streamwise Velocity U.

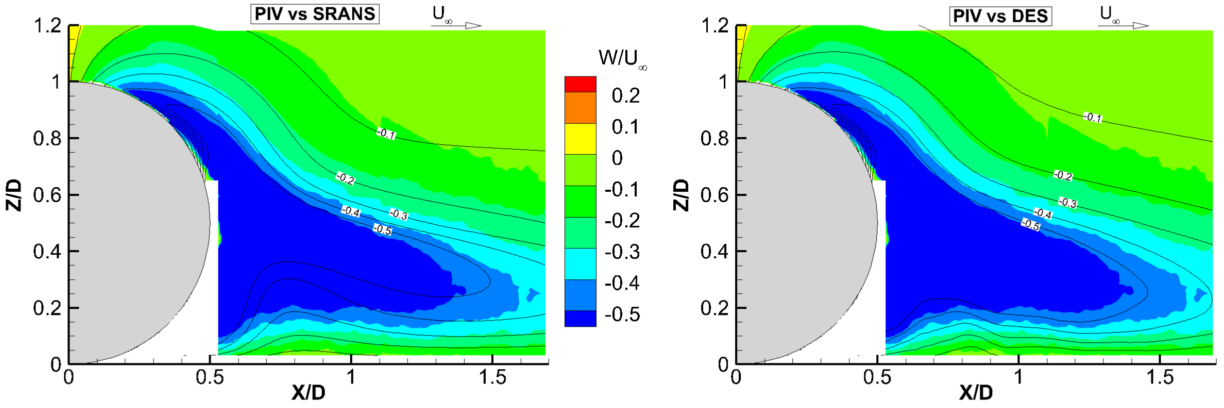

(b) Vertical Velocity W.

Figure 4.19: Contour plot of streamwise and vertical velocity for the stationary wheel at plane $Y = 0D$, including PIV results (flood) and CFD results (lines).

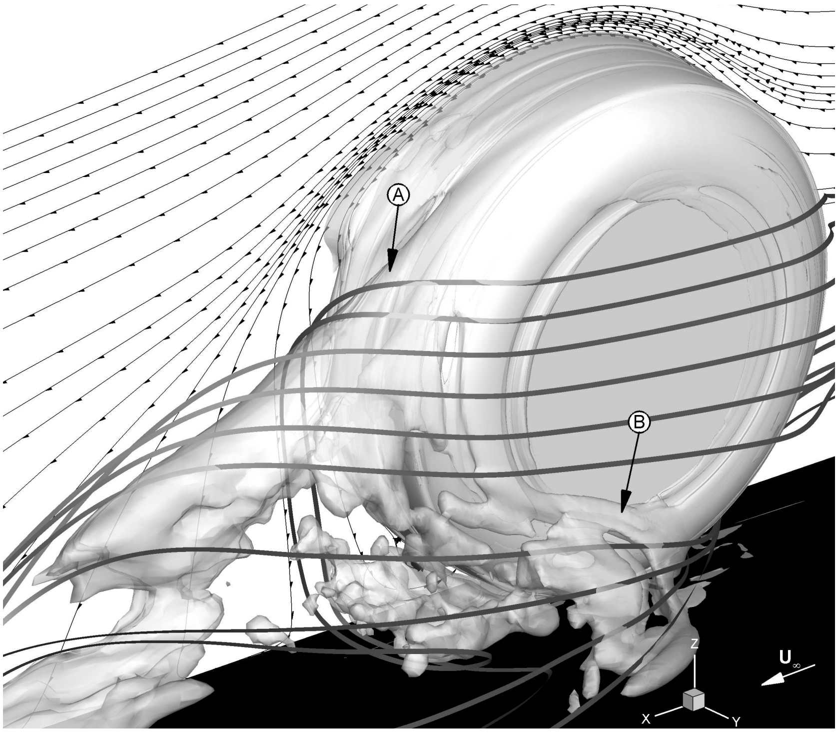

Figure 4.20: Time-averaged plot of the iso-surface of the Q-Criterion ($Q = 100000$) behind the stationary wheel with streamlines on the $Y = 0D$ plane and ribbons showing various flow structures. The results are from the DES model.

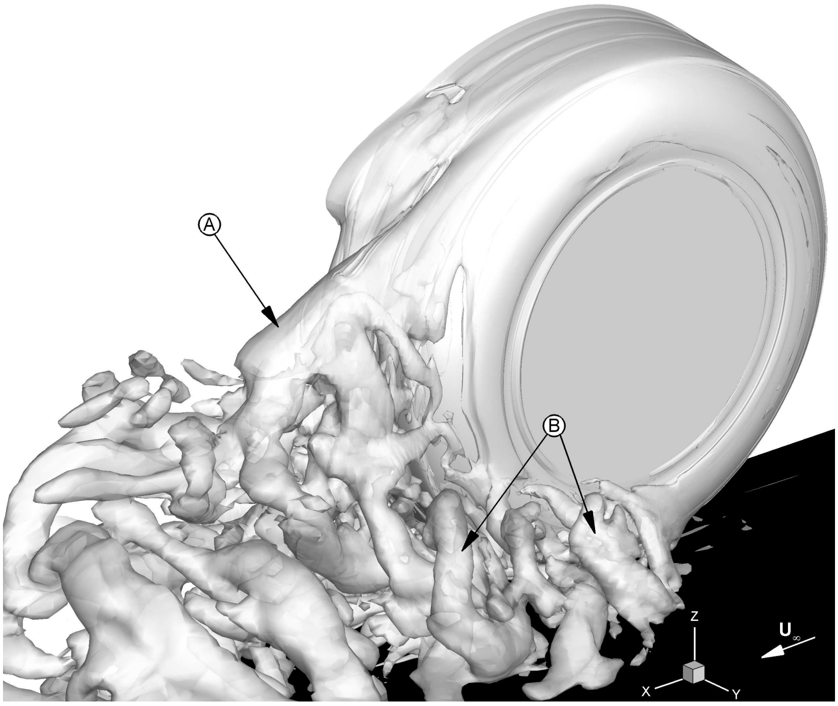

Figure 4.21: Instantaneous plot of the iso-surface of the Q-Criterion ($Q = 100000$) behind the stationary wheel, identifying the various flow structures. For clarity, the image is blanked at the plane $Y = 0D$. The results are from the DES model.

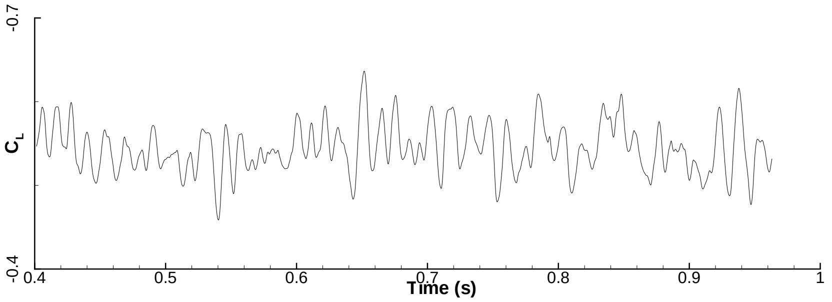

(a) C_L vs Time.

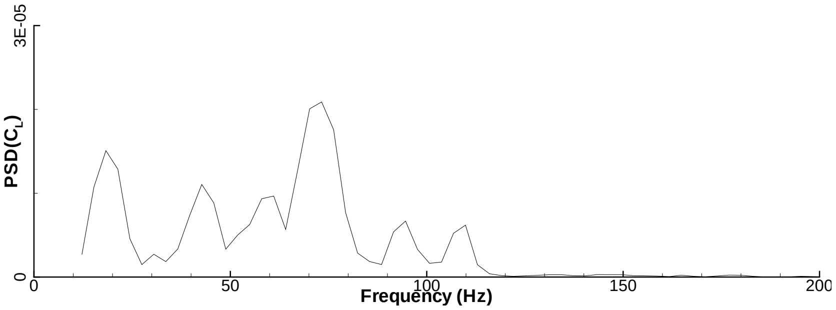

(b) C_L PSD.

Figure 4.22: Time history (a) and power spectral density (b) of the stationary wheel downforce coefficient. The results are from the DES model.

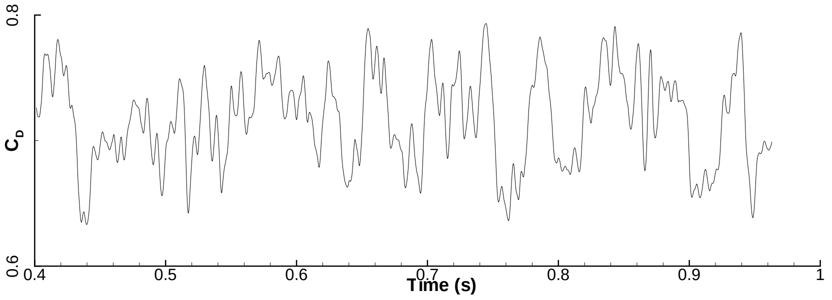

(a) C_D vs Time.

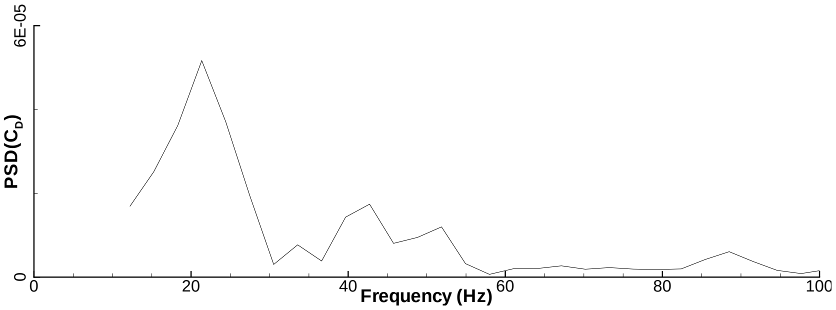

(b) C_D PSD.

Figure 4.23: Time history (a) and power spectral density (b) of the stationary wheel drag coefficient. The results are from the DES model.

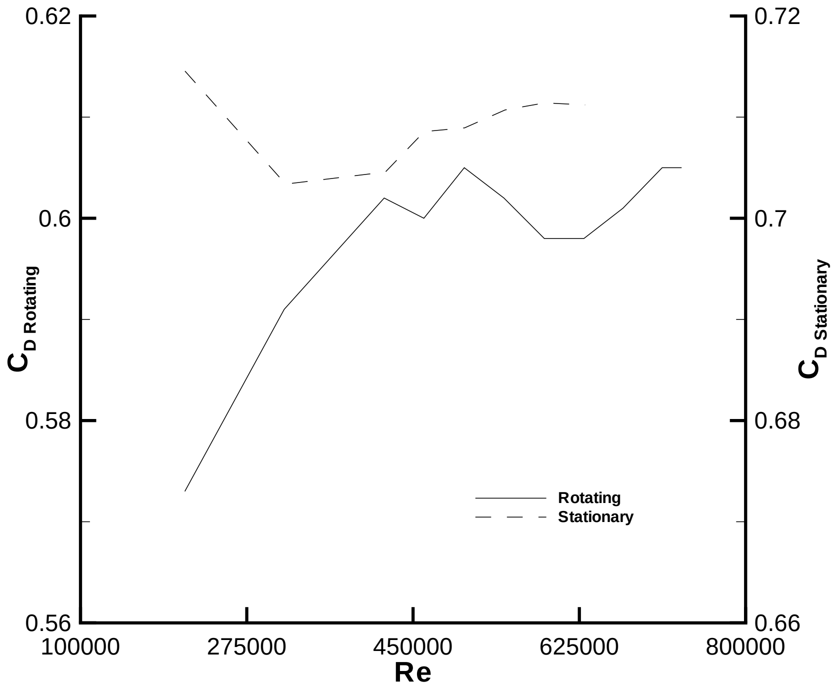

Figure 4.24: Plot of the experimental wheel drag coefficient at various Reynolds numbers (freestream velocity) for the stationary and rotating cases. Results from Van den Berg[18].

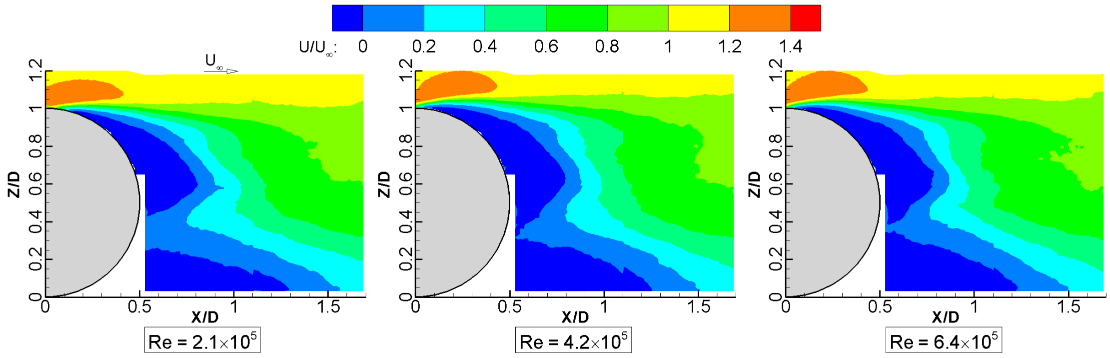

Figure 4.25: Contour plot of the non-dimensional streamwise velocity behind the rotating wheel at $Y = 0D$ for three different Reynolds numbers.

Chapter 5

Effect of Wheel Presence on Wing Aerodynamics

The wing and wheel have been analysed in isolation in the previous two chapters. This provides a good understanding of the flow characteristics associated to each case, but it is not representative of a realistic configuration. Combining the two components that were studied in isolation is the next step in improving our knowledge of the flow around the front of a racing car. This chapter investigates the flow around an inversed wing placed upstream of two rotating wheels, with a gap and overlap of $20mm$ as described in Section 2.3.1.

The first section analyses the trend of the wing downforce and drag with ride height, comparing the computational results (SRANS and DES) to experimental measurements. The results are also contrasted to the isolated wing case. The section which follows describes the various flow mechanisms present around the wing and the effects of the rotating wheel presence, while links are made where possible to the observed trends in force and pressure distribution. Finally, the last section uses the DES results to investigate the unsteady flow phenomena.

5.1 Analysis of Wing Forces

5.1.1 Overall Downforce and Drag Trend

Similarly to what was observed for the isolated case described in Section 3, the wing experiences a change in downforce and drag at different ride heights. Figures 5.1 and 5.2 plot the change of the force coefficients with ride height, comparing experimental measurements from Van den Berg [18] with the two numerical methods used in this research.

The results of the isolated case are also included for comparison purposes. The force results are divided into different regions, as defined in reference [18].

The overall trend of both downforce and drag is to increase as the ride height is reduced, at a higher rate than the isolated wing case. At higher ride heights the forces of the wing are below that of the isolated case, but at lower ride heights they are higher, reaching a maximum C_L of approximately 2.88 and C_D of 0.38 at $h/c = 0.067$ (respectively 21% and 27% greater than for an isolated wing). The peak of maximum downforce and drag is not yet reached at the lowest ride height investigated, in contrast to the isolated wing which reaches its peak downforce at approximately $h/c = 0.1$. It is noted that the wing in the combined case produces more downforce than the isolated wing below $h/c = 0.148$ whereas it already starts to produce more drag at $h/c = 0.349$. Therefore, the presence of the wheel in this position behind the wing has a negative effect on its efficiency.

Figure 5.1 shows that the downforce predicted by the simulations is within 5% of the measurements, closer than for the isolated wing, with the DES predicting lower forces than SRANS. Both simulations predict similar results at $h/c = 0.458$, but diverge at lower heights. In the lower part of Region II a change in the ride height sensitivity is observed from the measurements, where the forces become more sensitive to lower ride heights, and this is captured by the CFD, although the initial surge in downforce is underestimated. For the two lower ride heights simulated, the results compare well to the experimental data, with similar increases of downforce with ride height predicted. The crossover point, where the downforce produced by the wing is higher than for the isolated case, is similarly predicted by both SRANS and DES at $h/c = 0.154$ and $h/c = 0.161$ respectively. It is noted that the limited number of ride heights simulated for the combined wing and wheel case reduces the resolution of the captured trend and can affect the accuracy of the predicted crossover point.

The drag results, shown in Figure 5.2, follow a similar trend to the downforce. The CFD results tend to give higher values when compared to the experimental data, although it is believed that the measurements are underpredicted, as has been proposed in Section 3.3. Despite this, the trend is accepted as being valid and can be used for comparison. Both SRANS and DES generally show a similar trend but appear to fail capturing the lower rate of change in Region III, where the experiment shows a drop at $h/c = 0.211$. Overall, the DES predicts a better change in drag between the two lowest ride heights, whereas the SRANS captures the increase in drag in Region II more accurately. In contrast to the downforce results, the crossover point where the drag produced by the wing is higher than for the isolated case is predicted better by the SRANS simulation at $h/c = 0.344$, compared to the DES prediction of $h/c = 0.316$.

It is difficult to draw any conclusions from the force results alone. In order to get more detailed information, the following section compares and analyses the pressure distribution around the wing at two locations: centrespan($y/c = 0$) and wing tip ($y/c = -0.93$).

5.1.2 Surface Pressure Distributions

The surface pressure distribution around the wing centrespan and tip is shown in Figures 5.3 and 5.4 respectively. Focusing on the centrespan results, the suction peak of the main element is seen to increase as the ride height is lowered, with the trend staying similar until the lowest ride height is reached. At this point, the suction peak has become more rounded, extending further along the chord and the pressure recovery that follows is higher. The flap is less affected by changes in ride height, although it still experiences higher suction on the lower surface as it gets closer to the ground. This does not apply to the lowest ride height, where there is little change in the pressure distribution of the flap compared to $h/c = 0.211$. The upper surface of the wing is insensitive to ride height changes.

Little difference exists between the pressure distributions predicted by the two CFD models at centrespan. The major difference is the higher suction that is predicted on the lower surface of the wing by the SRANS simulation. The general trend for most ride heights is accurately captured although the suction is underpredicted on the lower surface of the main element. The different pressure distribution that exists at $h/c = 0.106$ is not captured as accurately by the simulations, although it does exhibit the features mentioned above (i.e. rounded suction peak with a higher pressure recovery).

The pressure trends at centrespan resemble those from the wing in isolation, with less suction on the lower surface of the main element at higher ride heights, and the opposite at $h/c = 0.106$. This agrees with the previously observed trend where the isolated wing produces less downforce below $h/c = 0.148$. The centrespan pressure distribution around the flap is not significantly affected by the presence of the wheel.

At the tip of the wing (Figure 5.4), the main element sees a drop in suction on the lower surface due to the pressure leakage around the edge of the endplate, but the pressure stays constant along the chord due to the presence of the lower edge vortex negating further pressure losses. The flap on the other hand exhibits a similar pressure distribution as at centrespan. Once again, the suction on the lower surface increases as the ride height is lowered and the pressure distribution stays similar throughout the range of ride heights. A difference in the pressure distribution does appear at $h/c = 0.106$, where the suction peak is no longer clearly defined close to the leading edge of the main element.

More severe discrepancies exist between the two CFD models at the wing tip. On the main element, the differences become more significant as the ride height is lowered, where the SRANS predicts a higher suction on the lower surface. The DES better predicts the change in pressure distribution with ride height when compared to the experimental data, especially at $h/c = 0.106$.

The CFD prediction of the pressure distribution of the flap for the combined case does not compare well with the measurements. After the suction peak, a stronger adverse pressure gradient is predicted and the pressure coefficient reaches a constant value at approximately $x/c = 0.65$. This indicates that the flow in this region has separated from the surface. To investigate the reason of this discrepancy, a comparison is made in Figure 5.5 between the predicted surface streamlines and the oil flow results from Van den Berg [18]. It can be seen that the CFD predicts a larger recirculation at the flap tip which crosses through the plane $y/c = -0.93$, whereas the oil flow result shows that there is a smaller recirculation lying just outside of the plane where the pressure distribution is measured. Thus, an inboard shift in the location of the pressure measurement to ensure the recirculation region is avoided would remove this large discrepancy.

For the comparison to the isolated wing results, observations similar to those from centrespan can be made, although the closer distance of the wing tip to the wheel means differences are greater. The suction on the lower surface of the wing is now also weaker for the flap, as well as for the main element, at the three higher ride heights. At $h/c = 0.106$ the trend is reversed, as there is more suction on the lower surface aft of $x/c = 0.15$. It is interesting to note that the trend of the experimental pressure distribution on the flap tip differs between the isolated and combined case at the two ride heights available ($h/c = 0.317$ and 0.211), where the addition of the wheel has removed the region of constant pressure which was measured near the flap trailing edge. The CFD fails to capture this change in trend and instead predicts more comparable trends between the isolated and combined case as the pressure on the flap reaches a constant value, albeit at a different location.

It is quickly noted that the discrepancy in the pressure measurement of the isolated wing at $x/c = 0.3$ is not present for the combined case, and it is believed that this is not physical but was caused by instrumental error present at the time of Mahon's isolated wing experiments [16].

5.1.3 Sectional Forces

The pressure distributions presented above have been used to extract sectional forces providing additional information and these are plotted in Figure 5.6 and 5.7 for the results at centrespan and tip respectively.

At centrespan, the main element produces 70% of the downforce and the flap produces most of the drag. Akin to the observation made in Section 5.1, less downforce is generated than for an isolated wing at higher ride heights. In addition, the rate of change of sectional downforce as the main element gets closer to the ground increases faster than for the isolated case, whereas the flap is once again little affected by the change in ride height due to its greater distance from the ground. On average, the sectional downforce at centrespan is 10% higher than the total downforce of the wing (from the experimental data), whereas the drag is approximately 20% lower[1].

At the wing tip (Figure 5.7), the wheel presence changes some of the trends observed for the isolated wing in Section 3.3. Whereas at low ride heights both the main element and flap experienced a drop in downforce, they now continue increasing at a steady rate. The experimental data shows an increase in both downforce and drag at $h/c = 0.32$, which the CFD does not fully capture. Compared to centrespan, this increase is not limited to the main element, as the flap also experiences a significant boost. From the experimental results, the flap produces more downforce than the isolated wing, even at $h/c = 0.317$. This can be explained by looking at the pressure distribution around the tip (see Figure 5.4), where it can be seen that the flap of the isolated wing experienced flow recirculation at $y/c = -0.93$, which results in lower sectional downforce and drag. This also applies to the CFD results, which predict the recirculation at $y/c = -0.93$, although this can be observed for both the isolated and combined cases, resulting in an underprediction of the flap forces for the combined case. The trends on the other hand are generally well captured by the computations, although the SRANS overpredicts the increases in sectional downforce and drag on the main element at lower heights.

The sectional forces show that in general the CFD underpredicts both the downforce and drag at both the locations investigated. This is in contrast to the overall forces (Figures 5.1 and 5.2) which show the computations underpredicting the downforce but not the drag. This is similar to what was observed for the isolated wing case and is once more believed to be associated to errors in the experimental drag measurements.

---

[1] The viscous drag is not taken into account.

5.2 Governing Flow Mechanisms

In the previous section, the forces and pressure distributions of the wing have been analysed. Following this analysis, the various flow features present around the wing which contribute to the observed trends are now investigated.

5.2.1 Channel Effect

The channel effect between the wing and the ground has been identified [8, 16] as the main downforce enhancement mechanism of the wing and this still applies to the combined case. Figure 5.9 presents a comparison of the streamwise velocity at the wing's centrespan between the isolated and combined case, for a range of ride heights.

At $h/c = 0.317$, the combined case shows lower acceleration beneath the main element, resulting in the lower suction peak observed from the pressure distribution. As the wing is moved closer to the ground, the flow velocity increases beneath the main element, and this occurs at a faster rate for the combined case. As a consequence, at $h/c = 0.106$ the combined case has a stronger suction peak below the main element and produces more downforce. In addition, the wake of the wing is reduced at low ride heights by the wheel presence. These differences between the isolated and combined case are caused by the effect of the wheel rotation and the wheel blockage which are discussed in the following sections.

5.2.2 Effect of Wheel Rotation

The effect the wheel rotation has on the wing can be investigated in CFD, where it is possible to set the wheel surface to be stationary while still allow a moving ground. This was done using the SRANS[2] model at two ride heights: $h/c = 0.317$ and $h/c = 0.106$. Van den Berg [18] proposed that the wheel rotation has a negative effect on downforce at high ride heights but a positive effect at low ride heights, where the wheel rotation contributes to the wing circulation, augmenting the channel effect and increasing the pressure on the top surface of the flap tip.

Figure 5.10 compares the streamwise velocity below the wing's centrespan, with the wheel rotation enabled and disabled, for the higher and lower ride height respectively. It is noted that at $h/c = 0.317$, the wheel rotation has a positive effect on the wing, as the velocity beneath the main element increases by 8%. At the lower ride height, the

---

[2] The use of SRANS is believed to be justified as it has shown to predict similar trends to experimental measurements of the wing.

effect of the wheel rotation is found to be a similar 8% increase in streamwise velocity beneath the main element. This leads to the conclusion that the added circulation from the wheel rotation contributes equally to the centrespan channel effect at high and low ride heights.

Although the wheel rotation has a similar influence on the centrespan channel effect at both high and low ride heights, it can be seen to reduce the size of the main element wake more at lower ride heights. The differences in the wing wake between the isolated and combined case observed in Figure 5.9 follow a similar pattern, where they are more significant at lower ride heights. It is believed this can be attributed to the wheel rotation effect.

Figure 5.11 shows the effect of the wheel rotation at the wing tip ($y/c = -0.93$) for two ride heights. Once again, the wheel rotation has a positive effect on the wing at both ride heights, where the maximum velocity is increased by approximately 14% at $h/c = 0.317$ and 10% at $h/c = 0.106$. This contradicts Van den Berg's hypothesis which stated that the wheel rotation would have an increasingly negative effect at higher ride heights. It is noted that at the lowest ride height, in addition to increasing the flow speed beneath the main element and flap, the wheel rotation significantly reduces the separation on the flap. Further investigating the effect of the wheel rotation on the flap's upper surface pressure shows that it does not affect it. From these results, it is concluded that the effect of the wheel rotation does not significantly contribute to the difference in the wing downforce trend between the isolated case and the combined case.

5.2.3 Effect of Wheel Blockage

The wheel presence behind the wing results in blockage which forces the flow to accelerate and turn between the endplate trailing edge and the wheel. It also causes the deflection of the wing edge vortices, which is discussed further in the following section. Furthermore, there is a region of flow stagnation on the front of the wheel close to its horizontal centreline. This affects the pressure distribution on the wing depending on the ride height.

At high ride heights (e.g.$h/c = 0.317$), the region of flow stagnation will be located beneath the flap trailing edge, increasing the pressure beneath the wing tip and therefore resulting in a loss of downforce. This negative effect is reduced at lower ride heights, as the low pressure flow travelling around the front lower part of the wheel has a greater influence, reducing the pressure beneath the wing, while the wheel stagnation region increasingly affects the upper surface pressure of the wing, as can be seen in Figure 5.4(c).

The wheel blockage is one of the mechanisms which contributes to the difference in the wing downforce trend between the isolated case and the combined case.

5.2.4 Edge Vortices

Two edge vortices were observed around an isolated wing in Section 3.4 and it was concluded that the DES model captured them with better accuracy than SRANS, although this did not always have a significant impact on the wing forces. Overall, the edge vortices play an important part in the force properties of the wing, especially the lower edge vortex which is one of the downforce enhancement mechanisms. Furthermore, their behaviour would have an impact on additional components downstream. These are now investigated for the combined wing and wheel case.

Figure 5.8 compares the streamwise velocity beneath the wing at $y/c = -0.93$ for the experimental and computational results of the combined case. At $h/c = 0.211$ the computational results show an overall underprediction in streamwise velocity, although the flow is qualitatively captured. Compared to the isolated wing results, the streamwise velocity is lower beneath the wing, and the region of low velocity at $x/c = 0.9$, which was associated to the vortex breakdown, is not present anymore. It can also be deduced from the vector plot that the lower edge vortex crosses the plane $y/c = -0.93$ earlier (at $x/c = 0.8$ instead of $x/c = 0.9$), moving inboard.

At the lower ride height of $h/c = 0.106$, a region of low velocity can be seen, which is a result of the edge vortex breaking down beneath the main element trailing edge. The DES captures this effect accurately, whereas the SRANS fails to capture the full extent of the lower velocity. From this perspective, it appears as if the presence of the wheel alters the trajectory of the lower edge vortex, diverting it downwards. But this is not the case as when the vortex is observed from a different perspective, it does not appear to be significantly diverted vertically. The DES compares well to the experimental data available for the wing, and the simulation's results are used to investigate the edge vortices further.

Figures 5.12 to 5.17 provide additional information on the origin and behaviour of the various vortices created around the wing endplate at various ride heights. Starting with the highest wing position of $h/c = 0.458$, three vortices are identified and labelled A, B and C in Figure 5.12(a). The lower edge vortex (labelled A) is created beneath the main element's leading edge and as it travels downstream, it is responsible for a local area of low pressure on the endplate. This vortex also induces a lower local pressure on the lower surface of the main element and is one of the force enhancement mechanisms by which the wing produces more downforce at lower ride heights. The vortex size remains the same as it travels further downstream and its vertical trajectory does not appear significantly affected by the wheel presence. On the other hand, the upper edge vortex (labelled B) sees its trajectory significantly altered as it has to move around the wheel.

This is better visualised using Figure 5.17(a), which shows a plane cutting through the vortices at $x/c = 0.995$[3], comparing the isolated case to the combined wing and wheel case. The presence of the wheel has a significant impact on the upper vortex, resulting in a strength reduction of 75% (when considering the Q-Criterion) accompanied by a deflection inboard ($\Delta y/c = 0.02$) and upwards ($\Delta z/c = 0.08$). This loss of strength is caused by the strong crossflow generated between the endplate trailing edge and the wheel, causing flow upstream to spill over the top and bottom edges of the endplate. This counteracts the top vortex but strengthens the lower vortex, which has a maximum Q-Criterion value twice that of the isolated wing case, and generates more upwash at centrespan. From this Figure, it is also noted that the lower edge vortex is deflected inboard ($\Delta y/c = 0.04$) by the presence of the wheel and that it is lower than for the isolated case. The latter observation is a direct result of the changes experienced by the top vortex in the combined case. In the isolated wing case, it interacted strongly with the lower vortex as they both wrapped around each other, diverting the top vortex downwards and the lower vortex upwards (see Figure 3.11(a)). The top vortex being weaker and further away due to the wheel means there is now little interaction between the two vortices.

The vortices investigated in the above paragraph also existed in the isolated wing case, but the third observed vortex (labelled C) is unique to the combined wing and wheel case. It originates from beneath the flap tip, where the region of flow stagnation shown in Figure 5.5 is located, and it is believed that it is created from the high speed crossflow between the endplate and the wheel. This vortex is weaker than the upper edge vortex, rotates in the same direction and further downstream it wraps around the lower edge vortex. It is noted that no experimental evidence of this vortex has been obtained due to the complexities associated with investigating it.

The vortical structures have been described at $h/c = 0.458$, and the effect of ride height is now investigated. The wing position of $h/c = 0.352$ is where a change of wing downforce and drag was recorded experimentally. Comparing Figures 5.12(a) and 5.13(a), the lower edge vortex is deflected upwards a greater amount as it travels downstream due to the wheel front lower wake (labelled E), while the upper edge vortex is deflected further inboard around the wheel and, following an initial upward deflection, is diverted below the tyre shoulder. At $h/c = 0.317$ (Figures 5.14(a)), the size of the lower edge vortex increases at a faster rate along the wheel and the other two vortices (labelled B and

---

[3] This plane is located in the gap between the wing and the wheel.

C) are lower (relative to the wing position) as they have to turn inboard sooner due to the wheel surface being closer to the top edge of the endplate at this ride height. From Figure 5.17(b), the top vortex was found to have moved inboard by $\Delta y/c = 0.02$ and slightly downwards by $\Delta z/c = 0.002$ (relative to the wing) compared to ride height $h/c = 0.458$, while its strength at this plane increases by 12%. The lower vortex also moves inboard and gains in strength, both by the same amount as the top vortex. The major difference which can be observed at $h/c = 0.317$ is the change in the wheel wake, and this will be discussed in Section 6.

Figure 5.15(a) shows the vortices at $h/c = 0.211$. The lower vortex (labelled A) experiences a sudden increase in size near the endplate trailing edge, due to vortex breakdown occurring, similarly to that observed for the isolated wing. At the beginning of this section, it was observed that no vortex breakdown was visible at the plane $y/c = -0.93$ shown in Figure 5.8. Van den Berg [18] concluded that the presence of the wheel delayed the onset of vortex breakdown to lower ride heights, short of having conclusive experimental data to detect the phenomenon. As the DES captured vortex breakdown with good accuracy for the isolated wing, it is believed that the detection of the phenomenon at $h/c = 0.211$ for the combined case is accurate. The plane $y/c = -0.93$ does not show the vortex breakdown bubble as a consequence of the inboard deflection of the lower vortex and the DES predicts its altered location to be at $y/c = -0.88$. The vortex breakdown is also identified in Figure 5.17(c) where the strength of the lower edge vortex is 80% lesser than at $h/c = 0.317$.

A ground vortex (labelled F) is now visible and is induced by the lower vortex which is stronger (upstream of breakdown) and closer to the ground. Although not visible from this perspective, the ground vortex is deflected inboard as a result of the wheel presence and it follows a similar trajectory to the lower vortex. It must be noted that the ground vortex is also present at higher ride heights, although it is created further downstream and is weaker, therefore making it difficult to visualise in the Figures presented. The upper edge vortex (labelled B) continues the trend described previously, where it rises less before turning inboard around the wheel shoulder. Looking at Figure 5.17(c), the third vortex (labelled C in Figure 5.15(a)) has moved lower relative to the wing and is 20% stronger than at $h/c = 0.317$. This is a consequence of the reduced strength of the lower vortex (due to the breakdown), which opposes the creation of the third vortex because of its sense of rotation.

Figures 5.16(a) and 5.17(d) present the results for the lowest ride height investigated ($h/c = 0.106$). The lower edge vortex breakdown is now further upstream, occurring below the main element trailing edge, and is followed by a large expansion. The vortex expands sufficiently to render it visible on the plane $y/c = -0.93$ (Figure 5.8) even though it is deflected inboard. The creation of the ground vortex has also moved upstream, as the wing gets closer to the ground, but it is dissipated by the lower edge vortex as it travels downstream. The observed flow structure is similar to the isolated wing case, but does not have the same effect on the wing tip downforce (see Figures 3.6(b) and 5.7(a)), as the negative impact of the vortex breakdown is counteracted by the wheel's beneficial effects.

The top vortex is aligned with the horizontal centreline of the wheel and as a result does not deflect upwards ($\Delta z/c = 0.02$ lower relative to the wing than at $h/c = 0.317$), although it still bends inboard and is forced to move above the endplate further upstream. Consequently, its strength has increased by 32% compared to $h/c = 0.211$, which is in contrast to a 7% loss of strength for the isolated case (see Figure 5.17(d)). The third vortex (labelled C in Figure 5.16(a)) is quickly dissipated by the expanded lower vortex at this low ride height. On a final note, the predicted upwash behind the wing centrespan, at $x/c = 0.995$, is higher for the combined case compared to the isolated case, as was the case for the higher ride height $h/c = 0.458$.

5.3 Unsteady Flow Phenomena

The mean flowfield around the wing has been investigated in the previous sections, but to further understand the behaviour of the wing in front of the wheel, the unsteady nature of the flow at various ride heights is analysed using the Detached-Eddy Simulation results.

Commencing with the highest ride height investigated ($h/c = 0.458$), Figure 5.18(a) shows the change with time of the downforce generated by the wing, accompanied by a power spectrum density plot. It is seen that the wing exhibits changes in downforce of the order of $\pm 2\%$, with a dominant frequency of $23Hz$. This is caused by the third vortex beneath the flap tip, labelled C in Figure 5.12(b), which is relatively unstable. As the region of instability is located close to the flap's trailing edge, the drag force is more severely affected, and it experiences variation of $\pm 4\%$ from the mean value. The lower edge vortex (labelled A in Figure 5.12(b)) is also a source of pressure fluctuations on the wing which can be seen as slightly higher RMS values on the endplate. Pressure monitors along the vortex path identify a dominant frequency of $23Hz$, which points to an interaction between the third vortex and the lower edge vortex. The upper edge vortex (labelled B) appears to be stable at this ride height as it travels above the shoulder of the wheel. In contrast to these results, the isolated wing did not show any variation in forces at this high ride height, and signs of unsteady behaviour only appeared below $h/c = 0.211$.

At $h/c = 0.317$, the instantaneous plot of the Q-Criterion presented in Figure 5.14(b) shows that the lower vortex breaks down as it travels along the side of the wheel (labelled A) and is then followed by a spiralling tail. The lower edge vortex created by the isolated wing at this ride height did not show signs of breakdown, and the vortex is destabilised by the flow alterations due to the presence of the wheel. It is also apparent that there is a link between the significant change in the wheel wake structure which occurs at this ride height and the lower edge vortex breakdown. The upper edge vortex (labelled B) is mostly steady as it curves around the wheel, experiencing only minor oscillations. Further downstream, it becomes less stable as it is affected by the other vortices around it. The third vortex and its associated recirculation region is responsible for a higher RMS pressure on the endplate and flap. It is surrounded by various smaller vortices, which are unstable as they oscillate and are continuously created and destroyed. The dominant frequency of $63Hz$ observed in the FFT plot of the wing downforce (see Figure 5.18(b)) is caused by the third vortex as it flaps up and down. Despite the difference in dominant frequency, the variation in wing forces is of a comparable amplitude to the ride height $h/c = 0.458$. It must be mentioned that the recirculation at the flap tip is larger than what has been observed from experimental data, and as the third vortex emanates from this area, it is not expected to have the same characteristics if it were observed experimentally.

The vortex breakdown moves forward as the wing is moved closer to the ground, as has been observed for the isolated wing. It is seen in Figure 5.15(b) to be level with the endplate trailing edge at $h/c = 0.211$ (labelled A), with a spiralling tail travelling along the wheel. The ground vortex (labelled F) is stable until it reaches the lower wheel wake (labelled E), where it is entrained sporadically by the spiralling tail of the lower edge vortex. This also occurs to the third vortex (labelled C).

The large vortex expansion previously observed from the mean flow at $h/c = 0.106$ (see Figure 5.16(a)) is composed of a recirculation region enclosed by the spiralling tail shed from the vortex breakdown (labelled A in Figure 5.16(b)). This causes high pressure fluctuations on the endplate and flap, resulting in a more unstable wing with variations in downforce and drag three times larger than at the higher ride heights. Compared to the isolated wing case, the power spectral density of the downforce (plotted in Figure 5.18(c)) shows a peak at $350Hz$ in addition to the lower frequency peaks, and it is associated to the spiralling tail of the lower vortex which has a stronger influence on the wing forces.

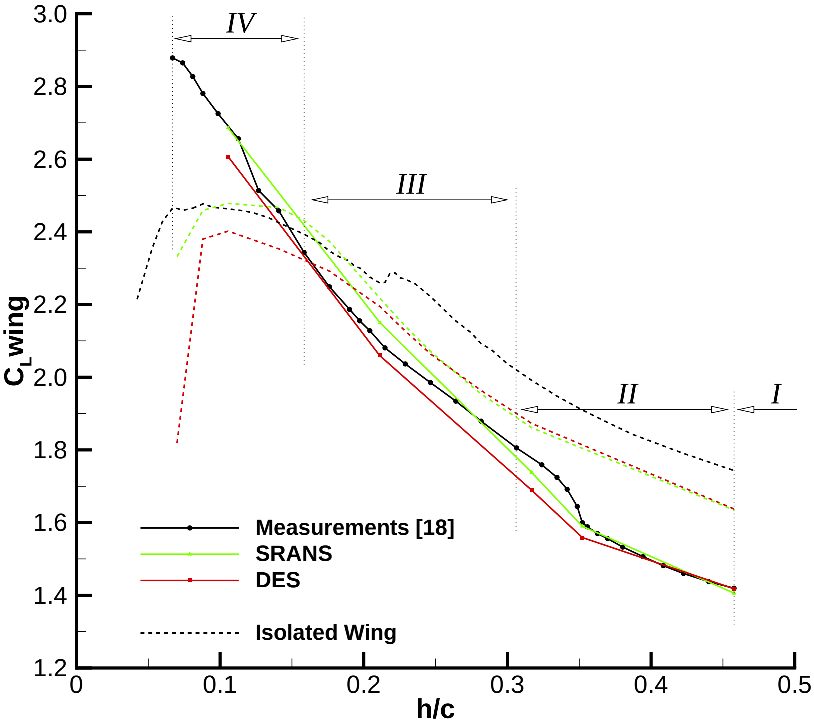

Figure 5.1: Variation of the wing downforce coefficient with ride height for the combined case. Includes results from the isolated wing for comparison purposes.

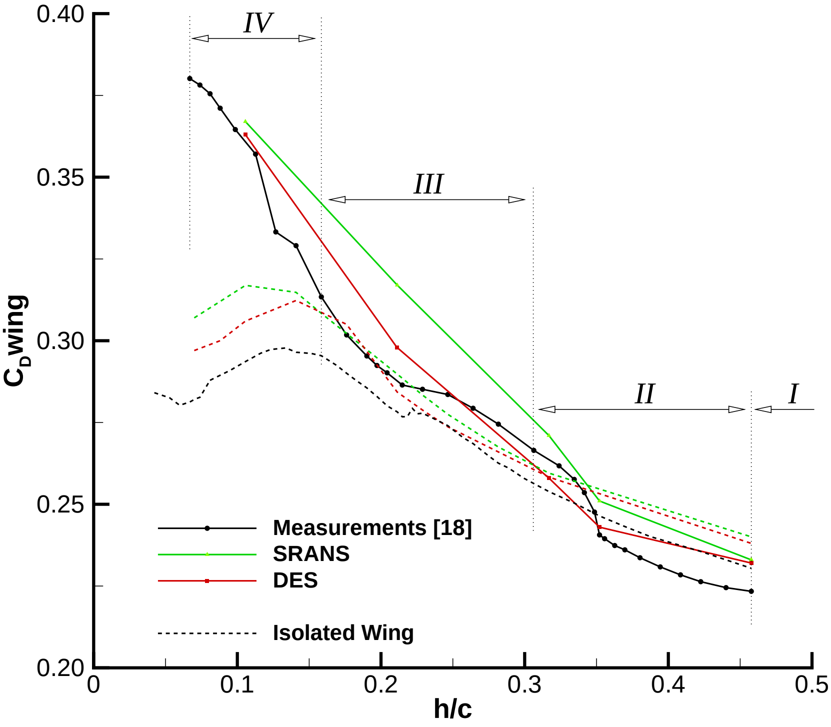

Figure 5.2: Variation of the wing drag coefficient with ride height for the combined case. Includes results from the isolated wing for comparison purposes.

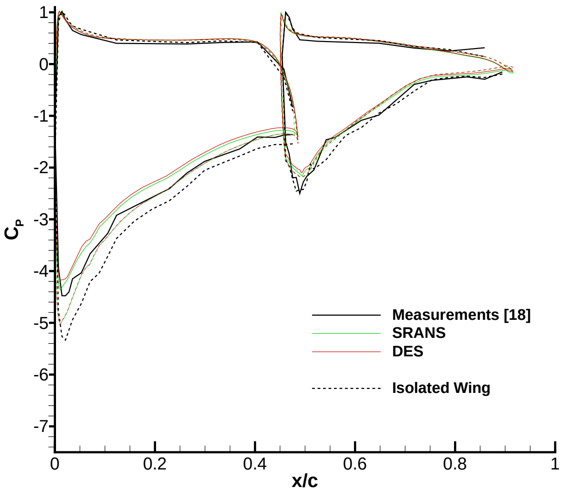

(a) $h/c = 0.317$

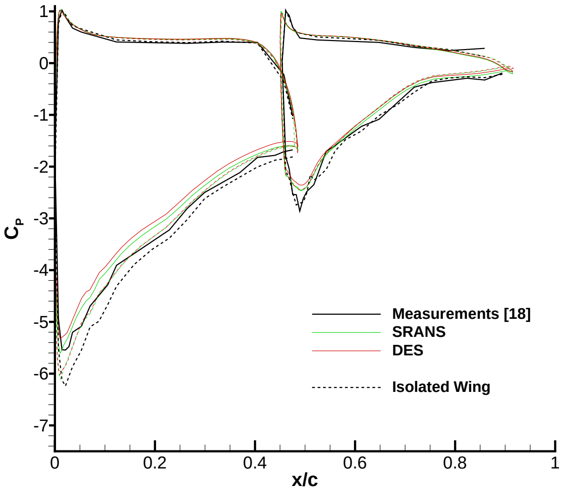

(b) $h/c = 0.211$

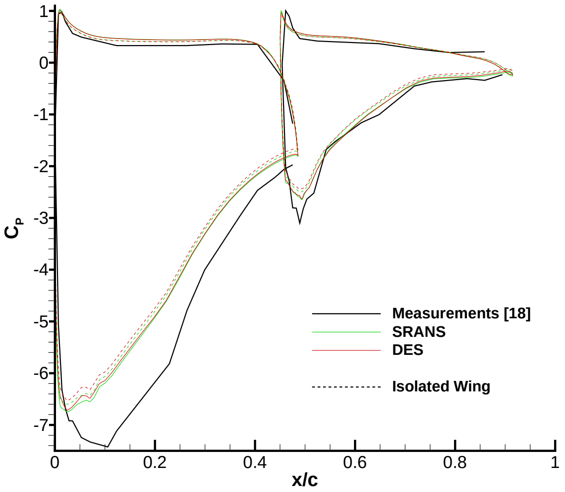

(c) $h/c = 0.141$

Figure 5.3: Pressure distributions at centrespan ($y/c = 0$) for different ride heights in the combined case.

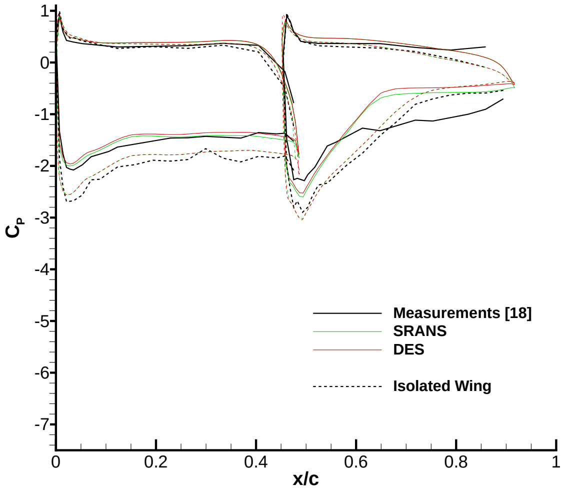

(a) $h/c = 0.317$

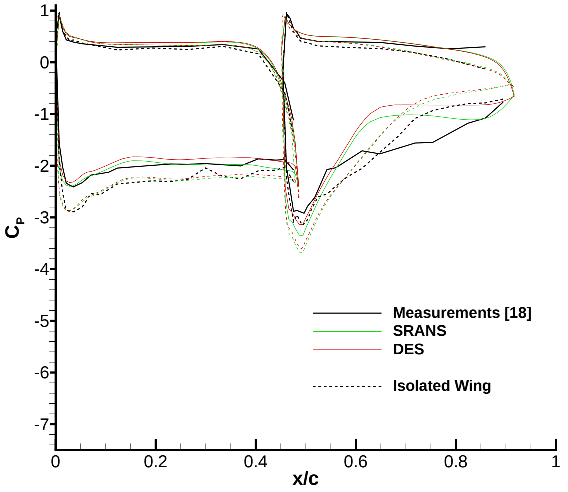

(b) $h/c = 0.211$ & 0.246

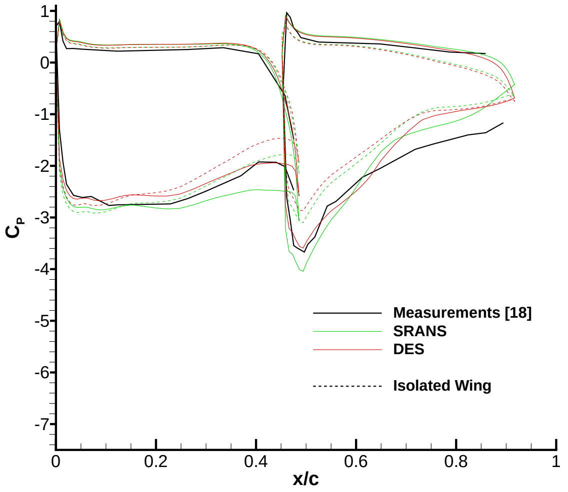

(c) $h/c = 0.141$

Figure 5.4: Pressure distributions at the wing tip ($y/c = -0.93$) for different ride heights in the combined case.

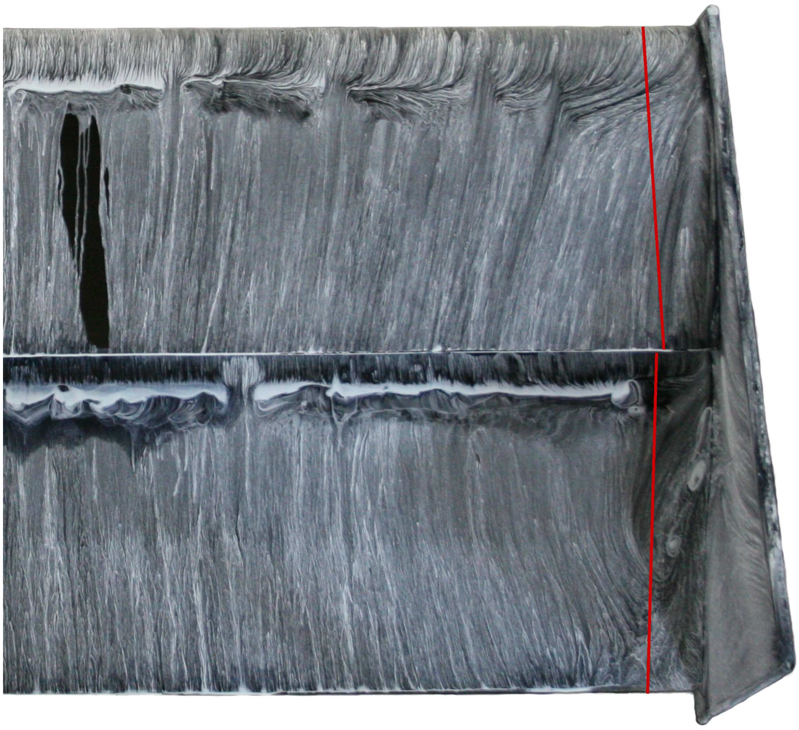

(a) Oil Flow [18].

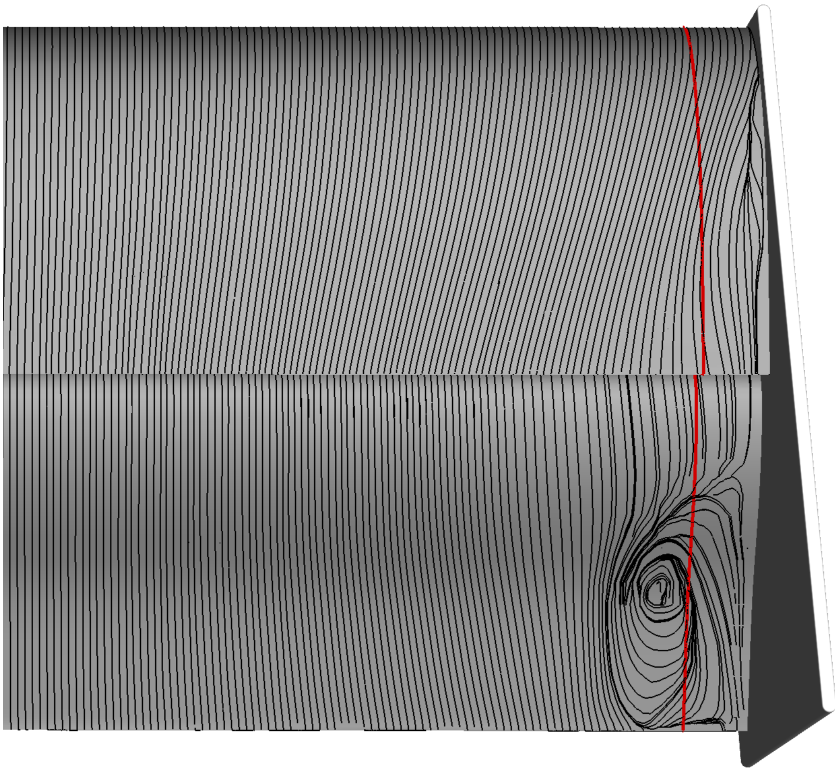

(b) DES.

Figure 5.5: Surface streaklines on the wing, at $h/c = 0.317$, for the combined case. The red line is located at $y/c = -0.93$.

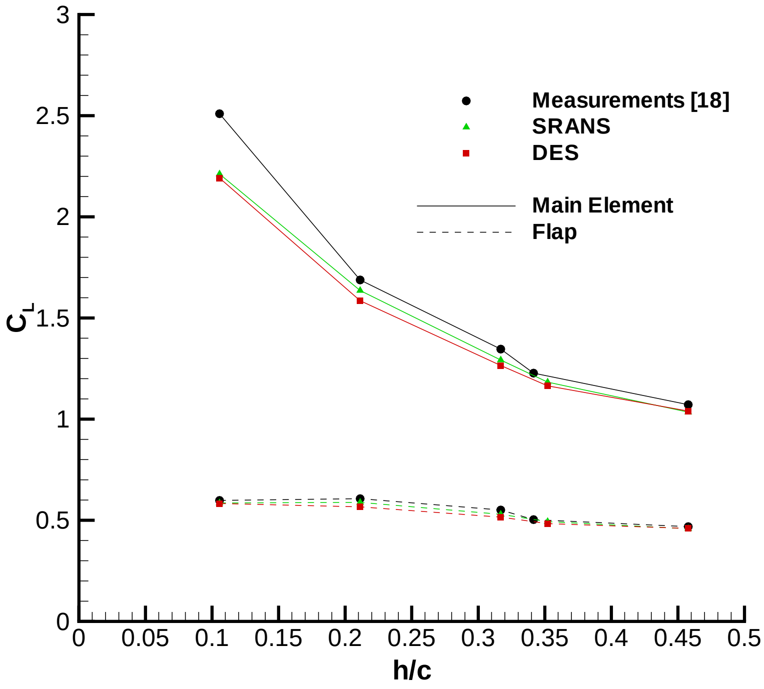

(a) C_L vs h/c.

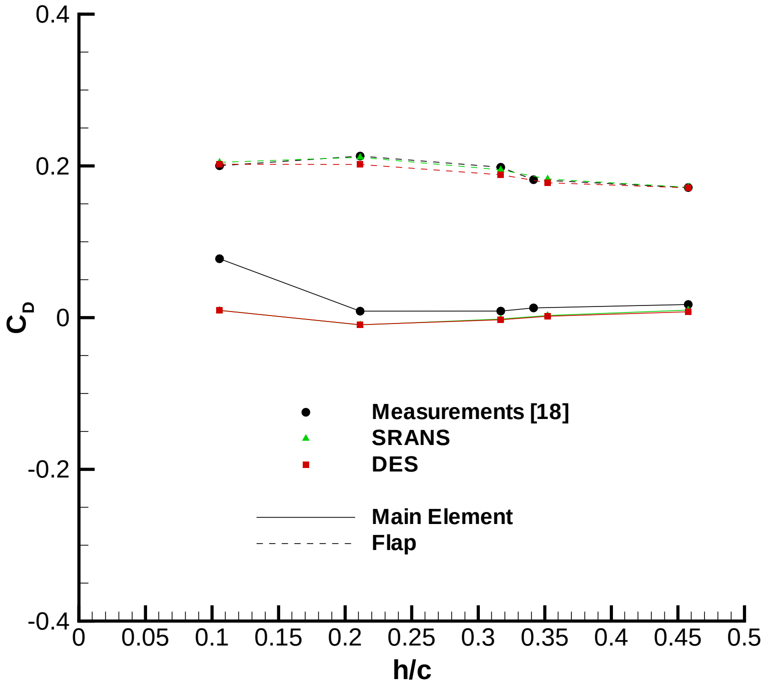

(b) C_D vs h/c.

Figure 5.6: Variation of the sectional downforce (a) and drag (b) coefficients with ride height at the wing centrespan ($y/c = 0$).

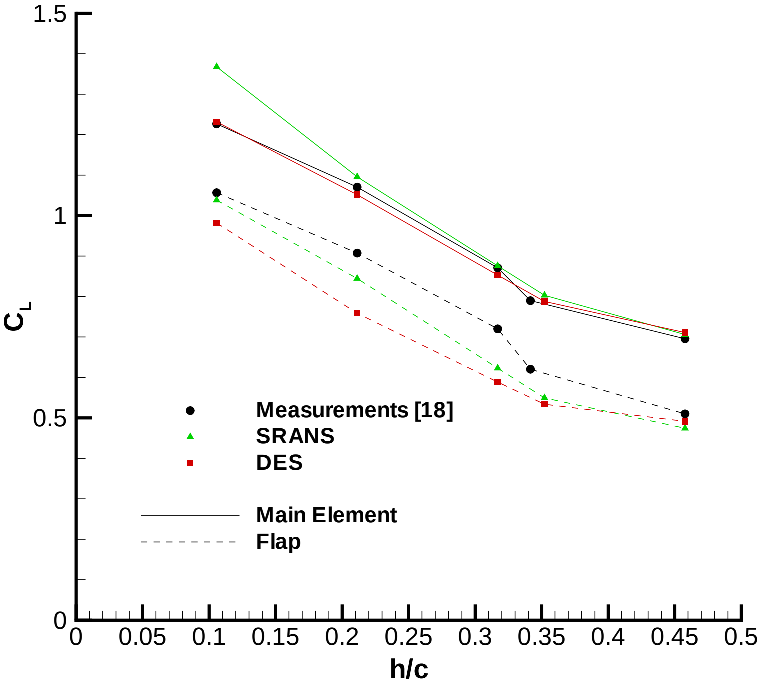

(a) C_L vs h/c.

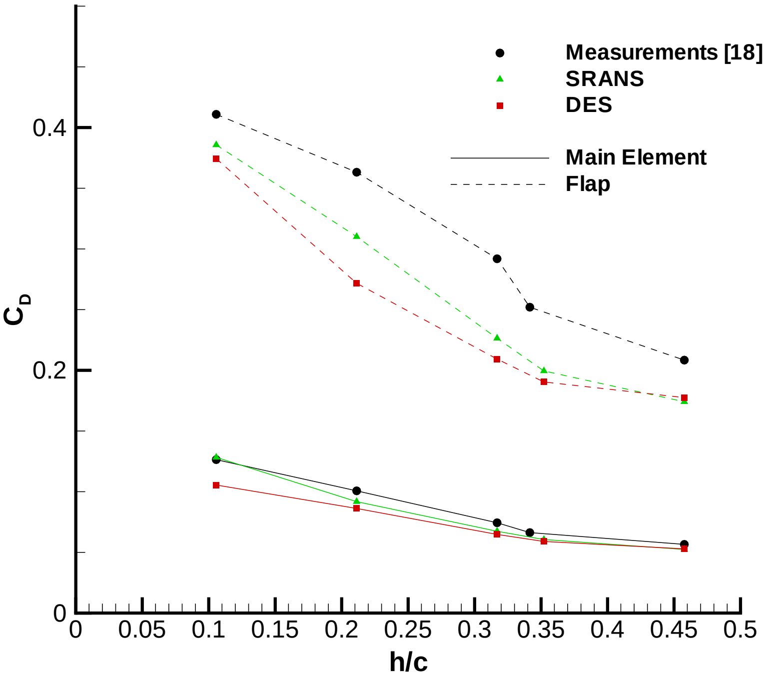

(b) C_D vs h/c.

Figure 5.7: Variation of the sectional downforce (a) and drag (b) coefficients with ride height at the wing tip ($y/c = -0.93$) for the combined case.

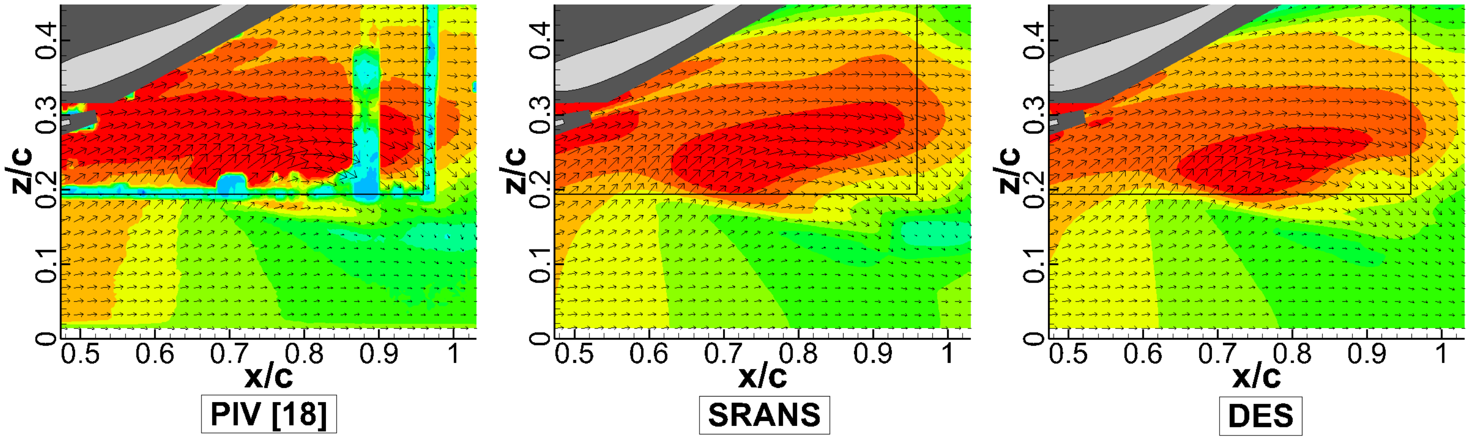

(a) $h/c = 0.211$

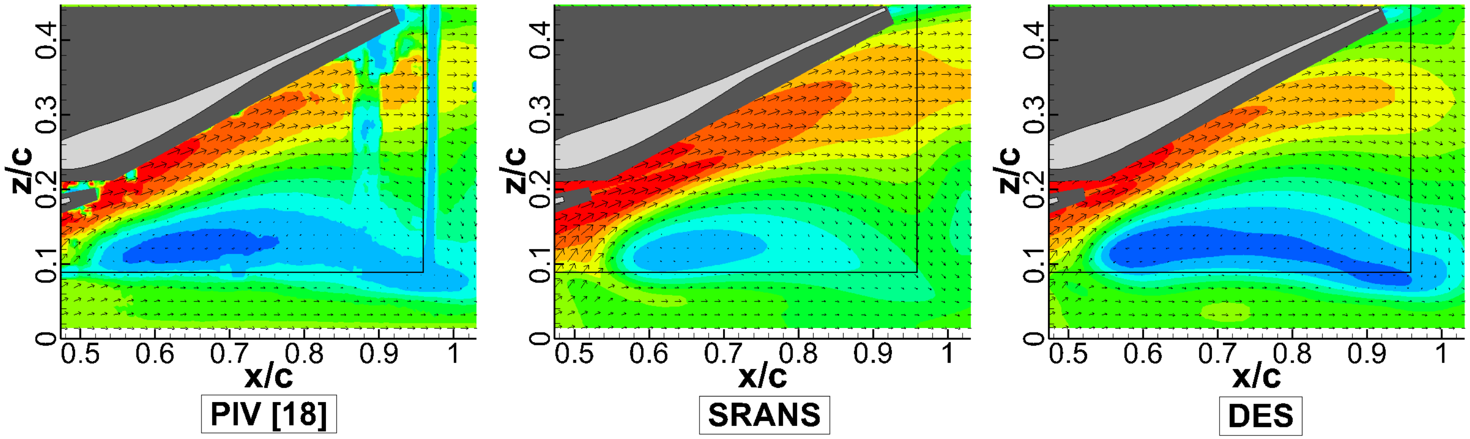

(b) $h/c = 0.106$

Figure 5.8: Comparison of the time-averaged streamwise velocity at plane $y/c = -0.933$ for different ride heights in the combined case. The grey areas hide the zones which the PIV could not capture.

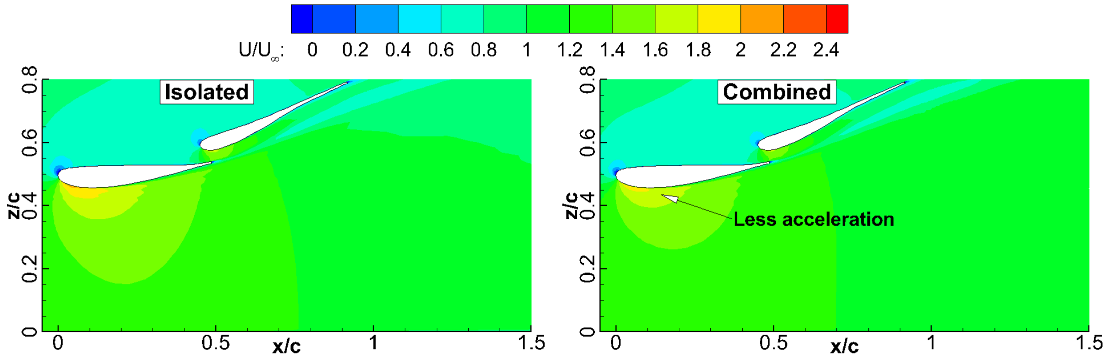

(a) $h/c = 0.458$

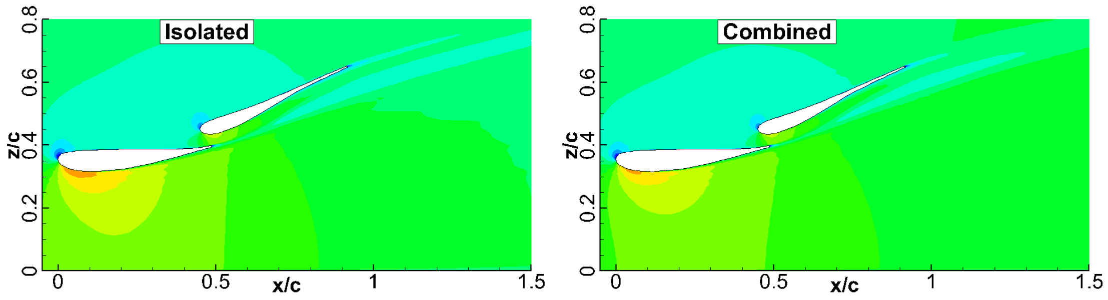

(b) $h/c = 0.317$

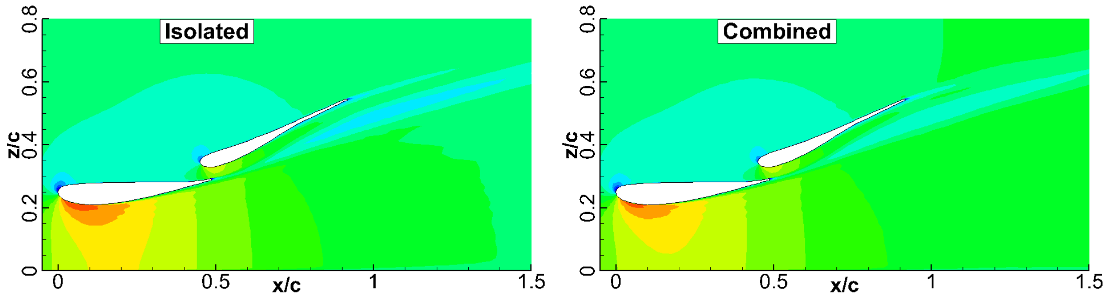

(c) $h/c = 0.211$

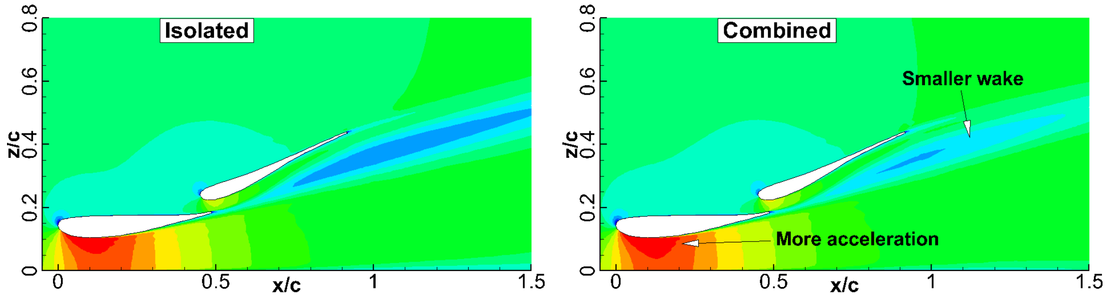

(d) $h/c = 0.106$

Figure 5.9: Contour plot comparing the time-averaged streamwise velocity at centrespan ($y/c = 0$) between the isolated and combined case at different ride heights. The results are from the DES model.

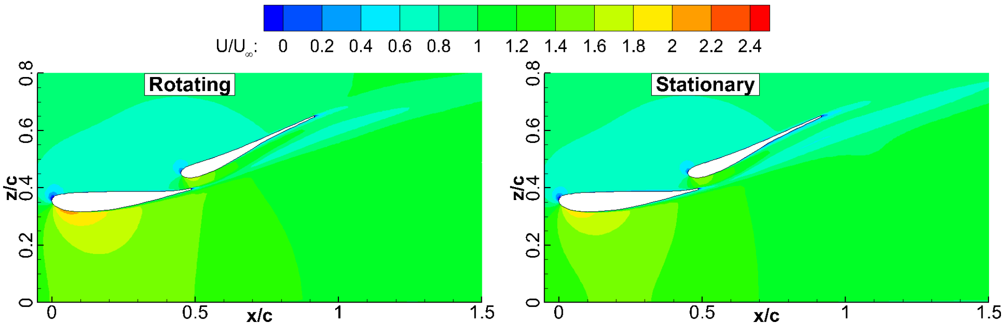

(a) $h/c = 0.317$

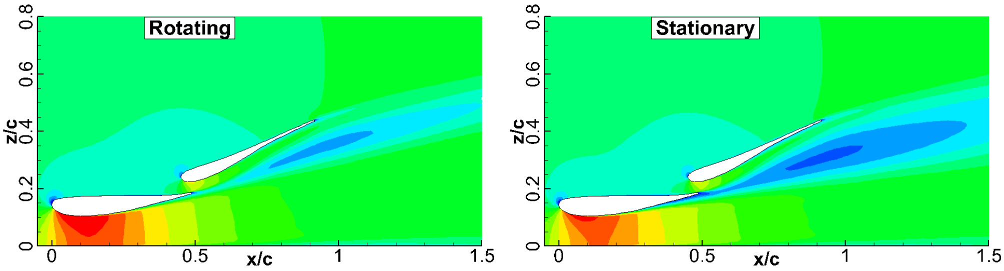

(b) $h/c = 0.106$

Figure 5.10: Contour plot of the time-averaged streamwise velocity for the combined case at centrespan ($y/c = 0$) with the wheel rotating and stationary. The results are from the SRANS model.

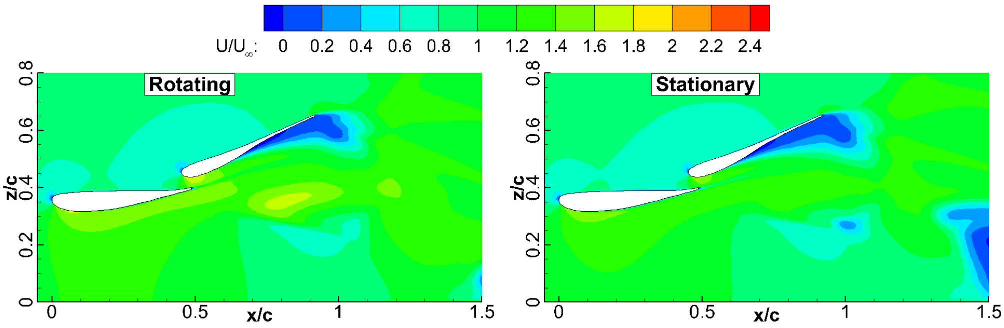

(a) $h/c = 0.317$

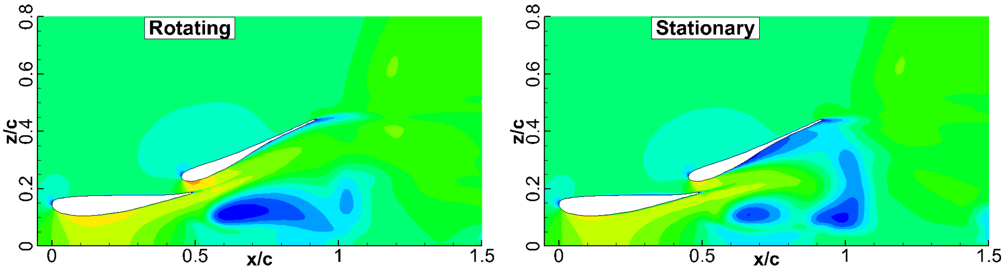

(b) $h/c = 0.106$

Figure 5.11: Contour plot of the time-averaged streamwise velocity for the combined case at the wing tip ($y/c = -0.933$) with the wheel rotating and stationary. The results are from the SRANS model.

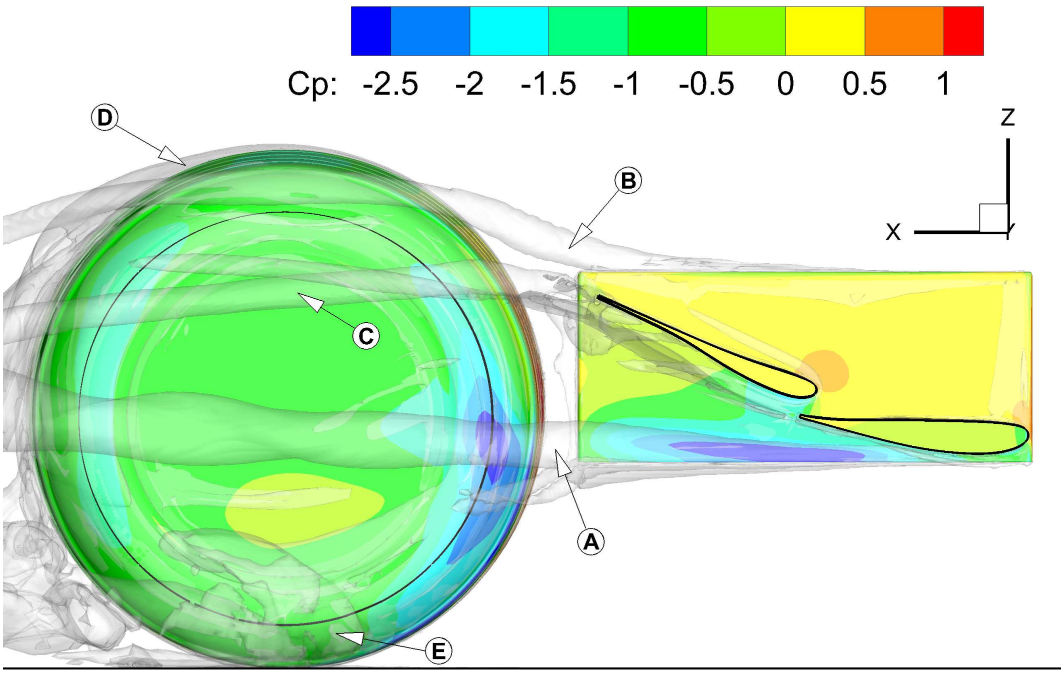

(a) Time-Averaged Flow.

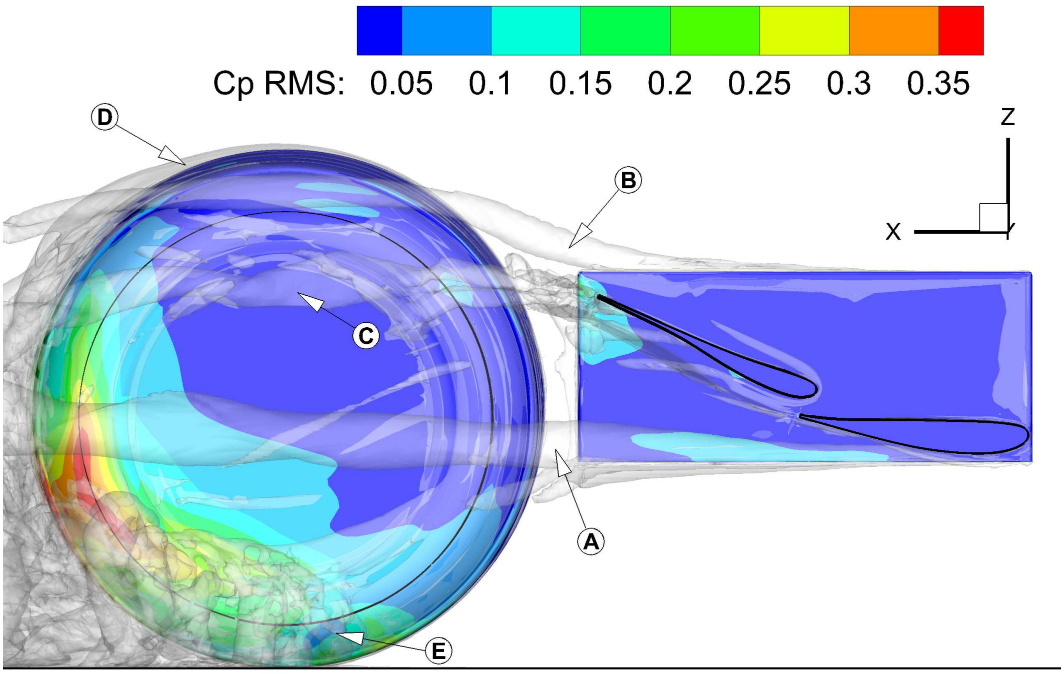

(b) Instantaneous Flow.

Figure 5.12: Time-averaged (a) and instantaneous (b) plots of the iso-surface of the Q-Criterion for the combined case at $h/c = 0.458$. Contours of the mean (a) and RMS (b) static pressure are also plotted. Results are from DES.

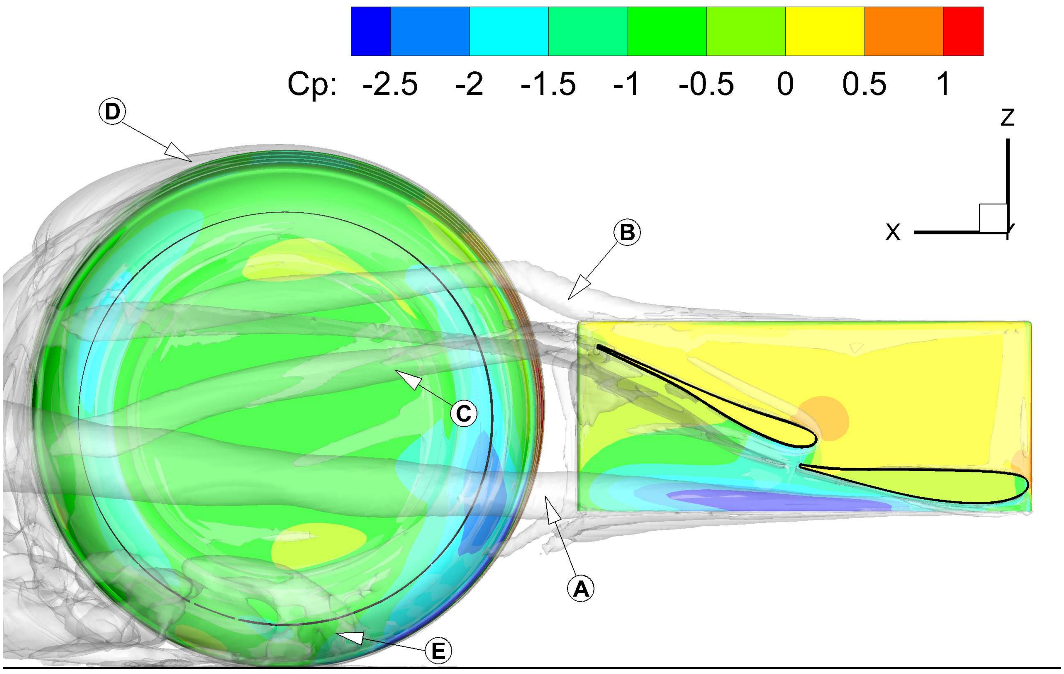

(a) Time-Averaged Flow.

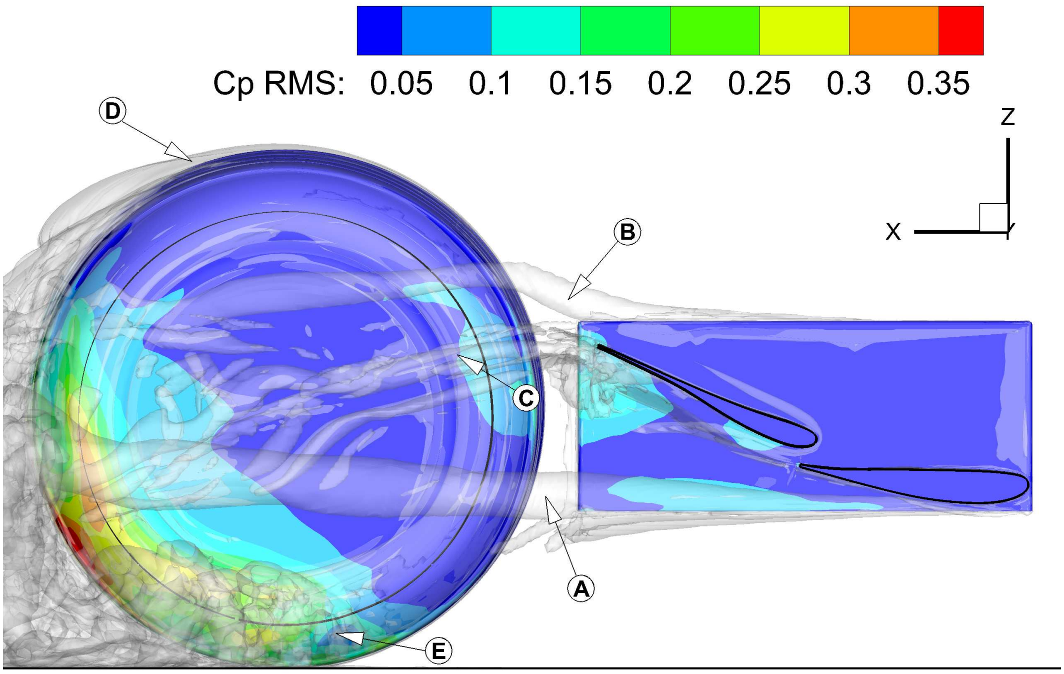

(b) Instantaneous Flow.

Figure 5.13: Time-averaged (a) and instantaneous (b) plots of the iso-surface of the Q-Criterion for the combined case at $h/c = 0.352$. Contours of the mean (a) and RMS (b) static pressure are also plotted. Results are from DES.

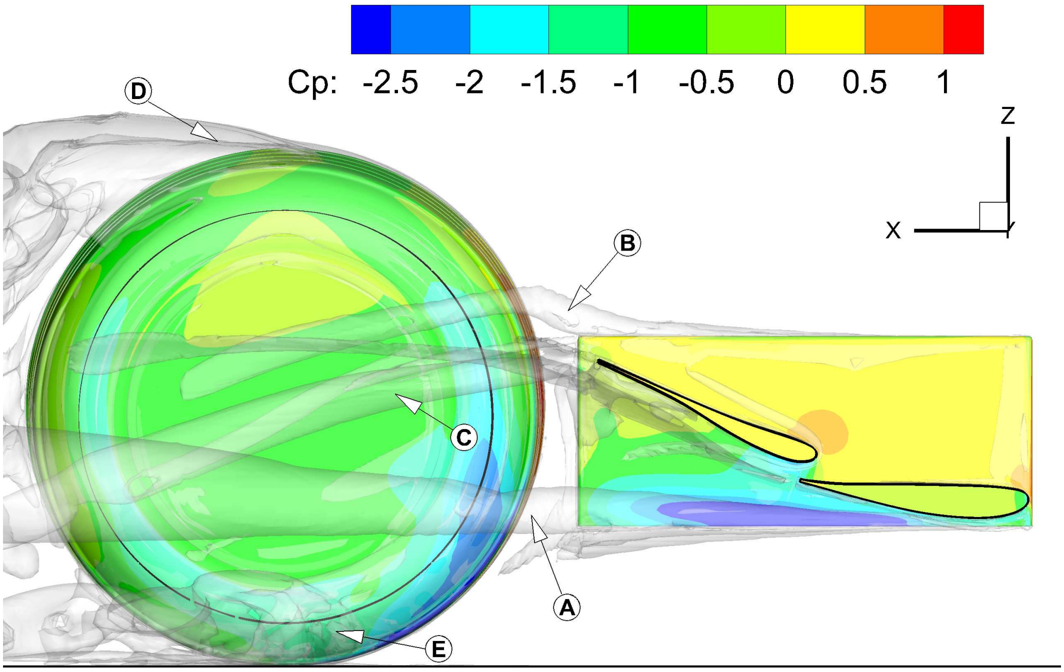

(a) Time-Averaged Flow.

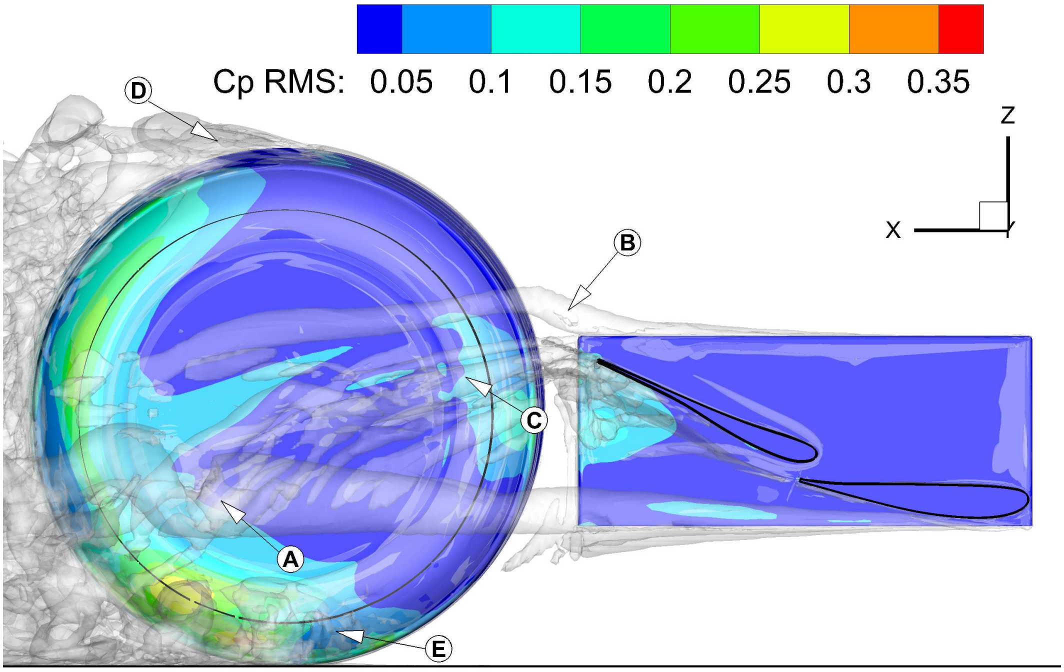

(b) Instantaneous Flow.

Figure 5.14: Time-averaged (a) and instantaneous (b) plots of the iso-surface of the Q-Criterion for the combined case at $h/c = 0.317$. Contours of the mean (a) and RMS (b) static pressure are also plotted. Results are from DES.

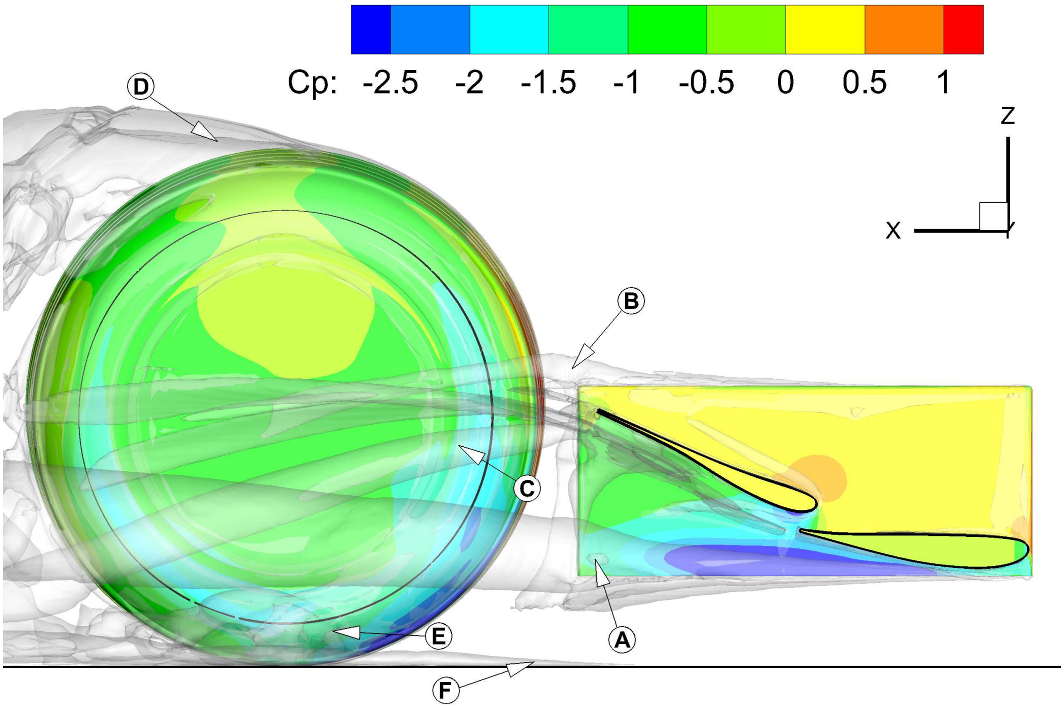

(a) Time-Averaged Flow.

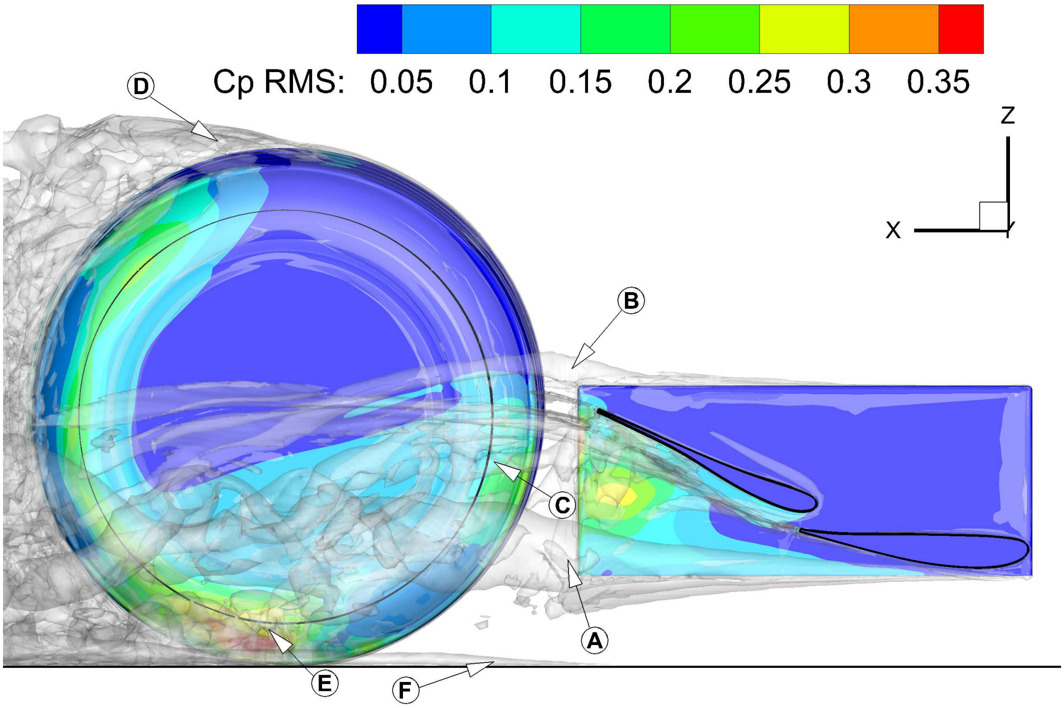

(b) Instantaneous Flow.

Figure 5.15: Time-averaged (a) and instantaneous (b) plots of the iso-surface of the Q-Criterion for the combined case at $h/c = 0.211$. Contours of the mean (a) and RMS (b) static pressure are also plotted. Results are from DES.

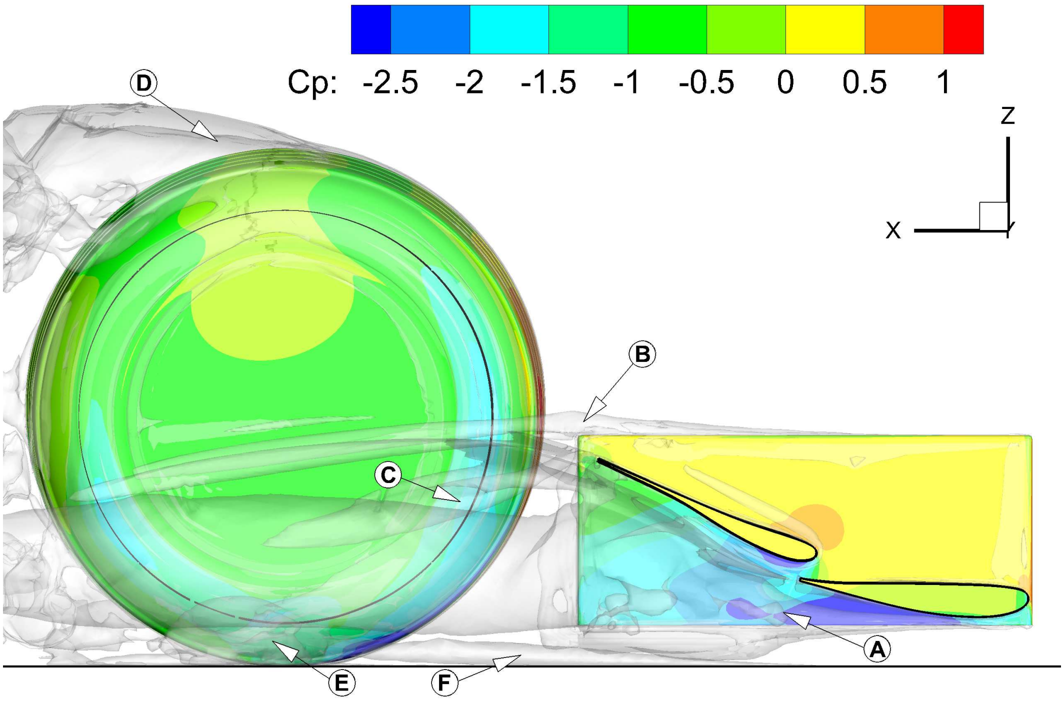

(a) Time-Averaged Flow.

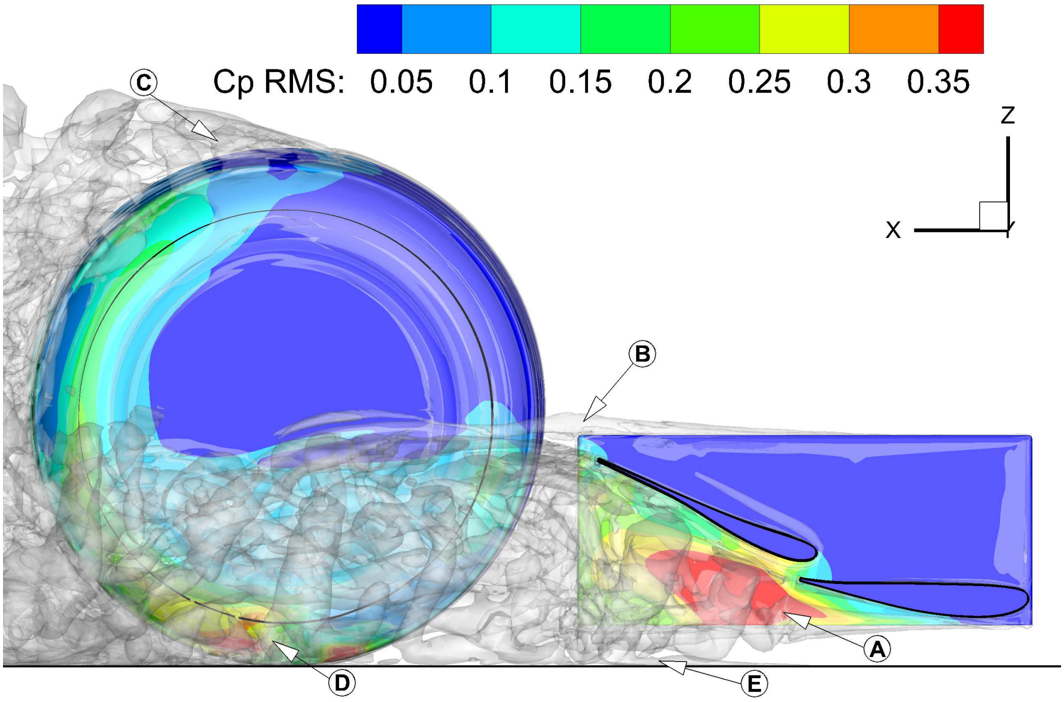

(b) Instantaneous Flow.

Figure 5.16: Time-averaged (a) and instantaneous (b) plots of the iso-surface of the Q-Criterion for the combined case at $h/c = 0.106$. Contours of the mean (a) and RMS (b) static pressure are also plotted. Results are from DES.

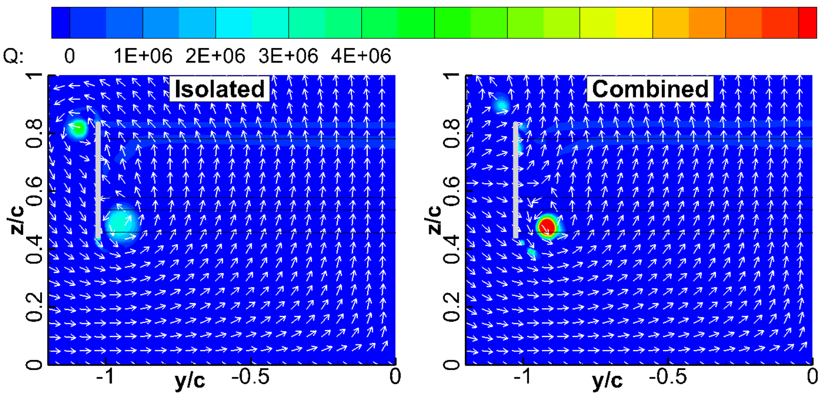

(a) $h/c = 0.458$

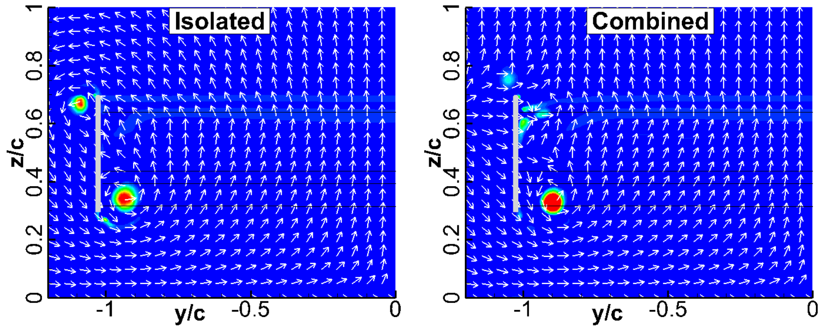

(b) $h/c = 0.317$

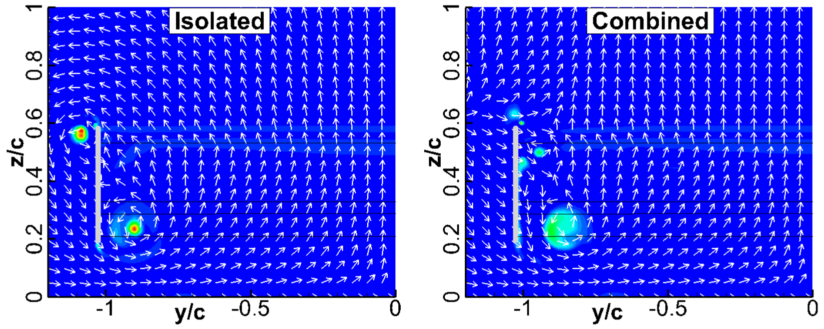

(c) $h/c = 0.211$

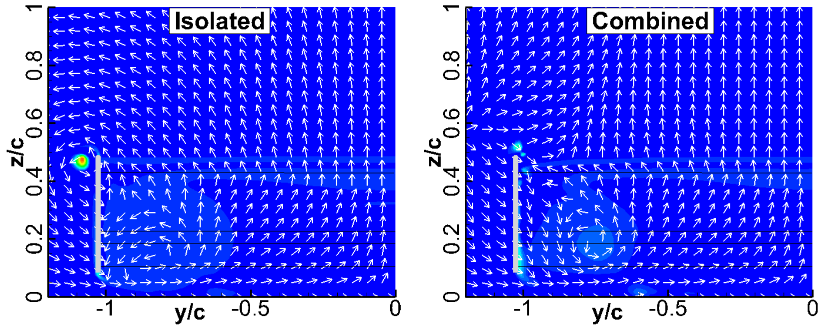

(d) $h/c = 0.106$

Figure 5.17: Contour plot of the time-averaged Q-Criterion at $x/c = 0.995$ for different ride heights in the combined case. Results are from DES.

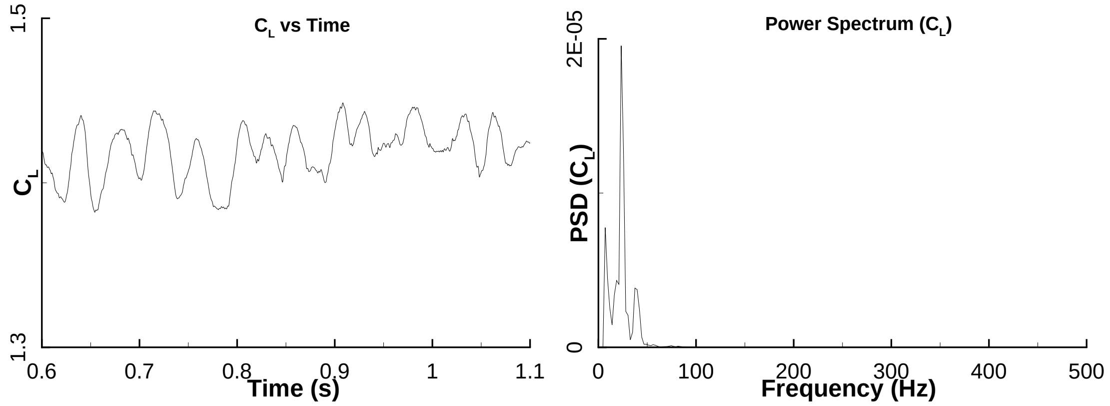

(a) $h/c = 0.458$

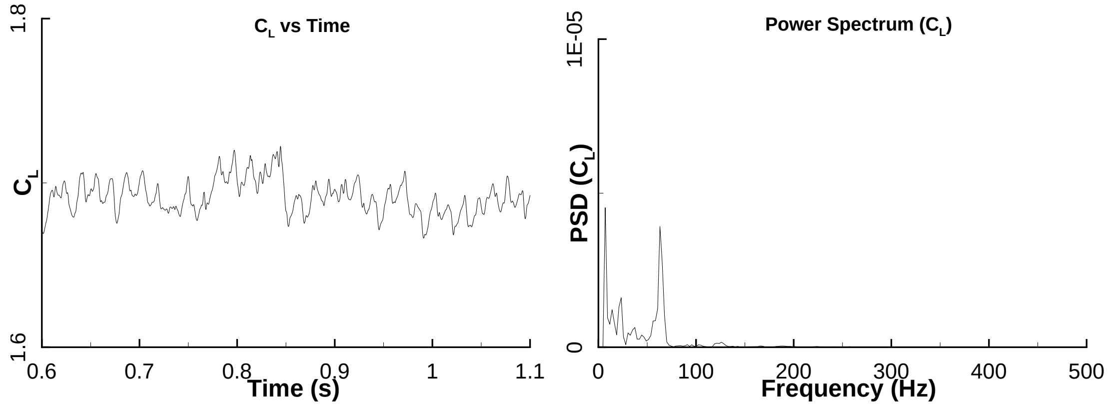

(b) $h/c = 0.317$

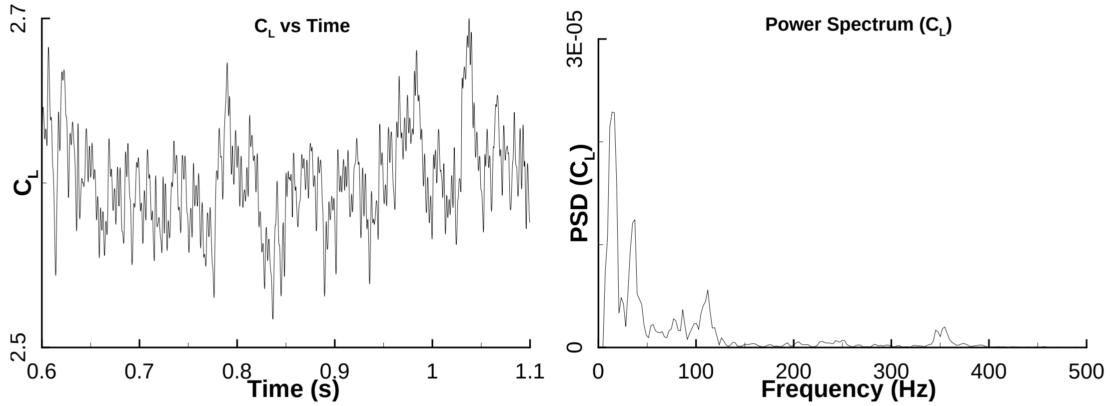

(c) $h/c = 0.106$

Figure 5.18: Time history and power spectral density of the wing downforce coefficient for the combined case at (a)$h/c = 0.458$, (b)$h/c = 0.317$ and (c)$h/c = 0.106$. The results are from the DES model.

Chapter 6

Effect of Wing Presence on Wheel Aerodynamics

The previous chapter focused on the aerodynamic effect the wheel presence has on the wing. This chapter now turns to the aerodynamic effect of the wing on the wheel flow. The first section analyses the trend of the wheel drag forces with changes in wing ride height, comparing the computational results to experimental measurements, and the wheel downforce is also described using the CFD results. This is then expanded upon by presenting the pressure distribution around the wheel. The section which follows describes the flow around the wheel and how the wing presence affects it, using PIV data where available and the DES results for additional information, while links are made where possible to the observed trends in force and pressure distribution. Finally, the last section uses the DES results to investigate the unsteady wake of the wheel.

6.1 Time-Averaged Analysis

6.1.1 Analysis of Wheel Drag

The effect of the wing presence at various ride heights on the wheel drag is presented in Figure 6.1, separated into the regions defined by Van den Berg [18]. The drag level for the isolated wheel is also included as a reference. Looking at the experimental measurements, the wheel drag is highest when the wing ride height is $h/c = 0.458$, at the upper boundary of Region II, and falls at an increasing rate with lowering ride height until the wing reaches $h/c = 0.352$. At this point, there is a sudden 22% drop in wheel drag and a local minimum is reached at the lower boundary of Region II. As the wing is lowered further, into Region III, the wheel drag increases once again and settles at an approximate drag coefficient of 0.55 for most of Region *III*. This is then followed by a linear drop in drag throughout Region *IV*.

The two CFD models differ in their wheel drag prediction for the combined case. The SRANS study shows a similar trend to Van den Berg's CFD results [18], but by avoiding non-conformal boundaries in the mesh, an overall higher drag is predicted. Even so, the value is still underpredicted throughout the ride height range, with up to a 23% error at high wing positions as a consequence of the drag change at $h/c = 0.352$ also being underpredicted.

The drag trend obtained using the DES model correlates better, with a maximum underprediction of 8% (at $h/c = 0.458$) and the sudden change of drag captured more accurately, although still underpredicted. In addition, the same observation can be made from the experimental data and the DES, with both of them showing the sudden change in drag crossing the isolated wheel drag (this is not the case with SRANS). Even though it had a negligible effect on the wing forces, the ability of the DES to model the wing vortices better than SRANS, as was demonstrated for the isolated wing in Section 3.4, is important in capturing their interaction with the wheel adequately.

At the two lower ride heights simulated, the DES does not appear to capture the force changes (in Regions *III* and *IV*) that were described above, although the lack of data at other ride heights renders further observations difficult. On the other hand, it does appear to predict a better trend than SRANS. As a final observation, it is noted that the drag of the wheel with the wing positioned at a high ride height approaches the drag of a stationary isolated wheel.

6.1.2 Analysis of Wheel Downforce

It is also of interest to look at the trend of the wheel downforce change with wing ride height. Because of the difficulties associated with obtaining this value experimentally, only CFD results are plotted in Figure 6.2. Having no directly comparable experimental data for validation, these results are only presented as a general overview of the wheel downforce.

The SRANS and DES show very similar trends, with the same discontinuity as for the drag in Region *II*. At high wing ride heights, the wheel produces more lift than the isolated case, but it starts producing downforce as the wing is lowered into Region *III*. It is noted that the SRANS predicts a bigger change in wheel downforce through the discontinuity compared to the DES, which is in contrast to what is observed for the drag. In addition, the DES predicts no change in downforce at low ride heights whereas the

SRANS shows a sharp drop. Overall, there appears to be a general correlation between the wheel drag and downforce, where higher drag values are accompanied by a lower downforce. This is not strictly adhered to as can be seen, for example, at $h/c = 0.458$ where an increase in wheel drag is accompanied by an increase in wheel downforce.

6.1.3 Surface Pressure Distribution

The surface pressure distribution around the wheel at the five locations defined in Figure 2.2 is plotted for various ride heights in Figures 6.3 to 6.7. They compare the CFD results with the experimental data available from Van den Berg [18], which it must be reminded was obtained with a different wheel geometry.

Figure 6.3 shows the pressure distribution around the centre of the wheel (location P3). Focusing on the results at $h/c = 0.458$, the pressure distribution around $\theta = 270°$ shares similar trends to the stationary isolated wheel results (see Figure 4.17). The pressure falls linearly as the flow travels around the top of the wheel until reaching a local minimum of $Cp = -1.2$ at $\theta = 274°$. It increases again as the flow moves further around the wheel, but the rate of change falls shortly afterwards. At this point, the CFD differs from the measurements whereby the former predicts a linear increase in pressure until reaching a maximum $Cp = -0.4$ whereas the experimental data shows the rate of change falling to zero before increasing sharply, reaching the same maximum Cp as the CFD. The high and low pressure peaks around the contact patch do not differ from the rotating isolated wheel results and the fall in pressure around the lower front part of the wheel shares the same smooth trend, but reaches a lower local minimum as the flow accelerates to a greater extent due to the presence of the wing. The SRANS model predicts the same pressure distribution as the DES while the flow is attached to the wheel. The main differences between the two models are in the wheel wake, where the DES appears to follow the experimental trend more accurately. Overall, both CFD models tend to overpredict the wheel base pressure which results in the underprediction of drag.

When the wing is lowered to $h/c = 0.352$, there is a large discrepancy in the pressure distribution around the top of the wheel between the measurements and CFD results. The experiments shows the local minimum pressure to be $Cp = -1.1$, as the separation point has moved by 8° around the front of the wheel compared to $h/c = 0.458$. The CFD on the other hand predicts a significantly higher rise of $\Delta Cp = 0.45$ in the local minimum compared to $h/c = 0.458$, accompanied by a 20° shift in the separation location around the front of the wheel. In addition, the predicted pressure distribution now resembles that of the rotating isolated wheel (see Figure 4.1). These changes predicted by the

CFD agree with the sudden change in drag and downforce discussed in Section 6.1.2. It is believed the reason the experimental pressure distribution does not show a significant change between the two ride heights is the difference in setup[1] used for the pressure data acquisition delaying the sudden change in wheel forces to a lower wing ride height. The front of the wheel is not significantly affected by this and both the experiment and simulations show a similar drop in the local minimum pressure of $\Delta Cp \approx -0.1$ between the two ride heights, as the lower wing accelerates the flow more around the front lower part of the wheel.

For the two lower heights of $h/c = 0.211$ and 0.106 shown in Figure 6.3(b), the experimental data now also has a similar pressure distribution to a rotating isolated wheel, with the separation around the top of the wheel occurring at $\theta > 270°$, followed by a drop in pressure. The CFD overpredicts the pressure around the top of the wheel (as it did for the isolated wheel) and predicts the separation too early by up to 5°. The DES once again captures the drop in pressure after the flow separates. As the wing is lowered, the separation point continues to move further towards the front of the wheel, resulting in lower suction above the wheel. The DES model captures this trend more accurately than the SRANS model. Finally, the stagnation point around the front of the wheel is correctly predicted by the CFD at $\theta \approx 356°$, just above the foremost point of the wheel. It is noted that the stagnation point around an isolated wheel occurs at $\theta \approx 5°$ and therefore, the presence of the wing has shifted it to a higher position. Its location is not very sensitive to ride height, moving 3° clockwise around the wheel when the wing is lowered from $h/c = 0.352$ to 0.106.

The pressure distributions for the other two probes located on the tyre tread (P2 and P4) are plotted in Figures 6.4 and 6.5. Comparing the position of the flow separation on the top of the wheel between locations P2, P3 and P4, it is observed to be constant along the tread as long as the flow separates at $\theta > 270°$ (i.e. for the lower wing ride heights). For $h/c = 0.458$, differences are present in the pressures recorded around the top of the wheel between the various locations on the tread. These differences are caused by the upper edge vortex of the wing travelling above the shoulder of the wheel at this ride height (see Figure 5.12(a)), therefore having a greater impact on the surface pressures at location P2.

As P2 is located behind the wing, the measured pressure around the front of the tyre is significantly affected by changes in ride height (in a similar way to what was described for location P3, albeit more pronounced). This can be seen in Figure 6.4(a), where as the wing is lowered from $h/c = 0.458$ to 0.352, there is a large decrease in pressure as the flow accelerates through the gap between the wing endplate and the wheel. The

---

[1] Different wheel geometry and lower freestream velocity ($20 m/s$)

discrepancy around the contact patch between the experiment and the CFD is caused by the difference in wheel geometry, as was explained in Section 4.1. In contrast, the pressure distribution around the front of the tyre measured at location P4 is not very sensitive to changes in ride height, with a small fall in maximum pressure as the wing is lowered. The CFD accurately captures the pressure around this part of the wheel. At the lower ride heights, the trend closely resembles that of an isolated wheel.

The pressure distribution at locations P1 and P5, plotted in Figures 6.6 and 6.7 respectively, show the pressure around either sides of the tyre. At P1, the pressure distribution is significantly altered by the wing wake when compared to the isolated wheel, as the vortices induce pressure changes on the wheel surface, and by analysing the trend in more details, the various flow features can be identified. Starting with the high ride height $h/c = 0.458$, the effect of the wing lower edge vortex on the wheel can be seen at $\theta = 8^\circ$ (labelled A in Figure 6.6(a)), causing much more suction than what is observed for an isolated wheel (see Figure 4.4). This effect can also be visualised in Figure 5.12(a) (the location of P1 is indicated by the black circular line on the wheel), where the lower edge vortex is seen to induce a local low pressure while being diverted around the wheel.

As the lower edge vortex travels downstream, it passes by the location P1 once again, at $\theta \approx 180^\circ$ (labelled A' in Figure 6.6(a)). Its effect is less evident than at the front of the tyre, as there is a local pressure maximum at this location, surrounded by two local minima. Looking at the isolated wheel trend (see Figure 4.4), the CFD predicted a continuous drop in pressure reaching a local minimum at $\theta \approx 180^\circ$. This did not correlate with the experimental data which recorded a local pressure maximum at this location. This discrepancy was explained in Section 4.1 as being caused by flow separation off the back of the experimental tyre shoulder caused by its different geometry. This theory is now reinforced by the DES results of the combined case (at $h/c = 0.458$), where the presence of the lower edge vortex causes the flow to separate from the tyre shoulder around $\theta = 180^\circ$, resulting in the local pressure maximum described above.

At the highest ride height, the upper edge vortex of the wing is not visible from the pressure distribution at P1. This is because it travels above the tyre shoulder, as can be observed in Figure 5.12(a), and therefore does not pass through P1. From the DES results, the third vortex (labelled C in Figure 5.12(a)) appears to have a very small effect on the pressure at $\theta \approx 330^\circ$, whereas the experimental data does not show any sign of the existence of the third vortex. Another discrepancy between the CFD and experiment can be observed at $\theta \approx 80^\circ$, where the latter shows a drop in pressure which the CFD fails to capture. This area is affected by the lower wheel wake (labelled E in Figure 5.12(a)) and the CFD predicts a similar trend to the isolated wheel. The difference measured in the wind tunnel could be associated to an interaction of the lower wheel wake with the wing lower edge vortex which is not captured by the CFD.

Going back to Figure 6.6(a) to investigate the lower ride height of $h/c = 0.317$, it can be seen that the peak suction (labelled A) has shifted to $\theta = 20°$ as the wing lower edge vortex has moved closer to the ground. In addition, the minimum pressure has increased by $\Delta Cp = 0.5$ because the vortex has more space to divert around the wheel as there is a larger gap between the endplate and the wheel at the vortex position (see Figure 5.14(a)). The high pressure peak which was at $\theta \approx 180°$ has also moved to a lower point on the wheel, while an overall higher pressure is predicted by the CFD between $180° < \theta < 270°$. This is caused by flow separation occurring behind most of the tyre shoulder as the wake structure has changed considerably compared to $h/c = 0.458$. As was discussed earlier, the experimental wheel does not appear to exhibit the change in wake structure until lower ride heights, resulting in the smaller differences observed at $180 < \theta < 270°$ between $h/c = 0.458$ and 0.317.

The upper edge vortex is visible for this ride height at $\theta = 325°$ (labelled B in Figure 6.6(a)), inducing a drop in pressure. The CFD underpredicts its effect, which is linked to an underpredicted strength of the wing upper edge vortex, as was observed for the isolated wing in Section 3.4. Finally, at $\theta \approx 80°$, the CFD still does not capture the large drop in pressure measured in the experiment, although it does capture the lower pressure than at $h/c = 0.458$. Comparing Figures 5.12(a) and 5.14(a), it can be deduced that the lower pressure is a consequence of the wing lower edge vortex (labelled A) constricting the size of the lower wheel wake (labelled E) as it comes closer to the ground.

When the wing is lowered to $h/c = 0.211$, the lower edge vortex continues to have an effect (albeit smaller) at $\theta = 30°$ (labelled A in Figure 6.6(b)) while the upper edge vortex moves down to $\theta = 345°$. It is noted that the drop in pressure at $\theta \approx 80°$ observed from the experimental data for the higher ride heights is now captured by the CFD (labelled C in Figure 6.6(b)), with the DES model predicting the trend with more accuracy. From Figure 5.15(a), the lower wheel wake (labelled E) is predicted to be smaller as it is further constrained by the wing lower edge vortex. Apart from this, the ground vortex (labelled F) is the only other visible flow feature change in the area which could explain the correctly predicted drop in pressure, although it is noted that it travels quite far from the wheel. Around the top of the wheel ($230° < \theta < 320°$), the pressure distribution has become less sensitive to ride height changes as the wing vortices are all located below this region.

At the lowest ride height plotted in Figure 6.6(b), the influence of the wing lower edge vortex at $\theta = 25°$ is much weaker as it undergoes breakdown early beneath the flap (see

Figure 5.16(a)), losing most of its strength. The CFD now underpredicts the maximum suction by 33% compared to 17% at the other ride heights. This is similar to the 29% underprediction for the isolated wheel case (see Figure 4.4). The upper edge vortex has moved to $\theta = 4°$ (labelled B) and contributes to the minimum suction peak in the experimental data. The CFD underpredicts its influence and the minimum pressure occurs further around the wheel.

Finally, to conclude this section, the pressure distribution on the other side of the tyre, at the position P5 (see Figure 6.7), is investigated. As it is located far from the wing, the results resemble the trend for the isolated wheel shown in Figure 4.5. The main changes caused by different wing ride heights occur between $160° < \theta < 270°$ when the structure of the wheel wake suddenly changes. Otherwise, the pressures are not very sensitive to the wing's vertical position. The discrepancy between the experimental data and the CFD at $\theta \approx 180$ is a result of the presence of the wheel support strut, as was already suggested in Section 4.1.

6.1.4 Wheel Flow

The results discussed so far have mainly been related to changes occurring to the wheel surface pressure, with little focus on the surrounding flowfield. This is now investigated using the velocity field on the various planes defined in Figure 2.11 and is then completed with a further analysis on the wheel wake using the DES results.

6.1.4.1 Plane Y=0D

This plane, shown in Figure 6.8, is focused on the area above the wheel where the flow separates and the upper wake of the wheel begins. At $h/c = 0.458$, there is a large acceleration as the flow stays attached around the highest point of the wheel. The maximum velocity reaches similar values to that observed above a stationary isolated wheel (see Figure 4.19(a)), although the flow separates earlier creating a taller wake. Both CFD models appear to predict separation later than the PIV, with a smaller shear layer angled more towards the ground.

At $h/c = 0.317$, the flow separation moves towards the front of the wheel, reducing the maximum velocity around the top of the wheel. This effect was previously observed from the pressure distribution at location P3 (Figure 6.3) using the CFD results, where there was an increase in pressure and a shift in the separation point when the wing was lowered to $h/c = 0.317$. The PIV result supports the suggestion that the discrepancy between the experimental and computational pressures around the top of the wheel at

$h/c = 0.317$ is caused by the different wheel geometry used to obtain the pressure data, which delays the sudden change in the wheel flowfield to a lower ride height. The different flow field now shares common features with a rotating isolated wheel (see Figure 4.6) resulting in a taller wake. In contrast to the CFD prediction at $h/c = 0.458$, the wake is now predicted to grow faster than what the PIV suggests and the wake height is overpredicted.

As the wing is lowered to $h/c = 0.211$ and then to $h/c = 0.106$, the separation continues to move forward while the wake grows taller. The SRANS model does not capture this trend and by $h/c = 0.106$ it underpredicts the height of the wake. In contrast, the DES model captures both the movement of the separation point and the changes in the wake growth.

6.1.4.2 Plane Z=0.53D

This plane, shown in Figure 6.9, focuses on the inner front corner of the wheel. The location of sensor P1 is indicated and is equivalent to $\theta = 356°$ in Figure 6.6. At $h/c = 0.458$, the flow, enhanced by the proximity of the wing lower edge vortex, accelerates around the tyre shoulder to velocities exceeding those around a rotating isolated wheel (see Figure 4.7). The CFD underpredicts this, which results in the higher pressure predicted at P1. Moving the wing to $h/c = 0.317$, the PIV shows a reduction in the maximum velocity as the lower edge vortex moves away, but the overall velocity field is similar. In contrast, the CFD shows a drop in velocity behind the wing tip ($X/D = -0.55$) followed by a band of lower velocity along the wheel. From this, it can be concluded that the CFD overpredicts the separation under the flap tip resulting in the creation of the third vortex, which is then responsible for the band of lower velocity further downstream. This discrepancy between the experiment and CFD should not significantly affect the predicted wheel downforce and drag, but would alter the wheel sideforce.

When the wing is lowered to $h/c = 0.211$, this plane intersects with the wing wake and as a consequence the velocity drops below the values of the isolated wheel (see Figure 4.7). The wing upper edge vortex passes above this plane but is too far to have a significant effect on the streamwise velocity. Finally, at $h/c = 0.106$ the velocity increases again as the wing wake has moved below this plane. The CFD once again underpredicts the flow acceleration around the tyre shoulder, which results in higher surface pressures.

6.1.4.3 Plane Z=0.55D

This plane, shown in Figure 6.10, focuses on the inner rear corner of the wheel. The location of sensor P1 is indicated and is equivalent to $\theta = 187°$ in Figure 6.6. At the highest ride height, the PIV results show a large acceleration around the tyre shoulder, followed by a small recirculation as the flow separates. There is a larger region of flow reversal concentrated around $Y/D = 0$, although it is smaller than for an isolated wheel (see Figure 4.8). The computations, especially the SRANS model, overpredict the separation from the tyre shoulder, which is accompanied by an underprediction in the velocity around P1. This agrees with the pressure distribution results at P1, where the CFD overpredicts the pressure rise which occurs at $\theta = 180°$. Another feature that can be observed from Figure 6.10(a) is the low streamwise velocity at $Y/D = 0.4$ where the plane intersects with the wing lower edge vortex. The DES model captures this feature more accurately than SRANS due to its better capability at modelling vortex development.

At $h/c = 0.317$, the wake structure changes significantly, where the flow separates earlier from the tyre shoulder, with a large flow reversal behind the wheel extending downstream to $X/D = 0.75$. The flow reversal region is larger than for a rotating isolated wheel, although the overall size and shape of the wake does not change significantly. Both CFD models predict similar flowfields, with the effect of the third vortex seen at $Y/D \approx 0.3$ where the velocities are underpredicted.

As the ride height is reduced, the region of flow reversal extends further downstream while the wake becomes slightly wider. The DES model captures the shape of the wake more accurately than the SRANS model, although it underpredicts the increase in length of the flow reversal region.

6.1.4.4 Plane X=0.6D

This plane focuses on the wake directly behind the wheel, with Figures 6.11 and 6.12 respectively showing the horizontal and vertical velocity field. In addition, Figure 6.13 plots the streamwise velocity obtained with the DES model. The presence of the wing has made the wheel wake more complex and asymmetric compared to an isolated wheel (see Figure 4.9). Starting with $h/c = 0.458$, a strong downwash is observed, with the flow then diverting both inboard and outboard[2] as it reaches the ground. This forms part of two vortical structures: an inner one at $Y/D = 0.4$ and an outer one at $Y/D = -0.1$. Because they are partly or fully within flow reversal regions, as can be seen in Figure 6.13,

---

[2] Inboard is towards the symmetry plane, behind the wing.

they are not considered to be longitudinal vortices. Looking at Figure 6.11(a), the flow is seen to enter the wheel wake from both sides. At the outboard side, the crossflow is concentrated around $Z/D = 0.5$, similarly to the isolated wheel. At the inboard side, the crossflow is stronger and located higher, at around $Z/D = 0.8$. Below this, at $Y/D = 0.4$, the wing lower edge vortex is visible and it contributes to the increased strength of the crossflow. The wing upper edge vortex travels above the wheel shoulder and into the wheel wake. Its position is marked with a white circle and it is noted that the vortex is responsible for the local reduction in crossflow. From Figure 6.13(b), it can be seen that the wake is vertically shorter than for a rotating isolated wheel (see Figure 6.13(a)), with the lower recirculation region extending inboard. The presence of the wing and its lower edge vortex at $h/c = 0.458$ increase the flow separation from the inboard lower front surface of the wheel, which results in the larger lower wake observed.

Figure 6.11(b) shows the horizontal velocity at $h/c = 0.352$. The crossflow is much lower around the inboard top corner of the wheel, as the wing lower edge vortex is closer to the ground and of lower strength after undergoing breakdown. The lower position of the vortex also results in the lower wheel wake being constrained, suppressing the inboard vortical structure near the ground. In the upper wake, two vortical structures are now visible and they are equivalent to the ones observed behind the rotating isolated wheel (see Figure 4.9). The downwash in the wake is greatly reduced, as shown in Figure 6.12(b), and as a consequence so is the crossflow near the ground. The stagnation point on the ground has moved from $Y/D = 0.1$ at $h/c = 0.458$ to $Y/D = 0.25$. It is noted that the PIV results at this ride height appear to contain some discontinuity between the four planes used to create the larger image. This is especially visible in Figure 6.12(b), where the stronger downwash in the lower inboard image does not match the velocity in the upper inboard image. It is believed that this is due to the proximity of $h/c = 0.352$ to the ride height where a sudden change in wheel flow structure occurs, whereby a small experimental change could cause large differences in the velocity field.

The streamwise velocity predicted by the DES is shown in Figure 6.13(c). Compared to a rotating isolated wheel (see Figure 6.13(a)), the recirculation region is of a similar height and the streamwise velocity in the region outboard of the wheel is nearly identical, as the wing has little effect on this side. The recirculation region is now contained behind the wheel and it does not spill out inboard close to the ground, as the wing lower edge vortex restricts the growth of the wheel's front lower wake (labelled E in Figure 5.14(a)).

As the wing is lowered further, the changes in the velocity field are less severe and mainly occur inboard of the wheel. From Figure 6.11 the crossflow around the inboard top corner of the wheel is seen to decrease, reaching values lower than the isolated wheel. The wing lower edge vortex is still visible in the lower inboard corner at $h/c = 0.211$, but it is no longer present at $h/c = 0.106$ as it breaks down more severely under the wing losing most of its strength and structure. The unsteady flow that emanates from the breakdown dissipates the lower wheel wake and also results in a region of lower streamwise velocity, which can be seen in Figure 6.13(d). As a consequence, the flow stays attached around the lower shoulder of the wheel and the recirculation region is reduced. From the streamwise velocity plot, it can also be noticed that the height of the wake increases with decreasing ride height, agreeing with the observation made when analysing the separation at the top of the wheel in Section 6.1.4.1.

Looking at the CFD results, there are inaccuracies in the flowfield predicted when using the SRANS model. From Figure 6.11, a large amount of crossflow from the outboard side of the wheel to the inboard side is predicted at all ride heights. In addition, the two lower vortical structures at $h/c = 0.458$ are not predicted in the same location, with a much weaker crossflow near the ground where the downwash is incorrectly predicted (see Figure 6.12). This crossflow is then overpredicted at $h/c = 0.211$ and $h/c = 0.106$, which shows the inadequacy of the SRANS model to capture the changes occurring in the wheel wake. In contrast, the DES model captures the various flow structures and the observed changes with good accuracy, despite some velocities being incorrectly predicted.

6.1.4.5 Further discussion

As it was shown in the previous sections, the DES can accurately capture the flowfield around a wheel interacting with the wake of a wing, thereby justifying the use of the numerical results to conduct some additional investigation into the wheel wake.

The sudden change in wheel drag which was discussed in Section 6.1.1 has already been associated to a large change in the wheel wake structure. This change can be seen comparing the structure labelled D in Figure 5.13(a) and 5.14(a). A novel observation is that at high ride heights (i.e. high drag mode), the wake resembles the structure seen behind a stationary wheel (see Figure 4.20) whereas at lower ride heights, in the low drag mode, it is similar to the wake of a rotating wheel (see Figure 4.10). It is interesting to note that when the wake is in the high drag mode and the flow looks similar to a stationary isolated wheel, the presence of the wing is essentially negating the effect the wheel rotation had on the flow separation in the isolated case.

Van den Berg [18] suggested that, in addition to the wing circulation effect, which delays the flow separation from the top of the wheel, the sudden change in wake structure was caused by the wing upper edge vortex travelling above the wheel. Using the results from the DES simulation, his theory does not appear to be valid when the wing is at

$h/c = 0.352$, as the upper edge vortex (labelled B in Figure 5.13(a)) travels along the side of the wheel and yet the wake structure (labelled D) is still in the higher drag mode.

It is proposed that, although the wing upper edge vortex does influence the wheel wake, it is not the main cause of the change in wheel wake structure and that the wing lower edge vortex also plays an essential role. At high ride heights, it increases the crossflow around the upper half of the wheel, feeding the region behind the tyre with high energy flow, while also inducing downwash (see Figure 6.14(a)). These effects are believed to contribute to promoting a wake similar to that of an isolated stationary wheel.

As the wing is moved closer to the ground, the lower edge vortex breaks down before reaching the rear of the tyre, weakening its influence on the wheel wake (see Figure 6.14(b)), which in turn becomes similar to that of an isolated rotating wheel.

6.2 Unsteady Flow Analysis

The mean flowfield around the wheel has been investigated in the previous section, but to further understand the effect of the wing on the wheel wake, the unsteady nature of the flow is analysed using the Detached-Eddy Simulation results.

The change in wheel drag with time at $h/c = 0.458$ is plotted in Figure 6.15(a). The drag oscillates with large amplitudes of ±29%, with a dominant frequency of $23Hz$. From the RMS value of pressure on the wheel and the analysis of various pressure monitors in the surrounding flow, it was deduced that these fluctuations originate from the rear lower half of the tyre. Interestingly, although the frequency of the oscillations is the same as what was observed from the wing forces (see Section 5.3), the large pressure fluctuations on the wheel appear to be concentrated around the outboard lower wake, which has a weak association with the wing. It is believed that the low frequency is connected to an interaction between the upper wake (labelled D in Figure 5.12(b)) and outboard wheel lower wake (the outboard counterpart of the structure labelled E in Figure 5.12(b)), which is composed of shed vortices as described in Section 4.1.2. With the wing lowered to $h/c = 0.352$, the amplitude of the drag fluctuations decreases to ±15%, although the frequency is still the same, and there are lower RMS values of pressure in the rear lower half of the wheel.

For the lower ride heights, the different upper wheel wake structure associated to the low drag mode is visible, labelled D in Figure 5.14(b). The separation from the top of the wheel sheds weak arch shaped vortices, similarly to what was described for a rotating isolated wheel in Section 4.1.2. The lower wheel wake (labelled E in Figure 5.14(b)) sheds vortices at a frequency of $\approx 200Hz$, which is of the same order of magnitude as the frequency of the spiralling tail emanating from the wing lower edge vortex breakdown (labelled A). As the latter is of a higher strength than the vortices shed from the lower wake, it absorbs them. The drag fluctuations with time at $h/c = 0.317$, plotted in Figure 6.15(b), shows a drop in the amplitude to ±10%, with a more broadband range of frequencies. On the other hand, a dominant low frequency of $7Hz$ is detected from the fluctuations in downforce. These have been linked to changes in pressure behind the contact patch of the tyre.

From Figure 5.15(b), with the wing at $h/c = 0.211$, the instantaneous wake structure remains similar, with the main difference being a higher RMS in pressure around the lower wheel wake (labelled E). Finally, at $h/c = 0.106$, the large amount of unsteady flow coming from the breakdown of the wing lower edge vortex quickly absorbs the vortices shed from the lower front of the wheel (labelled D in Figure 5.16(b)). The drag fluctuation with time now contains a dominant frequency of $9Hz$ (see Figure 6.15(c)), with an amplitude of ±13%, and it is caused by changes in the base pressure.

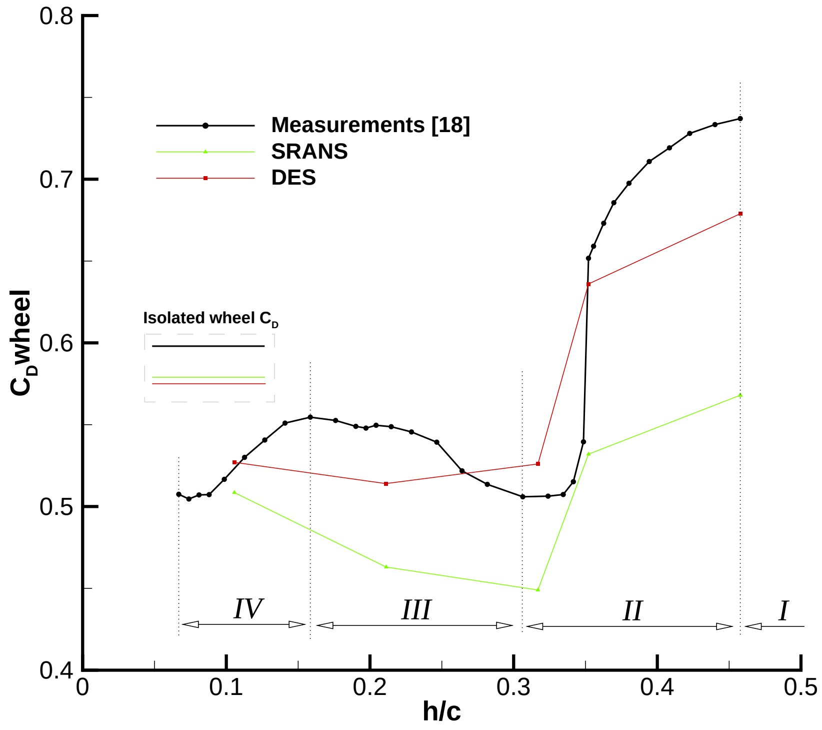

Figure 6.1: Variation of the wheel drag coefficient with ride height for the combined case. The results from the isolated wheel are indicated by horizontal lines.

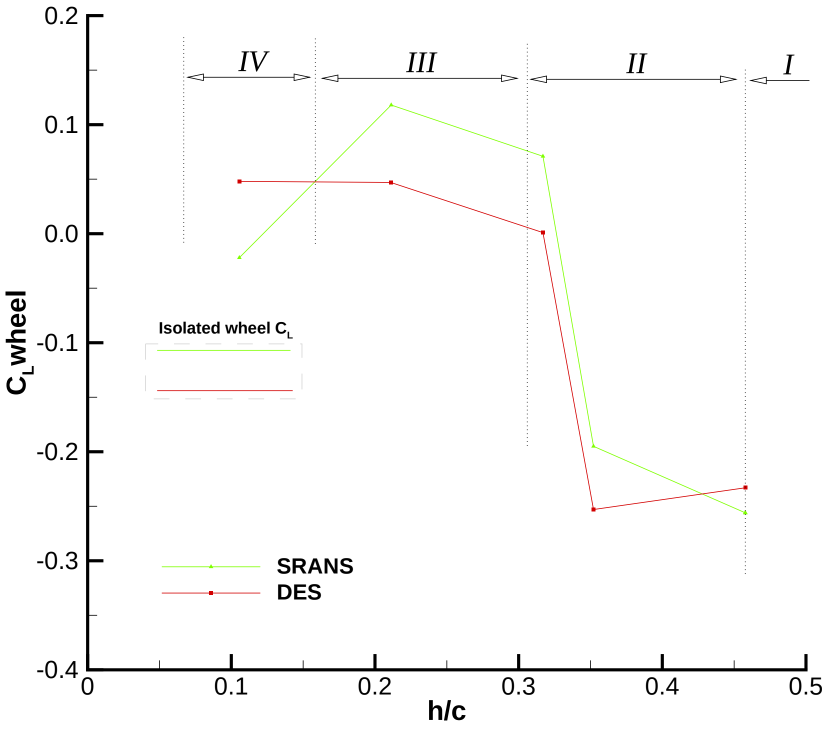

Figure 6.2: Variation of the wheel downforce coefficient with ride height for the combined case. The results from the isolated wheel are indicated by horizontal lines.

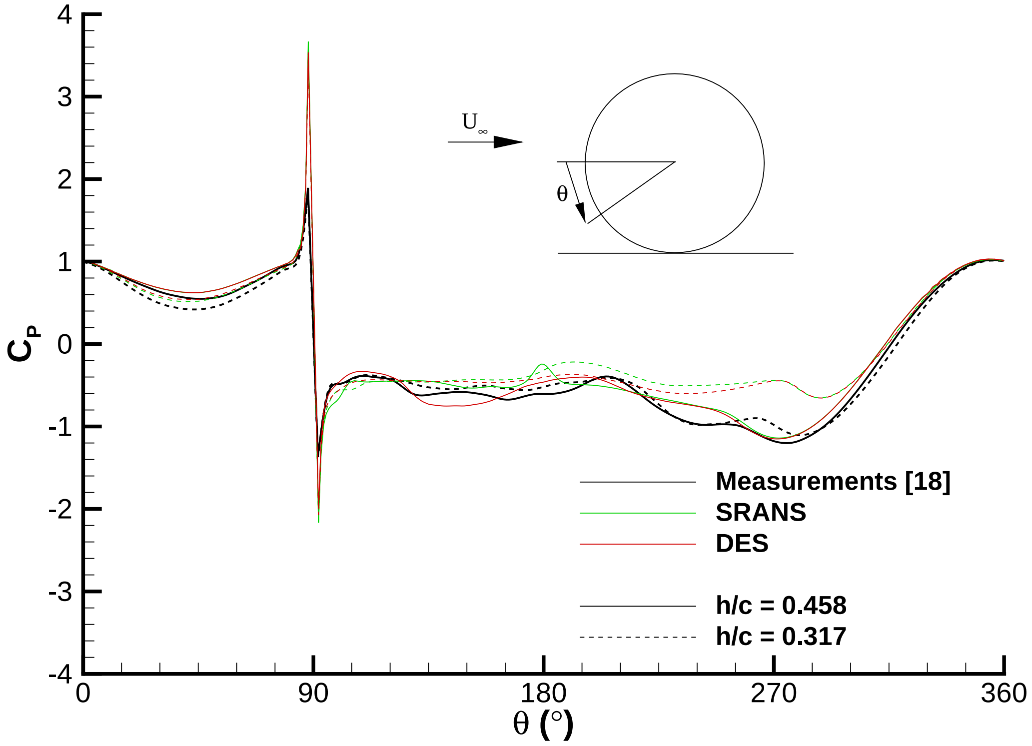

(a) $h/c = 0.458$ & $h/c = 0.317$

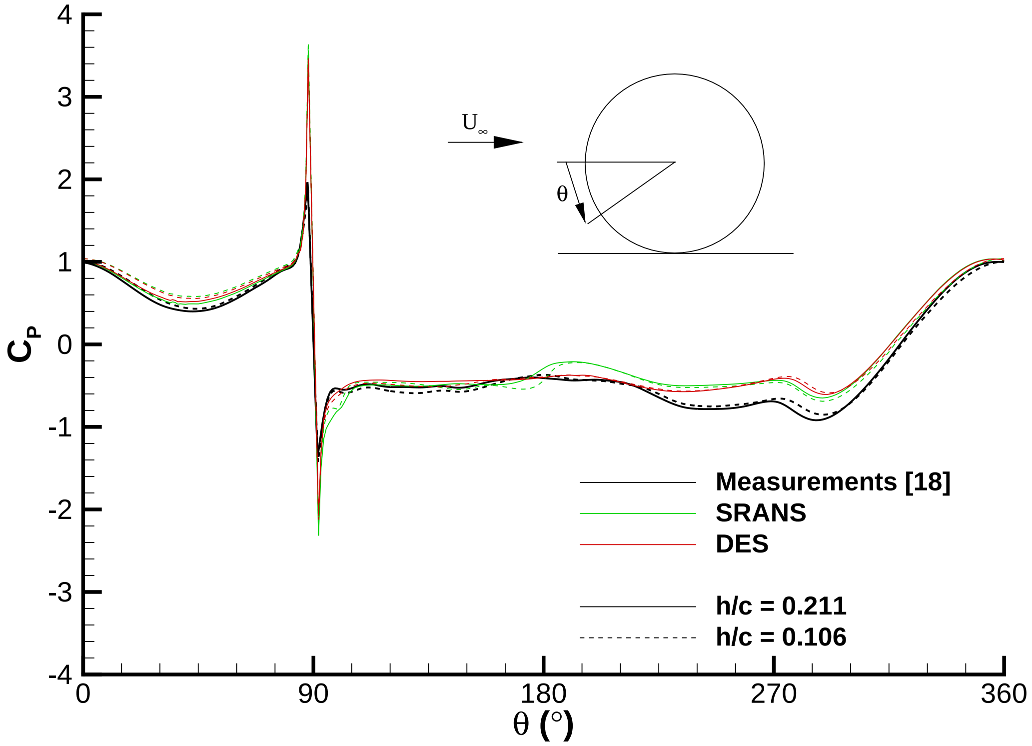

(b) $h/c = 0.211$ & $h/c = 0.106$

Figure 6.3: Experimental and computational pressure distribution around the rotating wheel centreline, at location P3, for the combined case at various ride heights.

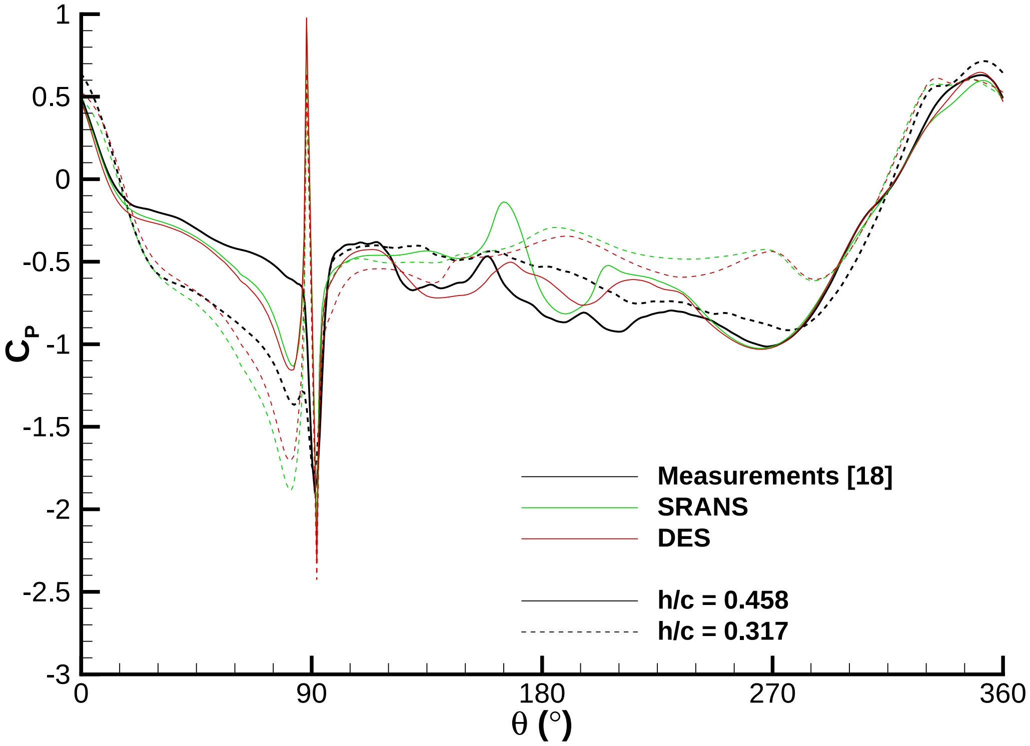

(a) $h/c = 0.458$ & $h/c = 0.317$

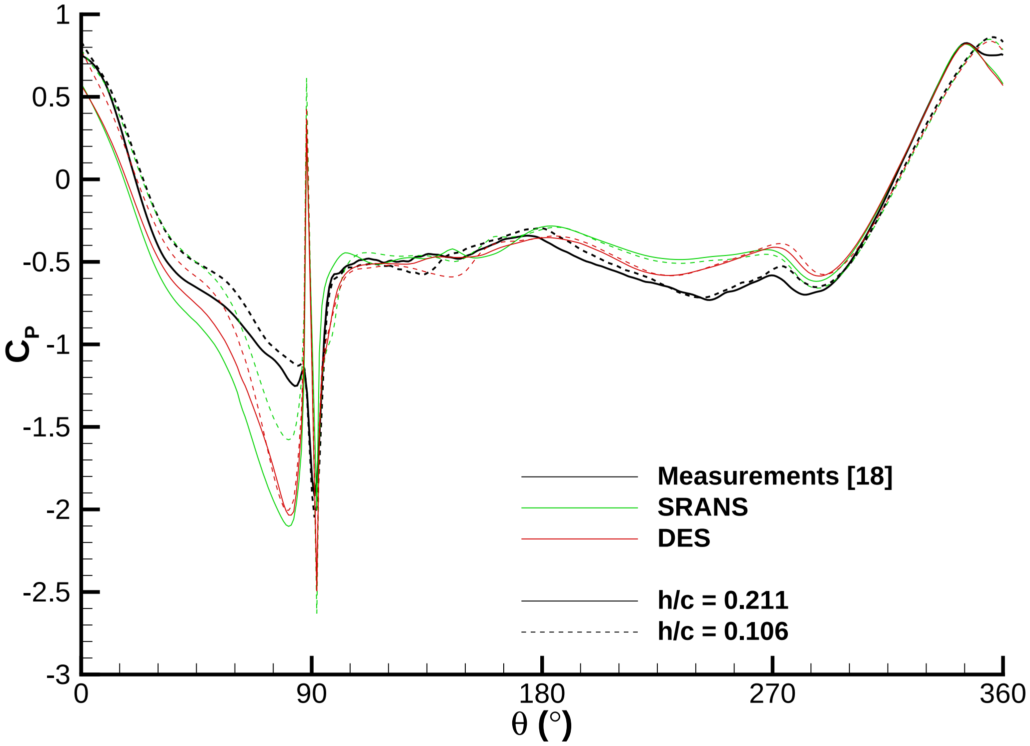

(b) $h/c = 0.211$ & $h/c = 0.106$

Figure 6.4: Experimental and computational pressure distribution around the rotating wheel at location P2 for the combined case at various ride heights.

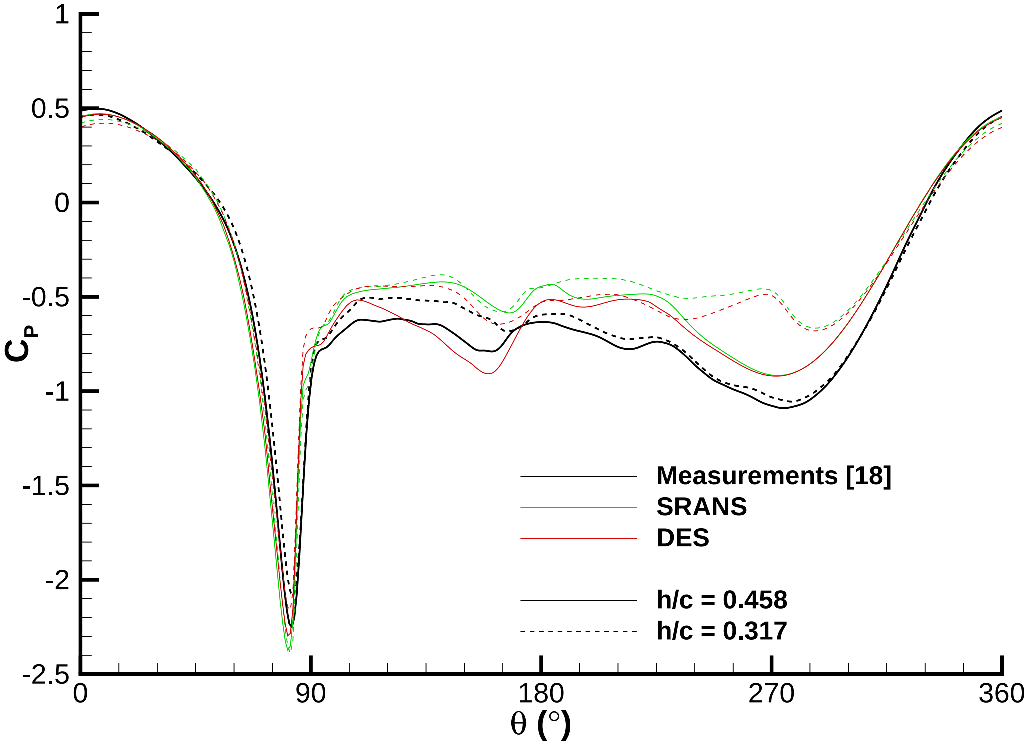

(a) $h/c = 0.458$ & $h/c = 0.317$

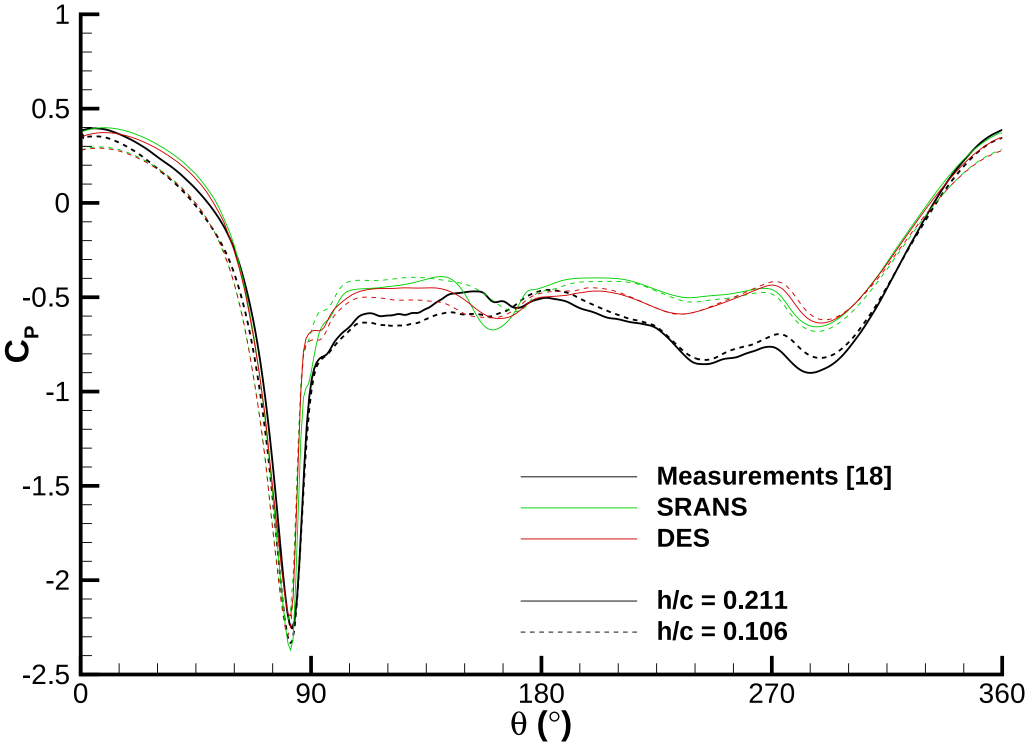

(b) $h/c = 0.211$ & $h/c = 0.106$

Figure 6.5: Experimental and computational pressure distribution around the rotating wheel at location P4 for the combined case at various ride heights.

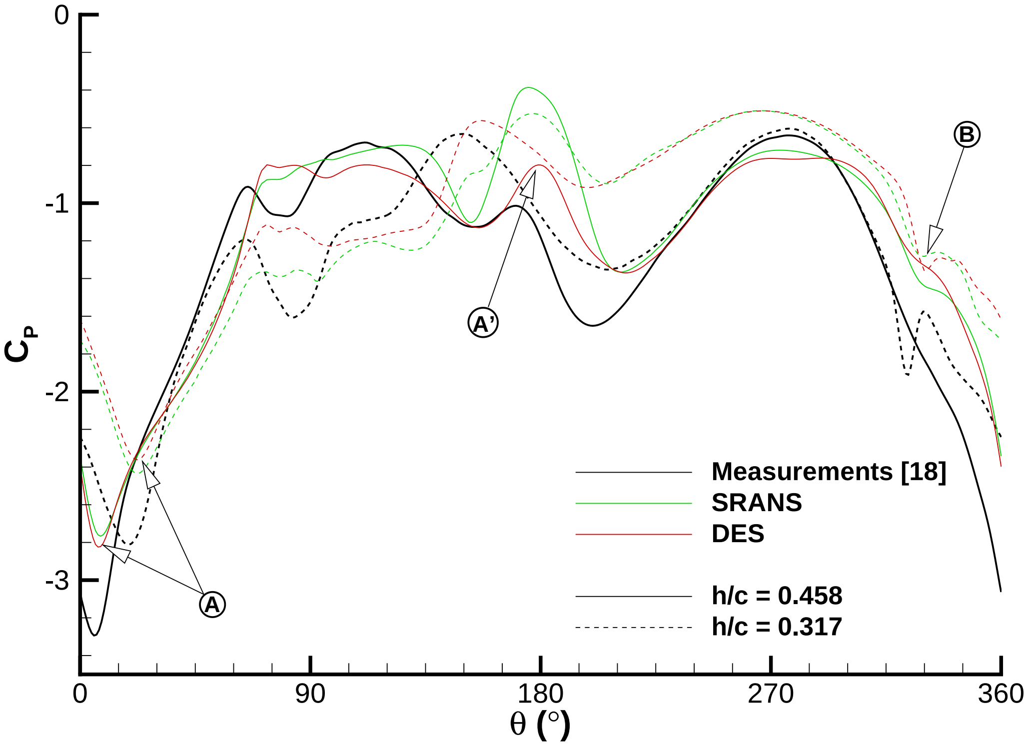

(a) $h/c = 0.458$ & $h/c = 0.317$

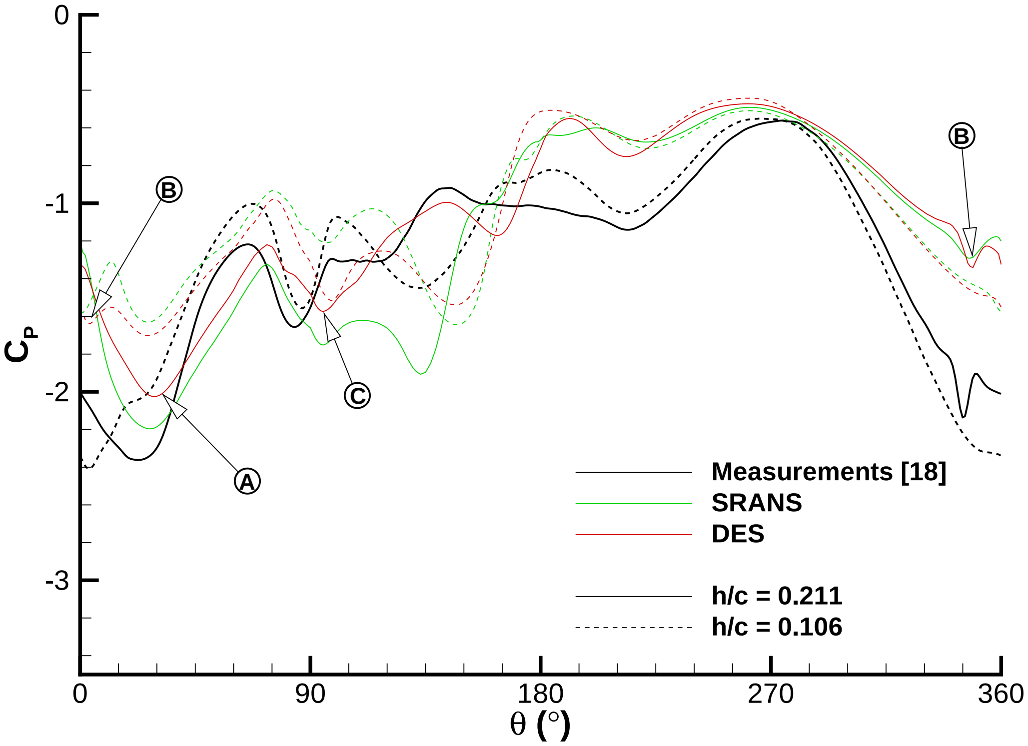

(b) $h/c = 0.211$ & $h/c = 0.106$

Figure 6.6: Experimental and computational pressure distribution around the rotating wheel at location P1 for the combined case at various ride heights.

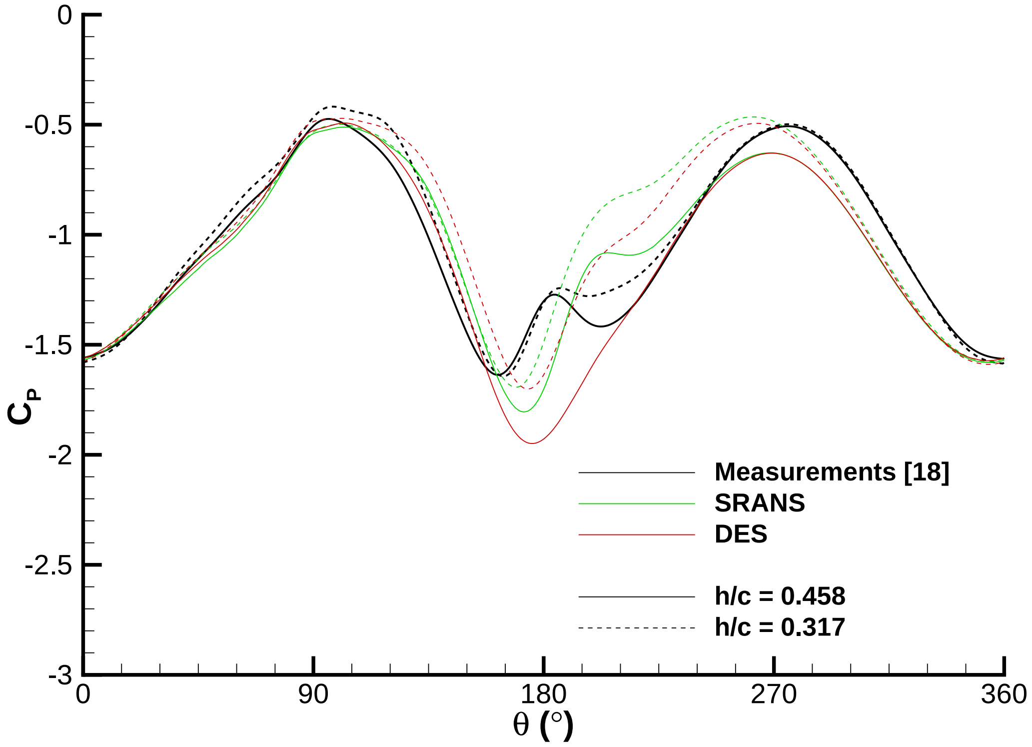

(a) $h/c = 0.458$ & $h/c = 0.317$

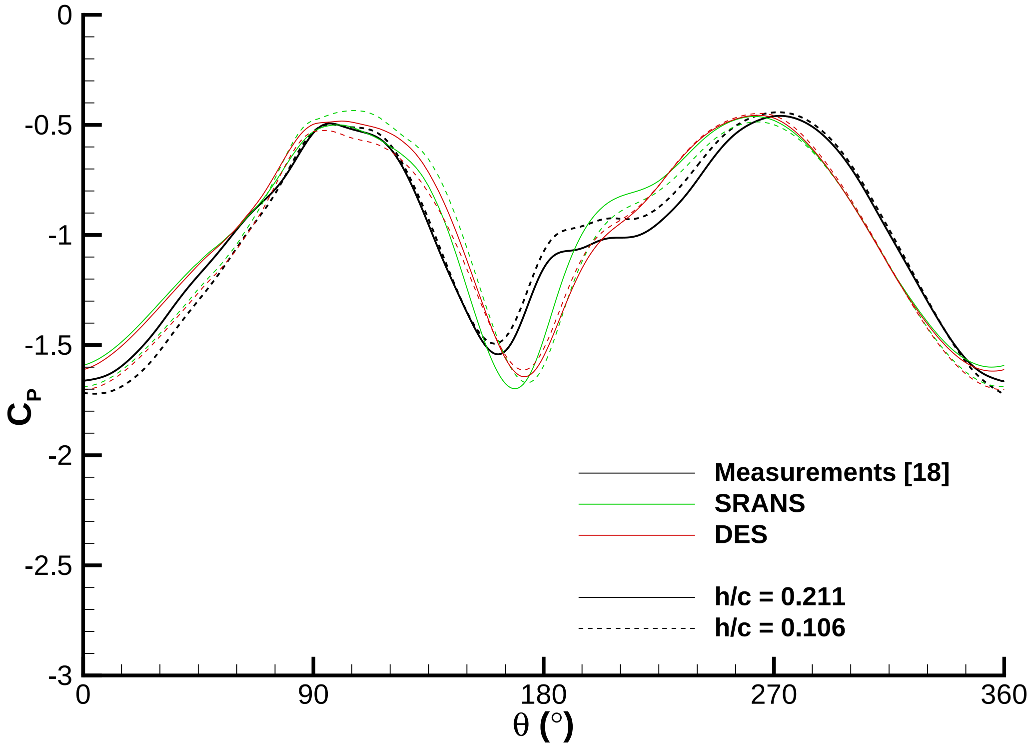

(b) $h/c = 0.211$ & $h/c = 0.106$

Figure 6.7: Experimental and computational pressure distribution around the rotating wheel at location P5 for the combined case at various ride heights.

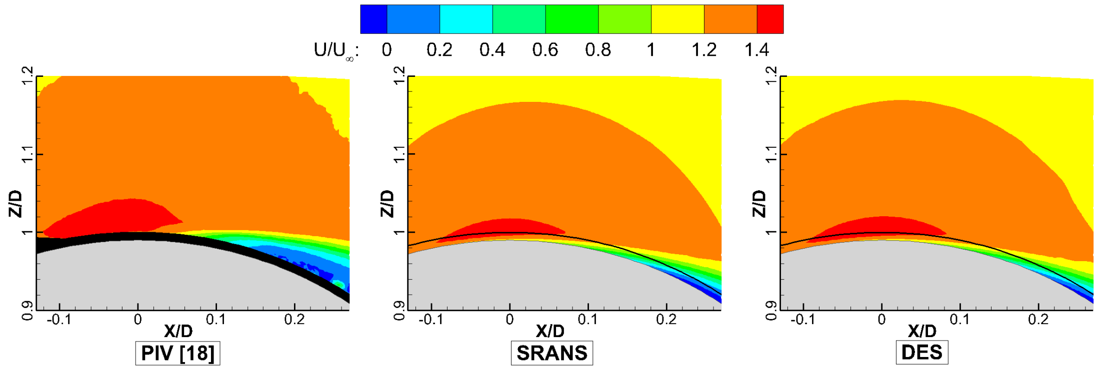

(a) $h/c = 0.458$

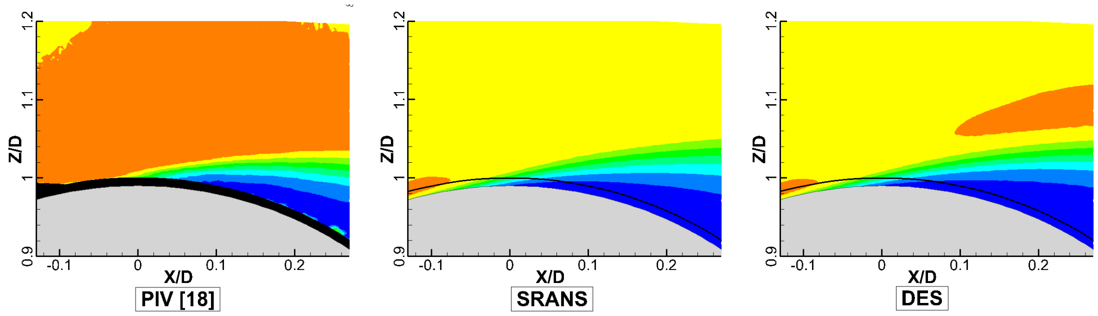

(b) $h/c = 0.317$

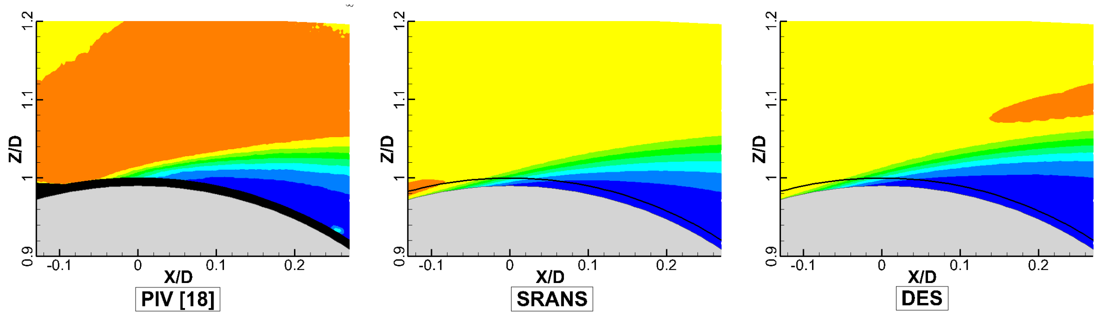

(c) $h/c = 0.211$

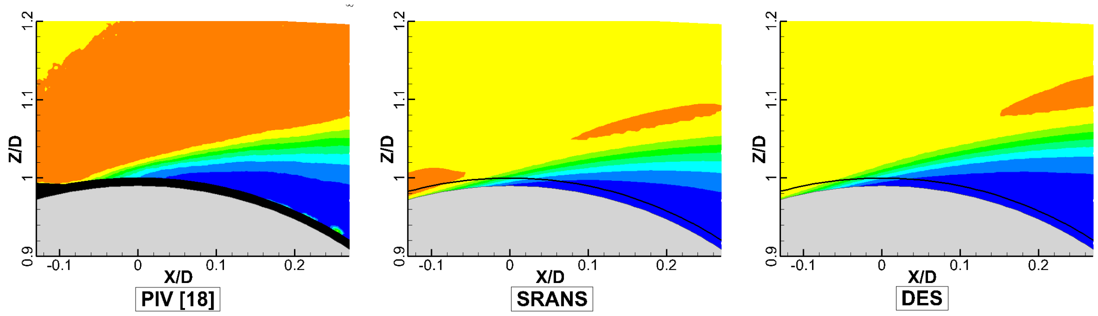

(d) $h/c = 0.106$

Figure 6.8: Contour plot of streamwise velocity on top of the rotating wheel at plane $Y = 0D$ for the combined case, at various ride heights.

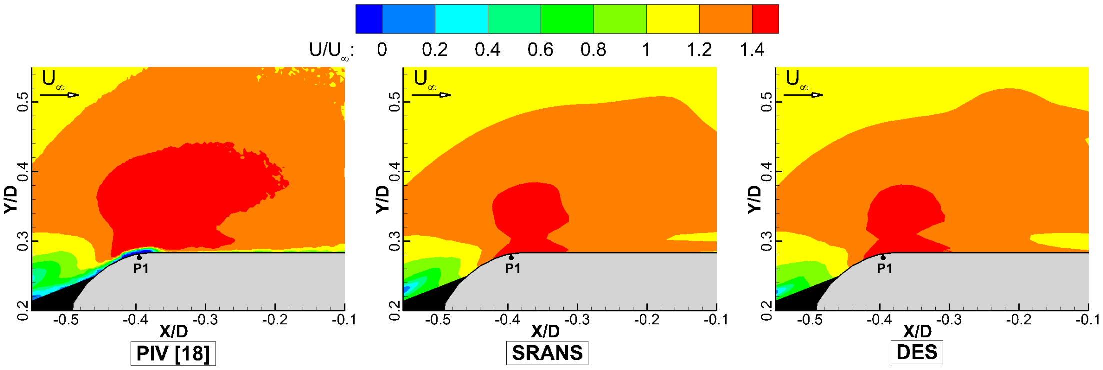

(a) $h/c = 0.458$

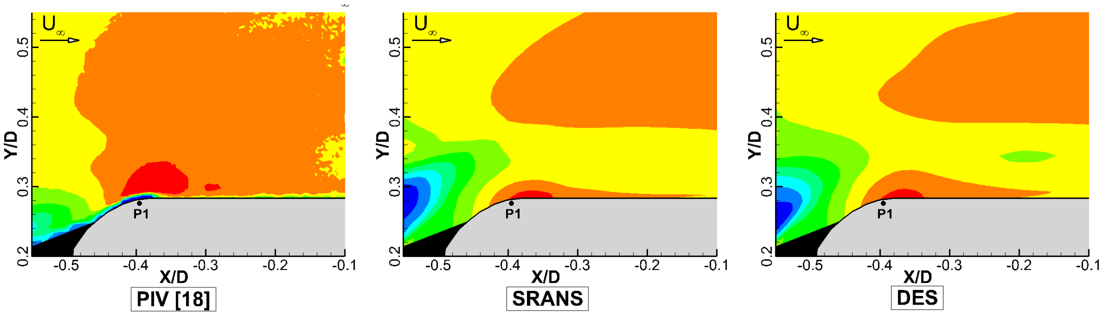

(b) $h/c = 0.317$

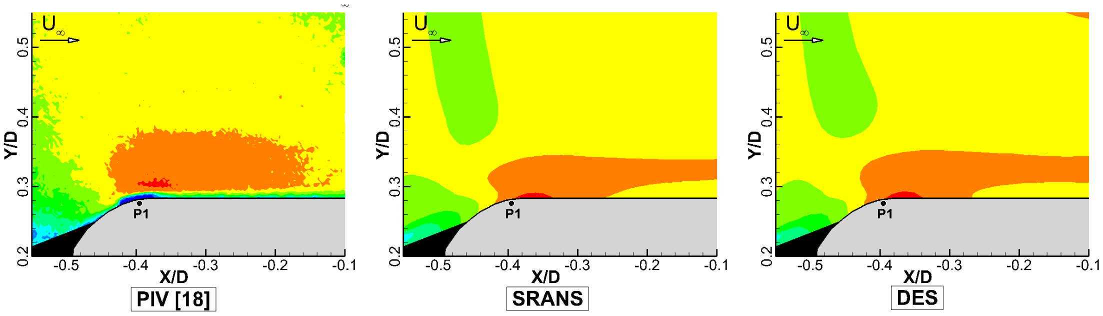

(c) $h/c = 0.211$

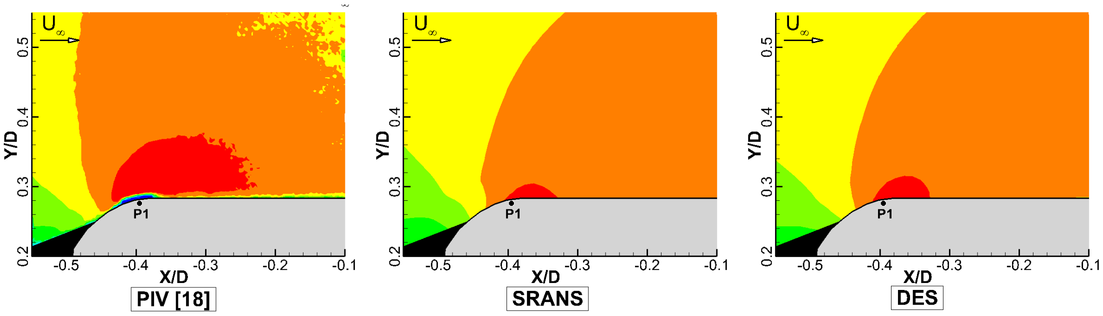

(d) $h/c = 0.106$

Figure 6.9: Contour plot of streamwise velocity in front of the rotating wheel at plane $Z = 0.53D$ for the combined case, at various ride heights.

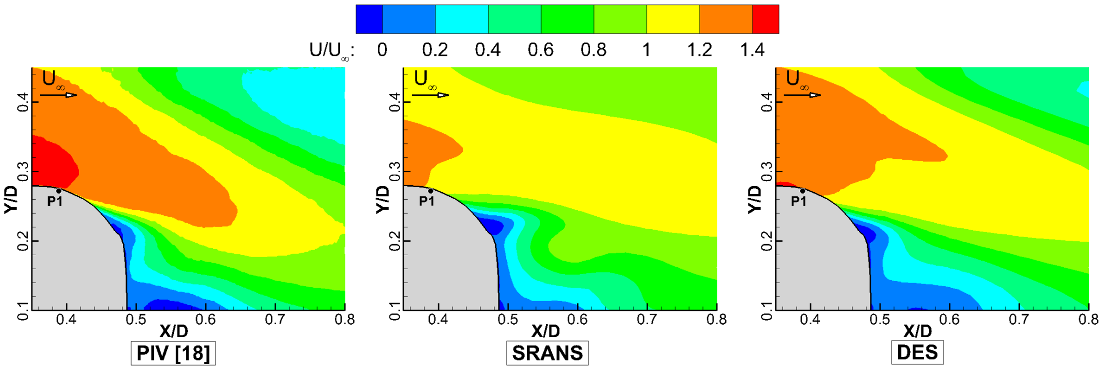

(a) $h/c = 0.458$

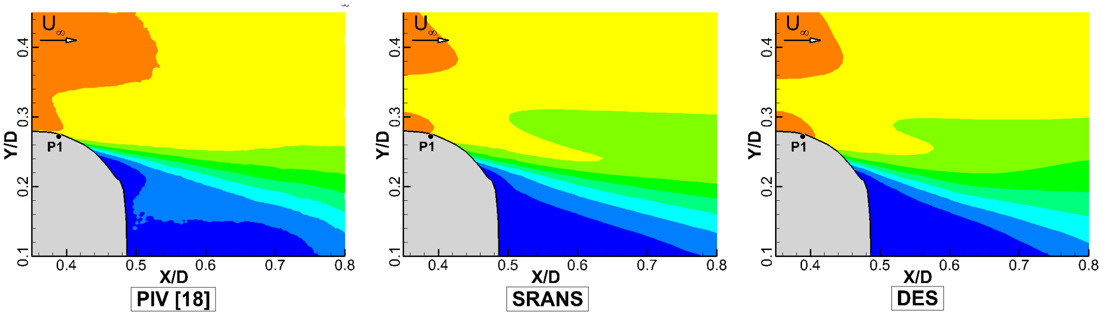

(b) $h/c = 0.317$

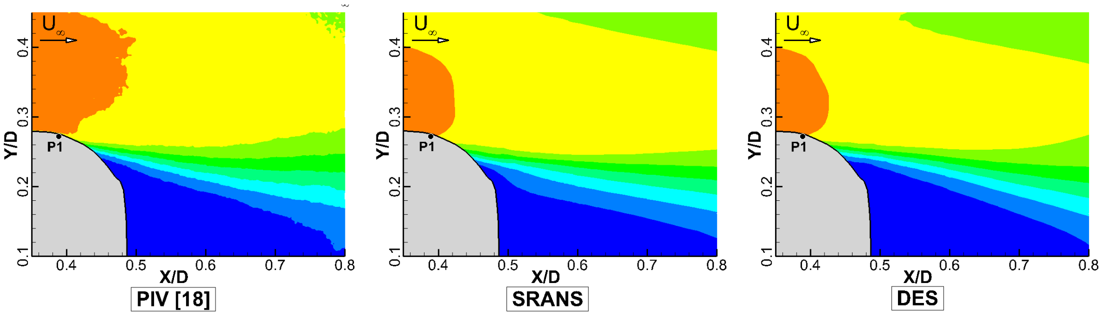

(c) $h/c = 0.211$

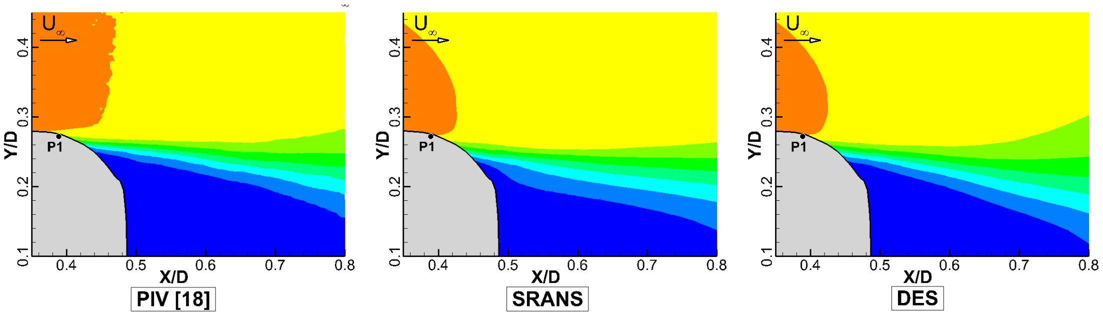

(d) $h/c = 0.106$

Figure 6.10: Contour plot of streamwise velocity behind the rotating wheel at plane $Z = 0.55D$ for the combined case, at various ride heights.

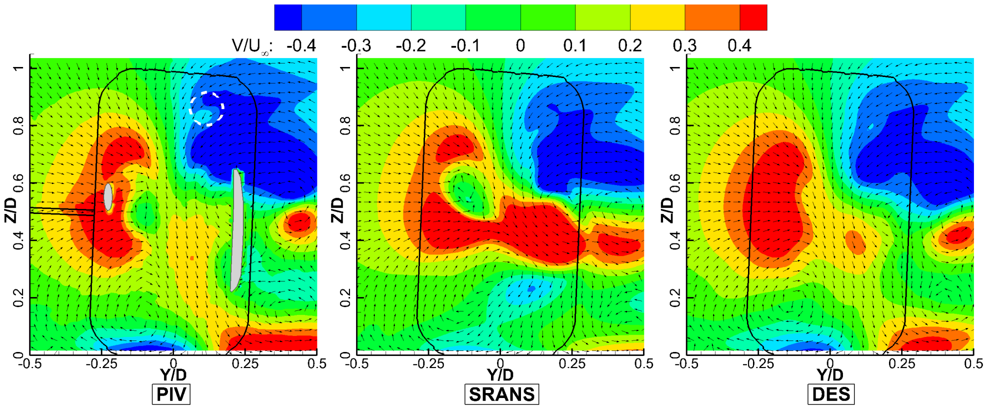

(a) $h/c = 0.458$

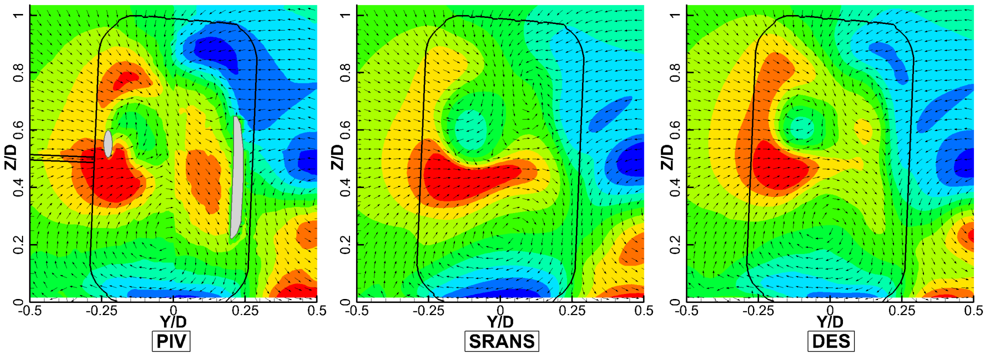

(b) $h/c = 0.352$

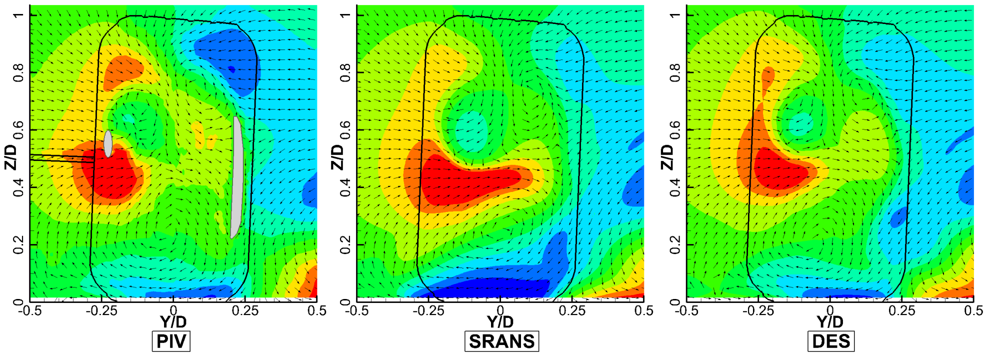

(c) $h/c = 0.211$

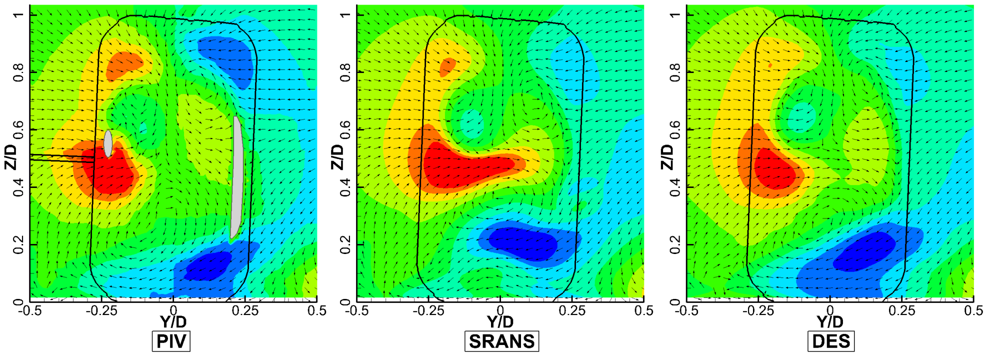

(d) $h/c = 0.106$

Figure 6.11: Contour plot of horizontal velocity behind the rotating wheel at plane $X = 0.6D$ for the combined case, including a uniform velocity vector plot to show the flow structures. Greyed out zones in the PIV results have no data due to reflections.

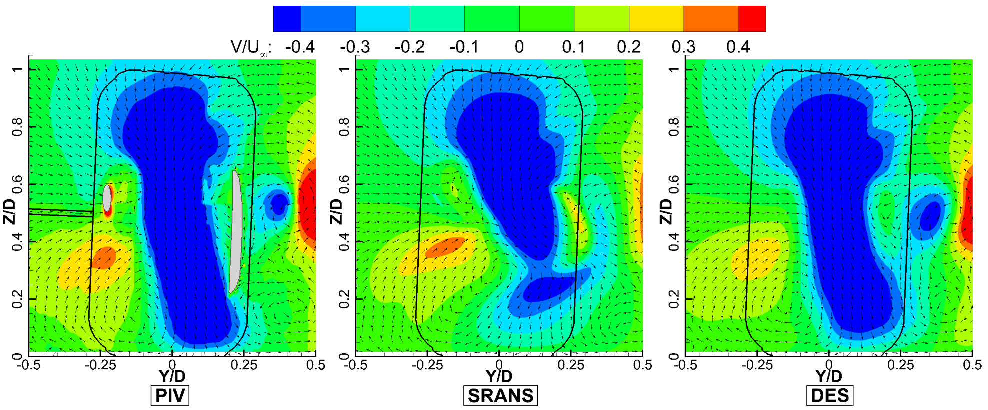

(a) $h/c = 0.458$

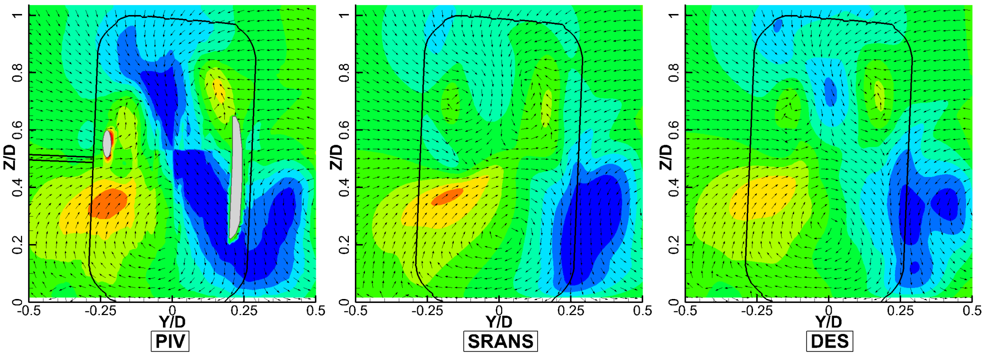

(b) $h/c = 0.352$

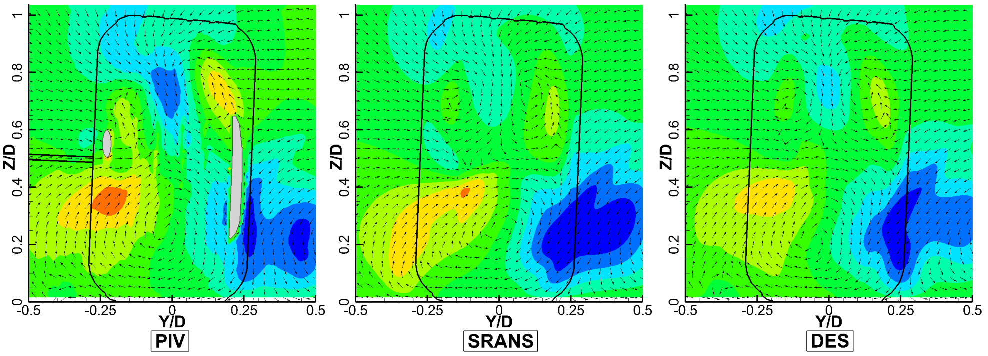

(c) $h/c = 0.211$

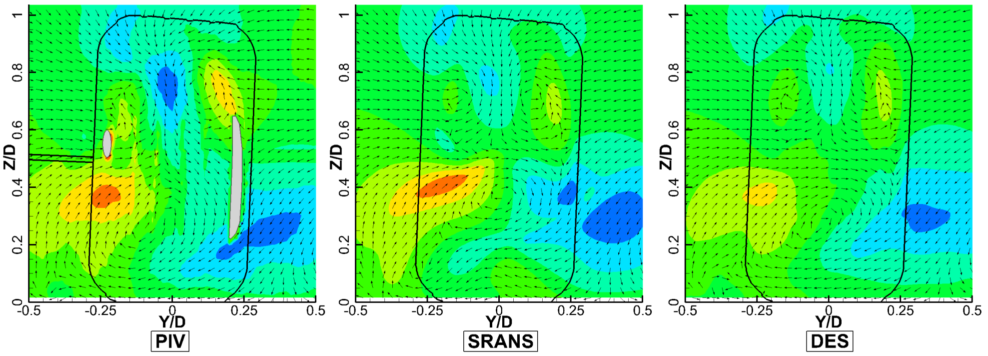

(d) $h/c = 0.106$

Figure 6.12: Contour plot of vertical velocity behind the rotating wheel at plane $X = 0.6D$ for the combined case, including a uniform velocity vector plot to show the flow structures. Greyed out zones in the PIV results have no data due to reflections.

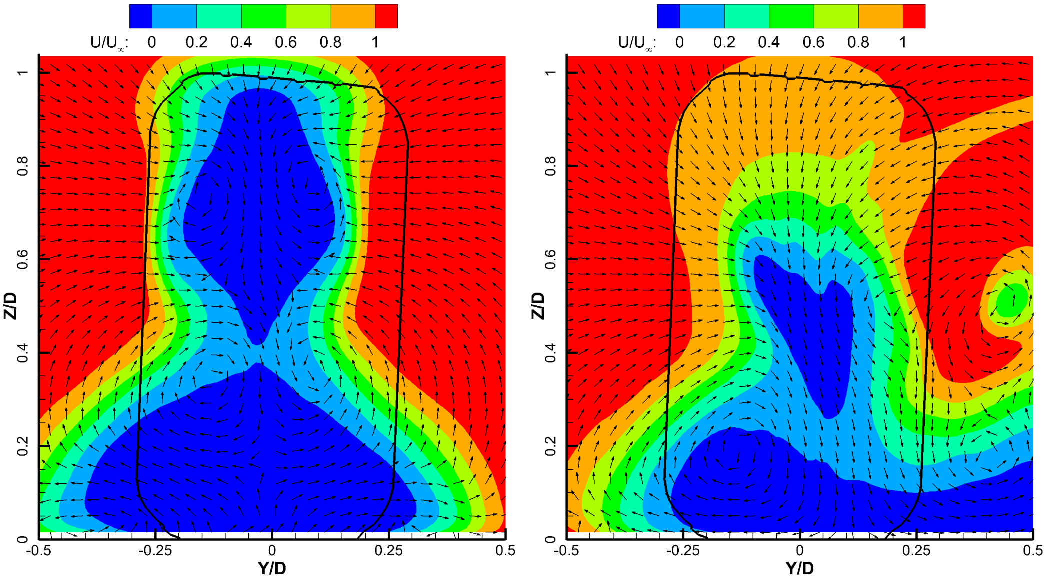

(a) Rotating Isolated Wheel.

(b) $h/c = 0.458$

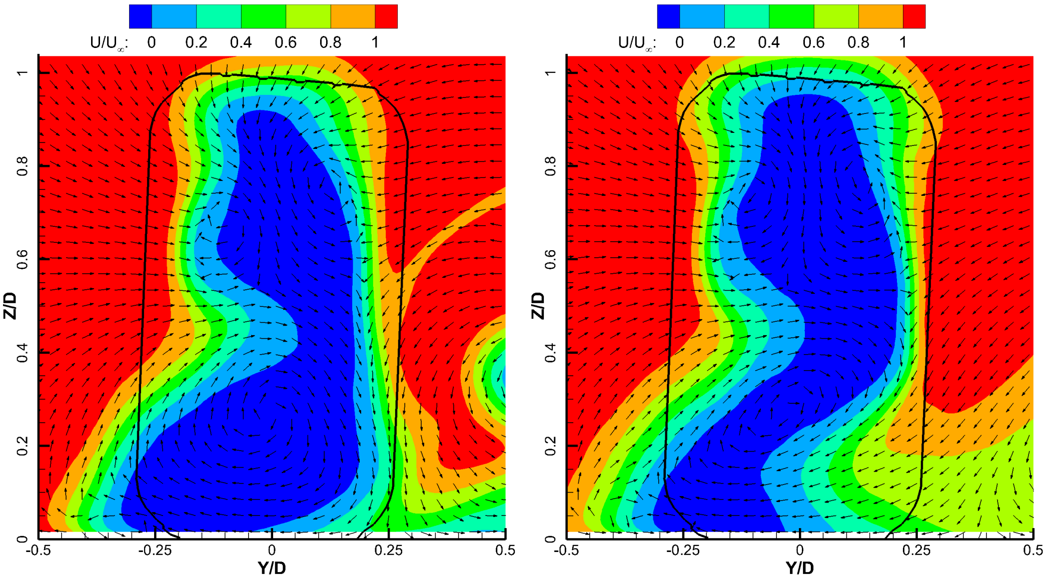

(c) $h/c = 0.317$

(d) $h/c = 0.106$

Figure 6.13: Contour plot of streamwise velocity behind the rotating wheel at plane $X = 0.6D$ from the DES, including a uniform velocity vector plot to show the flow structures

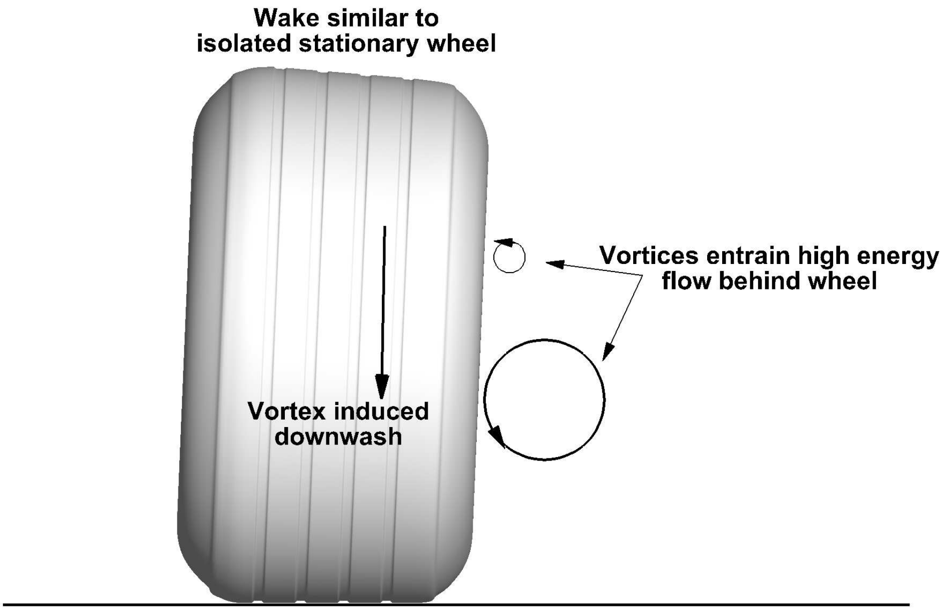

(a) $h/c = 0.352$

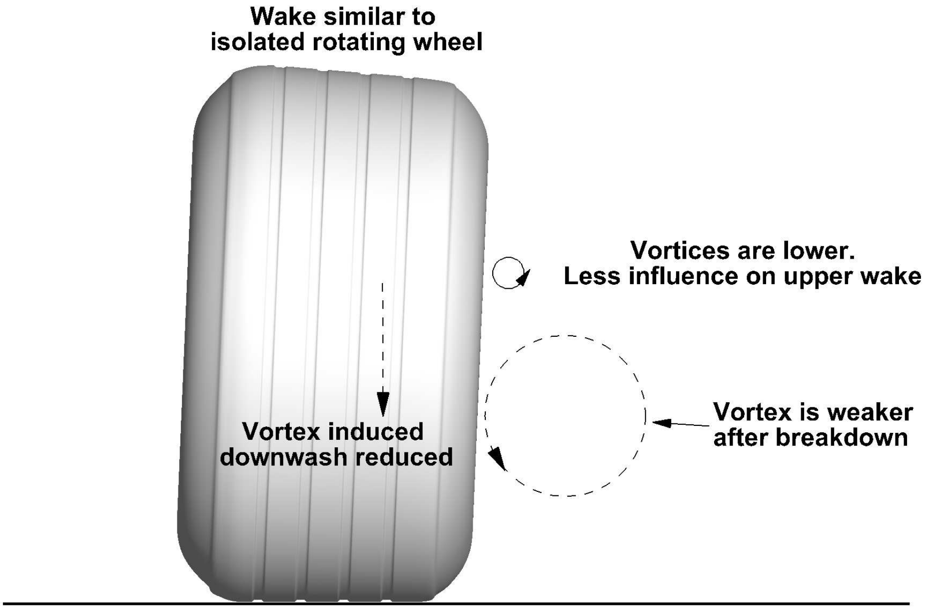

(b) $h/c = 0.317$

Figure 6.14: Sketch of the effect of the wing vortices on the wheel wake at (a)$h/c = 0.352$ and (b)$h/c = 0.317$.

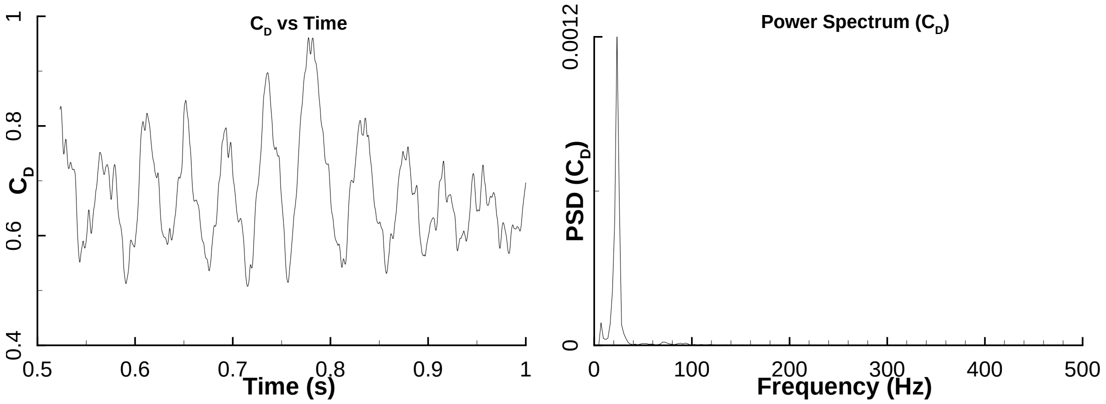

(a) $h/c = 0.458$

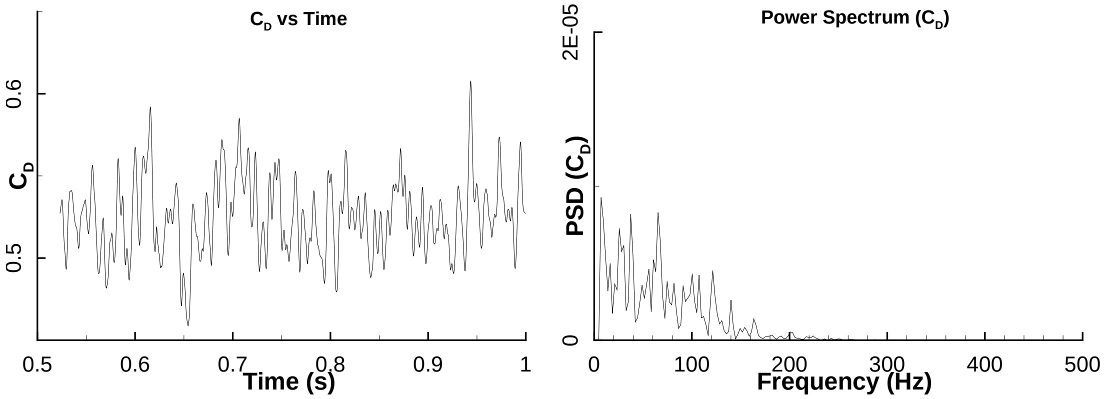

(b) $h/c = 0.317$

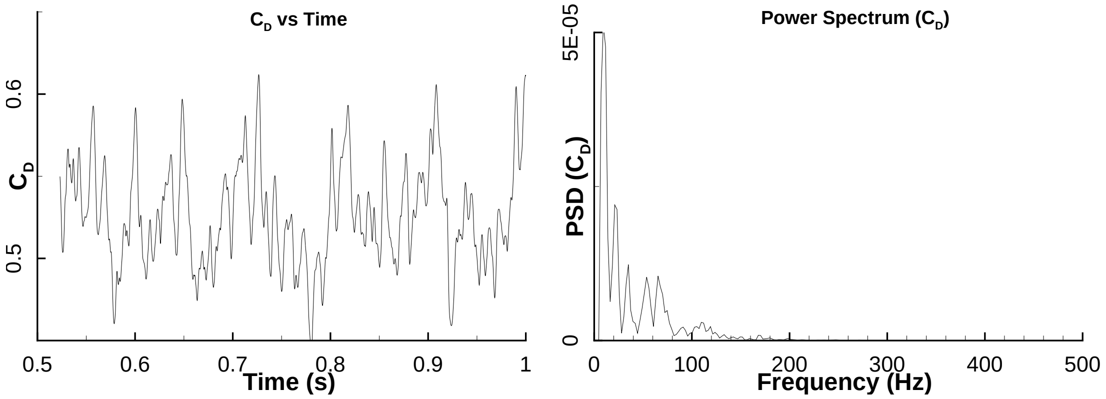

(c) $h/c = 0.106$

Figure 6.15: Time history and power spectral density of the wheel drag coefficient for the combined case at (a)$h/c = 0.458$, (b)$h/c = 0.317$ and (c)$h/c = 0.106$. The results are from the DES model.

Chapter 7

Conclusions and Future Work

This final chapter summarises the various findings made in this study, covering the main objectives defined in Section 1.3. In addition, possible sources of errors, some of which have been noted in the previous chapters, are listed. The chapter is then brought to a close with some recommendations on future research avenues.

7.1 Conclusions

A numerical investigation of an inverted double-element wing at various ride heights in ground effect has been undertaken using SRANS and DES. The latter CFD model produces better predictions of the main flow physics and force behaviours, including the trend with ride height and the lower edge vortex breakdown. The following conclusions can be drawn:

- The pressure distribution of an inverted double-element wing in ground effect is qualitatively predicted by the DES model, which also outperforms a SRANS approach at ride heights below $h/c = 0.211$ as it predicts the lower edge vortex breakdown accurately. The DES model therefore predicts a more accurate overall trend in downforce.
- The DES model captures both the top and lower edge vortex with more accuracy than SRANS when compared to PIV results. Although this does not always have an effect on the wing's pressure distribution, it is important if studying the interaction of the wing's wake with other components in more complex simulations.
- The vortex breakdown is of the bubble type, followed by a spiralling tail. At very low ride heights, the vortex breakdown becomes more severe causing a large region of flow recirculation.

- A refined computational mesh improves the vortex prediction by the DES model whereas the Spalart-Allmaras SRANS model is not sensitive to the change.
- The flow around the wing is steady at high ride heights and becomes unsteady when the lower edge vortex breaks down. But the wing downforce is not significantly affected until much lower ride heights are reached, where the lower edge vortex breakdown is more severe and occurs further upstream, beneath the wing.

A wheel in isolation, both rotating and stationary, was studied with a numerical approach using SRANS and DES. Additional experimental data was also obtained using PIV, providing further insight into the wheel wake. After analysing the available data, the following conclusions can be drawn:

- The DES model is qualitatively accurate when simulating the flow around a wheel, comparing well with the available experimental data. On the other hand, the SRANS approach, which is commonly used in industrial applications, is capable of capturing some features such as the surface pressure distribution around a rotating wheel, but contains inaccuracies in its wake prediction.
- From the time-averaged flow around a rotating wheel, the longitudinal vortices in the wheel wake which have been described in previous studies are not observed. Instead, the wake is separated into two regions: an upper wake, composed of an arch shaped vortex around the top of the wheel where the flow separates; a wider lower wake, which originates from underneath the front of the wheel, where the flow is pushed sideways at a high velocity, separating from the tyre shoulder before being diverted downstream by the surrounding flow.
- The instantaneous flow around a rotating wheel differs significantly from a time-averaged solution. Both the upper and lower wake are composed of periodically shed vortices released from the shear layer which is created as the flow separates from the wheel surface. The flow directly behind the wheel is composed of vortical structures of many sizes appearing randomly. The lift fluctuations are dominated by low frequency pressure fluctuations from both the upper and lower rear surface of the wheel whereas the drag experiences more broadband fluctuations.
- The flow around a stationary wheel stays attached around the top surface, creating a strong downwash behind the wheel and forming a vertically shorter wake than for a rotating wheel. This contributes to higher lift and drag forces. Two counter-rotating vortices are formed as the flow separating from the top half of the tyre shoulders is entrained in the strong downwash behind the wheel. The lower wake is wider than for a rotating wheel as the boundary layer which forms on the stationary

ground has less energy to divert the flow pushed sideways from underneath the front of the wheel.

- The rotating wheel flow is sensitive to changes in freestream velocity below Re= 4.0×10^5. Testing close to the desired Reynolds number is therefore required if the correct flow is to be reproduced.
- The effect of the wheel camber on the flow is small and the wake is quasi symmetric. Major asymmetries in the experimental results are associated to the support structure.

The front wing and the wheel were combined together in an arrangement representative of a typical racecar configuration. A numerical approach using SRANS and DES, with additional PIV experiments, was used to investigate the effect the components have on each other at various wing ride heights. The following conclusions can be drawn from this study:

- The simulations using the Spalart-Allmaras model overpredict the crossflow and incorrectly capture the downwash in the wheel wake. The force trends of the wing and wheel are qualitatively captured, but there is a significant underprediction of the wheel drag. In contrast, the Detached Eddy Simulation accurately captures all the main flow features observed experimentally around the two components and predicts the wheel drag with more precision.
- The wing produces less downforce at high ride heights but more downforce closer to the ground when compared to the isolated case. This is partly associated to the position of the wheel stagnation point relative to the wing, promoting a higher pressure beneath or above the wing tip depending on the ride heights. The wheel rotation does not contribute to the enhanced downforce at lower wing heights.
- The wing lower edge vortex breaks down as it travels along the wheel at high ride heights. At $h/c = 0.211$, vortex breakdown occurs at a similar streamwise position as for the isolated wing, but it is deflected inboard by the wheel presence. The top edge vortex is diverted upward and inboard by the wheel, and has a lower strength than for the isolated wing due to the inboard crossflow that develops between the endplate and the wheel.
- The wheel is sensitive to the wing position, producing more drag and lift at high wing ride heights. There is a critical wing position where a sudden change occurs to the wheel flow structure. At high ride heights, the flow around the wheel resembles that of an isolated stationary wheel. At low ride heights, the flow around the wheel

resembles that of an isolated rotating wheel. This change is associated to the position of the wing top edge vortex and to the circulation induced by the wing, but also to the lower edge vortex, which undergoes breakdown before reaching the wheel rear shoulder at the critical wing position.

- The crossflow induced through the gap between the wing endplate and the wheel increases the separation on the lower front of the inboard tyre shoulder. This wake structure is constricted by the lower edge vortex to varying degrees depending on the ride height.
- The instantaneous flow around the components is composed of similar structures as for the isolated cases. At low ride heights, the shed vortices in the inboard lower wheel wake are absorbed by the stronger wing lower edge vortex. At high wing ride heights, when the flow around the top of the tyre stays attached, there is a strong fluctuation in the wheel drag which is caused by changes in pressure in the lower rear half of the wheel. This is associated to the interaction between the upper and lower wheel wake.

7.2 Sources of Error

While comparing the experimental results with the CFD, the different possible sources of error must be remembered. The support struts were not modelled in the CFD and this has two consequences: the blockage effect is not accurately represented and the interference of the wake of the supporting structure is not simulated. The blockage due to the support structure, which has a combined frontal area of $0.1716m^2$, is around 5% based on the windtunnel area. Using the ESDU data sheets [72], it was estimated that they would increase the forces by approximately 1% on the wing, but have a smaller effect on the wheel force coefficients[1], increasing them by 0.5%.

The wheel used for the pressure data in the experiments had a different profile which affects the comparison between the CFD and experiments, although quantifying this error is not readily possible. Instead, it has been observed that the difference in profile appears to cause local separation from the back of the tyre shoulder.

The PIV data is affected by parallax error, reducing the accuracy of the measured velocities around the image edges (see Appendix B). Although this was corrected for Plane X behind the wheel, the DES streamwise velocity was used, which is only an approximation. Further uncertainty in the PIV setup has been detailed in Section 2.3.4.

---

[1] The wheel is a bluff body and therefore a different blockage correction is used

An uncertainty analysis of the experimental wing pressure data and force measurements has been done by Mahon [16] and Van den Berg [18] respectively.

The computational grid density might not fully resolve all the flow features. A grid refinement study showed that the baseline grid was enough to capture the main flow features, though it is believed that a finer grid would give results (with the DES model) more comparable to experimental data, but it would increase the required simulation resources significantly.

7.3 Recommendations for Future Work

The current study has expanded the field of an inverted wing and wheel aerodynamics in ground effect, proposing new descriptions of the flowfield and new explanations for observed trends. Nevertheless, many additional aspects are still to be investigated and the following section presents recommendations of future work to further increase the understanding in the field. It is divided in two categories: general recommendations and computational modelling.

7.3.1 General Recommendations

The wing and wheel used in this study are simplified versions of Formula 1 components in order to analyse the main flow features. More realistic models could be studied to make the study more practical. In the current FIA regulations, the wing span has changed, increasing the overlap with the wheel, and the tyre grooves have been removed.

Mahon studied the effect of a footplate mounted at the bottom of the endplate for an isolated wing. This could be investigated further and combined with a wheel to study the changes in the flowfield due to the footplate. Other areas of interest include changes in the wing profile to represent modern wings, more complex endplate shapes or additional wing elements.

The wheel rim was blocked with cover discs impeding any crossflow through the wheel. These could be removed to investigate the effect of the spokes on the flow around the tyre. Additional geometry such as brake ducts and suspension could be studied with their effect on the wheel wake analysed.

The wing ride height was the only parameter varied in the current research, with the wing and wheel placed at a constant overlap and gap of $20mm$. Additional wing positions could be tested, considering the latest FIA regulations, and the effect of the variation of other parameters could be studied, such as the flap angle of attack or its position relative to the main element.

7.3.2 Computational Modelling

Both the Spalart-Allmaras and Detached-Eddy Simulation models were used throughout this research, with little investigation done into the different turbulent models available. Although the DES model improved the accuracy of the results around both the wing and the wheel, there were still areas where it did not capture the experimental trend correctly. The mesh size used in this research was limited to approximately eight million cells due to hardware constraints, but refining the mesh improved the accuracy of the captured flow features with the DES model.

As the available computational power increases, simulations with a greater mesh density would improve the prediction of the wheel wake or the wing vortices. In addition, other approaches to simulate the flow, such as the Large Eddy Simulation model, become feasible alternatives with the potential of improved accuracy when modelling complex flow structures and interactions.

Appendix A

Wheel Drag Correction

The wheel drag is measured experimentally using a 1-component load cell. But, it will not only measure the aerodynamic drag because of the rolling road configuration at the University of Southampton $2.1m \times 1.7m$ wind tunnel. The wheel rotation is induced through the ground translation, creating non-aerodynamic forces which will be captured by the load cell. The following have been identified as possible sources of these forces: resistance in the wheel bearing, wheel camber, misalignment of the wheel and errors in wheel balance. Although the latter two can be removed through careful preparation, the friction in the wheel bearing will always be present, and the camber of a non-deformable wheel will introduce reaction forces as the tread is conic but is forced to travel in a straight line.

In the previous experimental study conducted by Van den Berg, this error in the measured drag was acknowledge and an attempt to remove it was made by measuring the wheel drag at low ground velocities ($2.5m/s$) without wind. It was assumed that at this low speed, the induced aerodynamic drag would be negligible, and the measured force would be purely caused by the various sources discussed previously. This measurement, in Newtons, was thereafter subtracted from the results.

Van den Berg decided not to use the force data he acquired with road only (no wind) at high velocities because of the induced aerodynamic drag which would be present as boundary layers on the ground and wheel surfaces develop. It is suggested here that his correction method, using a run at $2.5m/s$, would underestimate the sources of error when the testing velocity increases to $30m/s$. Therefore, it is instead proposed to use CFD to account for the induced aerodynamic drag at the high velocity runs, allowing for an estimate of the non-aerodynamic forces to be made. The numerical simulation, using SRANS with the S-A turbulence model, was setup as described in section 2.2. The fine grid of 7.0 million cells was used and the only change was to the velocity inlet, where the normal velocity was set to $0m/s$.

Figure A.1 compares the wheel drag from experimental measurements and numerical simulations for the road only configuration at various velocities. Also shown is the non-aerodynamic drag, which was computed by subtracting the aerodynamic drag (obtained computationally) from the total drag (obtained experimentally). It can be seen that at $2.5m/s$ there is only a very small contribution ($\approx 5\%$) from the aerodynamic drag to the total measured drag, confirming the assumption that the force measured by the load cell at this velocity would be in major part caused by the rolling road. But this is limited to low velocities as the induced aerodynamic drag increases with velocity, and at $30m/s$ it contributes to 30% of the measured drag.

From Figure A.1, the drag value measured experimentally at $2.5m/s$ is found to be 0.104N. This was used by Van den Berg as the non-aerodynamic drag to correct the wheel drag results at all the velocities investigated. Using the proposed method of correction, the non-aerodynamic drag varies from 0.238N to 0.788N between $10m/s$ and $30m/s$. Therefore, the higher the velocity, the larger the forces caused by the rolling road become. Figure A.2 shows the change of wheel drag with Reynolds number (based on the wheel diameter) in the wind and road configuration, comparing the two correction methods. Although it is acknowledged that the new correction method will not be exact, it is believed to be a better approximation than what was used previously.

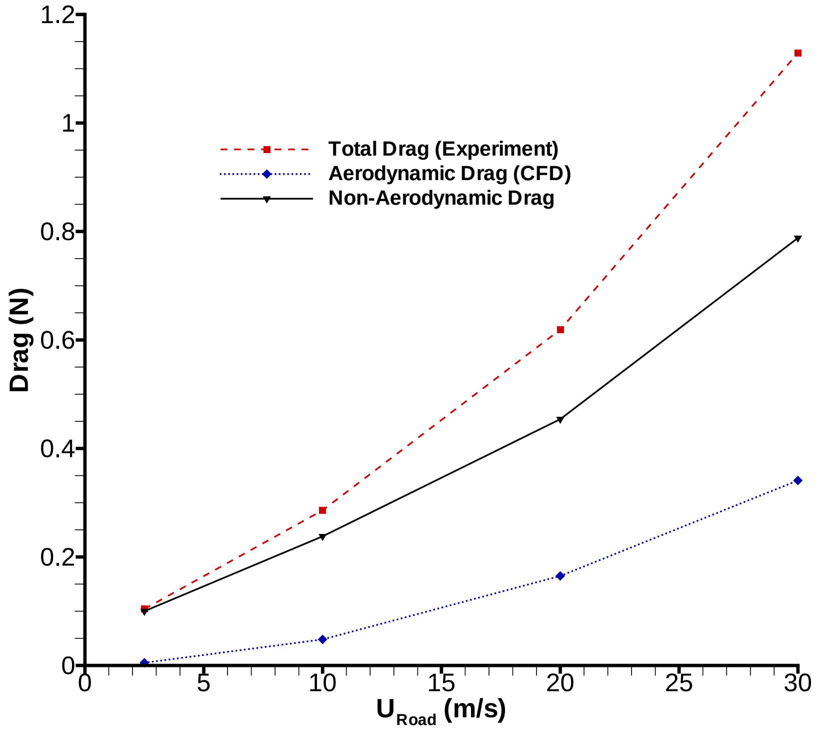

Figure A.1: Components of the measured wheel drag for road only case

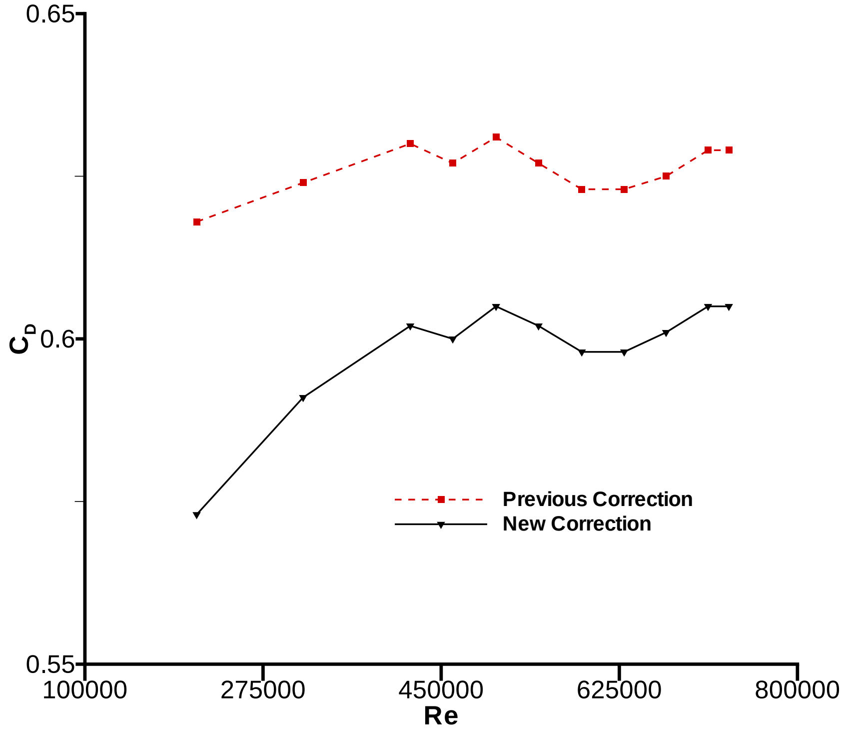

Figure A.2: Comparison of the isolated wheel drag correction methods at different Reynolds numbers

Appendix B

PIV Parallax Error Correction

Particle image velocimetry is a non-intrusive technique which allows the measurement of flow velocities to be made. The principle relies on comparing two pictures of flow particles taken at a short time interval, from which the trajectory and velocity of the particles can be extracted. The particles are illuminated by a powerful dual laser, which flashes twice (once for each image) for only a few nanoseconds and the images are captured by a dual CCD camera. Apart from the noise present in the results due to particles entering and exiting the investigated area between the first and second image, there is another source of error associated to this technique, which is related to the parallax effect.

The parallax effect can be described as an apparent displacement of an object when viewed along different lines of sight, with nearby objects having a larger parallax. As an example, two particles both at the centre of a 2D image, but each one at a different depth, would form a single point at the centre, but if the camera was moved (in-plane), the particle closest to the camera would appear to move further away, and both particles would be visible. The in-plane distance between these two particles becomes greater when they are further from the centre of the image.

Considering simple 2D PIV, as used in our experiments, the velocities are measured in a 2D plane and the third through-plane velocity is not captured. When the two images are taken with the specified time interval, the through-plane velocity of each particle will bring it closer or further from the camera. As explained previously, this will cause an apparent motion in the 2D plane and is defined as the parallax error. This error is increased if the through-plane velocity is high or if the particles are further from the image centre (the parallax error is null at the image centre). It is also affected by the distance of the camera to the 2D plane investigated, with larger distances reducing the parallax error.

The measured in-plane velocity can be corrected for parallax using the following equations:

$$D_X = \frac{\left(X - \overline{U}_m \bullet t\right)}{\left(1 + \frac{D_Z}{d_0 - D_Z}\right)} - X \tag{B.1}$$

$$D_Y = \frac{\left(Y - \overline{V}_m \bullet t\right)}{\left(1 + \frac{D_Z}{d_0 - D_Z}\right)} - Y \tag{B.2}$$

where

- X and Y are the in-plane horizontal and vertical positions of the interrogation window relative to the image centre.
- $\overline{U}_m$ and $\overline{V}_m$ are the uncorrected in-plane horizontal and vertical velocities measured with PIV.
- t is the time between the two exposures.
- d_0 is the distance of the camera from the investigated plane.
- D_X, D_Y and D_Z are the actual particle displacement between the two exposures in the horizontal, vertical and through-plane directions respectively.

The required values are D_X and D_Y which can then be converted back to velocity using t. The only unknown is the through-plane displacement D_Z. This was estimated using CFD, where the mean streamwise velocity from the DES results, which can be seen for the isolated wheel case at plane $X = 0.6D$ in Figure B.1, was used to obtain D_Z. This correction was only applied to plane $X = 0.6D$ as the through-plane velocities were high in some areas and the parallax error was clearly visible when the 4 images were recomposed to form the whole plane (see Figure B.2). As it can be observed from Figure B.2, the correction mainly affects the borders of each image, and results in a qualitatively similar velocity distribution.

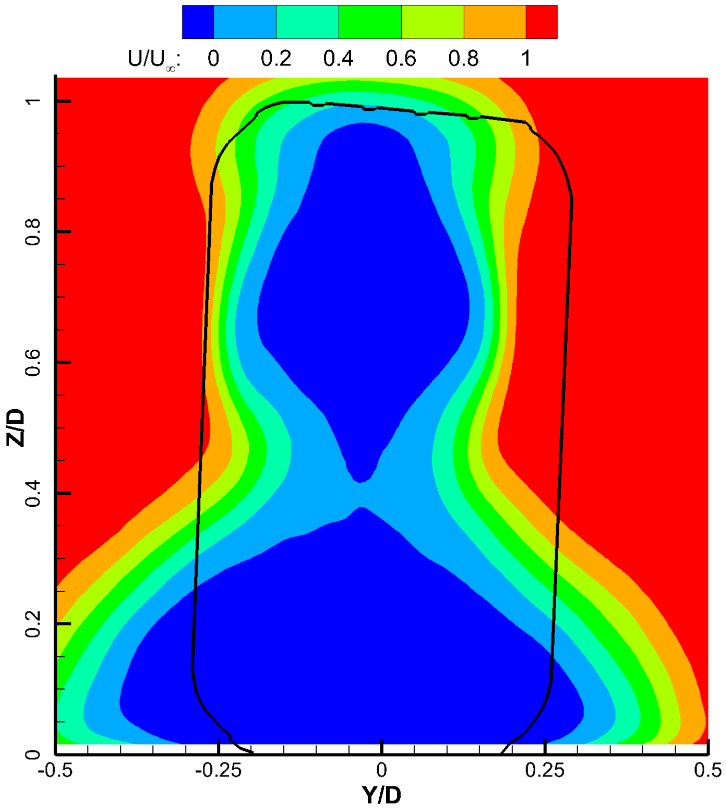

Figure B.1: Streamwise velocity from DES for the isolate wheel case at plane X=0.6D

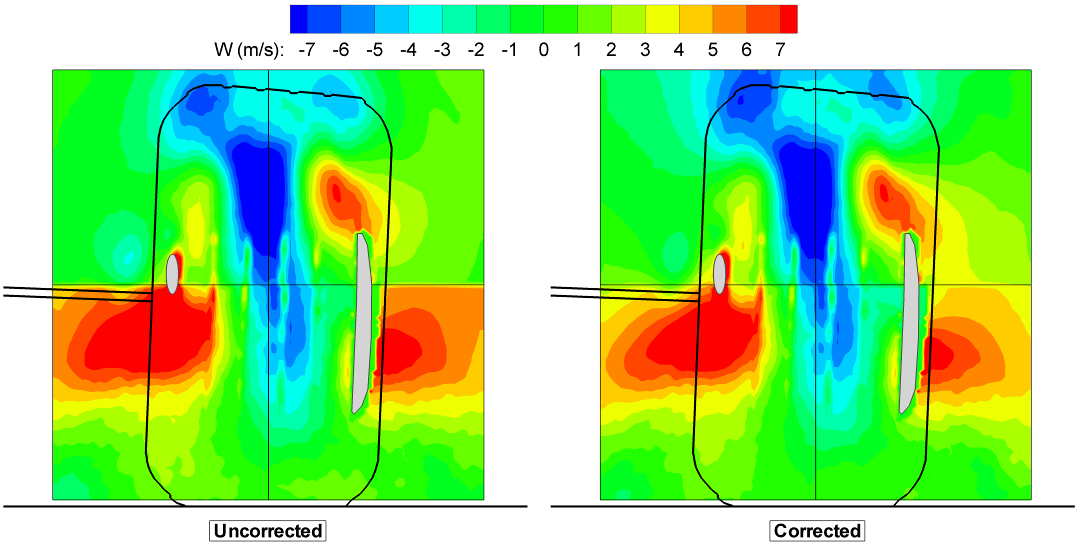

Figure B.2: Comparison of the vertical velocity from PIV for the isolated wheel case at plane X=0.6D with and without parallax correction

Bibliography

[1] Wright, P.G. The influence of aerodynamics on the design of formula one racing cars. *International journal of vehicle design*, vol. 3,num. 4:383–397, 1982.

[2] Agathangelou, B. and Gascoyne, M. Aerodynamic design considerations of a formula 1 racing car, 1998. SAE Publication 980399.

[3] Knowles, K., Donahue, D. T., and Finnis, M. V. A study of wings in ground effect. *RAeS conference on vehicle aerodynamics*, pages 22.1–22.13, 1994.

[4] Ranzenbach, R., and Barlow, J.B. Two-dimensional airfoil in ground effect, an experimental and computational study, 1994. Society of automotive engineers, Paper 94-2509.

[5] Ranzenbach, R., and Barlow, J.B. Cambered airfoil in ground effect: wind-tunnel and road conditions, 1995. AIAA paper 95-1909.

[6] Ranzenbach, R., and Barlow, J.B. Cambered airfoil in ground effect - an experimental and computational study, 1996. Society of automotive engineers, Paper 96-0909.

[7] Zerihan, J.D.C. *An investigation into the aerodynamics of wings in ground effect.* PhD thesis, University of Southampton, Southampton, UK, 2001.

[8] Zerihan, J.D.C. and Zhang, X. Aerodynamics of a Single Element Wing in Ground Effect. *Journal of Aircraft*, 6:1058–1064, 2000.

[9] Zhang, X. and Zerihan, J.D.C. Turbulent wake behind a single element wing in ground effect. Technical report, 10th International Symposium: Applications of laser techniques to fluid mechanics, 2000.

[10] Zhang, X., Zerihan, J.D.C., Ruhrmann, A. and Deviese, M. Tip vortices generated by a wing in ground effect. Technical report, 11th International Symposium: Applications of laser techniques to fluid mechanics, 2002.

[11] Zerihan, J.D.C. and Zhang, X. A single element wing in ground effect; comparisons of experiments and computation, 2001. AIAA 2001 - 0423.

[12] Mahon, S. and Zhang, X. Computational analysis of a inverted double-element airfoil in ground effect. *Journal of Fluids Engineering, ASME*, 128(6):1172–1180, 2006.

[13] Ranzenbach, R., and Barlow, J.B. Multielement airfoil in ground effect: an experimental and computational study, 1997. Society of automotive engineers, Paper 97-2238.

[14] Jasinski, W.J. and Selig, M.S. Experimental study of open-wheel race car front wings. Technical Report SAE 98–3042, SAE, 1998.

[15] Zhang, X. and Zerihan, J.D.C. Aerodynamics of a double-element wing in ground effect. *AIAA Journal*, 41:1007–1016, 2003.

[16] Mahon, S.A. *The aerodynamics of multi-element wings in ground effect.* PhD thesis, University of Southampton, Southampton, U.K., 2005.

[17] Petrov, A.V. Certain Types of Separated Flow over Slotted Wings. *Fluid Mechanics, Soviet Research*, 7(5):80–88, 1978.

[18] Van den Berg, M.A. *Aerodynamic interaction of an inverted wing with a rotating wheel.* PhD thesis, University of Southampton, Southampton, U.K., 2007.

[19] Bearman, P. W. Near wake flows behind two- and three-dimensional bluff bodies. *Journal of Wind Engineering and Industrial Aerodynamics*, pages 33–54, 1997.

[20] Morelli, A. Aerodynamic effects on an automobile wheel, 1969. Technical Report Translation 47/69, MIRA.

[21] Stapleford, W.R. and Carr, G.W. Aerodynamic characteristics of exposed rotating wheels. Technical Report 1970/2, MIRA, 1970.

[22] Cogotti, A. Aerodynamic characterisitcs of car wheels, 1983. International Journal of Vehicle Design, Special Publication SP3, no. 33.

[23] Fackrell, J.E. and Harvey, J.K. The flow field and pressure distribution of an isolated road wheel, 1973. Advances in Road Vehicle Aerodynamics, BHRA Fluid Engineering.

[24] Fackrell, J.E. and Harvey, J.K. The aerodynamics of an isolated road wheel, 1975. Proceedings of the Second AIAA Symposium of Aerodynamics of Sports and Competition Automobiles.

[25] Mears, A.P., Dominy, R.G. and Sims-Williams, D.B. The flow about an isolated rotating wheel - effects of yaw on lift, drag and flow structure, 2002. 4th MIRA International Vehicle Conference, 2002, Gaydon, UK.

[26] Mears, A.P., Dominy, R.G. and Sims-Williams, D.B. The air flow about an exposed racing wheel, 2002. SAE Publication 2002-01-3290.

[27] Mercker, E., Breuer, N., Berneburg, H. and Emmelmann, H.J. On the aerodynamic interference due to the rolling wheels of passenger cars, 1991. SAE Publication 910311.

[28] Skea, A.F., Bullen, P.R. and Qiao, J. CFD simulations and experimental measurements of the flow over a rotating wheel in a wheel arch, 2000. SAE Publication 2001-01-0487, Reprinted from Vehicle Aerodynamics (SP-1524), SAE 2000 World Congress, March 6–9, 2000, Detroit, Michigan.

[29] Oswald, L.J and Browne, A.L. The airflow field around an operating tire and its effect on tire power loss, 1981. SAE Technical Report 810166.

[30] Mears, A.P., Crossland, S.C. and Dominy, R.G. An investigation into the flow-field about an exposed racing wheel, 2004. SAE Publication 2004-01-0446.

[31] Axerio, J., Iaccarino, G., Issakhanian, E., Lo, K., Elkins, C. and Eaton, J. Computational and Experimental Investigation of the Flow Structure and Vortex Dynamics in the Wake of a Formula 1 Tire. Technical Report SAE Technical Paper Series 2009-01-0775, SAE, 2009.

[32] Axerio, J. and Iaccarino, G. Asymmetries in the wake structure of a formula 1 tire, 2009. 6th International Symposium on Turbulence and Shear Flow Phenomena, June 2009, Seoul, Korea.

[33] Wäschle, A., Cyr, S., Kuthada, T. and Wiedemann, J. Flow around an Isolated Wheel - Experimental and Numerical Comparison of Two CFD Codes. Technical Report SAE Technical Paper Series 2004-01-0445, SAE, 2004.

[34] Saddington, A., Knowles, R., and Knowles, K. Laser Doppler anemometry measurements in the near-wake of an isolated Formula One wheel. *Sports Engineering*, 42:671–681, 2007.

[35] Diasinos, S. and Gatto, A. Experimental Investigation into Wing Span and Angle-of-Attack Effects on Sub-Scale Race Car Wing/Wheel Interaction Aerodynamics. *Exp Fluids*, 45:537–546, 2008.

[36] Knowles, R., Saddington, A. and Knowles, K. On the near wake of rotating 40%-scale champ car wheels, 2002. SAE Publication No. 2002-01-3293, Reprinted from Proceedings of the 2002 SAE Motorsports Engineering Conference and Exhibition (P-382), December 2–5,2002, Indianapolis, Indiana.

[37] Purvis, A.R. and Garry, K.P. The Wake Behind a Deformable Racing Tyre, 2004. 5th MIRA International Vehicle Conference, 2004, Gaydon, UK.

[38] Axon, L., Garry, K. and Howell, J. An evaluation of CFD for modeling the flow around stationary and rotating wheels. Technical report, SAE, 1998. SAE Publication 980032.

[39] Skea, A.F., Bullen, P.R. and Qiao, J. The use of CFD to predict the air flow around a rotating wheel, 1998. Proceedings of the 2nd International Conference On Vehicle Aerodynamics, UK.

[40] Basara, B., Beader, D. and Przulj, V. Numerical simulation of the air flow around a rotating wheel, 2000. 3rd MIRA International Vehicle Aerodynamics Conference, 2000, Rugby, UK.

[41] McManus, J. and Zhang, X. A computational study of the flow around an isolated wheel in contact with the ground. *Journal of Fluids Engineering, Transactions of the ASME*, 128(3):520–530, 2006.

[42] Knowles, R., Saddington, A. and Knowles, K. Simulation and experiments on an isolated racecar wheel rotating in ground contact, 2002. 4th MIRA International Vehicle Conference, 2002, Gaydon, UK.

[43] Mears, A.P., Crossland, S.C. and Dominy, R.G. Racing car wheel aerodynamics - comparisons between experimental and CFD derived flow-field data, 2004. SAE Publication 2004-01-0445.

[44] Kellar, W.P., Pearse, S.R.G and Savill, A.M. Formula 1 car wheel aerodynamics. *Sports Engineering*, 2:203–212, 1999.

[45] Van den Berg, M. and Zhang, X. The Aerodynamic Interaction Between an Inverted Wing and a Rotating Wheel. *Journal of Fluids Engineering, Transactions of the ASME*, 131:1–13, 2008.

[46] Spalart, P.R., Jou. W.-H., Strelets. M., and Allmaras, S.R. Comments on the feasibilty of LES for wings, and on a hybrid RANS/LES approach, 1997. First AFOSR International Conference on DNS/LES. In advances in DNS/LES, C. Liu & Z. Liu, Greyden Press, Columbus, OH.

[47] Spalart, P.R. and Allmaras, S.R. A one-equation turbulence model for aerodynamic flows, 1992. AIAA paper 92-0439.

[48] Squires, K.D. Detached-eddy simulation: current status and perspectives. Technical report, MAE Department, Arizona State University, 2004.

[49] Constantinescu, G., Chapelet, M. and Squires, K.D. Turbulence modeling applied to flow over a sphere. *AIAA Journal*, 41(9):1733–1742, 2003.

[50] Achenbach, E. Experiments on the flow past spheres at very high Reynolds number. *Journal of fluid mechanics*, 54(3):565–575, 1972.

[51] Nishino, T. Dynamics and stability of flow past a circular cylinder in ground effect, 2007. PhD, Doctoral Thesis, University of Southampton.

[52] Maddox, S., Squires, K.D., Wurtzler, K.E. and Forsythe, J.R. Detached-eddy simulation of the Ground Transportation System, 2002. United Engineering Foundation, The Aerodynamics of Heavy Vehicles: Trucks, Buses and Trains.

[53] Storms, B.L., Ross, J.C., Heineck, J.T., Walker, S.M., Driver, D.M., Zilliac, G.G. An experimental study of the Ground Transportation System (GTS) model in the NASA Ames 7- by 10-ft wind tunnel. Technical report, NASA/TM-2001-209621, 2001.

[54] Hedges, L.S., Travin, A. K. and Spalart, P.R. Detached-eddy simulations over a simplified landing gear. *Journal of fluids engineering*, 124:413–423, 2002.

[55] Lazos, B. Mean flow around the inline wheels of four-wheel landing gear. *AIAA Journal*, 40(2):193–198, 2002.

[56] Cummings, R.M., Morton, S.A. and Forsythe, J.R. Detached-eddy simulation of slat and flap aerodynamics for a high-lift wing, 2004. AIAA paper 2002-0425.

[57] Morton, S., Forsythe, J., Mitchell, A., Hajek, D. Detached-eddy simulation and Reynolds–averaged Navier–Stokes simulations of delta wing vortical flowfields. *Journal of fluids engineering*, 124:924–932, 2002.

[58] Mitchell, A. M., Molton, P., Barberis, D., and Delery, J. Oscillation of vortex breakdown location and control of the time-averaged location by blowing. *AIAA journal*, 38(5):793–803, 2000.

[59] Morton, S., Forsythe, J., Squires, K., Wurtzler, K. Assessment of unstructured grids for detached-eddy simulation of high Reynolds number separated flows, 2002.

[60] Spalart, P.R. Young-Person's Guide to Detached-Eddy Simulation Grids, 2001.

[61] Mahon, S. and Zhang, X. Computational analysis of pressure and wake characterisitcs of an aerofoil in ground effect. *Journal of Fluids Engineering, Transactions of the ASME*, 127(2):290–298, 2005.

[62] Constantinescu, G., Pacheco, R. and Squires, K.D. Detached-eddy simulation of flow over a sphere, 2002. AIAA paper 2004-1233.

[63] Breuer, M., Jovicic, N. and Mazaev, K. Comparison of DES, RANS and LES for the separated flow around a flat plate at high incidence. *Int. J. Numer. Meth. Fluids*, 41:357–388, 2003.

[64] Forsythe, J.R., Wentzel, J.F., Squires, K.D., Wurtzler, K.E. and Spalart, P.R. Computation of Prescribed Spin for a Rectangular Wing and for the F-15E Using Detached-Eddy Simulation, 2003. 41st Aerospace Sciences Meeting, AIAA 2003 0839.

[65] Pointwise. Gridgen version 15 manual, 2005.

[66] Fluent Incorporated. Fluent version 6.2 manual, 2005.

[67] M. Shur, P. R. Spalart, M. Strelets, and A. Travin. Detached-Eddy Simulation of an Airfoil at High Angle of Attack, 1999. 4th Int. Symposium on Eng. Turb. Modeling and Experiments, Corsica, France.

[68] Welch, P.D. The Use of Fast Fourier Transform for the Estimation of Power Spectra: A Method Based on Time Averaging Over Short, Modified Periodograms. *IEEE Trans. Audio Electroacoustics*, Vol. AU-15:70–73, 1967.

[69] The Mathworks, Inc. Matlab version 7.6 manual, 2008.

[70] Jeong, J. and Hussain, F. On the identification of a vortex. *Journal of Fluid Mechanics*, 285:69–94, 1995.

[71] Harvey, J.K. and Perry, F.J. Flowfield produced by trailing vortices in the vicinity of the ground. *AIAA Journal*, 9(8):1659–1660, 1971.

[72] Engineering Sciences Data Unit. Blockage corrections for bluff bodies in confined flows, 1998. ESDU Data Unit 80024.